Graz University of Technology

Mingqiu Wu, MSc.

Microscopic Models for the Comprehensive Investigation of Wet Powder Blending

DOCTORAL THESIS

to achieve the university degree of 'Doktor der technischen Wissenschaften' at the

Graz University of Technology

Supervisor

Univ.-Prof. Dipl.-Ing. Dr.techn. Johannes G. Khinast

Institute of Process and Particle Engineering

Graz University of Technology

Co-supervisor

Ass.Prof. Dipl.-Ing. Dr.techn. Stefan Radl

Institute of Process and Particle Engineering

Graz University of Technology

Graz, Austria, July 2017

Mingqiu Wu

Microscopic Models for the Comprehensive Investigation
of Wet Powder Blending

Dissertation

First assessor

Univ.-Prof. Dipl.-Ing. Dr.techn. Johannes G. Khinast

Institute of Process and Particle Engineering

and

Research Center Pharmaceutical Engineering GmbH

Graz University of Technology

External assessor

Assoz. Univ.-Prof. Dr. Stefan Pirker

Department of Particle Flow Modelling

Johannes Kepler University, Linz

STATUTORY DECLARATION

I declare that I have authored this thesis independently, that I have not used other than the declared sources / resources, and that I have explicitly marked all material which has been quoted either literally or by content from the used sources.

(Ich erkläre an Eides statt, dass ich die vorliegende Arbeit selbstständig verfasst, andere als die angegebenen Quellen/Hilfsmittel nicht benutzt, und die den benutzten Quellen wörtlich und inhaltlich entnommene Stellen als solche kenntlich gemacht habe.)

July, 2017 .....

MSc. Mingqiu Wu

Für meine Familie

Acknowledgements

First of all, I would like to thank my main advisor Prof. Johannes Khinast giving me the opportunity to this research project of wet powder blending and putting extra support for me to finish the thesis. I would like to thank my external assessor Prof. Stefan Pirker for his valuable time reading this manuscript and join in as my examiner. Specially, I would like to thank Dr. Stefan Radl who is my co-advisor during this thesis, for his superior expertise in the field, fruitful discussions and faith in me. Dr. Radl spends an enormous amount of time helping me writing papers (and correcting them), reading this thesis and preparing presentations. It was not always easy, but in the end it is mainly due to his constant pushes and hard work that this thesis became possible. I would like to thank all the colleagues and friends at the Institute, who create a good and friendly environment during my stay here. Especially, my colleagues in simulation science group (Benedict, Christian, Federico, Jakob, Sadegh, Thomas, and Theresa) who made the time inside and outside the office much more enjoyable.
Furthermore, I would like to thank the secretary group, namely Adela, Michaela and Silvia, for all the helps with administrative forms. Also, Stefan (Scheer) helped a lot, along with all the technical support as well as setup the virtual sandbox. Furthermore, I would like to express my gratitude to Professor Gernot Krammer for his brilliant talk with me not only regarding with academy but also life. I would like to thank the Continuous Processes group (Dr. Gruber-Wölfler, Bianca, Peter1 and Peter2) for creating such a friendly atmosphere to work in.
Also, the Austrian Science Fund (FWF, P23617 and WKP 67) and Prof. Khinast's Institute made this thesis possible through its financial support. I gratefully acknowledge support from NAWI Graz by providing access to dcluster.tugraz.at, as well as TU Graz icluster.tugraz.at.

Finally, by far the biggest gratitude belongs to my whole family, especially my wife Yi who gives me a lot of patience and always believed in me.

Preface

This cumulative PhD thesis in chemical engineering consists of two parts.

The first one is the research part which is concerned with the research project "Comprehensive Investigation of Wet Powder Blending". The objective of this project is the development of microscopic models to comprehensively study wet granular system. The numerical approaches for particle simulations employed here are mainly direct numerical simulation and the discrete element method. The analysis is mainly carried out numerically and theoretically. Specifically, numerical strategies to directly simulate wet granulate flows at high saturation levels have been developed. Also, a model to predict liquid transport from particle surfaces into liquid bridge regions has been developed. This newly developed model has been used to simulate particle systems involving several hundred thousand of particles in small periodic domains. These simulations focused on evaluating the effect of the liquid bridge model on hydrodynamic of a fluidized bed of particles.

The second part is the educational part which is concerned with the educational and communication project "The Virtual Sandbox". The objective of the second part is building a virtual sandbox, and presenting the sandbox to public audience. In the end, a virtual model of the real-world sand surface should be reconstructed, and the benefits of such a virtual sand model should be explorable by the user.

This thesis is based on the following peer-review papers:

Paper 1. **Wu, M.**, Radl, S., Khinast, J. G., *A Model to Predict Liquid Bridge Formation between Wet Particles Based on Direct Numerical Simulations*, AIChE Journal, 2016, p.1877-1897, volume 6, doi:10.1002/aic.15184.

Paper 2. **Wu, M.**, Khinast, J., Radl, S., *Liquid Transport Rates during Binary Collisions of Unequally-sized Particles*. Powder Technology, 2017, p. 95-109, volume 309, doi: 10.1016/j.powtec.2016.12.080

Paper 3. **Wu, M.**, Khinast, J., Radl, S., *The Effect of Liquid Bridge Model Details on the Dynamics of Wet Fluidized Beds*, AIChE Journal, revised manuscript in preparation, July 2017.

Paper 4. Reichel, E., Redlinger-Pohn, J. D., **Wu, M.,** Ecker, K., Wachtler, L., Bahar, B., Khinast, J., Eck, J. & Radl, S, *The Virtual Sandbox: Forschendes Lernen am Beispiel der Partikelphysik*,. 2016 In: Plus Lucis 3/2016, p. 43-47

Kurzfassung

Die Flüssigkeitsbrückenbildung ist für die Mischeigenschaften von feuchten Pulvern von Bedeutung, da sie (i) die während der Kollisionen übertragene Flüssigkeitsmenge bestimmt, sowie (ii) die Größe von Kohäsionskräften zwischen Partikeln durch viskose und kapillare Effekte beeinflusst. Diese Dissertation beschäftigt sich mit mikroskopischen Modellen die erforderlich sind um diese beiden Phänomene vorherzusagen.

Während eine Vielzahl von Literatur existiert, die ein solides Verständnis der Kohäsionskräfte dokumentiert, ist dies bei dem Brückenvolumen nicht der Fall: die in der Literatur verfügbaren Modelle konzentrieren sich auf statische Brücken, oder den Brückenbruch allein. Zudem wurden diese Modelle meist nicht durch experimentelle, theoretische oder numerische Untersuchungen abgesichert. Zum Beispiel basiert das in der Literatur oft verwendete Modell von Shi und McCarthy (Powder Technology 2008, 184: 64-75) lediglich auf geometrischen Argumenten, denen keine physikalische Argumentation zu Grunde liegt.

Der erste Teil dieser Arbeit zeigt, dass dieses Modell aus der Literatur sogar qualitativ falsch ist: Das Modell von Shi und McCarthy kann die nichtlineare Zunahme des Brückenvolumens mit der auf den Partikeln vorhandenen Flüssigkeitsmenge nicht vorhersagen. Folglich wird eine korrekte geometrische Analyse eines Referenz-Brückenvolumens präsentiert. Insbesondere wird festgestellt, daß im Falle einer Flüssigkeitsbrücke zwischen zwei benetzten Partikeln eine nichtlineare Beziehung zwischen der Filmdicke, dem Partikel-Partikel-Abstand und dem Flüssigkeitsbrückenvolumen besteht. Auch die Geschwindigkeit der Brückenbildung wird zum ersten Mal analysiert, was zur Formulierung eines dynamischen Flüssigkeitsbrückenmodells führt. Dieses Modell wird folglich angewendet, um Brückenfüllraten in monodispersen Partikelschüttungen zu untersuchen. Es zeigt sich, dass diese Füllraten für

Systeme mit hochviskosen Flüssigkeiten und kurzen Kollisionen von entscheidender Bedeutung sind.

Der zweite Teil der Arbeit beschäftigt sich mit der Verallgemeinerung des dynamischen Brückenmodells für polydisperse Systeme. Es wird gezeigt, dass die für monodisperse Systeme entwickelte funktionelle Form des dynamischen Flüssigkeitsbrückenmodells vielversprechend ist: auch die Übertragungsraten in Systemen mit ungleichgroßen Partikeln können damit beschrieben werden.

Der dritte Teil der Arbeit beschäftigt sich mit der Anwendung der mikroskopischen Flüssigkeitsbrückenmodelle auf feuchte Wirbelschichten. Die zentrale Motivation dieser Studie ist es, die Grenzen der verfügbaren mikroskopischen Flüssigkeitsbrückenmodelle zu untersuchen. Dazu werden feuchte Wirbelschichten in kleinen periodischen Bereichen mit dem CFD-DEM-Verfahren simuliert. Eine Flüssigkeitsbrücke wird bei Partikel-Partikel-Kollisionen gebildet, die dann bricht, wenn die Partikeldistanz einen kritischen Wert übersteigt. Die Simulationen berücksichtigen sowohl oberflächenspannungs-induzierte, als auch viskositätsinduzierte Kohäsionskräfte aufgrund der Flüssig-keitsbrücken. Eine Reihe von Simulationen wird durchgeführt, die auf verschiedenen Flüssigbrückenbildungsmodellen basieren: (i) dem statischen Brückenmodell von Shi und McCarthy, (ii) einer einfachen statischen Version des Modells von Wu et al. (Wu et al., AIChE Journal, 2016, 62:1877-1897), sowie (iii) das von den letztgenannten Autoren entwickelte vollständige dynamische Brückenmodell. Unterschiede, die durch verschiedene Flüssigbrückenbildungs-modelle resultieren werden systematisch untersucht, sowie auch die Sensitivität gegenüber relevanten Systemparametern. Schließlich geben wir Empfehlungen für welche Systeme ein dynamisches Flüssigkeitsbrückenmodell verwendet werden muss, und für welche Anwendungen dies weniger wichtig erscheint.

Schließlich wurde am Institut für Prozess- und Partikeltechnik der TU Graz eine virtuelle Sandbox aufgebaut. Das damit verbundene virtuelle „Sandkastenprojekt“ konzentriert sich auf die Erhöhung der allgemeinen

öffentlichen Wahrnehmung der Forschung im Bereich (feuchter) granularer Medien. Dies geschieht durch eine physikalische Sandbox, die mit der Partikelsimulationsumgebung LIGGGHTS® integriert wurde. Insbesondere wird die Oberfläche des Sandes mit einer 3D-Kamera aufgenommen, und die Geometrie anschließend in LIGGGHTS® eingespielt, um Untersuchungen an einem digitalen Zwilling des Sandkastens zu ermöglichen.

der TU Graz eine virtuelle Sandbox aufgebaut. Das damit verbundene virtuelle Sandkastenprojekt konzentriert sich auf die Erhöhung der allgemeinen öffentlichen Wahrnehmung der Forschung im Bereich der nassen körnigen Materialien. Dies geschieht durch eine physikalische Sandbox, die mit der Partikelsimulationsumgebung LIGGGHTS® integriert ist. Insbesondere wird die Oberfläche des Sandes mit einer 3D-Kamera aufgenommen und die Geometrie wird anschließend in LIGGGHTS® eingegeben, um einen digitalen Zwilling des Sandkastens zu realisieren.

Abstract

Liquid bridge formation is relevant for wet powder blending since it (i) determines the amount of liquid transferred during collisions, as well as (ii) the formation of cohesive forces between particles due to viscous and capillary effects. This thesis is concerned with microscopic models that are required to predict the outcome of these two phenomena: (i) the volume of liquid in the bridge, as well as (ii) the resulting cohesive forces. While a plurality of literature exists that establishes a sound understanding of the latter, this is not the case for the bridge volume: despite a number of models available in literature claim to be able to describe the bridge formation phase, almost all of them focus on static bridges, and/or bridge rupture. They often lack of experimental, theoretical, or numerical support. For example, a cornerstone of modern literature on liquid bridge formation, i.e., the work of Shi and McCarthy (Powder Technology 2008, 184:64-75), purely relies on geometrical arguments that are void of any physical reasoning.

The first part of this thesis indeed demonstrates that this model from literature is even qualitatively incorrect: the model of Shi and McCarthy cannot predict the non-linear increase of the liquid bridge volume with the amount of liquid present on the particles that is obvious from a proper geometric analysis of the bridge shape. Specifically, it is found that in case a liquid bridge forms between two wetted particles, a non-linear relationship exists between film thickness, separation distance, and liquid bridge volume. Also, the rate of bridge formation is analyzed for the first time, leading to the formulation of a *dynamic* liquid bridge model. This model is then applied to study liquid bridge filling rates in monodisperse particle beds. It is shown that these filling rates are of critical importance for systems involving highly viscous liquids and short collisions.

The second part of the thesis is concerned with the generalization of the dynamic bridge model to polydisperse systems. It is demonstrated that the functional form

of the dynamic liquid bridge model developed for monodisperse systems also holds great promise to describe liquid transfer rates in more complex systems involving unequally-sized particles.

The third part of the thesis deals with the application of the microscopic liquid bridge models to wet fluidized beds. The key motivation of this study is to probe the limits of available microscopic liquid bridge models. We simulate wet fluidized beds of particles in small periodic domains using the CFD-DEM approach. A liquid bridge is formed upon particle-particle collisions, which then ruptures when the particle separation exceeds a critical distance. The simulations take into account both surface tension and viscous forces due to the liquid bridge. We perform a series of simulations based on different liquid bridge formation models: (i) the static bridge model of Shi and McCarthy, (ii) a simple static version of the model of Wu et al. (Wu et al., AIChE Journal, 2016, 62:1877-1897), as well as (iii) the full dynamic bridge model developed by the latter authors. We systematically compare the differences caused by different liquid bridge formation models, as well as their sensitivity to system parameters. Finally, we provide recommendations for which systems a dynamic liquid bridge model must be used, and for which application this appears to be less important.

Finally, a virtual sandbox has been built up at the Institute of Process and Particle Engineering at TU Graz. The associated virtual sandbox project focusses on increasing the general public perception of research in the area of wet granular materials. This is realized by means of a physical sandbox, which is integrated with the particle simulation environment LIGGGHTS®. Specifically, the surface of the sand is recorded using a 3D camera, and the geometry is subsequently fed into LIGGGHTS® to realize a digital twin of the sandbox.

Contents

1 Wet Granular Flows 1

1.1 Introduction to Wet Granular Flows 2
1.2 Thesis Scope 3
1.3 Abbreviations 4
1.4 References 5

2 Goals and Content 7

2.1 Goals 8
2.2 Thesis Overview 9
2.2.1 Part 1 - Wet Granular Flows 9
2.2.2 Part 2 - The Virtual Sandbox 10
2.3 Abbreviations 11
2.4 References 11

3 Models and Simulation Approaches 13

3.1 Direct Numerical Simulations (DNS) Methods 14
3.2 Discrete Element Methods (DEM) 15
3.2.1 Coupling of Microscale Model into Discrete Element Method 18
3.3 Abbreviations 18
3.4 References 18

4 A Model to Predict Liquid Bridge Formation between Wet Particles Based on Direct Numerical Simulations 23

4.1 Introduction 24
4.1.1 Objectives 27
4.2 Methodology 29
4.2.1 Initial and Boundary Conditions 29
4.2.2 Volume of Fluid Simulation Approach 30
4.2.3 Liquid Bridge Volume Calculation 34
4.2.4 Proposed Model for Liquid Bridge Filling 35

4.3 Geometrical Bridge Volume 38
4.3.1 Type I 38
4.3.2 Type II 39
4.4 Results 43
4.4.1 Early Stage Model (Stage I) 43
4.4.2 Viscous Filling Stage Model (Stage II) 46
4.4.3 Film Rupture and Grid Refinement 52
4.4.4 Reynolds Number and Density Ratio Effects 54
4.4.5 Initial Bridge Shape Effects 56
4.5 Discussion 58
4.5.1 Particle Interaction Time Scales 58
4.5.2 Viscous Effects during Particle Approach 62
4.5.3 Typical Impact Speeds in Sedimenting Suspensions 66
4.6 Conclusions 67
4.7 Appendices 69
4.8 Nomenclature 76
4.9 References 79

5 Liquid Transport Rates during Binary Collision of Unequally-sized Particles 85

5.1 Introduction 86
5.1.1 Goals and Structure 89
5.2 Methodology 89
5.2.1 Setup and Initial Conditions 89
5.2.2 Simulation Approach and Liquid Bridge Volume Calculation Strategy 92
5.2.3 Proposed Model for Liquid Bridge Filling 95
5.3 Geometrical Bridge Volume 97
5.4 Results 102
5.4.1 Early Stage Model 102
5.4.2 Viscous Filling Model 107
5.4.3 Film rupture and Driving Pressure 113
5.5 Discussion 113

5.6 Conclusions 118
5.7 Appendices 121
5.8 Nomenclature 125
5.9 References 128

6 The Effects of Liquid Bridge Model Details on the Dynamics of Wet Fluidized Beds 133

6.1 Introduction 134
6.1.1 Particle-based Models for Wet Fluidized Beds 135
6.1.2 Goals and Structure 136
6.2 Methodology 137
6.2.1 Simulation Methodology 137
6.2.2 Liquid Bridge Filling Model 141
6.2.3 Bridge Rupturing Model 144
6.2.4 Bridge Force Models 145
6.3 Theoretical Analysis 146
6.4 Results and Discussion 154
6.4.1 Influence of Bond and Capillary number 154
6.4.2 Comparison of Static Bridge Models 157
6.4.3 Comparison of Static and Dynamic Bridge Models 158
6.4.4 Effect of the Global Liquid Content 162
6.4.5 Partitioning of Liquid between Surface and Bridge 165
6.4.6 Influence of Viscosity 167
6.4.7 Regime Map for Effect of Model Details 168
6.5 Conclusions 170
6.6 Appendices 173
6.7 Nomenclature 176
6.8 References 180

7 The Virtual Sandbox 185

7.1 Introduction 186
7.1.1 Goals and Structure 186

7.2 Methodology 187
7.2.1 The Virtual Sandbox 187
7.2.2 Surface Reconstruction and Simulations 188
7.3 Results 190
7.4 Conclusions 192
7.5 References 192

8 Conclusions and Outlook 195

8.1 Conclusions 196
8.2 Outlook 199
8.3 References 201

“人之為學有難易乎？學之，則難者亦易矣；不學，則易者亦難矣”

（清代 彭端淑，1699－1779）

1

Wet Granular Flows

Wet granular flows and granular matters are frequently encountered in a wide range of industries, such as food making, pharmaceutical, the energy sector and metallurgical engineering. However, it is still a big challenge to predict liquid transport between particles during particle-particle collisions. These collisions may result in cohesive liquid bridges, which may lead to the agglomeration of particles [1,2] which are either wanted (in the case of wet granulation), or unwanted (e.g., in wet fluidized beds used for coking). Consequently, a complex and potentially unpredictable system behavior may result, impacting the product quality, e.g., by formation of permanent particle agglomerates. In addition to its industrial relevance, many general scientific disciplines, such as geomechanics and astronomy, are also concerned with wet granular flows. For example, as suggested by Herminghaus [3], the probability of two grains sticking together is of considerable interest in the context of structure formation in the universe.

1.1 Introduction to Wet Granular Flows

Due to viscous effects, evaporation or condensation, capillary forces and inhomogeneous liquid distribution in wet granular flows, the liquid transport is difficult to describe and complex flow behaviour is generally observed [5]. Specifically, liquid bridges between particles may lead to particle agglomeration [1] which is either wanted (in the case of wet granulation), or unwanted (e.g., in wet fluidized beds used for coking). Clearly, a better understanding of the formation of liquid bridges will aid in controlling these processes. Previous studies on liquid bridges between particles mainly focused on static bridges, [6] bridge deformation during stretching and rupture [5,7–9], or the energy dissipated upon rupture [5,10,11]. However, few theoretical and experimental studies provided a detailed understanding of the initial bridge formation process, and the accompanying liquid transfer rate from the particle surface into the bridge. Experimental results, and the resulting empirical models, have been summarized by Herminghaus [3], mainly focusing on the effect of roughness, as well as evaporation and re-condensation. Unfortunately, these models cannot be applied to engineering problems, since they (i) focus on the long-term behaviour of the bridge and (ii) do not provide a rigorous enough closure expression for some model parameters.

Despite its significant industrial and scientific impact, the description of the flow of granular materials, especially when wet, is still a challenge. Typical examples are large tumbling blenders and high-shear granulators used in the pharmaceutical industry to mix and granulate active ingredients and inert materials. In such blenders there are zones with rapid movement, and zones which virtually do not experience any flow and shear. However, tools to design and optimize such processes do not yet exist. Clearly, current theoretical and computational tools for granular flows still do not match the tools available to fluid mechanicists and researchers working with Computational Fluid Dynamics tools. The reason for this is that in contrast to fluid mechanics, no generally valid

constitutive relationships between stress and strain exist in granular flows. Continuum models are valid for many conditions (e.g., smooth monodisperse particle beds) - for many they are not (e.g., polydisperse cohesive powders). Thus, it is our belief - and that of many others - that only microscopic (i.e., particle-based) approaches will eventually yield simulation tools that can be used to design, optimize and control granular flow processes. Microscopic methods can also be used to develop constitutive relationships for continuum models.

1.2 Thesis Scope

The microscopic methods that are the focus of this work are based on Direct Numerical Simulations (DNS) and the Discrete Element Methods (DEM). The DNS methods are able to take into account the details of granular microstructure and hence possess a great potential to predict the liquid distribution in highly saturated granular matter. DEM is a powerful tool to simulate granular flows by accounting for all forces on all particles. While this method has been used for several years, only lately it has attracted interest of the engineering community. What has not been addressed satisfactorily in the literature, however, are DEM-based simulations of cohesive flows, especially the case when liquid is present between the particles. Specifically, the detailed and local description of the impact of liquid-bridge forces and moisture on granular flows and the (re-) distribution of liquid in the granular bed are still open questions. In the first stage, we develop a new simulation approach that allows highly resolved direct simulation of complex three-phase systems relevant for wet particle flow. In the second stage, we use the results of these direct micro-scale simulations to develop models that can predict liquid bridge between two wet particles. We then use these models to incorporate them in existing DEM codes (e.g., LIGGGHTS®). These newly developed models cover liquid distribution, capillary forces and viscous forces of bridge in wet granular system. We then use these models in CFD-DEM simulations of the dynamics of wet fluidized beds to explain the formation of agglomerates and mixing on a particle level. Also, we are able to answer the

questions of for which system the newly developed models are essential and what are the critical parameters for these models.

1.3 Abbreviations

DNS	Direct Numerical Simulation
DEM	Discrete Element Method
CFD	Computational Fluid Dynamics

1.4 References

[1] M. Scheel, R. Seemann, M. Brinkmann, M. Di Michiel, A. Sheppard, B. Breidenbach, et al., Morphological clues to wet granular pile stability., Nat. Mater. 7 (2008) 189–193. doi:10.1038/nmat2117.

[2] M. Girardi, S. Radl, S. Sundaresan, Simulating wet gas-solid fluidized beds using coarse-grid CFD-DEM, Chem. Eng. Sci. 144 (2016) 224–238. doi:10.1016/j.ces.2016.01.017.

[3] S. Herminghaus, Dynamics of wet granular matter, Adv. Phys. 54 (2005) 221–261. doi:10.1080/00018730500167855.

[4] S. Herminghaus, Dynamics of wet granular matter, Advances. 54 (2005) 221–261. doi:10.1080/00018730500167855.

[5] P. Darabi, K. Pougatch, M. Salcudean, D. Grecov, A novel coalescence model for binary collision of identical wet particles, Chem. Eng. Sci. 64 (2009) 1868–1876.

[6] F.M. Orr, L.E. Scriven, A.P. Rivas, Pendular rings between solids: meniscus properties and capillary force, J. Fluid Mech. 67 (1975) 723. doi:10.1017/S0022112075000572.

[7] P. Darabi, T. Li, K. Pougatch, M. Salcudean, D. Grecov, Modeling the evolution and rupture of stretching pendular liquid bridges, Chem. Eng. Sci. 65 (2010) 4472–4483. doi:10.1016/j.ces.2010.04.003.

[8] S. Dodds, M. Carvalho, S. Kumar, Stretching liquid bridges with moving contact lines: The role of inertia, Phys. Fluids. 23 (2011). doi:10.1063/1.3623427.

[9] S. Dodds, M.S. Carvalho, S. Kumar, The dynamics of three-dimensional liquid bridges with pinned and moving contact lines, J. Fluid Mech. 707 (2012) 521–540. doi:10.1017/jfm.2012.296.

[10] X. Pepin, D. Rossetti, S. Iveson, S. Simons, Modeling the Evolution and

Rupture of Pendular Liquid Bridges in the Presence of Large Wetting Hysteresis., J. Colloid Interface Sci. 232 (2000) 289–297. doi:10.1006/jcis.2000.7182.

[11] D. Rossetti, S.J.R. Simons, A microscale investigation of liquid bridges in the spherical agglomeration process, Powder Technol. 130 (2003) 49–55. doi:10.1016/S0032-5910(02)00225-5.

"Living without an aim is like sailing without a compass."

(John Ruskin, 1819-1900)

2

Goals and Content

2.1 Goals

The outcome of the present thesis should be a thorough documentation of an entirely new approach to investigate wet granular flows in great detail. The approach should be designed such that it is applicable to a wide range of problems encountered in chemical, pharmaceutical and mechanical engineering, as well as geomechanics. The specific goals of this thesis are:

- Development of a numerical strategy to directly simulate wet agglomerates - even at high liquid saturation levels - using sophisticated Direct Numerical Simulation (DNS) of gas-liquid-solid flow. Specifically, a DNS based on the Volume of Fluid method should be employed to simulate both the motion of the liquid and the surrounding gas. By reconstructing the interfaces between these two fluid phases, the bridge's shape and size should be identified, e.g. by extracting the interface position at discrete points. Specifically, the liquid bridge should be defined by detecting the neck positions of the liquid film on each particle surface (for details see the Chapter 4). A direct integration method (DIM) should then be used to calculate the liquid bridge volume, and hence the bridge's filling rate, based on the known interface position at each instant in time. The goal is then building a dynamic model for the liquid bridge volume during the filling process based on this DNS data. Therefore, DNS data should be fitted to a postulated liquid bridge filling model.
- Studies of the liquid transport rate between unequally-sized particles should extend the dynamic bridge model to be available for bi-and polydisperse particle systems. Specifically, a VoF-based DNS approach should be used to simulate both the motion of the liquid and the surrounding gas. The goal is building a dynamic model to predict the liquid bridge volume during the filling process between two unequally-sized particles.

- Application of the newly developed models and methodology to relevant systems and investigation of the predicted effects. Specifically, one should simulate wet fluidized beds considering different liquid bridge models (i.e., the model of Shi and McCarthy [1], the dynamic model of Wu et al., [2] and a simplified version of the model of Wu et al. [2]). Specifically, one should aim on answering the following questions: (1) for which systems the dynamic liquid bridge model of Wu et al. [2] is essential, i.e., for which situations the drainage rate of liquid into the bridge is relevant? (2) Which model is the most suitable one in terms of picturing effects originating from changes in the liquid surface tension and viscosity? (3) What are the most critical parameters for each model that need to be determined, e.g., during a calibration procedure?
- The goal of the virtual sand box project is to increase the general public perception of research in the area of wet granular materials. This should be realized by means of a physical sandbox, which should be integrated with the particle simulation environment LIGGGHTS®. Specifically, the surface of the sand should be recorded using a 3D camera, and the geometry should be then fed into LIGGGHTS®. Finally, a virtual model of the real-world sand surface should be reconstructed, and the benefits of such a virtual sand model should be explorable by the user, e.g., via liquid imbibition simulations.

2.2 Thesis Overview

2.2.1 Part 1 - Wet Granular Flows

Chapter one gives an introduction of wet granular flows encountered in the pharmaceutical industry and hence constitutes the motivation of this work. Chapter two sketches the goals and contents of this thesis. Chapter three introduces the modelling and simulation approaches employed in the simulations.

Chapter four also analyzes the rate of liquid bridge formation, and formulates a novel *dynamic* liquid bridge model [2].

Chapter five is concerned with the generalization of the dynamic bridge model to polydisperse systems [3]. It is demonstrated that the functional form of the dynamic liquid bridge model developed for monodisperse systems also holds great promise to describe liquid transfer rates in more complex systems involving unequally-sized particles.

Chapter six deals with the application of the microscopic liquid bridge models to wet fluidized beds. The key motivation of this study is to probe the limits of an array of microscopic liquid bridge filling models.

2.2.2 Part 2 - The Virtual Sandbox

Chapter seven details on the virtual sandbox project. The goal is to present a sandbox to three target groups: (I) publics in primary schools, (II) pupils in secondary schools, as well as (III) students and interested individuals. A number of exercises are proposed to answer the following questions: “What are important particle properties, and how can they be measures?”, or “How dense can we pack particles, and why is this important?”. The strategy to transport the content is developed to conform with Austria’s national education strategy focusing on competence-based teaching.

2.3 Abbreviations

DEM	Discrete Element Method
DNS	Direct Numerical Simulation
DIM	Direct Integration Method

2.4 References

[1] D. Shi, J.J. McCarthy, Numerical simulation of liquid transfer between particles, Powder Technol. 184 (2008) 64–75. doi:10.1016/j.powtec.2007.08.011.

[2] M. Wu, S. Radl, J.G. Khinast, A model to predict liquid bridge formation between wet particles based on direct numerical simulations, AIChE J. 62 (2016) 1877–1897. doi:10.1002/aic.15184.

[3] M.. Wu, J.G.. b Khinast, S.. Radl, Liquid transport rates during binary collisions of unequally-sized particles, Powder Technol. 309 (2017) 95–109. doi:10.1016/j.powtec.2016.12.080.

"We must believe that we are gifted for something, and that this thing, at whatever cost, must be attained."

(Marie Curie, 1867-1934)

3

Models and Simulation Approaches

The aim of this chapter is to briefly introduce the methods which have been used to study film flow on the surface of spheres, as well as the motion of particles in wet fluidized beds.

3.1 Direct Numerical Simulations (DNS) Methods

DNS methods directly resolve the solid and liquid interface in great details (i.e., on the so-called microscale), and hence allow the simulation of a few particles only. Usually, the DNS method is only used to predict static liquid bridges between particles, and the dynamics of the bridge formation process have attracted far less attention: Previous studies on liquid transfer mainly focused on static bridges and bridge rupture [1–3], and only a few studies provide a detailed understanding of the liquid bridge formation process and the associated liquid transfer rates. The DNS method takes into account the details of the granular medium's microstructure, and hence is able to calculate the liquid transport rate and liquid distribution in highly saturated granular matter. Specifically, we employ two approaches to study the transport of liquid in dense granular flows:

i) **Volume of Fluid (VoF) method**: The Volume of Fluid method is classify as a Eulerian approach to modeling the evolving shape of interface. The first publication introduced Volume of Fluid method for studying the dynamic of free surface is presented by Hirt and Nichols [4]. Recent years, researchers employed the VoF approach to handle two-phase flows of different situations [5–7]. The implemented VoF method in OpenFOAM® has been documented by Maric et al. [8]. With respect to this approach [8], the interface is captured by a color function which is defined as the fraction of volume of each cell of the fluid. The interface has been reconstructed using the volume function [4]. This VoF approach in our work has been used to simulate both the motion of the liquid phase and the surrounding gas phase for liquid bridge filling applications. By reconstructing the interface between these two phases, the interface positions have been extracted to identify the bridge shape and size. A direct integration method (DIM) is then used to calculate the liquid bridge volume form the interface position. Subsequently, a dynamic model for the bridge volume during the filling process has been built based on this DNS data. Details of the method are documented in Chapter 5, and our publication [9].

ii) **Combination of Immersed Boundary method (IB) and VoF:** in CFD, the immersed boundary method is firstly developed to simulated fluid-particle interaction problems of blood flow by Peskin [10]. Uhlmann [11] later introduced the IB approach for the direct simulation of particle flows. Hager et al. [12] initially implemented a resolved immersed fictitious domain method into the CFDEM®project. This method has later been improved and re-implemented by Blais et al. [13] to study the viscous mixing in rotating tank. Municchi and Radl [14] enhanced this IB method by using a hybrid approach to study heat and mass transfer over particle surface in bi-disperse particles suspension system. In this thesis work, the combination approaches are based on IB approach [13,14] and VoF approach [8]. Specifically, we employ the immersed boundary (IB) method to model rigid fluid-particle interfaces, as well as the VoF approach to model a deformable fluid-fluid interface. The new solver has been developed using the OpenFOAM® software package in combination with the CFDEM® package [15], and is able to perform efficient DNS in parallel. This combining approach can directly simulate particle-gas-liquid systems involving moving particle.

3.2 Discrete Element Methods (DEM)

The motion of each individual particle of granular system by DEM approach [16,17] is predicted. Specifically, each individual particle in the bulk solid is tracked by solving Newton's equation of motion. Naturally, a granular flow system contains a large number of particles. DEM approach can handle particulate systems in the order of $O(10^6)$ particles, compared to DNS methods for which $O(10^2)$ are already challenging. Hence, the DEM approach has the great advantage of applicability to a wider range of granular flow regimes ranging from dilute granular matters to densely-packed systems. Therefore, the DEM model performs the most natural way for modeling granular flows in which collective phenomena (e.g., the formation of agglomerates) are essential.

The major advantage of DEM is that multiple particle-particle contact forces can be tracked and calculated at the same time. However, this requires a time-

resolved calculation of the deformation process at each contact point. (i.e., it requires time steps in the order of 10^{-6} s to be used in the numerical simulation). Generally, around 80% of computational time is spent on particle-particle contacting detection and calculation [18]. Therefore, DEM is the one of the expensive tool for simulating granular flows from a computational point of view. However, with the progress of computing capacity of computer, studies on granular flow using DEM has increased rapidly [19–23]. Recent advances enable the efficient study of large granular beds (i.e., $O(10^7)$ particles [24]), or non-spherical particles [19,25]. The latter has been frequently realized by using super-quadric particles in systems with a size of $O(10^5)$ particles [26]. Also, non-spherical particles in fluidized beds have been studied recently [25,27]. The DEM, as a cutting-edge simulation technique, has the highest potential to become the dominating powder flow simulation tool in many engineering applications (i.e. mixing and segregation in pharmaceutical engineering). This is especially true when the system has densely-packed and dilute regions, as well as the number of particles in the system is relatively small, and the particles have a wide size and shape distribution.

The major challenge connected to DEM in applications to granular flow is the account of particle-particle interaction forces. The following paragraphs introduce a sophisticated particle-particle force approach which is called the soft sphere approach. The soft-sphere DEM approach firstly introduced by Cundall and Strack [28] has been used widely to study granular flows in the past decades [25,29]. The soft sphere approach relies on the calculation of the particle-particle forces during collisions by calculating a typical particle deformation distance at the contact point: The biggest challenge is that the particle's deformations cannot be computed directly when one aims on tracking millions of individual particles. Therefore, simplified models have to be used for particle-particle collisions that rely on the knowledge of a typical particle deformation distance. The most classical and general models are spring-dashpot models which were firstly introduced by Cundall and Strack [28] for modelling rock mechanics. These

models are based on a parallel combination of a spring which is characterized stiffness $\boldsymbol{k}$ and a dashpot which is characterized by a damping coefficient $\boldsymbol{\gamma}$ (see Figure 3.1). Here the normal and tangential directions are denoted by the subscripts n and t, respectively. This simplified model can be used for both normal and tangential direction to simulate particle compressing and shearing deformation, respectively. Due to particles sliding against each other during contacting, a frictional slider has been used with the tangential deformation model.(see Figure 3.1, characterized by μ)

$$\mathbf{f}_{cont,ij}^{n} = -k_n \delta_{ij}^{n} \mathbf{n}_{ij} - \gamma_{d,n} \mathbf{v}_{ij}^{n} \tag{3.1}$$

$$\mathbf{f}_{cont,ij}^{t} = \begin{cases} -k_t \delta_{ij}^{t} \mathbf{t}_{ij} - \gamma_{d,\mathrm{t}} \mathbf{v}_{ij}^{t} & \text{for } \left|\mathbf{f}_{cont,ij}^{t}\right| < \mu_{pp} \left|\mathbf{f}_{cont,ij}^{n}\right| \\ -\mu_{pp} \left|\mathbf{f}_{cont,ij}^{n}\right| \dfrac{\delta_{ij}^{t} \mathbf{t}_{ij}}{|\delta_{ij}^{t} \mathbf{t}_{ij}|} & \text{for } \left|\mathbf{f}_{cont,ij}^{t}\right| \geq \mu_{pp} \left|\mathbf{f}_{cont,ij}^{n}\right| \end{cases} \tag{3.2}$$

The particles contact forces have been formulated by Equations 3.1 and 3.2. Specifically, cohesive forces due to liquid bridge are exhibited in wet granular matters. In these cases, particle-particle forces can be taken into account directly to DEM, so DEM can be successfully used. Hence, direct consideration of micro-scale particle-particle forces on the macro-scale flow can be achieved with DEM.

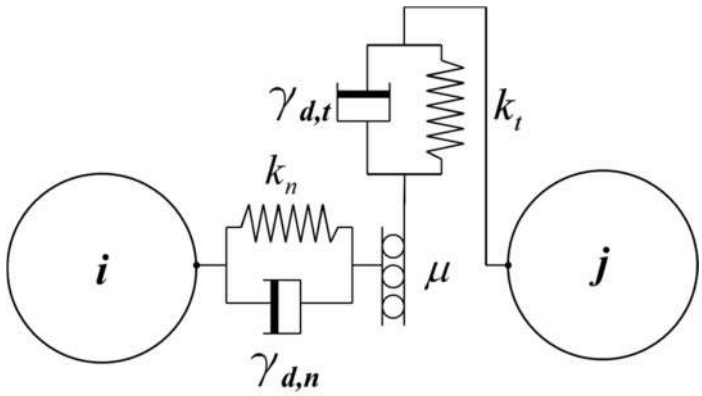

Figure 3.1: Typical spring-dashpot model used in the soft sphere approach adapted from [28].

3.2.1 Coupling of Microscale Model into Discrete Element Method

We then use the model presented by Mikami et al. [30] and Pitois et al. [31] describing the relationship between local saturation and bridge forces. Basically, these authors inactivate forces due to liquid bridges when the pores are saturated with the liquid. Thus, they introduce a threshold for the maximal number of "active" bridges, and hence are able model the (experimentally observed) decrease in the mechanical strength of the wet particle bed. However, our newly developed model includes the effects of liquid transportation between particles, and makes bridge models fully predictive in the sense that the local liquid content is a part of the solution. Specifically, a postulated bridge filling model is fitted based on microscale simulation results. The resulting model is then be implemented into the DEM code. Using these models it is possible - for the first time - to simulate wet granular flows with high pore saturation based on physical insight and experimentally verified microscale models. This significantly decreases the total number of particles to be tracked.

3.3 Abbreviations

CFD	Computational Fluid Dynamics
DEM	Discrete Element Method
DIM	Direct Integration Method
IB	Immersed Boundary (method)
VoF	Volume of Fluid (method)

3.4 References

[1] P. Darabi, T. Li, K. Pougatch, M. Salcudean, D. Grecov, Modeling the evolution and rupture of stretching pendular liquid bridges, Chem. Eng. Sci. 65 (2010) 4472–4483. doi:10.1016/j.ces.2010.04.003.

[2] S. Dodds, M. Carvalho, S. Kumar, Stretching liquid bridges with moving contact lines: The role of inertia, Phys. Fluids. 23 (2011) 92101.

doi:10.1063/1.3623427.

[3] P. Darabi, K. Pougatch, M. Salcudean, D. Grecov, A novel coalescence model for binary collision of identical wet particles, Chem. Eng. Sci. 64 (2009) 1868–1876.

[4] C.W. Hirt, B.D. Nichols, Volume of fluid (VOF) method for the dynamics of free boundaries, J. Comput. Phys. 39 (1981) 201–225. doi:10.1016/0021-9991(81)90145-5.

[5] L. Jofre, O. Lehmkuhl, J. Castro, A. Oliva, A 3-D Volume-of-Fluid advection method based on cell-vertex velocities for unstructured meshes, Comput. Fluids. 94 (2014) 14–29. doi:10.1016/j.compfluid.2014.02.001.

[6] N. Balcázar, O. Lehmkuhl, L. Jofre, J. Rigola, A. Oliva, A coupled volume-of-fluid/level-set method for simulation of two-phase flows on unstructured meshes, Comput. Fluids. 124 (2016) 12–29. doi:10.1016/j.compfluid.2015.10.005.

[7] M. van Sint Annaland, N.G. Deen, J. a. M. Kuipers, Numerical simulation of gas bubbles behaviour using a three-dimensional volume of fluid method, Chem. Eng. Sci. 60 (2005) 2999–3011. doi:10.1016/j.ces.2005.01.031.

[8] T. Maric, H. Marschall, D. Bothe, voFoam - A geometrical Volume of Fluid algorithm on arbitrary unstructured meshes with local dynamic adaptive mesh refinement using OpenFOAM, (2013) 1–30. http://arxiv.org/abs/1305.3417 (accessed September 29, 2014).

[9] M. Wu, S. Radl, J.G. Khinast, A model to predict liquid bridge formation between wet particles based on direct numerical simulations, AIChE J. 62 (2016) 1877–1897. doi:10.1002/aic.15184.

[10] C.S. Peskin, Numerical analysis of blood flow in the heart, J. Comput. Phys. 25 (1977) 220–252. doi:10.1016/0021-9991(77)90100-0.

[11] M. Uhlmann, An immersed boundary method with direct forcing for the

simulation of particulate flows, J. Comput. Phys. 209 (2005) 448–476. doi:10.1016/j.jcp.2005.03.017.

[12] A. Hager, C. Kloss, S. Pirker, C. Goniva, Parallel open source CFD-DEM for resolved particle-fluid interaction, (2012) 1–6.

[13] B. Blais, M. Lassaigne, C. Goniva, L. Fradette, F. Bertrand, A semi-implicit immersed boundary method and its application to viscous mixing, Comput. Chem. Eng. 85 (2016). doi:10.1016/j.compchemeng.2015.10.019.

[14] F. Municchi, S. Radl, Consistent closures for Euler-Lagrange models of bi-disperse gas-particle suspensions derived from particle-resolved direct numerical simulations, Int. J. Heat Mass Transf. 111 (2017) 171–190. doi:10.1016/j.ijheatmasstransfer.2017.03.122.

[15] C. Kloss, C. Goniva, A. Hager, S. Amberger, S. Pirker, Models , algorithms and validation for opensource DEM and CFD-DEM, Prog. Comput. Fluid Dyn. 12 (2012) 140–152. doi:10.1504/PCFD.2012.047457.

[16] J.A. Gantt, E.P. Gatzke, High-shear granulation modeling using a discrete element simulation approach, Powder Technol. 156 (2005) 195–212. doi:DOI 10.1016/j.powtec.2005.04.012.

[17] G. Lian, C. Thornton, M.J. Adams, Discrete particle simulation of agglomerate impact coalescence, Chem. Eng. Sci. 53 (1998) 3381–3391. doi:10.1016/S0009-2509(98)00152-3.

[18] J.R. Williams, R.O. Connor, Discrete Element Simulation and the Contact Problem, Methods Eng. 6 (1999) 279–304. doi:10.1007/BF02818917.

[19] G. Lu, J.R. Third, C.R. Müller, Discrete element models for non-spherical particle systems: From theoretical developments to applications, Chem. Eng. Sci. 127 (2015) 425–465. doi:10.1016/j.ces.2014.11.050.

[20] C. O'Sullivan, Particulate discrete element modelling: a geomechanics perspective, 2011. doi:10.1061/(ASCE)GM.1943-5622.0000024.

[21] J.S. Marshall, Discrete-element modeling of particulate aerosol flows, J. Comput. Phys. 228 (2009) 1541–1561. doi:10.1016/j.jcp.2008.10.035.

[22] H.P. Zhu, Z.Y. Zhou, R.Y. Yang, A.B. Yu, Discrete particle simulation of particulate systems: Theoretical developments, Chem. Eng. Sci. 62 (2007) 3378–3396. doi:10.1016/j.ces.2006.12.089.

[23] Q.F. Hou, S.B. Kuang, A.B. Yu, A DEM-based approach for analyzing energy transitions in granular and particle-fluid flows, Chem. Eng. Sci. 161 (2017) 67–79. doi:10.1016/j.ces.2016.12.017.

[24] C. Radeke, S. Radl, J. Khinast, Granular Flows - Showing Size Effects by Using High-Performance Simulations on GPUs, in: Multi-Scale Model. Symp., 2009: pp. 1–6.

[25] W. Zhong, A. Yu, X. Liu, Z. Tong, H. Zhang, DEM/CFD-DEM Modelling of Non-spherical Particulate Systems: Theoretical Developments and Applications, Powder Technol. 302 (2016) 108–152. doi:10.1016/j.powtec.2016.07.010.

[26] P.W. Cleary, Industrial particle flow modelling using discrete element method, Eng. Comput. 26 (2009) 698–743. doi:10.1108/02644400910975487.

[27] J.E. Hilton, L.R. Mason, P.W. Cleary, Dynamics of gas-solid fluidised beds with non-spherical particle geometry, Chem. Eng. Sci. 65 (2010) 1584–1596. doi:10.1016/j.ces.2009.10.028.

[28] P.A. Cundall, O.D.L. Strack, A discrete numerical model for granular assemblies, Géotechnique. 29 (1979) 47–65. doi:10.1680/geot.1979.29.1.47.

[29] H.P. Zhu, Z.Y. Zhou, R.Y. Yang, A.B. Yu, Discrete particle simulation of particulate systems: A review of major applications and findings, Chem. Eng. Sci. 63 (2008) 5728–5770. doi:10.1016/j.ces.2008.08.006.

[30] T. Mikami, H. Kamiya, M. Horio, Numerical simulation of cohesive powder

behavior in a fluidized bed, Chem. Eng. Sci. 53 (1998) 1927–1940. doi:10.1016/S0009-2509(97)00325-4.

[31] O. Pitois, P. Moucheront, X. Chateau, Liquid Bridge between Two Moving Spheres: An Experimental Study of Viscosity Effects., J. Colloid Interface Sci. 231 (2000) 26–31. doi:10.1006/jcis.2000.7096.

"Take up one idea. Make that one idea your life - think of it, dream of it, live on that idea. Let the brain, muscles, nerves, every part of your body be full of that idea, and just leave every other idea alone. This is the way to success."

(Swami Vivekananda, 1863-1902)

4

A Model to Predict Liquid Bridge Formation between Wet Particles Based on Direct Numerical Simulations*

We study dynamic liquid bridge formation, which is relevant for wet granular flows involving highly viscous liquids and short collisions. Specifically, the drainage process of liquid adhering to two identical, non-porous wet particles with difference initial film heights is simulated using Direct Numerical Simulations (DNS). We extract the position of the interface, and define the liquid bridge and its volume by detecting a characteristic neck position. This allows us building a dynamic model for predicting bridge volume, and the liquid remaining on the particle surface. Our model is based on two dimensionless mobility parameters, as well as a dimensionless time scale to describe the filling process. In the present work model parameters were calibrated with DNS data. We find that the proposed model structure is sufficient to collapse all our simulation data, indicating that our model is general enough to describe liquid bridge formation between equally sized particles.

I. * This chapter is based on: M. Wu, J.G. Khinast, S. Radl. A Model to Predict Liquid Bridge Formation between Wet Particles Based on Direct Numerical Simulations. AIChE J. 62 (2016), 1877 – 1897.

4.1 Introduction

Flow of highly saturated wet granular matter is encountered in a wide range of engineering applications, particularly in the energy sector, or the pharmaceutics and food industry [1]. Due to viscous effects, evaporation or condensation, capillary forces and inhomogeneous liquid distribution in wet granular flows, the liquid transport is difficult to describe and complex flow behaviour is generally observed.[2] Specifically, liquid bridges between particles may lead to particle agglomeration[3] which is either wanted (in the case of wet granulation), or unwanted (e.g., in wet fluidized beds used for coking). Clearly, a better understanding of the formation of liquid bridges will aid in controlling these processes. Previous studies on liquid bridges between particles mainly focused on static bridges [4] bridge deformation during stretching and rupture [2,5–7] or the energy dissipated upon rupture [2,8,9]. However, few theoretical and experimental studies provided a detailed understanding of the initial bridge formation process, and the accompanying liquid transfer rate from the particle surface into the bridge. Experimental results, and the resulting empirical models, have been summarized by Herminghaus[10], mainly focusing on the effect of roughness, as well as evaporation and re-condensation. Unfortunately, these models cannot be applied to engineering problems, since they (i) focus on the long-term behaviour of the bridge and (ii) do not provide a closure for the model parameters.

Studies of liquid bridges between two identical particles were initiated in 1920's[11,12] and were later extended to cover pendular bridges between unequal-sized particles, or a particle and a wall [4,13]. Studies of moving particles and the associated liquid bridge formation were carried out, starting with the work of Pitois et al.[14] which found that the particle relative velocity significantly influences the liquid bridge force. Rossetti and Simons[9] introduced an important improvement, i.e., a novel Micro Force Balance (MFB) device which is capable of observing the liquid bridge between particles and measuring the force

exerted by liquid bride. Darabi et al.[2] presented a new coalescence model for binary collision between two identical wet particles, considering capillary and viscous forces exerted by (instantaneously formed) pendular bridges. Despite a variety of researchers[7,15–22] that has broadened our understanding of liquid bridges, a study describing a detailed model on the time evolution of a single (pendular) liquid bridge during its formation phase is still missing. This is due to the lack of our understanding how quickly liquid is transported into a liquid bridge, and how much of the liquid (initially present on the particles) is able to flow into the bridge. One reason for this lack of understanding is that experimental investigations to quantify the liquid present in the bridge are tedious, and that simulations require an enormous spatial and temporal resolution to picture the filling process.

Wet particle collisions, or collisions in a viscous fluid, have been studied by a variety of researchers. For example, Davis et al.[23] experimentally studied particle collisions with wet smooth surfaces, and they demonstrate that the lubrication forces play an important role on the particle rebound. Donahue et al.[24] further studied the collisions between liquid-coated spheres using a three-body Newton's Cradle, and they revealed that fluid lubrication resistance upon rebound plays a key role in the dynamics of the collision. Li et al.[25] calibrated a model with experimental results of wet particle collisions. Gondret et al.[26] focused on the bouncing motion of spherical particles in a viscous fluid, and they quantified the wet restitution coefficient by varying the density and the elastic properties of the solid sphere, as well as liquid film viscosity. Gollwitzer et al.[27] revealed that the dimensionless film thickness is a crucial parameter that affects the restitution coefficient. A rough estimate of the liquid bridge volume, i.e., $V_b \approx d_p^3/16$, was used in their work to determine the rupture energy. Sutkar et al.[28] provided a new approach for the estimation of wet restitution coefficients between a particle and a wet surface based on a dimensional and energy budget analysis. However, their data is only in fair agreement with the proposed model,

and they have not provided a model for the prediction of the liquid bridge volume. In summary, a large number of researchers have focused on particle collision dynamics without a detailed analysis of liquid bridge formation [25,29,30].

In this paper we focus on applying simulations to elucidate the complex flow processes associated with bridge formation. In general, three categories of simulations methods that aim at modelling liquid bridges can be distinguished: (i) solving the Young-Laplace equation (YLE), (ii) solving an approximated version of the YLE based on geometrical simplifications and (iii) a full numerical solution of the Navier-Stokes equation of the gas-liquid systems.

The first approach yields analytical solutions only for certain geometrical configurations[4], and hence, one has to employ a numerical integration for a general geometrical configuration [31–33]. For example, Lian et al.[32] provided a simple numerical scheme for solving the YLE and revealed that the rupture distance of equally-sized particles can be written as the cube root of the liquid bridge volume for small contact angles. They also obtained a bridge force model based on a simple approximation method, which was independent of the contact angle. Similarly, Mikami et al.[34] and Willett et al.[35] proposed a simple capillary force model by fitting the numerical solution of the YLE. However, as shown in Pepin et al.[8] the drawbacks when solving the Young-Laplace equation to study liquid bridges are that (i) a fixed contact angles is required and (ii) that the effect of liquid flow into (or out of) the bridge cannot be predicted.

The second approach is to obtain a simple approximation of the liquid bridge shape, typically by assuming a toroidal [13,36,37] or parabolic shape (see, e.g., Pepin et al.[8]). The benefits of using simplified approximation models are obvious: there is no need to solve the full Young-Laplace equation and an analytical solution can be obtained that can be readily implemented into particles simulation codes. However, approximate solutions become increasingly inaccurate

for increasing particle separation [38] and they suffer the same drawbacks as the solution of the YLE.

The third approach is the numerical solution of the Navier-Stokes equations describing (i) the flow of the liquid, or (ii) the liquid and the surrounding gas. In the past two decades this approach has been used with increasing frequency. Early research was based on a simplified version of the Navier-Stokes equation, i.e., modified boundary conditions were used at the interface (see, e.g., Eggers et al.[39] as well as Papageorgiou[40]). Later, Zhang et al.[41] investigated the stretching of a liquid bridge between two circular disks by using a similar method. A fair amount of work to simplify the Navier-Stokes equations for the situation of liquid bridges between two circular disks (but not actual spherical particles) has been performed. Hence, these previous work is only able to provide qualitative information, and has little value for practical application. Only very recently, direct numerical simulations of the Navier-Stokes equation have been attempted to simulate liquid bridge formation in an axisymmetric setup [42–45]. These methods provide a full description of the liquid bridge dynamics, and hence are a promising approach for studying the bridge formation process.

4.1.1 Objectives

Only few theoretical and experimental studies in the literature were concerned with the bridge formation process and the accompanying liquid transfer rate into the bridge. While models for liquid transfer upon bridge rupture exist Lian et al.[32] as well as Shi and McCarthy[46] these models still require additional assumptions for the liquid volume present in the bridge. With this in mind, we have started investigations to establish a detailed model that is able to predict liquid transport and the distribution of liquid between two spheres in our recent work [43]. In the present work, we systematically study the liquid bridge and drainage process of liquid adhering to two identical wet particles. We use a Direct Numerical Simulation (DNS) based on the Volume of Fluid method, i.e., we simulate both the motion of the liquid and the surrounding gas. By

reconstructing the interface between these two fluid phases, we extract the interface position to identify the bridge shape and size. Specifically, the liquid bridge is defined by detecting the neck positions of the liquid film on each particle surface (for details see the Liquid Bridge Volume calculation section). We then use a direct integration method (DIM) to calculate the liquid bridge volume based on the interface position at each instant in time. Our ultimate goal is then building a dynamic model for the liquid bridge volume during the filling process based on these DNS data. Therefore, we fit our DNS data to a postulated liquid bridge filling model, which is an extension of the ideas of Mohan et al.[47] but still allows for an analytical solution to predict the bridge volume. Specifically, our postulated model assumes that the filling rate is not affected by the particles' relative motion, and that the filling rate is linear in the difference between the liquid present on a particle and the bridge volume. Such a model requires the specification of only three dimensionless parameters, as we will show in the following. While our work is currently limited to smooth particles of identical size, the model proposed by us can be easily re-calibrated to account for, e.g., particle roughness, or particle size differences once data for the amount of liquid in the bridge is available for these situations.

In the following, we first describe the methodology used to establish the liquid bridge model, including (i) the initial bridge and boundary conditions that have been used in our simulations, (ii) the interface feature extraction procedure, as well as (iii) the postulated model itself. Subsequently, we introduce a geometrical bridge volume, which is used to normalize the bridge volume measured from our detailed simulations. Then we present results, starting with the calibration of the sub-models for the initial bridge volume and the subsequent viscous filling stage, and we are the first to provide a dynamic model for predicting liquid bridge formation. Also, the effect of grid refinement, as well as that of the Reynolds number, are carefully analysed as well. Finally, we discuss our findings and provide conclusions that should guide the application and future extension of our model.

4.2 Methodology

4.2.1 Initial and Boundary Conditions

We consider two identical smooth spheres, which are fixed in space, i.e., the spheres' relative velocity is zero. In this work, we consider the general situation of an asymmetric liquid bridge, i.e., the thickness of the films initially present on the particle surfaces are different. In what follows, we define that particle 1 always has less liquid compared to particle 2, as shown in Figure 4.1 (panel a). R is the sphere radius for two particles, and h_1 and h_2 are the initial film heights of particle 1 and particle 2, respectively. S is defined as the half separation distance between the particle surfaces.

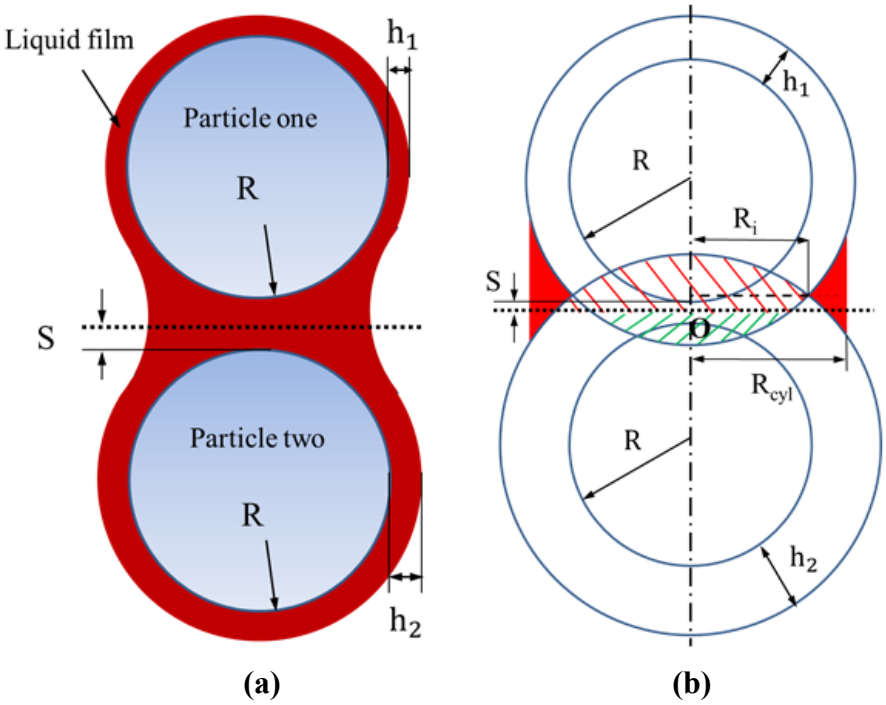

Figure 4.1: Sketch of the simulation setup, as well as the initial bridge shape

The initial shape of the liquid bridge has been set according to the initial film height and the particle separation. Because we do not simulate the approach of the spheres, and hence cannot predict the deformation of the liquid films on the particle prior to coalescence, we must assume the initial bridge shape right after the films have coalesced. Specifically, we assume that the liquid in the overlapping

region of the liquid films (i.e., red and green shaded regions in Figure 4.1b) is instantaneously displaced laterally, and flows into a ring-shaped region. The latter is illustrated by the red solid area in Figure 4.1b, i.e., the bridge has been considered to be cylindrical at time zero. Geometrical considerations, discussed in greater detail in Geometrical Bridge Volume section, can now be used to predict the size of the ring-shaped region. These considerations, as well as the assumption of zero initial velocity and uniform pressure distribution, have been used to initialize all our simulations.

Most important, in our simulations there is no gravity, or other force acting on the system. The physical reason why liquid in the films on the particle surfaces flows into the liquid bridge is as follows: the pressure in the film (adhering to the particle surface, and far away from the bridge) can be estimated as $p_s \approx 2\sigma/R$, while the pressure in the liquid bridge region can be approximated as $p_{V_b} \approx -\sigma/R_{curve}$. Here R_{curve} is the radius of curvature of the liquid bridge surface. Thus, the pressure in the liquid bridge region is always negative or zero, while that in the film is always positive. Hence, a pressure difference between the particle surface and the liquid bridge region exists, driving the liquid into the bridge. This liquid flow will not stop until the pressure difference reaches zero, or the liquid film on the particle surface ruptures (for details about film rupture see Section 'Film Rupture and Grid Refinement').

4.2.2 Volume of Fluid Simulation Approach

A Volume of Fluid (VoF) method,[48] which is available as "interFoam" solver in the open-source software package OpenFOAM®, has been employed in our simulation. The interFoam solver has been verified extensively by Deshpande et al.[48] and we have also made several tests, e.g., calculating the pressure distribution in a liquid film coating a single sphere. For a typical grid resolution of $\Delta h = \Delta x / h_1 = 0.10$ (here Δx is the grid spacing, and h is the film height), these test show that the pressure can be predicted within an acceptable error tolerance of ca. -4.6%. In addition, we have tested the grid dependency of our results, and

found that $\Delta h = 0.12$ gives acceptable results for most situations of interest (see the Film Rupture and Grid Refinement section for more details).

Another critical point when it comes to two-phase flows is the prediction of the dynamic contact angle, since this is not a constant, but is influenced by the speed of the three-phase contact line. Unfortunately, the current implementation of dynamic contact angles in the "interFoam" solver has not been verified, and hence we are unable to accurately simulate the motion of three-phase contact lines. However, we have spared out this detailed by simply assuming that the spheres are completely coated, and hence there is (initially) no three-phase contact line in our simulations. This allows us to apply the "interFoam" solver for our studies of two coated particles without additional modifications. It must be mentioned here that for long times we observe a rupture of the liquid film present on the spheres. In such a situation a three-phase contact line forms, and hence, our solver will deliver inaccurate (but still physical) predictions of the liquid bridge shape after rupture. We accept this inaccuracy for the time being, and simply have not considered data collected after film rupturing events in our analysis.

The transport equation for a color function, representing the volume fraction of the liquid phase, is solved together with the continuity and momentum equations:

$$\frac{\partial(\rho \boldsymbol{U})}{\partial t} + \nabla \cdot (\rho \boldsymbol{U}\boldsymbol{U}) = -\nabla p + \mu \left[\nabla \boldsymbol{U} + (\nabla \boldsymbol{U})^T \right] + \boldsymbol{f}_b \tag{4.1}$$

$$\nabla \cdot \boldsymbol{U} = 0 \tag{4.2}$$

$$\frac{\partial \alpha}{\partial t} + \nabla \cdot (\boldsymbol{U}\alpha) = 0 \tag{4.3}$$

Where $\boldsymbol{U}$ is the velocity field shared by the two fluids (i.e., the liquid on the spheres and the surrounding gas) throughout the flow domain, and α is the phase fraction indicator. ρ is density, p is pressure, and f_b are body forces, which include (i) surface tension effects at the interface, and (ii) gravity. However, effects due to gravity have been neglected in our simulation, because viscous and

capillary effects are dominant in situations involving relevant particles (i.e., in situations in which particles have a diameter that is smaller than the capillary length). The phase function α can proceed within the range $0<\alpha<1$, with alpha being zero (or unity) in regions occupied by the gas (or the liquid), respectively.

The physical properties are computed as averages based on the distribution of the liquid volume fraction α. Specifically, we use:

$$\rho = \rho_l \alpha + \rho_g (1-\alpha) \tag{4.4}$$

$$\mu = \mu_l \alpha + \mu_g (1-\alpha) \tag{4.5}$$

where ρ_l (or μ_l) and ρ_g (or μ_g) are the density (or the dynamic viscosity) of the liquid and gas, respectively.

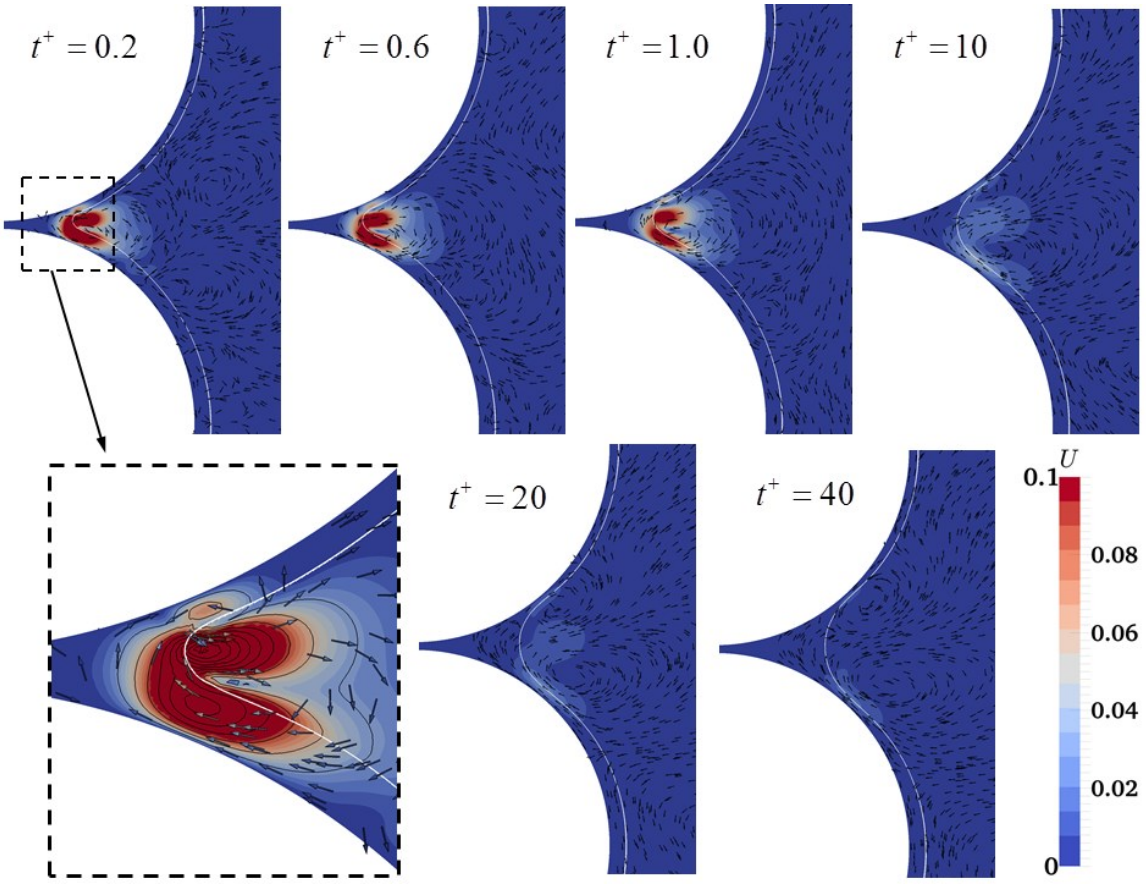

Figure 4.2: Typical velocity field for fluids flow over two fully coated particles using DNS.

Relevant dimensionless quantities describing the problem can be readily identified: the dimensionless initial film heights, the dimensionless separation distance, the bridge volume and the amount of liquid on particle surface normalized by a reference volume (i.e., the particle radius cubed R^3), the density and viscosity ratio between the liquid and the ambient gas, the pressure scaled with a typical capillary pressure (i.e., surface tension over the particle radius) and the velocity scaled with a typical capillary speed (i.e., the ratio of surface tension and viscosity of the liquid). The relevant time scale can be based on a corresponding viscous time scale, which is chosen to be the ratio of the particle radius and the capillary speed. Finally, we may want to consider the effect of the fluid's inertia on the filling process, and hence a Reynolds number can be defined based on the capillary speed, the particle radius, and the fluid viscosity. Note, that alternatively an Ohnesorge number can be defined, with is simply the inverse of the square root of the Reynolds number as summarized below:

- $h_1^+ = h_1/R$, $h_2^+ = h_2/R$, $h_0^+ = \left(h_1^+ + h_2^+\right)/2$, $S^+ = S/R$;
- $L_{p1}^+ = L_{p1}/R^3$, $L_{p2}^+ = L_{p2}/R^3$, $V_b^+ = V_b/R^3$;
- $\rho_{ratio} = \rho_l/\rho_g$, $\mu_{ratio} = \mu_l/\mu_g$;
- $u_{ref} = \sigma/\mu_l$, $p_{ref} = \sigma/R$, $t_{ref} = R\mu_l/\sigma$;
- $t^+ = t/t_{ref}$
- $Re = \sigma R\rho_l/\mu_l^2$, $Oh = \mu_l/\sqrt{\rho_l\sigma R} = 1/\sqrt{Re}$, $Ca = \mu_l|\mathrm{U}|/\sigma$.

A typical result of our DNS is shown in Figure 4.2, in which we illustrate the dimensionless flow velocity for various dimensionless times. Most important, this figure illustrates that the dimensionless velocity strongly decrease with time, and it can be expected that the rate with which the bridge is filled decreases with increasing time. All relevant simulation parameters and numerical scheme are defined in Table 4.1.

Parameter	Value	Comment
Δt^+	$5 \cdot 10^{-3}$	Dimensionless time step
Δh	0.05 - 0.33	Dimensionless mesh resolution
Time derivative scheme	backward	Second order, implicit
Laplacian scheme	Gauss linear corrected	Unbounded, second order, conservative
Convection scheme (for U)	Gauss linear	Unbounded, second order
Convection scheme (for α)	Gauss vanLeer	van Leer limiter

Table 4.1: Simulation parameters and numerical schemes used in the VoF simulations.

4.2.3 Liquid Bridge Volume Calculation

The gas-liquid interface can be easily determined from the DNS data by analysing the distribution of the phase fraction. Hence, we have taken a simple, yet effective sampling method to detect the gas-liquid of the film and the bridge formed between the particles.

As can be seen in Figure 4.3, the sampling procedure takes place between O_1 and O_2 with an interval of δx and a large enough sample distance in the y-direction. By applying the sampling interval from O_1 and O_2, we obtain a list of data for the phase value along each sampling line, and consequently the interface position can be determined at $\alpha = 0.5$.

Next, we need to define which portion of the fluid in the system is considered to be in the liquid bridge. As can be seen from Figure 4.2 and Figure 4.3 (panel b), there exists a minimal liquid film thickness on each of the two spheres. Thus, if one would analyze the thickness profile on each particle, one can observe a certain angular position where the film is thinnest. We have used this local minimum to define the extent of the liquid bridge. Specifically, we denote these positions of the minima as the “neck” positions, which separate the bridge from the film

adhering to the particle surface. These neck positions are the basis for the subsequent bridge volume calculation.

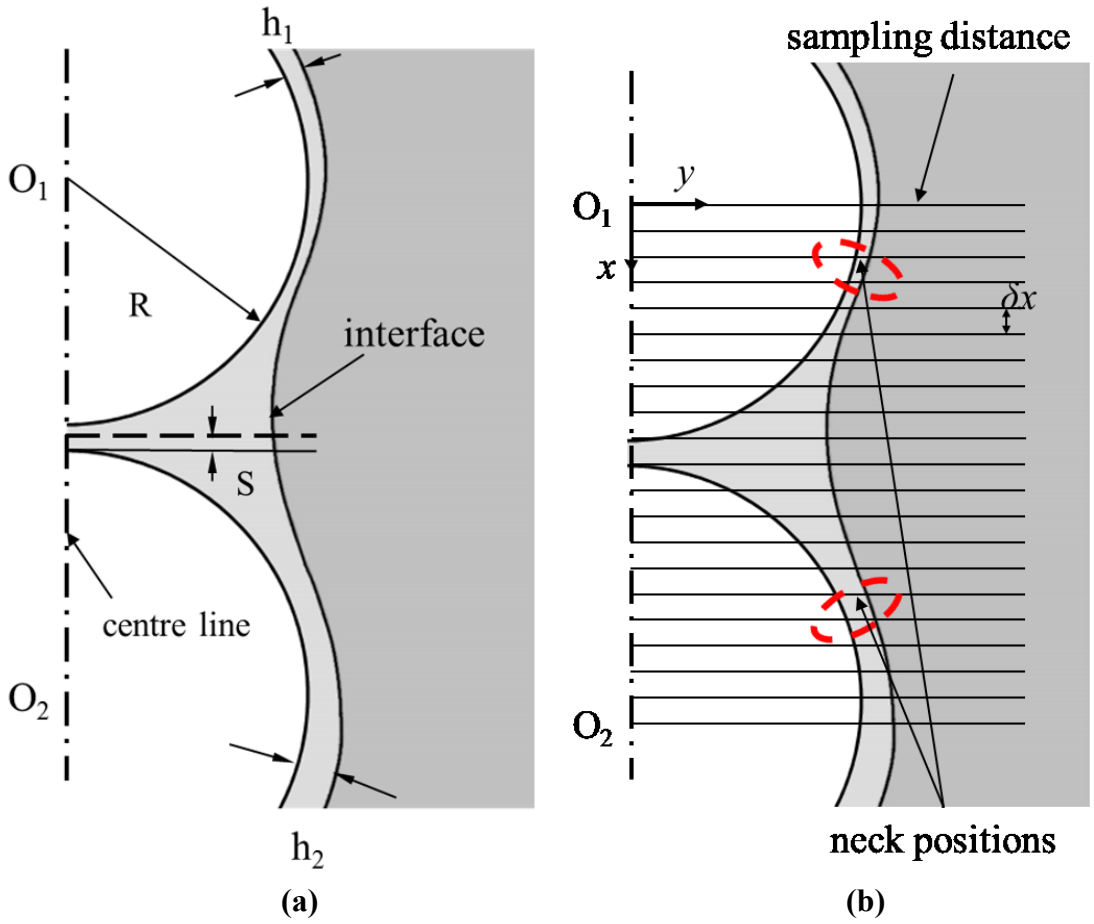

Figure 4.3: Sketch of (a) the gas-liquid interface between two particles, as well as (b) the sampling procedure used to detect the neck position.

After the interface positions and neck position have been determined, we can calculate the liquid bridge volume by using a direct integration method. Specifically, we use slices with thickness δx (see Figure 4.3, panel b), as well as the known neck positions, to determine the bridge volume by numerical integration using the trapezoidal rule.

4.2.4 Proposed Model for Liquid Bridge Filling

Our DNS indicate that the mechanism of liquid bridge formation consists of the following steps: after the coated particles get close to each other (caused by the relative motion in a real-world granular flow), the films coalesce, a liquid bridge is

then formed between the particles, and finally liquid drains into the bridge. Thus, it is reasonable to assume that there is (i) a very fast initial formation processes (immediately after coalescence; since we cannot resolve this process, we will simply assume a certain initial bridge volume), and (ii) and a comparably slow filling process. Consequently, we differentiate between two stages of the filling process of liquid bridge: (I) a capillary-force driven initial stage (fast filling), and (II) a viscous filling stage (slower filling). Although these two stages will overlap in physical reality, we define stage I to end after a (viscous) reference time scale of t_{ref}, i.e., a dimensionless time of $t^+=1$. As shown next, we employ two different sub-models to predict the liquid bridge volume in these two stages. By employing an overall mass balance it is then straight forward to predict the liquid residing on the contacting particles.

For the initial stage we simply aim on correlating the bridge volume after $t^+ = 1$ with the most important process parameters. Specifically, we simply choose the key geometrical parameters, which are (i) the initial film height h_0, as well as (ii) the half separation distance S.

The next section of the paper details on a postulated model to predict the time evolution of liquid bridge volume in stage II. Specifically, we use a phenomenological closure for the flow rate between the film and bridge compartment. We assume the flow rate to be proportional to the difference of the mobile fraction of the liquid on the particle and half of the bridge volume. In order to compute the mobile fraction of the liquid present on the particle, we use a single parameter which is called the mobility parameter $\phi_{m,i}$. This parameter is simply the ratio of the mobile liquid (i.e., the portion of liquid which flows into liquid bridge region) on a particle divided by the total liquid content on particle i. We will see in the Results section that the mobility parameter itself is a function of the initial film height and the particle separation, but is invariant in time. For now, we simply use $\phi_{m,i}$ as a parameter that is constant during the filling process. Using a dimensionless filling rate parameter a_i (which one can assume to be

specific for each particle i) and the reference time scale t_{ref}, we finally arrive at the following differential equations for predicting the liquid content $L_{p,i}$ on each particle i:

$$\frac{dL_{p,i}}{dt} = \frac{-a_i}{t_{ref}}\left(L_{p,i}\phi_{m,i} - \frac{V_b}{2} \right) \tag{4.6}$$

This closure is linear in the unknown variables. Hence, an analytical solution for the liquid bridge volume and the liquid content remaining on the particles can be obtained. A simple mass balance yields the governing equation for the volume $V_{b,j}$ of bridge j:

$$\frac{dV_{b,j}}{dt} = -\sum_{i \in l_j} \frac{dL_{p,i}}{dt} \tag{4.7}$$

Here j is the list of particle indices that is in contact with bridge j. We now re-write these equations in dimensionless variables, and apply them to a two-particle system. Together with appropriate initial conditions, as well as the assumption that a_i is a constant for a pair of particles sharing the same bridge, we arrive at the following analytical solution:

$$V_b^+ = V_{b,0}^+ + C_1 \frac{\frac{2r_1}{a_i} + 2\phi_{m1}}{r_1}\left(e^{r_1 t^+} - 1 \right) + C_2 \frac{\frac{2r_2}{a_i} + 2\phi_{m1}}{r_2}\left(e^{r_2 t^+} - 1 \right) \tag{4.8}$$

$$L_{p1}^+ = L_{p1,0}^+ + \frac{C_1}{r_1}\left(e^{r_1 t^+} - 1 \right) + \frac{C_2}{r_2}\left(e^{r_2 t^+} - 1 \right) \tag{4.9}$$

$$L_{p2}^+ = L_{p2,0}^+ - C_1 \frac{\frac{2r_1}{a_i} + 2\phi_{m1} + 1}{r_1}\left(e^{r_1 t^+} - 1 \right) - C_2 \frac{\frac{2r_2}{a_i} + 2\phi_{m1} + 1}{r_2}\left(e^{r_2 t^+} - 1 \right) \tag{4.10}$$

where r_1, r_2, C_1, and C_2 are dimensionless coefficients that are detailed in Appendix A. Using this solution it is now straight forward to calibrate the model parameters (i.e., a_i and $\phi_{m,i}$) with the results of our DNS (i.e., the time evolution of L_p and V_b).

4.3 Geometrical Bridge Volume

In order to close the proposed model (see the Results section), it is useful to define a reference bridge volume based on geometrical arguments. For such a geometrical bridge volume we have considered two types which are illustrated in Figure 4.4. Our goal is to study liquid bridge formation between particles having initially a different liquid content. Thus, it is useful to define a bridge volume based on the average (i.e., arithmetic mean) film height h_0 (see the definition in previous section: Volume of Fluid Simulation Approach). The expressions for the geometrical bridge volume detailed below need to be understood as the typical volume of a liquid bridge when making certain assumptions about its shape.

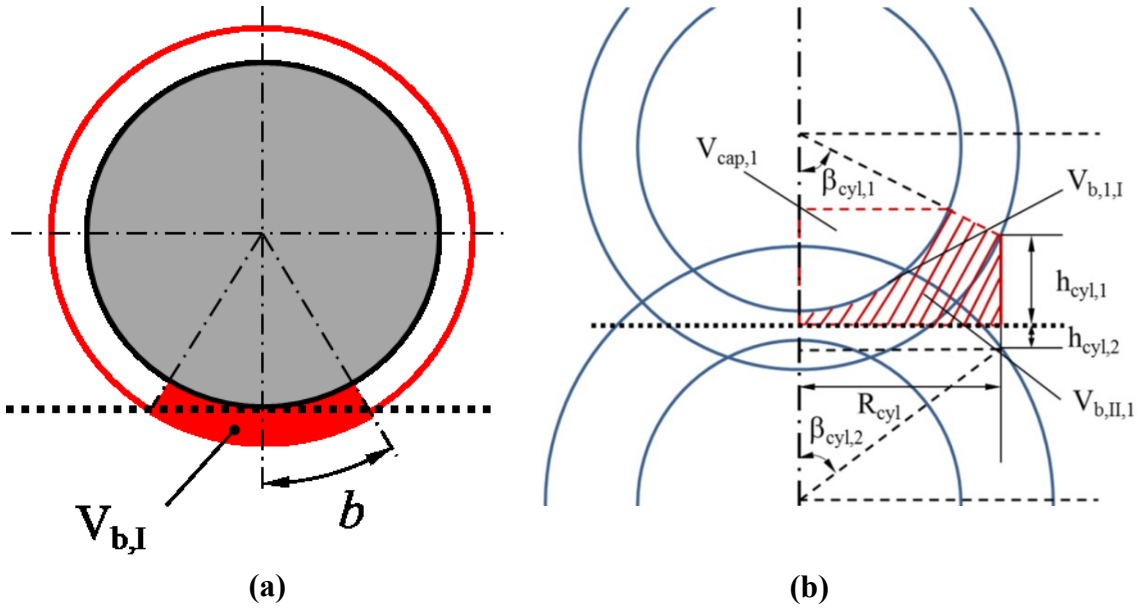

Figure 4.4: Geometrical bridge volume: (a) type I (the dashed line indicates the symmetry plane of two contacting particles), (b) type II.

4.3.1 Type I

Type I (Figure 4.4a) is a simple definition based on the assumption that the initial bridge volume is that in the cap-shaped region of the particle. This definition is similar to the idea of Shi and McCarthy[46], which assumed that a fixed fraction of the liquid present on the particle forms the bridge. This previous definition of Shi and McCarthy would predict a linear relationship between the bridge volume

and the liquid film thickness (and, to a first approximation, also with the liquid content on each particle's surface). However, we argue that this previous definition is unrealistic. The reason for this is that the lateral extent (i.e., the length b) of the cap-shaped region defined by the gas-liquid interface and the symmetry plane between contacting particles is clearly a function of the film thickness (see Figure 4.4, left panel). Hence, for the present work we assume that the geometrical bridge volume of "type I" is a non-linear function of the liquid film thickness. Specifically, we assume that the bridge volume is equal to the red-shaded cap-shaped region in Figure 4.4 (left panel). For this situation the liquid bridge volume can be calculated analytically:

$$V_{b,g,I} = 2h_0 b^2 \pi \text{ , with} \tag{4.11}$$

$$\frac{b}{R} = \left(1 + h_0^+\right) \cos^{-1}\left(1 / \left(1 + h_0^+\right)\right) \tag{4.12}$$

4.3.2 Type II

Type II considers another shape of the liquid bridge, which is shown in Figure 4.4b. Here, we take the separation distance of the particle into account, implying that the type II geometrical bridge volume is more realistic for large separations. Specifically, we assume that the liquid in the overlapping regions (given by the assumed spherical shape of the liquid films on the particle) must be laterally displaced when the particles approach each other. This liquid is assumed to flow into a ring-shaped region. One can then compute the liquid bridge volume from the red shaded area (see Figure 4.4, right panel). Specifically, the volume of the type II bridge geometry can be calculated as follows:

$$V_{b,g,II} = V_{b,\mathrm{i,I}} - V_{cap} \tag{4.13}$$

The evaluation of the above equation involves lengthy expressions, and is detailed in Appendix B. Unfortunately, this evaluation also requires an iterative procedure, making it less attractive for direct evaluation during large-scale DEM-based simulation.

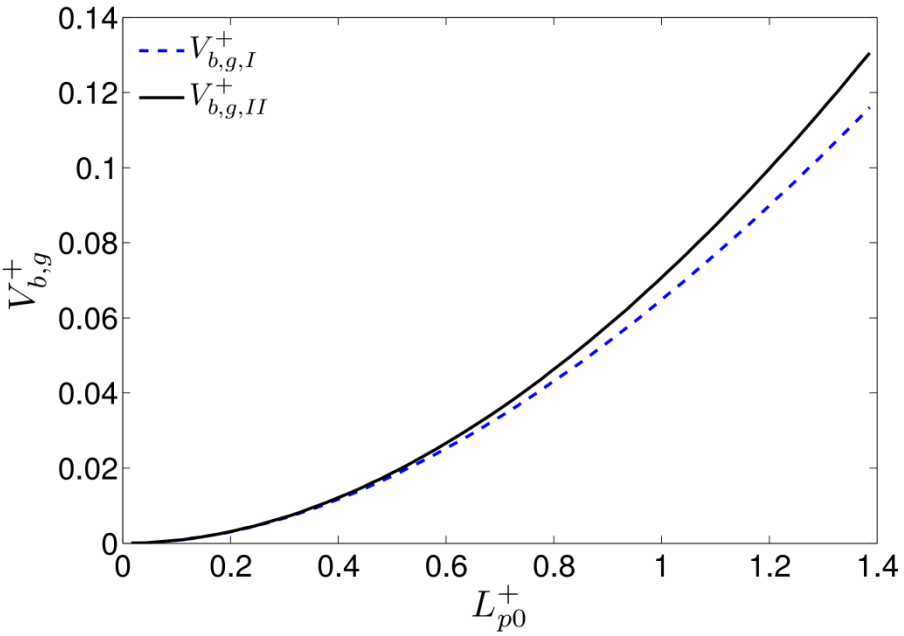

Figure 4.5: Comparison of the type I and type II model for computing the geometrical bridge volume in situation A: increasing liquid content on the particles at $S^{+} = 0$.

We next compare these two types of models for the geometrical bridge volume for two situations: in situation A we increase the liquid content (i.e., the initial film heights), but assume contacting particles (i.e., zero separation between particles). Results for this situation are shown in Figure 4.5, which shows the dimensionless bridge volume as a function of the L_{p0}^{+}, where L_{p0}^{+} is dimensionless form of average amount of initial liquid content of the two particles and defined by $L_{p0}^{+} = \frac{4}{3}\pi\left(\left(R+h_0\right)^3 - R^3\right)/R^3 = \frac{4}{3}\pi\left(\left(1+h_0^{+}\right)^3 - 1\right)$. We observe that for both types of definitions the bridge volume increase with the liquid content non-linearly. Note, that in the definition of Shi and McCarthy[46] the bridge volume increases linearly. Furthermore, we see that the two curves for type I and type II nearly overlap, and that type II predictions are slightly larger than that of type I. Thus, the two curves agree well with each other for thin initial films, while they do not agree with each other for thicker films. Since the definition of the type II model at zero separation is close to that of type I, this is expected and explained as follows: the type II model takes into account that the laterally displaced liquid forms a bridge with a certain height $h_{cyl,1}$ and $h_{cyl,2}$ (see Figure 4.4, right panel).

Consequently, a certain amount of the liquid on the particle (in addition to that accounted for in the type I model) is considered to be in the bridge. Thus, when using the type II definition, the (geometrical) bridge volume is somewhat larger compared to that predicted by type I. In summary, we see that the type I approximation is appropriate for thin films and at zero separation, while type II should be considered for all other situations.

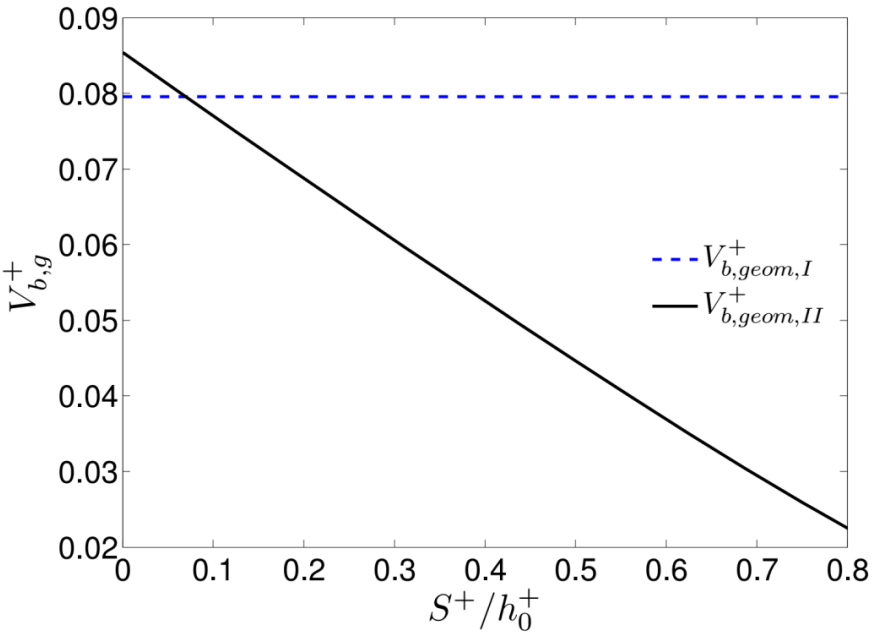

Figure 4.6: Comparison of the type I and type II model for computing the geometrical bridge volume in situation B: fixed initial film height $h_0^+ = 0.08$ and variation of the separation distance.

Situation B is now investigated to demonstrate the effect of the particle-particle separation distance on the predicted (geometrical) bridge volume. Specifically, a certain (constant) initial film height was assumed for both types of models, and the separation between particles was varied. Results are illustrated in Figure 4.6. One can observe that the prediction of the type I model is not affected by the separation distance. However, for the type II model, the geometrical bridge volume remarkably decreases when the separation distance increases. Also, the type II model predicts a somewhat larger bridge volume (compared to type I) at zero separation as it should be. In summary, the type II model is more realistic,

and we will demonstrate in following that our results (based on DNS) are very close to the predictions of this model.

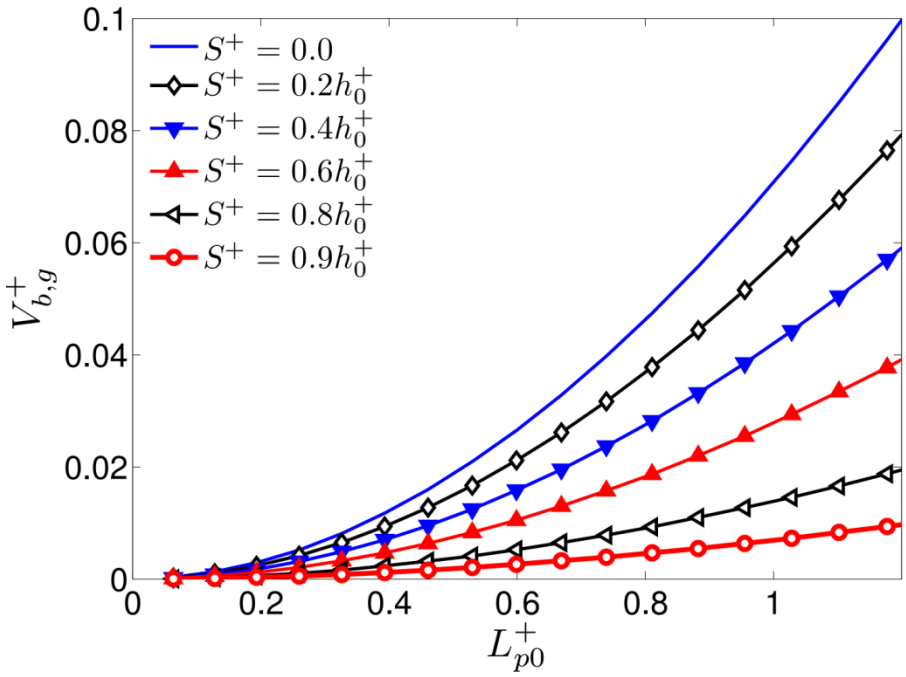

Figure 4.7: Effect of the separation distance on the bridge volume as a function of the initial liquid content (type II model).

Figure 4.7 further illustrates how the separation distance affects the prediction of the (geometrical) bridge volume when using the type II model. As can be seen from Figure 4.7 the bridge volume increases monotonically, but non-linearly, with increasing (initial) liquid content for every choice of separation distance. In the situation of zero separation the largest bridge volume is predicted. Also, it can be observed that the bridge volume decreases almost linearly with increasing separation distance, finally approaching zero for $S^{+}/h_0^{+} = 1$as it should be. The physical interpretation of this fact is that for the situation in which the separation equals the initial film thickness, the overlapping region of thin films between two particles vanishes. Thus, the geometrical bridge volume becomes zero. In summary, the type II model shows the correct behaviour for a variety of limiting cases. Hence we argue that it is physically more relevant compared to previous work.

4.4 Results

4.4.1 Early Stage Model (Stage I)

The initial bridge forms very quickly, and the inertia of the fluid may play a certain role. Inertia is difficult to model due its inherent non-linearity. We hence define a fixed initial bridge volume for "early times". Specifically, we have chosen the early stage to end after one reference viscous time scale, i.e., at $t^+ = 1$.

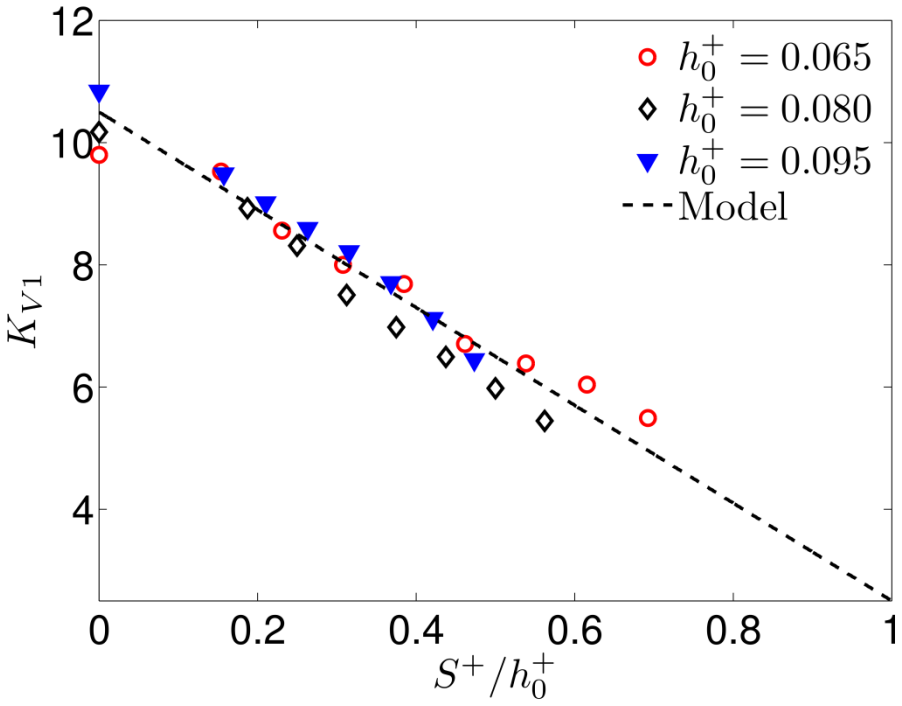

Figure 4.8: Normalized initial bridge model K_{VI} vs. normalized separation distance.

We now attempt to model the initial bridge volume by defining the variable K_{VI}, which is the ratio of the simulated (total) initial bridge volume ($V_{b,0}^+$ is the liquid bridge volume at $t^+=1$) and the average initial film height h_0^+ to the power of some exponent n:

$$K_{V1} = \frac{V_{b,0}^+}{\left(h_0^+\right)^n} \tag{4.14}$$

This definition is based on the simple idea that the initial bridge volume is only a function of the (initial) film height, similar to the idea we used to define the

geometrical bridge volume of type I. We see from Figure 4.8 that when choosing n = 1.5 we can collapse our DNS results for a variety of film thicknesses with the expression:

$$K_{V1} = -8.0\left(\frac{S^+}{h_0^+}\right) + 10.5 \tag{4.15}$$

Thus, we see that we can obtain a reasonable collapse of our data on a straight line for this choice of n and for $S^+/h_0^+ < 0.7$. We also note that (i) the normalized bridge volume linearly decreases with increasing separation distance, and (ii) that the bridge volume is a super-linear function of the film height. The former fact is in agreement with the type II geometrical bridge volume (refer to Geometrical Bridge Volume section). The latter again stresses the fact that the assumption of Shi and McCarthy[46] that liquid is "harvest" from a fixed (area) fraction of the particle surface is not supported by our results. A model based on "harvesting" from a fixed (area) fraction of the particle surface would result in a linear increase of the bridge volume with film height, i.e., n = 1. Clearly, this is not supported by our DNS data.

In summary, our model for K_{V1} could already be used to compute $V_{b,0}^+$ for a collision involving two wet particles using Eqn. 4.15. However, we next aim at using the geometrical bridge volume of type II to normalize the calculated initial bridge volume. We do this since this model accounts for the effect of the separation distance on the bridge volume, and we expect that normalization with this geometrical bridge volume yields a variable that is independent of S^+.

Specifically, we define the variable K_{V2} as the ratio of the measured initial bridge, the geometrical bridge volume calculated using the type II model (refer to Type II section), and a function of h_0^+:

$$K_{V2} = \frac{V_{b,0}^+}{V_{b,g,II}^+\left(h_0^+\right)^n} \tag{4.16}$$

Again, n is a parameter that is used as an exponent of the initial film height, and helps to collapse all data into a single curve. We expect that n is close to zero, i.e., that the geometrical bridge volume based on the type II model is sufficient to account for any effects due to the film height. The results of our analysis are displayed in Figure 4.9, which illustrates that the variable K_{V2} is independent of the average film height, when choosing $n = 0.2$. For the K_{V2} model, we also suggest a linear relationship between the normalized liquid bridge volume and the separation distance:

$$K_{V2} = 0.7\left(\frac{S^+}{h_0^+}\right) + 2.2 \tag{4.17}$$

In addition we note that assuming $n = 0$, i.e., using a normalization purely based on the geometrical bridge volume, would be also a good approximation (data not shown). Interestingly, we find that $K_{V2}\left(h_0^+\right)^n \approx 1.3$ for zero separation, indicating that the geometrical bridge volume of type II is indeed a good approximation of the initial bridge volume. Also, we find that K_{V2} increases with increasing separation, indicating that the geometrical bridge volume of type II over-compensates the decrease of the bridge volume. Thus, our DNS data suggest that the bridge volume is systematically larger for $S^+ > 0$ than that based on geometrical arguments. The exact reason for this is could not be isolated. However, it is clear that in the DNS the deformation of the gas-liquid interface is also taken into account. We speculate that this deformation leads to an additional lateral shift of the neck position (in addition to the shift caused by to the displaced fluid), which is more pronounced for larger separations.

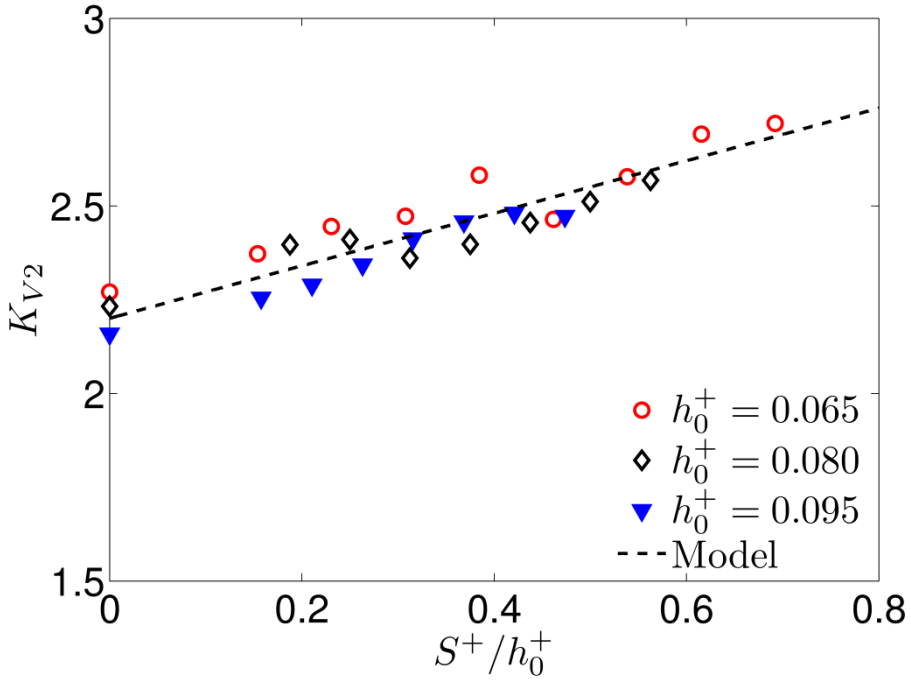

Figure 4.9: Initial bridge model, K_{V2} vs. normalized separation distance.

In summary, the model for K_{V2} presented above, together with its definition, and the geometrical bridge volume (type II) can be used to compute the bridge volume at $t^+ = 1$. We next focus on the calibration of the parameters in the proposed bridge viscous filling model (see section: Proposed Model for Liquid Bridge Filling), that can be used to predict the time evolution of the liquid bridge after this point in time.

4.4.2 Viscous Filling Stage Model (Stage II)

We start with looking at the time evolution of bridge volume and liquid present on the particle for the situation of zero separation start by taking one case for example (see Figure 4.10). We obtain the following parameter set $\phi_{m1} = 0.49$, $\phi_{m2} = 0.38$, and find that mobility parameter of particle 1 is somewhat larger than that of particle 2 (particle 1 initialized with less liquid content than particle 2). Furthermore, we find that the dimensionless filing rate coefficient a_i (i.e., the inverse of a dimensionless filling time scale) is approximately 0.025. This value fits all our data reasonably well, and hence we accept a_i to be a universal constant from now on.

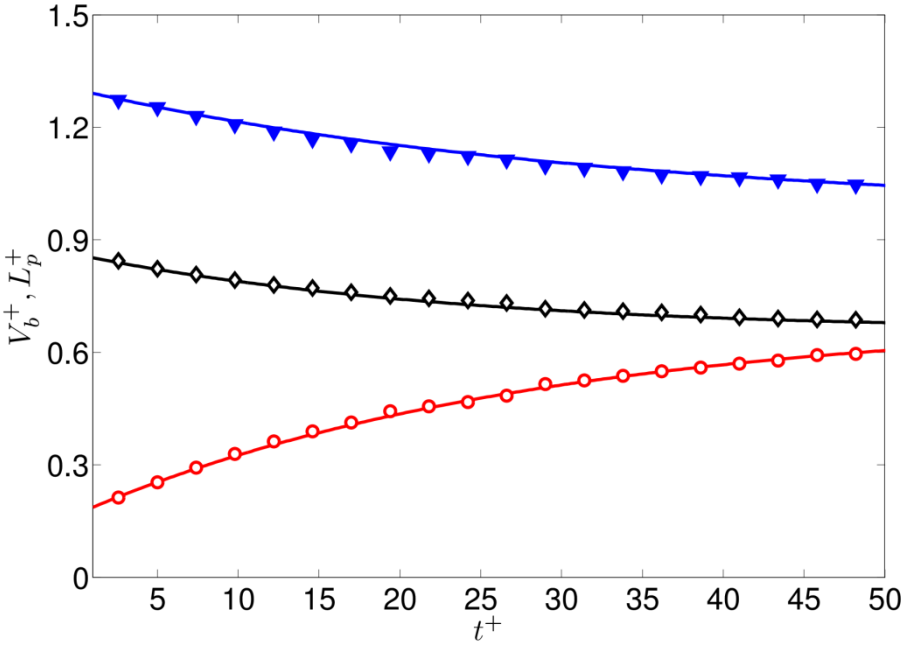

Figure 4.10: Fitted model (lines) vs. DNS data (symbols) over time for $S^+ = 0$, $h_1{}^+ = 0.07$ and $h_2{}^+ = 0.1$. Red circles: liquid bridge volume ($V_b{}^+$); Black diamonds: liquid content on particle 1 ($L_{P1}{}^+$); Blue triangles: liquid content on particle 2 ($L_{p2}{}^+$).

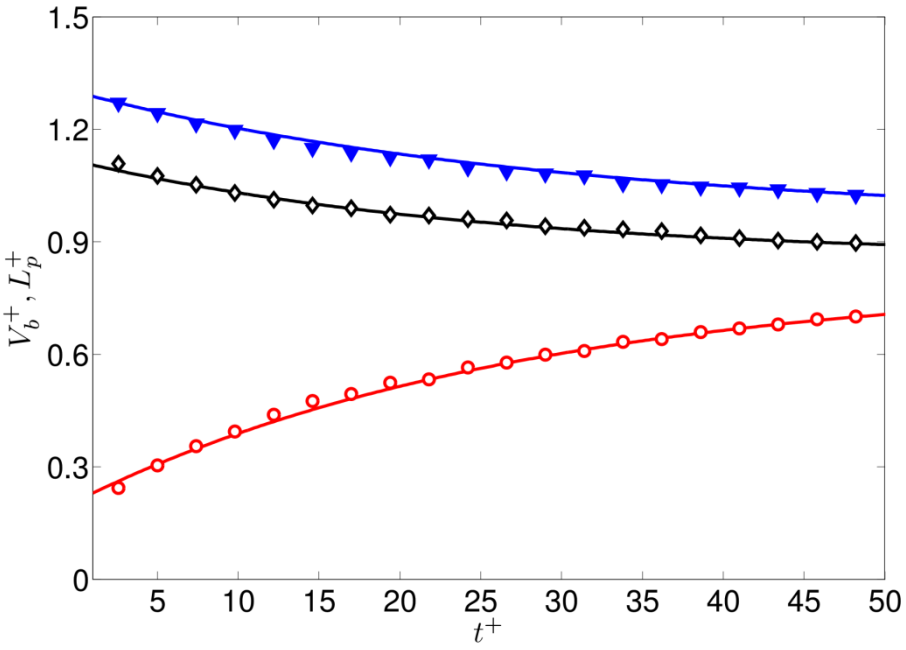

Figure 4.11: Fitted model (lines) vs. DNS data (symbols) over time for $S^+ = 0$, $h^+{}_1 = 0.09$ and $h_2{}^+ = 0.1$. Red circles: liquid bridge volume ($V_b{}^+$); Black diamonds: liquid content on particle 1 ($L_{P1}{}^+$); Blue triangles: liquid content on particle 2 ($L_{p2}{}^+$).

Results in Figure 4.11 are also obtained for the zero separation case, however, for a different combination of film thicknesses. The mobility parameters for this case

are $\phi_{m1} = 0.45$ and $\phi_{m2} = 0.43$, respectively. By comparing Figure 4.10 and Figure 4.11, we observe that the trend of liquid transport between two particles are similar, and the model approximates the filling process reasonably well. As expected, the case with the larger (average) initial film height yields a larger liquid bridge volume.

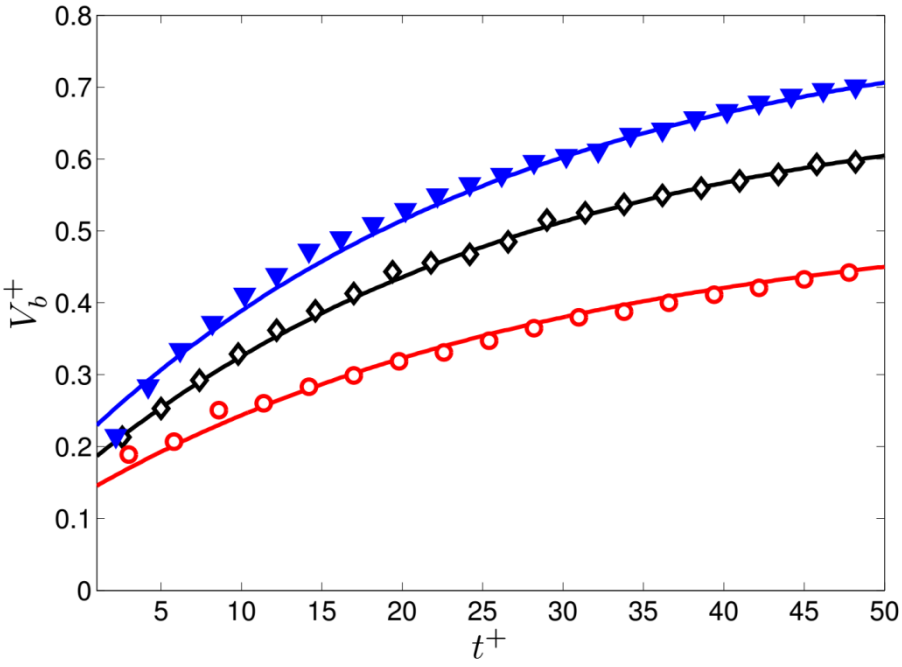

Figure 4.12: Liquid bridge volume over time: fitted model (lines) vs. DNS data (symbols), $S^+ = 0$. Red circles: $h_0^+ = 0.075$; Black diamonds: $h_0^+ = 0.085$; Blue triangles: $h_0^+ = 0.095$.

Further testing of our model for other combinations of thickness reveals that our model is indeed able to describe the filling process well. As we can see from Figure 4.12, larger film height always leads to larger bridge volume, which is obvious. We also can see that the filling process levels off after about 50 dimensionless time units. This is also suggested by the inverse of the constant a_i, which has been fixed before. However, the filling process has not completely stopped at $t^+ = 50$. Indeed, we find that when running the simulation for a longer duration the filling process will end at some point due to the rupture of the film on one of the two particle surfaces. We will discuss this peculiar behavior later (see the Film Rupture and Grid Refinement section).

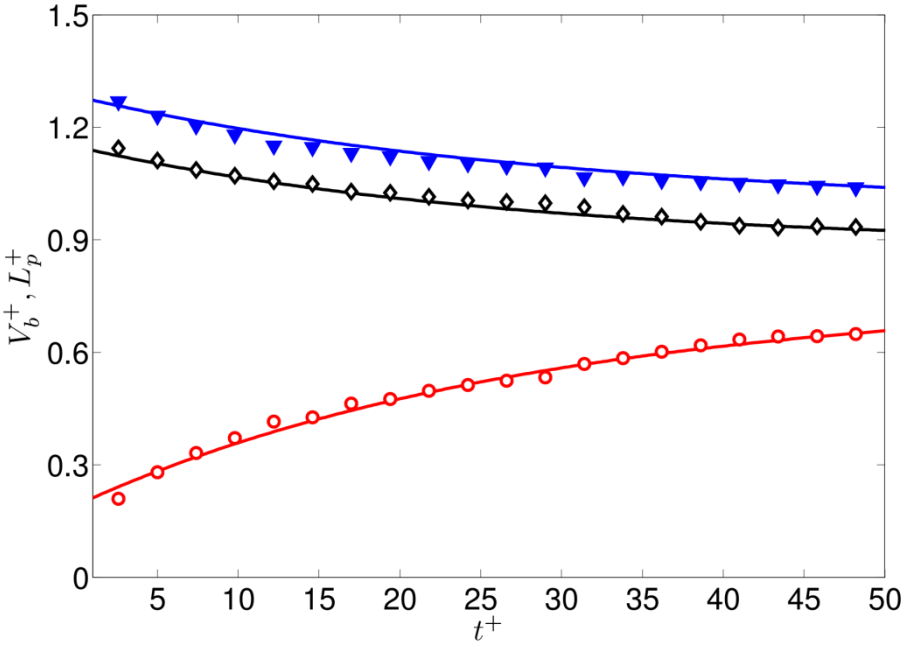

Figure 4.13: Fitted model (lines) vs. DNS data (symbols) over time for $S^+ = 0.045$, $h_1{}^+ = 0.09$ and $h_2{}^+ = 0.1$. Red circles: liquid bridge volume ($V_b{}^+$); Black diamonds: liquid content on particle 1 ($L_{P1}{}^+$); Blue triangles: liquid content on particle 2 ($L_{p2}{}^+$).

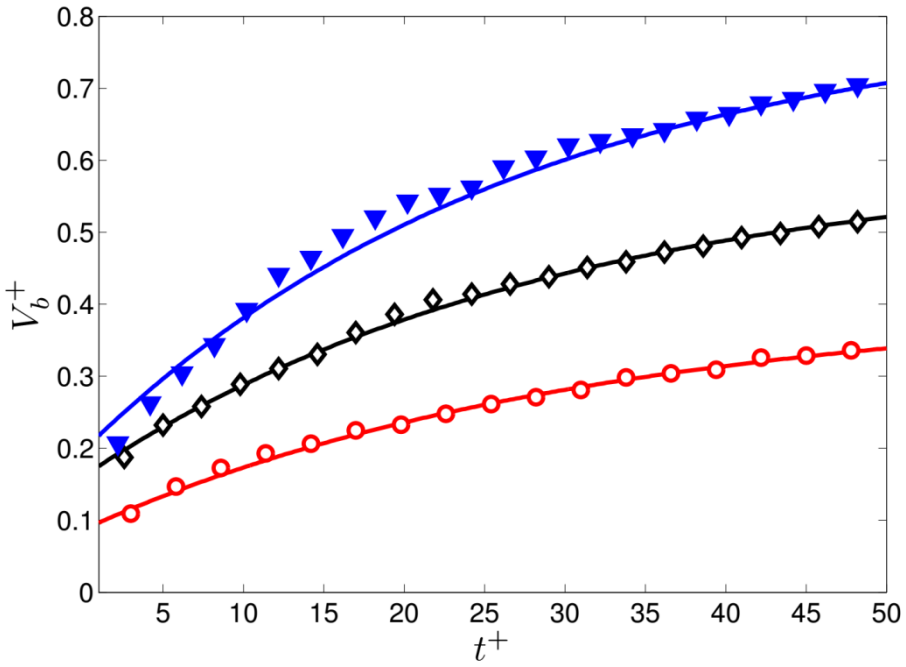

Figure 4.14: Combined effect of film height and separation distance: liquid bridge volume over time: fitted model (line) vs. DNS data (symbols). Red circles: $S^+ = 0.045$ and $h_0{}^+ = 0.065$; Black diamonds: $S^+ = 0.025$ and $h_0{}^+ = 0.08$; Blue triangles: $S^+ = 0.035$ and $h_0{}^+ = 0.095$.

Considering now separations larger than zero, we again see that the model is able to approximate the DNS data well (see Figure Figure 4.13, for $S^+ = 0.045$, $h_1{}^+ =$

0.09 and $h_2^+ = 0.1$). However, we find that the parameters ϕ_{m1} and ϕ_{m2} change. Specifically, the value of the mobility parameters is now $\phi_{m1} = 0.42$ and $\phi_{m2} = 0.39$, respectively. Thus, the mobility of the liquid on the particles becomes smaller for $S^+ > 0$ compared to the case with $S^+ = 0$. Our interpretation of this fact is that less liquid is mobile to flow into the bridge when the particles have a certain separation. Again, we can see from Figure 4.14 that larger initial film height causes larger liquid bridge volume, as expected.

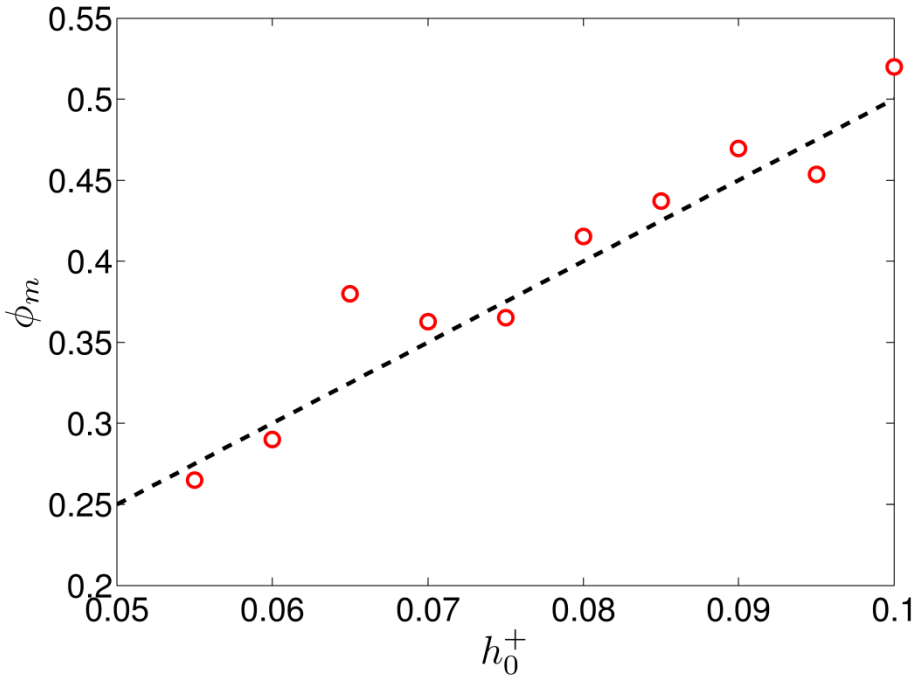

Figure 4.15: ϕ_m as a function of h_0^+ for a separation of $S^+ = 0$.

We now aim on demonstrating that our model is able to represent data for a variety of dimensionless initial film heights. Since the key parameter that is influenced by the film height is the mobility (i.e., $\phi_{m,i}$), we have collected these parameters for a large set of separation distances and dimensionless initial film heights. We now make an attempt of modeling $\phi_{m,i}$ by first computing an average mobility ϕ_m (see equation 4.18), that is simply defined as the arithmetic mean of the motilities of the particles in contact. We now look at the trends of this average parameter as a function of the initial average film height. As we can see from

Figure 4.15, ϕ_m changes linearly with the average initial film height for zero separation. Specifically, we obtain the following relationship for ϕ_m:

$$\phi_m = \frac{\phi_{m1} + \phi_{m2}}{2} \tag{4.18}$$

$$\phi_m = 5h_0^+ \tag{4.19}$$

For the difference in the mobilities, denoted as $\Delta\phi_m = |\phi_{m1} - \phi_{m2}|$ and illustrated in Figure 4.16, we find the following approximation:

$$\Delta\phi_m = 2.9\Delta h_0^+ \tag{4.20}$$

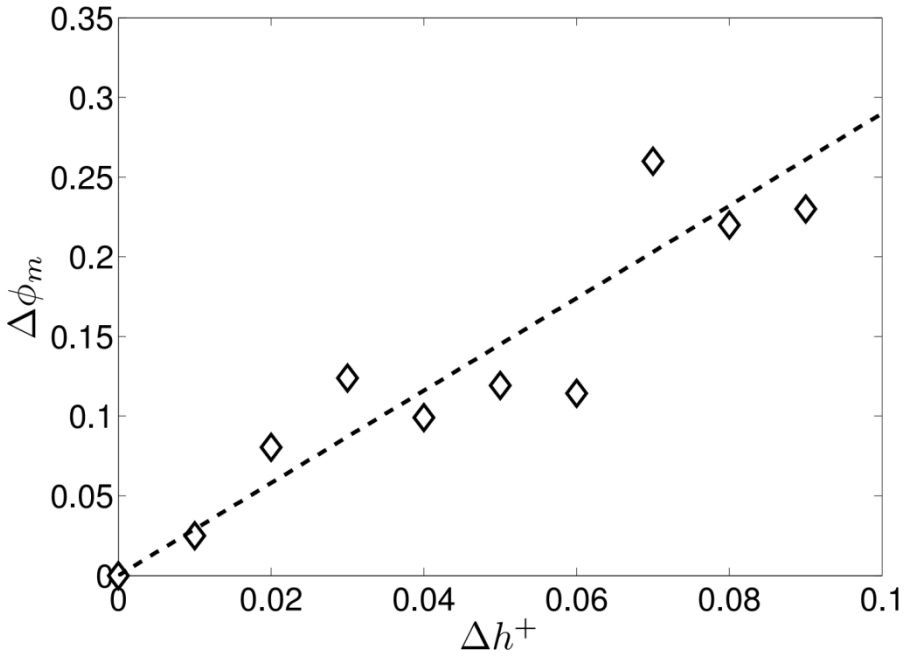

Figure 4.16: $\Delta\phi_m$ as a function of the dimensionless difference of the film heights.

Next, we aim at correlating ϕ_m with the separation distance. Specifically, we consider data sets for variations in the initial film height and separation distance shown in Figure 4.17. Again, we can collapse all data for different initial film heights when normalizing it with some function of the initial film height. Specifically, we define the variable $K_{\phi m}$ to be

$$K_{\phi_m} = \frac{\phi_m}{5h_0^+} \tag{4.21}$$

Based on the data shown in Figure 4.17, we find the following relationship for $K_{\phi m}$:

$$K_{\phi_m} = 1 - 0.32\left(\frac{S^+}{h_0^+}\right) \tag{4.22}$$

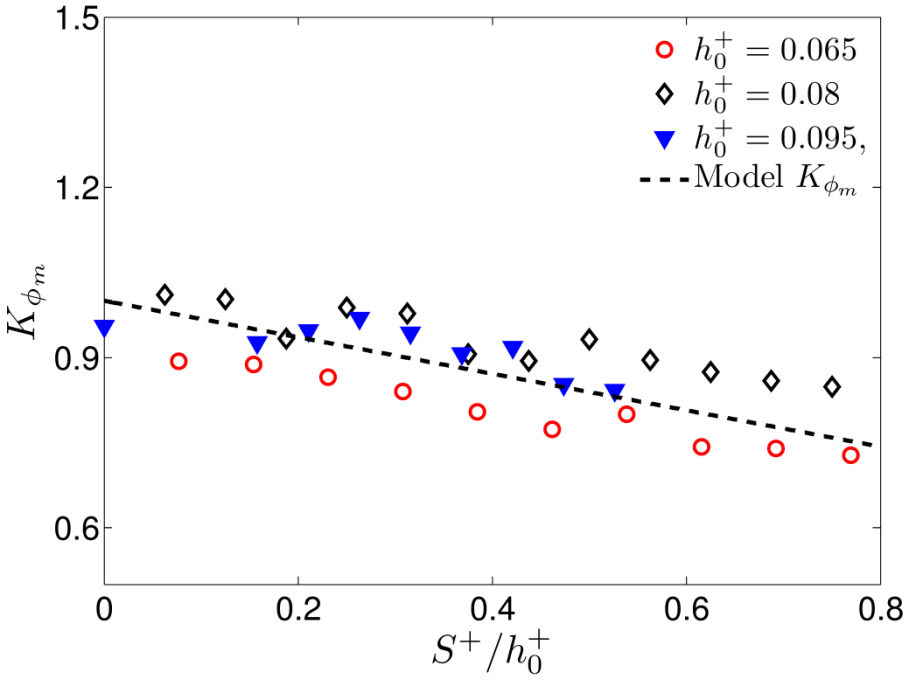

Figure 4.17: K_{ϕ_m} as a function of the normalized separation distance for contacting and non-contacting particles.

The meaning of these relationships is that the average mobility of the liquid on the particle surfaces systematically decreases with increasing separation distance. The physical interpretation of this fact is that smaller bridges (implied by larger separation distances and constant overall liquid content) simply allow proportionally less liquid to flow from the particle surface into the bridge. In contrast, at small separation distances, and hence larger bridges, a larger fraction of the particle's surface area is connected to the bridge, and hence the mobility parameter is large.

4.4.3 Film Rupture and Grid Refinement

We also show some interesting findings which we observe for very long simulation times and thin films: as can be seen in Figure 4.18 the film ruptures at the neck

position for sufficiently long time. Specifically, we observe that for thin films the film ruptures on the particle with initially less liquid (i.e., particle 1). This means that the bridge filling process stops after a certain time, which is also the case for the proposed model. Unfortunately, we cannot accurately predict the rupturing process, simply because the film at the rupturing point must become thinner than the (finite) grid resolution. It is therefore essential how the grid resolution affects the film rupturing event. This is discussed next.

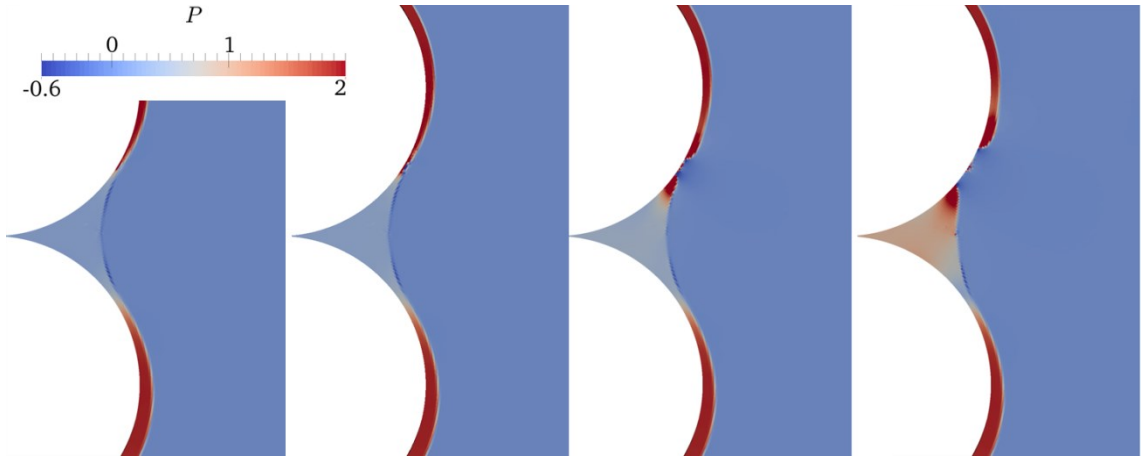

Figure 4.18: Pressure distribution before and after the film rupture moment $t^+ = 220$, $S^+ = 0$, $h_1^+ = 0.06$, $h_2^+ = 0.10$ (the rupture time scale is small, i.e., below $t^+ < 1$).

We start our investigation of the effect of grid refinement by defining a dimensionless grid size Δh. Specifically, we choose $\Delta h = \Delta x / h_1$, where Δx is the mesh size and h_1 is the initial film height of the particle with the lower amount of liquid on its surface. As can be seen from Figure 4.19, the grid refinement affects the filling process only negligibly, with the largest deviations observed for long times, i.e., $t^+ > 100$. As can be seen in the Figure for the case of a grid size of $\Delta h = 0.17$ (blue circles) film rupture is observed at $t^+ = 175$. However, in case of a larger grid resolution, i.e., $\Delta h = 0.12$ (black diamonds), we do not observe film rupture and the filling process continues until the simulation was terminated. Therefore, grid refinement plays an important role for predicting the final rupturing process. Moreover, it can be observed that a finer mesh yields a rather smooth curve, in contrast to the results for the coarser grid in which the bridge

volume appears to fluctuate. This is again caused by the more challenging detection of the neck position in the case of a (comparably) coarse grid.

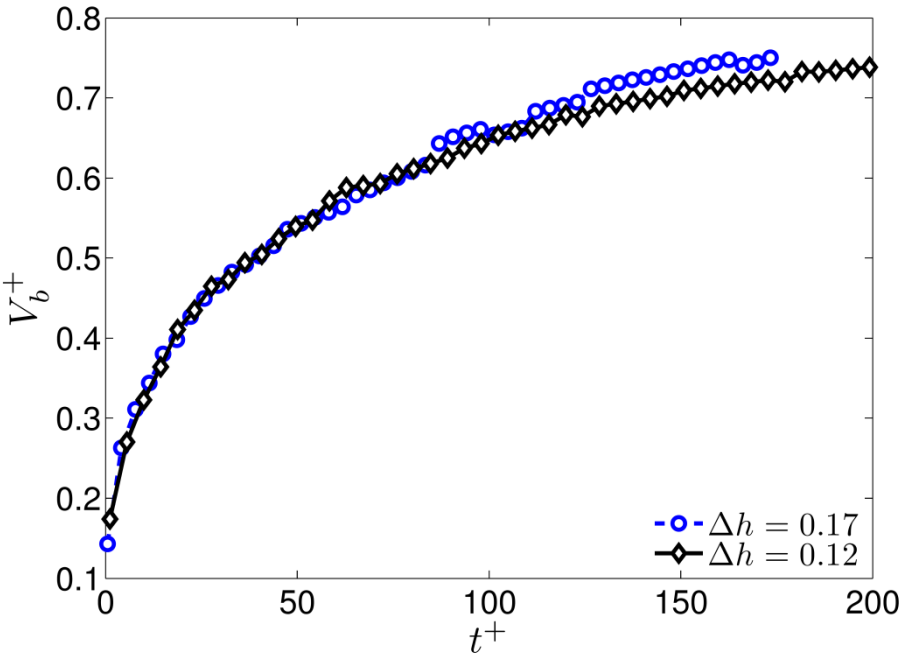

Figure 4.19: Grid refinement effects on the liquid bridge filling, $h_1^+ = 0.04$, $h_2^+ = 0.08$, $S^+ = 0.02$.

We have observed in our simulations that the film rupturing phenomena occurs on particles with less liquid. The obvious reason for film rupturing in the simulation is inadequate resolution of the liquid film in the neck region. The thinning of the film there is caused by the pressure difference over the neck region, which drives the flow of liquid into the bridge: due to the complex shape of the gas-liquid interface in this region, the pressure changes in a non-linear way in the neck region. The pressure distribution is such that more liquid exits the neck region than can flow from the film towards the neck. This leads to a thinning of the film, and once the film thickness is in the order of the grid resolution, it will rupture. We hence must limit the applicability of our model to situations well before the rupture event occurs in the simulation, i.e., to $t^+ < 100$.

4.4.4 Reynolds Number and Density Ratio Effects

In order to further investigate the model's ability to reflect various real-world situations, we checked the effect of the Reynolds number on the filling process.

Therefore, we have chosen a situation with rather thin films (i.e., $h_1^+ = 0.04$, $h_2^+ = 0.08$, $S^+ = 0.02$). We choose $Re = 1$, $Re = 100$ and $Re = 10{,}000$ for investigating Reynolds number effects.

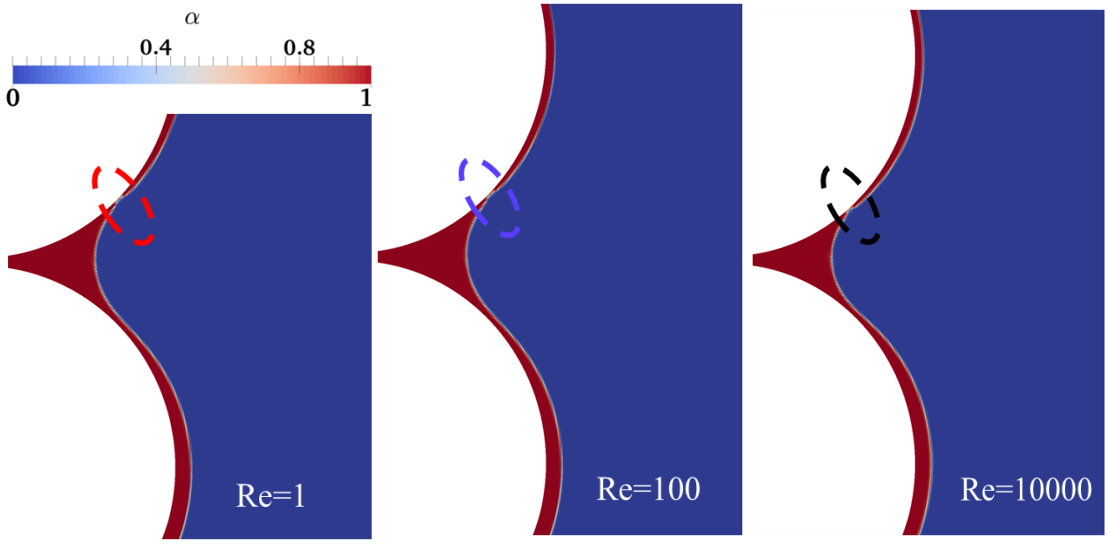

Figure 4.20: Liquid film distribution at the rupture moment, $h_1^+ = 0.04$, $h_2^+ = 0.08$, $S^+ = 0.02$.

As we can see from Figure 4.20, the points at which film rupture occurs are almost identical. Also, we observe that larger Reynolds number lead to an earlier film rupturing event (see Figure 4.21). However, the filling process of the bridge is not substantially affected by the Reynolds number. Hence, we draw the conclusion that the Reynolds number plays a negligible role for the bridge filling process, at least in the range of parameters we have investigated.

Finally, we have investigated the effect of the density ratio on the liquid bridge filling process (see our results in Figure 4.22 for the density ratios of $\rho = 10$, and $\rho = 1000$). The density ratio is a critical parameter for the numerical simulation, since simulations with a smaller density ratio are typically easier to conduct. As can be seen from Figure 4.22 the density ratio has little effect on the liquid bridge filling process as long as $\rho \geq 10$, and the rupturing event is delayed by about 5 dimensionless time units in the case of the low density ratio that has been investigated. Therefore, we can safely neglect effects due to the ambient gas density when considering bridge filling in gas-liquid-particle systems.

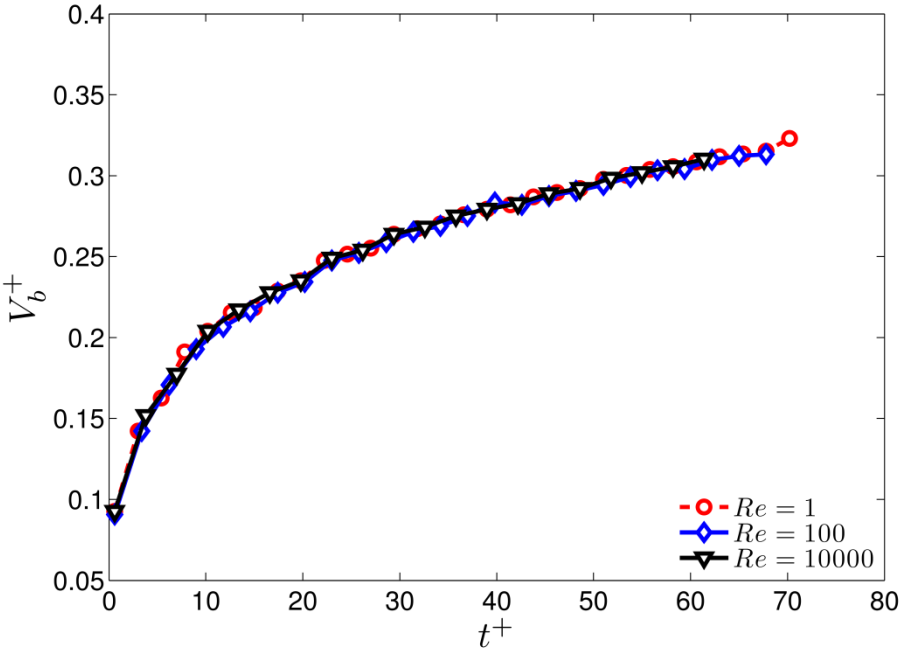

Figure 4.21: Reynolds number effect on liquid bridge filling, $h_1^+ = 0.04$, $h_2^+ = 0.08$, $S^+ = 0.02$.

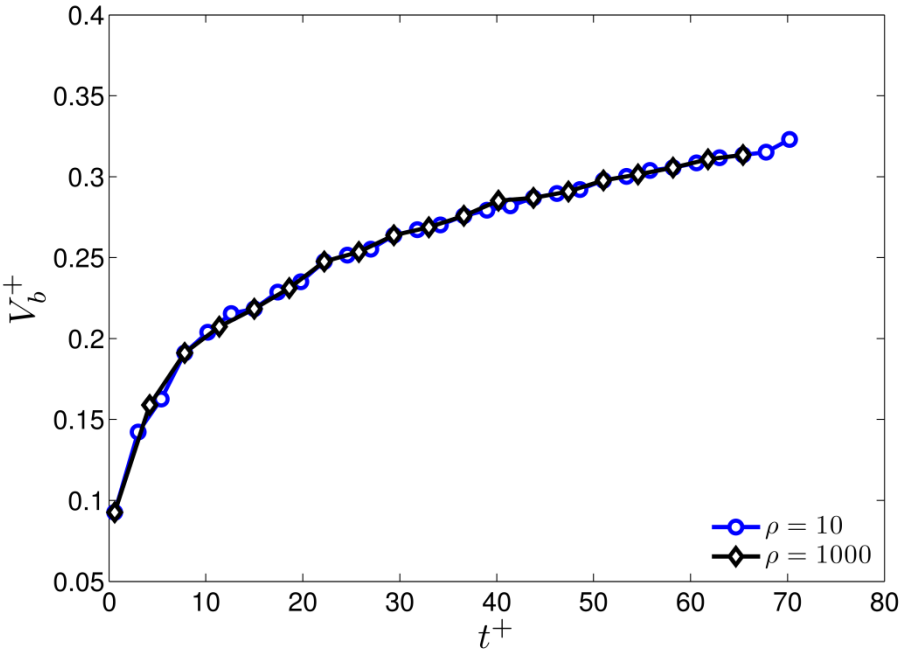

Figure 4.22: Density ratio effect on bridge volume filling, $h_1^+ = 0.04$, $h_2^+ = 0.08$, $S^+ = 0.02$.

4.4.5 Initial Bridge Shape Effects

In this section we summarize data on the effect of the initial shape of the liquid bridge on the bridge filling process. As shown in Figure 4.24, four types of initial bridge shapes have been investigated i.e., the standard cylinder (denoted as "cylinder"), no bridge ("none"), a too large cylinder ("large cylinder"), i.e., the

radius is 20% larger than standard cylinder, and a smooth curve in the form of a circle ("circle"). The results are shown in Figure 4.23, and we observe that the initial liquid bridge shape has generally a small effect on the filling process, except for the situation "large cylinder". For this situation significantly more liquid is in the bridge, however, the qualitative behavior of the filling process is preserved. Hence, we conclude that as long as the bridge is initialized with a realistic shape (i.e., a cylinder containing the displaced fluid), the effect of the exact initial shape is in the order of 3.3% between "none" and "cylinder", and 3.9% between "circle" and "cylinder".

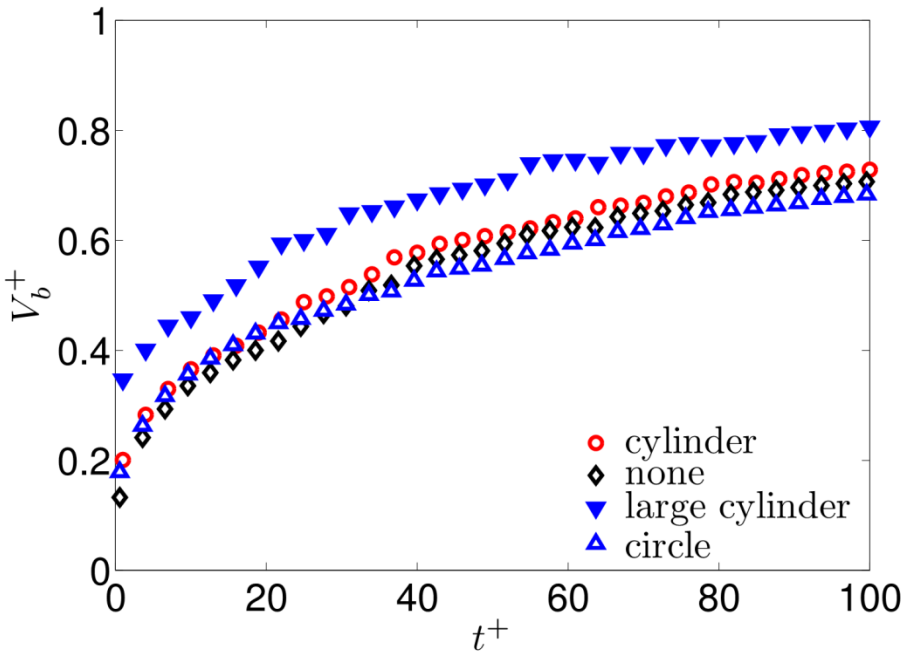

Figure 4.23: Effect of the initial bridge shape on the bridge filling process ($h_1^+ = 0.06$, $h_2^+ = 0.10$, $S^+ = 0.01$).

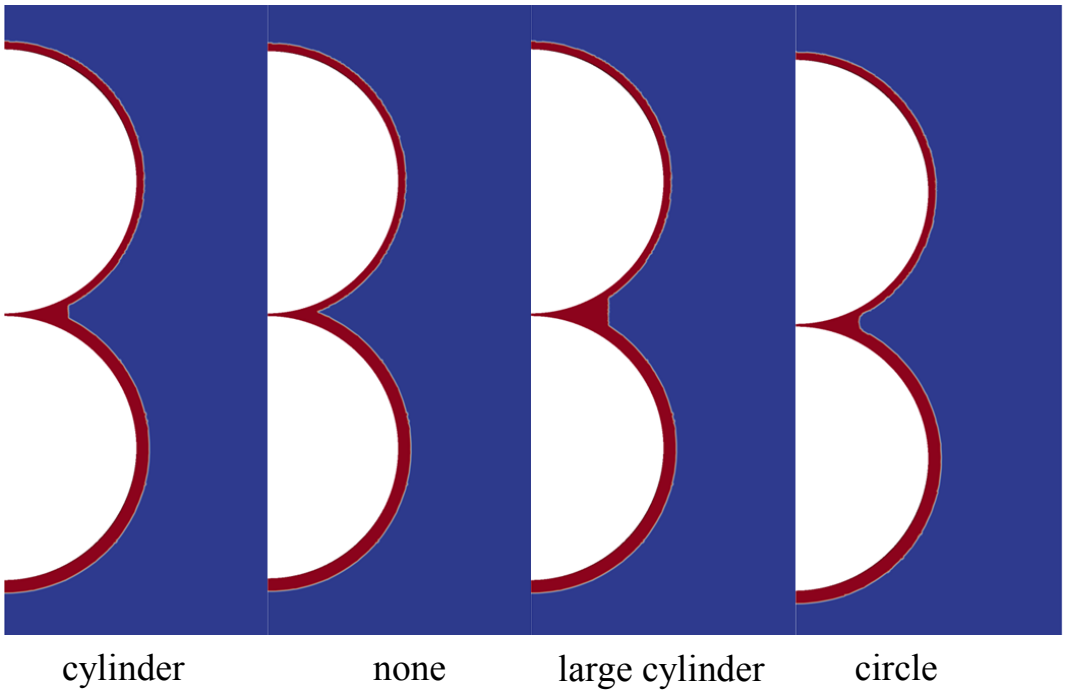

Figure 4.24: Different shapes of the initial liquid bridge ($h_1^+ = 0.06$, $h_2^+ = 0.10$, $S^+ = 0.01$).

4.5 Discussion

In our study, we investigate the liquid bridge and drainage process of liquid adhering to two wet particles based on key dimensionless parameters. We provide a model for the prediction of dynamic liquid-bridge formation between two particles by assuming that the filling rate of the liquid bridge is not affected by the particles' relative motion. Thus, we assume a quasi-static situation in which particles do not move, but only liquid is mobile to flow into the bridge. We next perform a time scale analysis to probe situations for which such a quasi-static assumption is appropriate.

4.5.1 Particle Interaction Time Scales

A key question that could not be answered in the current paper is what happens in case the particles move relative to each other, and hence the above mentioned quasi-static assumption breaks down. In order to do so, we must identify the limits of the models proposed in the current work. Specifically, there are two criteria that need to be satisfied to accept the assumption of zero relative particle velocity:

(i) the time scale for bridge formation must be smaller than a characteristic time scale (denoted as t_{acc}) for the particles to accelerate to a typical speed of liquid flow (i.e., $u_{ref} = \sigma / \mu_l$). Physically this means that the speed of the particle relative motion is smaller than the speed of liquid flow.

(ii) the time scale for bridge formation must be smaller than the time (denoted as t_{cross}) it takes for the particles to cross the film.

The acceleration time scale t_{acc} can be calculated from the force balance on a particle. Assuming that the liquid bridge only exhibits a cohesive force due to surface tension, the dimensional acceleration time scale (such that the particle have accelerated to the typical liquid flow speed u_{ref}) is $t_{acc} = R^2 \rho_p / \mu_l$. The corresponding dimensionless acceleration time scale (with $t_{ref} = R\mu_l / \sigma$ being the reference time scale) is:

$$t_{acc}^{+} = \frac{R\rho_p \sigma}{\mu_l^{\,2}} \tag{4.23}$$

The time for an approaching particle to cross the film, i.e., t_{cross}, can be calculated from a typical particle-particle relative velocity u_{rel} and the film thickness, i.e, $t_{cross} = h_0 / u_{rel}$. Using Stokes settling velocity as u_{rel}, one obtains for the dimensionless crossing time scale:

$$t_{cross}^{+} = \frac{9 h_0^{+} \mu_g \sigma}{2R^2 \mu_l \left(\rho_p - \rho_g\right) g} \tag{4.24}$$

Here $h_0^{+} = h_0 / R$ is the dimensionless film-thickness, μ_g is the ambient gas viscosity, and ρ_p is the particle density. Note, that the alternative assumption of $u_{rel} = u_{ref} = \sigma / \mu$ would lead to $t_{cross,u_{ref}}^{+} = h_0^{+}$. However, as explained above in the discussion of t_{acc}, it takes time to accelerate the particles to the capillary speed. Hence, the latter velocity scale is certainly of lower importance for typical applications that are characterized by a large particle Stokes number.

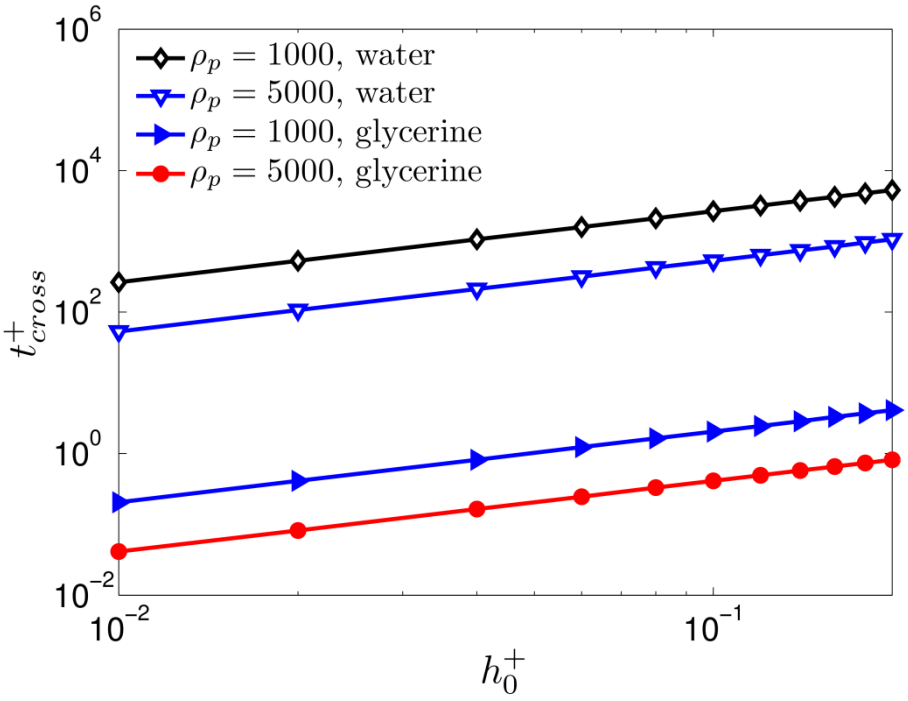

Figure 4.25: $t_{cross}{}^+$ for water and pure glycerine in typical fluidized bed operations.

In case both dimensionless time scales are much larger than unity, the assumption of non-moving particles in our simulations is acceptable. By assuming typical properties of various water-glycerine mixtures,[49] and using parameters typical for a fluidized bed, we have summarized key dimensionless parameters in Table 4.2. and Figure 4.25. It can be seen that for most fluidized bed systems the assumption of zero relative particle velocity when modeling liquid transfer is justified. Table 4.2 and Table 4.3 list relevant system parameters for particulate systems involving pure water, as well as mixtures of glycerine and water (60% and 40%). In general, situations with highly viscous fluids (i.e., pure glycerine), appear to conflict with our quasi-static assumption. For these situations the relative velocity of the particles might influence the bridge filling process. However, for most systems involving typical liquids with a water-like viscosity (see Table 4.2 and Table 4.3, as well as the illustration in Figure 4.25), we find that the assumption of zero relative particle velocity is adequate.

Glycerine/water	$R\ [m]$	$\rho_p\ [kg \cdot m^{-3}]$	h_0^+	$t_{ref}\ [s]$	t_{acc}^+	Oh
water	5e-6	1000	0.01	6.86e-8	363.5	0.052
Glycerine/water-60/40%	5e-6	1000	0.01	8.54e-7	2.54	0.58
Glycerine/water-79/21%	5e-6	1000	0.01	3.86e-6	0.13	2.53
Glycerine/water-90/10%	5e-6	1000	0.01	1.74e-5	6.55e-3	11.1
Pure glycerine	5e-6	1000	0.01	8.87e-5	2.52e-4	56.13
water	5e-6	1000	0.1	6.86e-8	363.5	0.052
Glycerine/water-60/40%	5e-6	1000	0.1	8.54e-7	2.54	0.58
Glycerine/water-79/21%	5e-6	1000	0.1	3.86e-6	0.13	2.53
Glycerine/water-90/10%	5e-6	1000	0.1	1.74e-5	6.55e-3	11.1
Pure glycerine	5e-6	1000	0.1	8.87e-5	2.52e-4	56.13
water	5e-3	1000	0.1	6.86e-5	3.64e5	1.66e-3
Glycerine/water-60/40%	5e-3	1000	0.1	8.54e-4	2.54e3	1.85e-2
Glycerine/water-79/21%	5e-3	1000	0.1	3.86e-3	130	0.08
Glycerine/water-90/10%	5e-3	1000	0.1	1.74e-2	6.55	0.35
Pure glycerine	5e-3	1000	1e-4	8.87e-2	0.25	1.77
water	5e-6	5000	0.1	6.86e-8	1717	0.052
Glycerine/water-60/40%	5e-6	5000	0.1	8.54e-7	12.7	0.58
Glycerine/water-79/21%	5e-6	5000	0.1	3.86e-6	0.65	2.53
Glycerine/water-90/10%	5e-6	5000	0.1	1.74e-5	0.033	11.1
Pure glycerine	5e-6	5000	0.1	8.87e-5	1.25e-3	56.13

Table 4.2: Summary of parameters relevant for liquid transfer in typical fluidized beds (for t_{cross}^+ refer to Figure 4.25).

cases	$R\ [m]$	$\rho_p\ [kg \cdot m^{-3}]$	h_0^+	$t_{ref}\ [s]$	t_{acc}^+	t_{cross}^+	Oh
1	5e-6	1500	1e-2	8.54e-7	3.82	14.2	0.58
2	5e-6	1500	0.2	8.54e-7	3.82	284	0.58
3	1e-5	1500	0.1	1.71e-6	7.63	35.5	0.41
4	1e-5	2000	0.1	1.71e-6	10.18	26.6	0.41
5	1e-5	5000	0.1	1.71e-6	25.44	10.6	0.41

Table 4.3: Effect of selected particle parameters on dimensionless bridge filling parameters for glycerine/water-60/40% mixtures.

4.5.2 Viscous Effects during Particle Approach

The acceleration time scale defined above is based on Newton's law of motion considering capillary forces only. Clearly, viscous forces will retard the particles' relative motion, and hence we expect that the typical particle interaction time is larger than t_{acc}^+. Next, we analyze such a situation by including lubrication effects due to the liquid between two approaching wet particles. For such a situation we have:

$$\vec{F}_{vis} + \vec{F}_{cap} = m\frac{d\vec{u}}{dt} \tag{4.25}$$

Where $\vec{F}_{vis}$ is the viscous force, $\vec{F}_{cap}$ is the capillary force, and m is the mass of one particle. For small particles (i.e., in case the particle size is smaller than the capillary length), the gravitational forces can be neglected, and only capillary and viscous forces affect particle motion. Pitois et al.[14] and Darabi et al.[2] applied the lubrication approximation for liquid flow between the two particle surfaces, and arrived at the following expression for the viscous force:

$$\vec{F}_{vis} = -\frac{3}{2}\pi\mu R^2 X_v^2 \frac{1}{S}\frac{dS}{dt}\ , \tag{4.26}$$

$$X_v = 1 - 1 \Big/ \sqrt{1 + \frac{2V_b}{\pi R S^2}} \quad . \tag{4.27}$$

Where R is the particle radius, S is the half separation distance between the particle surfaces, and V_b is the liquid bridge volume. Pitois et al.[14] and Darabi et al.,[2] also provided a model for the capillary force that accounts for the bridge volume effect. For fully wetted particles their capillary force model is:

$$\overrightarrow{F}_{cap} = 2\pi R \sigma X_v \tag{4.28}$$

Substituting the model for the viscous and capillary force into Eqn. 4.25, and using typical initial conditions (i.e., an initial separation of 10% of the particle radius, and particles initially at rest), we obain the following differential equation:

$$\begin{cases} -\frac{3}{2}\pi \mu_l R^2 X_v^2 \frac{1}{S}\frac{dS}{dt} + 2\pi R \sigma X_v = m\frac{d^2 S}{dt^2} \\ S(0) = 0.1R \; ; \quad S'(0) = 0. \end{cases} \tag{4.29}$$

Integrating the above equation in time is straight forward (e.g., using Matlab®), and we have chosen two sets of parameters, i.e., that of water and pure glycerine to illustrate the solution. Relevant properties for these liquids are listed in Table 4.4. The particle size is chosen to be 10 μm, the liquid bridge volume is chosen to be 20% of the particle volume, the Reynold number is defined by the capillary speed, the particle radius, and the fluid viscosity (i.e., $Re = \sigma R \rho_l / \mu_l^2$). One can also define a capillary number Ca to quantify the ratio of viscous and capillary effects. This number is based on the Stokes setting velocity (as a proxy for the relevant particle-particle relative speed), the viscosity of the liquid, and the surface tension, i.e., $Ca = \mu_l u_{rel} / \sigma = \left(2\mu_l R^2 \left(\rho_p - \rho_g\right) g\right) / \left(9\mu_g \sigma\right)$. In summary, we obtain for

- pure glycerine: Re = 6.34 · 10^{-4} , Ca = 0.975, and for
- water: Re = 730, Ca=7.54 · 10^{-4}

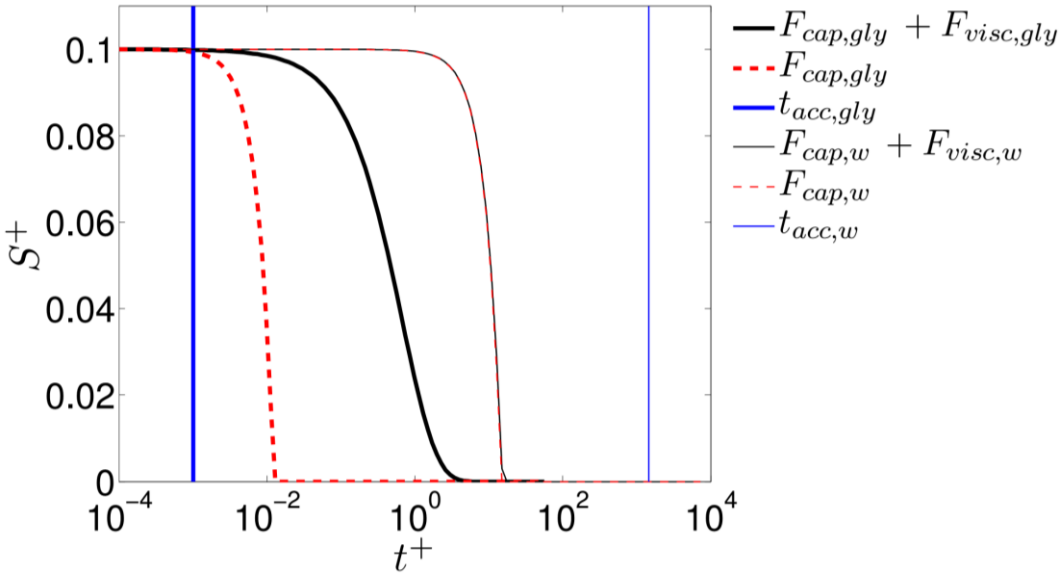

Figure 4.26: Time evolution of the half separation distance S^+ during the acceleration phase of two approaching particles (ρ_p = 2000 [kg/m^3], d_p = 10 [μm], V_b^+=0.1).

Figure 4.26 illustrates the time evolution of the particle separation distance, as well as the acceleration time scale derived above. Figure 4.27 summarizes the corresponding relative velocity scaled with the reference velocity, i.e., a typical speed of the adhering liquid when flowing into the bridge. We can observe from Figure 4.26 (dashed and continuous bold line) that the time until contact is larger than t_{acc}^+ for the glycerine system. Thus, the particles accelerate, but only for the situation where viscous forces are neglected the particle accelerate beyond u_{ref} (see Figure 4.27). In contrast, in the system involving water the particles' relative speed never excees u_{ref}, and the impact speed is in the order of $0.01 \cdot u_{ref}$ (see thin dashed and continuous line in Figure 4.26 and Figure 4.27). As expected, lubrication forces resist the particle's relative motion and delay the time until contact (see continuous lines in Figure 4.26 and Figure 4.27). This effect is more pronounced for the viscous systems, while the effect in the system involving water is rather small. Clearly, in case one does not take into account the viscous term for the glycerine system, the particles accelerate to an unphysically large relative velocity. In case we account for viscous forces, however, we expect typical particle relative speeds smaller than $0.1 \cdot u_{ref}$, even for highly viscous systems (see Figure

Figure 4.27). These particle velocities are below the typical liquid speed for early times (i.e., $t^+ = 1$, see Figure 4.2). For longer times both the liquid and particle speed decreases rapidly, the particles' surfaces touch (at t^+ between 5 and 50 depending on the viscosity of the liquid, see Figure 4.27). Hence, bridge filling is also unaffected by particle motion for longer times, simply because the particles are already in contact. Based on the above consideration of particles accelerating from zero velocity, it appears that our assumption of a quasi-static liquid bridge formation is valid for a wide range of wet particulate systems.

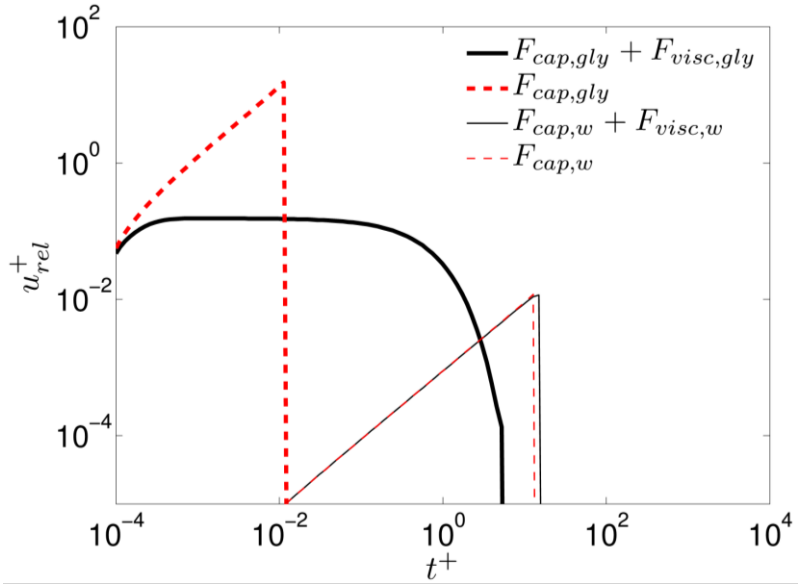

Figure 4.27: Time evolution of the relative particle velocity during the acceleration phase of two approaching particles (parameters are the same as in figure 4.26).

Mixture	$\mu\,[Pa\cdot s]$	$\rho[kg\cdot m^{-3}]$	$\sigma\,[N/m]$
Water	$1\cdot10^{-3}$	1000	0.073
Glycerine/water-60/40%	0.0115	1153	0.0673
Glycerine/water-79/21%	0.05	1204	0.0647
Glycerine/water-90/10%	0.22	1238	0.0634
Pure glycerine	1.12	1262	0.0631

Table 4.4: Properties of different water-glycerine mixtures (adapted from Eddi, Winkels and Snoeijer[49])

4.5.3 Typical Impact Speeds in Sedimenting Suspensions

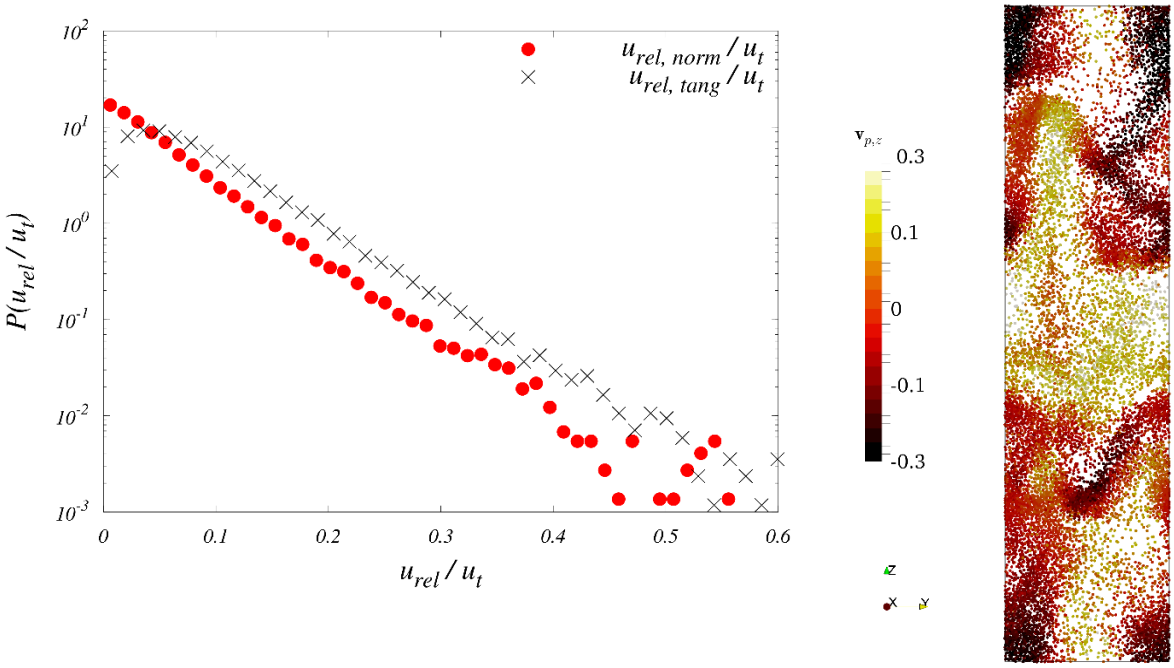

Figure 4.28: Distribution of particle collision velocities in the normal and tangential direction (left panel), as well as illustration of the vertical particle velocity distribution (right panel, d_p = 150 [µm], ρ_p = 1500 [kg/m³], ϕ_p = 0.10, particles sediment in air at ambient conditions).

The typical relative particle velocity at impact is important for our analysis, since it affects the scale for film crossing. We have therefore performed simulations of a typical application we are interested in (i.e., wet granulation in a fluidized bed). Specifically, we considered a freely sedimenting suspension, and have recorded the speed and orientation of particle-particle collisions. The simulations followed the approach used by Radl and Sundaresan[50], with identical fluid and particle properties. Our results are summarized in Figure 4.28, highlighting that collisions in typical applications we are interested in (i.e., fluidized beds) are mostly gentle: the typical impact speed is in the order of 10% of the particles' terminal settling velocity. Also, we observe from Figure 4.28 that particle collisions are primarily oblique, i.e., the particles' relative speed in the tangential direction (at the contact point) is smaller than that in the normal direction. In Appendix C we summarize more data for sedimenting suspensions, which show a similar qualitative behavior and a moderate increase of the impact speed when decreasing the particle concentration. Clearly, our data supports our assumption of quasi-static bridge

filling for a wide range of wet particulate systems with rather thick liquid films and a rather low liquid viscosity.

Of course, the relative speed of particles in a wet collision event is set by the process, and we have only considered a wet fluidized bed here. Clearly, it is necessary to check the appropriateness of our model for a specific application via a prior analysis of typical particle relative velocities.

4.6 Conclusions

A new model to predict dynamic liquid bridge formation between two wet particles has been presented in this paper. This model is based on DNS data, which were obtained by extracting the interface position from VoF-based simulations of the bridge filling process. The liquid bridge volume was defined based on a characteristic neck position, and a direct integration method was employed to calculate the liquid bridge volume. This allowed us building a dynamic model for predicting the bridge volume, and the liquid remaining on the particle surfaces. Such a model might help to refine our picture of wet particle collisions that previously focused exclusively on predictions of the coefficient of restitution (Donahue et al.,[24], Sutkar et al.[28]).

Our model differentiates between (i) a fast initial bridge formation stage where the dimensionless time is less than a reference time for capillary-driven viscous flow, and (ii) a subsequent slower viscous filling stage where viscous effects are dominant. The initial stage model is based on a geometrical reference volume, and has been calibrated with DNS data at a dimensionless time of $t^+ = 1$. Our initial stage model can be used as a first estimate for the liquid bridge volume in short particle collisions, and is an extension of the model prosed by Shi and McCarthy[46]. The postulated model for the viscous filling stage model relies on a universal parameter a_i (i.e., a characteristic dimensionless filling time), as well as dimensionless liquid mobility parameters ϕ_{m1} and ϕ_{m2} of the contacting particles. A model equation for these mobility parameters has been proposed. Specifically, we

consider that the mobilities are functions of the film height and the separation distance. In summary, our model is valid for liquid bridge formation between two identical particles coated with thin continuous films (i.e., an initial relative film height of less than 10% of the particle radius).

We observed that our results obtained from the DNS are independent of the Reynolds number, as well as the density ratio between the liquid coating the particles and the ambient gas. This suggests that our model is applicable to a wide range of gas-particle systems involving wet particulate systems.

However, our simulation study indicates that grid refinement plays an important role in the final stages of film flow where the film ruptures. In order to get a precise model for the filling process at long times, as well as to correctly predict film rupture, it is essential to use a fine enough computational mesh in the simulations (i.e., the dimensionless grid resolution Δh should be 0.12 or smaller). This clearly limited the current study to axisymmetric configurations. Hence, our study is only a step forward to better understand the equilibration of liquid on particles and in liquid bridged in a particle bed. Still work needs to be done in the future, specifically, it would be interesting to

- experimentally support the observed film rupturing event for long times,
- investigate the wetting of initially completely dry particle, and particles that have a complex morphology,
- quantify the effect of particle relative motion on the liquid bridge formation process.

4.7 Appendices

Appendix A - Analytical Solution for a Two-Particle System

The mass balance equations detailed in the manuscript can be normalized and written for the simplest case of a two-particle collision:

$$\frac{dL_{p1}^{+}}{dt^{+}} = -a_i\left(L_{p1}^{+}\phi_{m1} - \frac{V_b^{+}}{2}\right) \qquad (A.1)$$

$$\frac{dL_{p2}^{+}}{dt^{+}} = -a_i\left(L_{p2}^{+}\phi_{m2} - \frac{V_b^{+}}{2}\right) \qquad (A.2)$$

$$\frac{dV_b^{+}}{dt^{+}} = -\left(\frac{dL_{p1}^{+}}{dt^{+}} + \frac{dL_{p2}^{+}}{dt^{+}}\right) \qquad (A.3)$$

The initial conditions are:

$$V_b^{+}|_{t=0} = V_{b,0}^{+},\ L_{p1}^{+}|_{t=0} = L_{\mathrm{p1,0}}^{+}, L_{p2}^{+}|_{t=0} = L_{\mathrm{p2,0}}^{+} \qquad (A.4)$$

Exploiting the total mass balance, i.e., Eqn. A.3, assuming that a_i is a constant for the pair of particles, and taking the time derivatives of the above equations, we arrive at:

$$\frac{dL_{p1}^{+}{}'}{dt^{+}} = -a_i\left(\left(\phi_{m1} + \frac{1}{2}\right)L_{p1}^{+}{}' + \frac{1}{2}L_{p2}^{+}{}'\right) \qquad (A.5)$$

$$\frac{dL_{p2}^{+}{}'}{dt^{+}} = -a_i\left(\left(\phi_{m2} + \frac{1}{2}\right)L_{p2}^{+}{}' + \frac{1}{2}L_{p1}^{+}{}'\right) \qquad (A.6)$$

where $L_{p1}^{+}{}' = \frac{dL_{p1}^{+}}{dt^{+}}$, $L_{p2}^{+}{}' = \frac{dL_{p2}^{+}}{dt^{+}}$. By rearranging Eqn A.5, we now obtain an expression of $L_{p2}^{+}{}'$ in terms of $L_{p1}^{+}{}'$

$$L_{p2}^{+}{}' = -2\left(\frac{1}{a_i}\frac{dL_{p1}^{+}{}'}{dt^{+}} + \left(\phi_{m1} + \frac{1}{2}\right)L_{p1}^{+}{}'\right) \qquad (A.7)$$

We then substitute equation A.7 into equation A.6, to arrive at the following second-order constant coefficient homogeneous linear differential equation in for $L_{p1}^{+}{}'$,

$$\frac{2}{a_i}\frac{d^2 L_{p1}^{+}{}'}{dt^{+2}} + 2\left(\phi_{m1}+\phi_{m2}+1\right)\frac{dL_{p1}^{+}{}'}{dt^{+}} + a_i\left(2\phi_{m1}\phi_{m2}+\phi_{m1}+\phi_{m2}\right)L_{p1}^{+}{}' = 0 \qquad \text{(A.8)}$$

Using the Ansatz

$$L_{p1}^{+}{}' \equiv e^{r\,t^{+}} \qquad \text{(A.9)}$$

We obtain the characteristic equation

$$\frac{2}{a_i}r^2 e^{r\,t^{+}} + 2\left(\phi_{m1}+\phi_{m2}+1\right)r e^{r\,t^{+}} + a_i\left(2\phi_{m1}\phi_{m2}+\phi_{m1}+\phi_{m2}\right)e^{r\,t^{+}} = 0 \qquad \text{(A.10)}$$

which has the real-numbered roots:

$$r_1 = \frac{-a_i\left(\phi_{m1}+\phi_{m2}+1+\sqrt{\left(\phi_{m1}-\phi_{m2}\right)^2+1}\right)}{2} \qquad \text{(A.11)}$$

$$r_2 = \frac{-a_i\left(\phi_{m1}+\phi_{m2}+1-\sqrt{\left(\phi_{m1}-\phi_{m2}\right)^2+1}\right)}{2} \qquad \text{(A.12)}$$

Hence, the general solution for equation (A.8) is given by

$$\frac{L_{p1}^{+}}{dt^{+}} = C_1 e^{r_1 t^{+}} + C_2 e^{r_2 t^{+}}, \qquad \text{(A.13)}$$

$$\frac{L_{p2}^{+}}{dt^{+}} = -2\left(\frac{1}{a_i}\left(C_1 r_1 e^{r_1 t^{+}} + C_2 r_2 e^{r_2 t^{+}}\right) + \left(\phi_{m1}+\frac{1}{2}\right)\left(C_1 e^{r_1 t^{+}} + C_2 e^{r_2 t^{+}}\right)\right) \qquad \text{(A.14)}$$

and

$$\frac{dV_b^{+}}{dt^{+}} = \left(\frac{2r_1}{a_i}+2\phi_{m1}\right)C_1 e^{r_1 t^{+}} + \left(\frac{2r_2}{a_i}+2\phi_{m1}\right)C_2 e^{r_2 t^{+}} \qquad \text{(A.15)}$$

Using the initial conditions, i.e., $V_b^+ |_{t=0} = V_{b,0}^+$, $L_{p1}^+ |_{t=0} = L_{\mathrm{p1},0}^+$, and $L_{p2}^+ |_{t=0} = L_{\mathrm{p2},0}^+$, and after rearrangement we arrive at:

$$C_1 = \frac{-a_i^2 \phi_{m2} L_{p2,0}^+ - \left(2a_i r_2 \phi_{m1} + 2a_i^2 \phi_{m1}^2 + a^2 \phi_{m1}\right) L_{p1,0}^+}{2\left(r_2 - r_1\right)} + \frac{\left(a_i^2 \phi_{m1} + a_i^2 + a_i r_2\right) V_{b,0}^+}{2\left(r_2 - r_1\right)} \tag{A.16}$$

$$C_2 = \frac{a_i^2 \phi_{m2} L_{p2,0}^+ + \left(2a_i r_1 \phi_{m1} + a_i^2 \phi_{m1} + 2a_i^2 \phi_{m1}^2\right) L_{p1,0}^+ - \left(a_i r + a_i^2 \phi_{m1} + a_i^2\right) V_{b,0}^+}{2\left(r_2 - r_1\right)} \tag{A.17}$$

By integration of Eqn. A.15, as well as using the initial condition for the bridge volume, we obtain

$$V_b^+ = V_{b,0}^+ + C_1 \frac{\frac{2r_1}{a_i} + 2\phi_{m1}}{r_1}\left(e^{r_1 t^+} - 1\right) + C_2 \frac{\frac{2r_2}{a_i} + 2\phi_{m1}}{r_2}\left(e^{r_2 t^+} - 1\right) \tag{A.18}$$

Similarly, we obtain the following equations for the dimensionless liquid content on particle 1 and particle 2:

$$L_{p1}^+ = L_{p1,0}^+ + \frac{C_1}{r_1}\left(e^{r_1 t^+} - 1\right) + \frac{C_2}{r_2}\left(e^{r_2 t^+} - 1\right) \tag{A.19}$$

$$L_{p2}^+ = L_{p2,0}^+ - C_1 \frac{\frac{2r_1}{a_i} + 2\phi_{m1} + 1}{r_1}\left(e^{r_1 t^+} - 1\right) - C_2 \frac{\frac{2r_2}{a_i} + 2\phi_{m1} + 1}{r_2}\left(e^{r_2 t^+} - 1\right) \tag{A.20}$$

Appendix B – Details on the Geometrical Bridge Volume Type II

The key to calculate the volume of liquid bridges of type II is the calculation of the radius R_{cyl} of the compensation cylinder region. The known parameters, as shown in Figure 1 (panel a), are the particle radius R, the initial film heights h_1 and h_2, and the half separation between particles S. Once two particles have been fixed in space, the liquid in the overlap regions of the liquid films (i.e., the red and green shaded regions in Figure 4.1, panel b) is displaced and flows into a ring-shaped region (i.e., red solid area in Figure 4.1, panel b). One can compute the volume of the ring-shaped region as follows:

First, the overlap liquid volume that is contributed by particle 1 (i.e., the green shaded area in Figure 4.1, panel b) and particle 2 (i.e., the red shaded area in Figure 4.1, panel b) can be computed from:

$$\begin{aligned} V_{\text{overLap}} = \frac{1}{24}\frac{1}{R+S}\Big(\pi\big(&12h_1^2R^2 - 24h_1^2S^2 + 4Rh_1^3 + 16h_1^3S - 3h_1^4 - 48R^2h_1S \\ &-48Rh_1S^2 + 96R^2S^2 + 128RS^3 + 32S^4 + 12R^2h_2^2 - 24h_2^2S^2 + 4Rh_2^3 \\ &+16h_2^3S - 3h_2^4 - 48R^2h_2S - 48Rh_2S^2\big)\Big) \end{aligned} \tag{B.1}$$

Second, the intersection radius R_i can be calculated using equation (B.2) as illustrated in Figure B1.

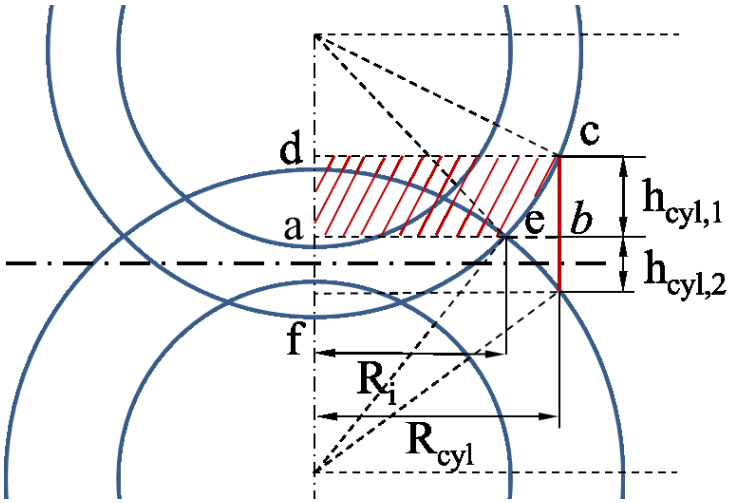

Figure B1: Sketch illustrating the unknown variables in the calculation of the geometrical bridge volume type II.

$$\sqrt{\left(R+h_1\right)^2-R_i^2}+\sqrt{\left(R+h_2\right)^2-R_i^2}=2\left(R+S\right) \tag{B.2}$$

Third, the ring-shaped region is divided into two sub-regions, which have the heights $h_{\mathrm{cyl},1}$ and $h_{\mathrm{cyl},2}$ as sketched in Figure B1. The ring-shaped sub-region 1 has the volume $V_{\mathrm{cyl},1}=V_{\mathrm{abcd}}$ - V_{aecd}, where V_{aecd} = V_{dcf} – $V_{\mathrm{cap,aef}}$. The cap height is $h_{\mathrm{af}}=R+h_1-\sqrt{\left(R+h_1\right)^2-R_i^2}$, and thus the cap volume is $V_{\mathrm{cap,aef}}=\frac{\pi h_{\mathrm{af}}}{6}\left(3R_i^2+h_{\mathrm{af}}^2\right)$. The liquid volume in sub-region 2, i.e., $V_{\mathrm{cyl},2}$ can be computed in the same fashion.

Finally, we sum up the two sub-regions, and use the known volume of the displaced liquid, i.e., $V_{overLap}$, to arrive at the following expression involving the unknowns R_{cyl}, h_1, h_2, S and R:

$$V_{\mathrm{overLap}}=V_{\mathrm{cyl}}=V_{\mathrm{cyl},1}+V_{\mathrm{cyl},2}=f\left(R_{\mathrm{cyl}},h_1,h_2,S,R\right) \tag{B.3}$$

This expression cannot be solve directly to obtain R_{cyl}, however, one can solve it numerically using for example a Newton algorithm. Once R_{cyl} is known, we can calculate the geometrical bridge volume based on the contribution from each particle i and as illustrated in shown in Figure 4.4 (panel b):

$$\beta_{\mathrm{cyl},i}=\arcsin\left(\frac{R_{\mathrm{cyl}}}{R+h_i}\right) \tag{B.4}$$

$$h_{\mathrm{cyl},i}=\left(R+S\right)-\left(R+h_i\right)\cos\beta_{\mathrm{cyl},i} \tag{B.5}$$

$$V_{\mathrm{cap},i}=\frac{\pi R^3}{3}(1-\cos\beta_{\mathrm{cyl},i})^2(2+\cos\beta_{\mathrm{cyl},i}) \tag{B.6}$$

$$V_{\mathrm{b},i,\mathrm{I}}=\pi R_{\mathrm{cyl}}^2 h_{\mathrm{cyl},i}+\frac{1}{3}\pi h_i\cos\beta_{\mathrm{cyl},i}\sin^2\beta_{\mathrm{cyl},i}\left(R^2+\left(R+h_i\right)^2+R\left(R+h_i\right)\right) \tag{B.7}$$

$$V_{\mathrm{b,g,II},i}=V_{\mathrm{b},i,\mathrm{I}}-V_{\mathrm{cap},i} \tag{B.8}$$

Appendix C –Relative Particle Velocity at Impact in a Sedimenting Suspension

We summarize statistics of the relative particle speed at impact in a fully periodic domain using soft-sphere Euler-Lagrange simulations using the code CFDEM® (Kloss et al. [51]). Particles were allow to sediment under the action of gravity, while their weight (and that of the surrounding gas) was balanced by a pressure gradient, similar to our previous work (Radl and Sundaresan [50]). Also numerical parameters and drag models were identical to this previous work (a dimensionless grid resolution of $\Delta x/(2R) = 3$, as a domain size of 53 x 53 x 213 d_p was used). The statistics reported below were collected by sampling impact velocities over a sufficiently long time, i.e., 40 times the particle relaxation time $t_{relax} = u_t^2 / g$. Note that the particles were initialized homogeneously distributed in the computational domain, and that a statistical steady state was reached after ca. $5 \cdot t_{relax}$.

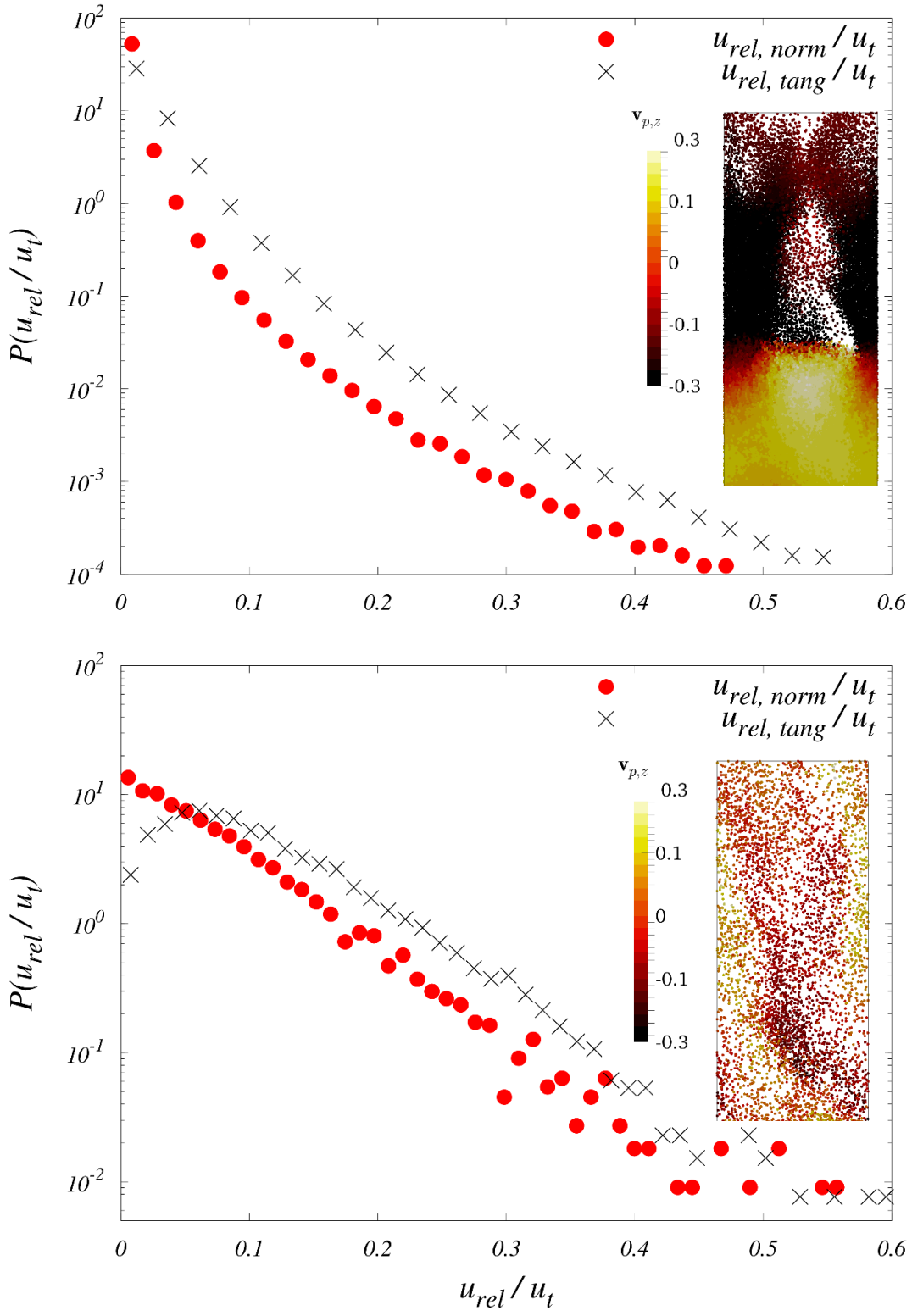

Figure C1: Distribution of the relative particle velocity at impact in a dilute (bottom panel; ϕ_p = 0.05) and dense (top panel; ϕ_p = 0.30) cloud of freely sedimenting particles (the inserts illustrate individual-particle velocities in the vertical direction).

4.8 Nomenclature

Latin Symbols

a_i .....Dimensionless filling rate parameter [-]

Ca .....Capillary number [-]

d_p .....Particle diameter [m]

$\vec{F}_{vis}$ .....Viscous force acting on the particle [kg · m /s^2]

$\vec{F}_{cap}$ .....Capillary force acting on the particle [kg · m /s^2]

g .....Gravity [m/s^2]

h_0 .....Average initial film height of the particle pair [m]

h_i .....Initial film height of particle i [m]

$h_{cyl,i}$ .....The height of the red shade cylinder on particle i [m]

$L_{p,0}$ .....Reference volume of liquid on the particle [m^3]

$L_{p,i}$ .....Volume of liquid present on the particle i [m^3]

m .....Mass of the particle [kg]

$\mathbf{n}_{ij}$ .....Unit normal vector [-]

Oh .....Ohnesorge number [-]

p .....Pressure [Pa]

p_{ref} .....Reference pressure [Pa]

p_s .....Pressure at the particle surfaces [Pa]

p_{V_b} .....Pressure at the liquid bridge [Pa]

R .....Particle radius [m]

R_{cyl} .....Radius of the initial cylinder region [m]

R_{curve} ..... Radius of curvature of the liquid bridge surface [m]

Re ..... Reynolds number [-]

S ..... Half separation distance between particles [m]

t ..... Time [s]

t_{acc} ..... Acceleration time scale [s]

t_{cross} ..... Film crossing time scale [s]

t_{relax} ..... Particle relation time [s]

t_{ref} ..... Reference time scale [s]

u_{ref} ..... Reference fluid velocity [m·s]

u_{rel} ..... Relative particle-particle velocity [m/s]

U ..... Fluid velocity [m/s]

V_b ..... Liquid bridge volume [m^3]

$V_{b,0}$ ..... Initial bridge volume [m^3]

$V_{b,\mathrm{g,I}}$ ..... Geometry bridge volume: type I [m^3]

$V_{b,\mathrm{g,II}}$ ..... Geometry bridge volume: type II [m^3]

$V_{b,i,I}$ ..... Integration volume of the red framed region in Figure 4 (b) [m^3]

$V_{cap,i}$ ..... The cavity volume of particle [m^3]

$V_{overLap}$ ..... The displaced volume of liquid of the overlap region [m^3]

DIM ..... Direct integration method

DNS ..... Direct Numerical Simulation

MFB ..... Micro force balance

YLE .....Young-Laplace equation

Greek Symbols

α .....Phase fraction indicator [-]

$\beta_{cyl,i}$ .....Initial filling angle on particle i that cause by geometry bride [rad]

Δt .....Time step [s]

Δx .....Grid spacing [m]

Δh .....Dimensionless grid spacing by initial film height [-]

ϕ_p .....Particle volume fraction [-]

ϕ_{mi} .....Fraction of liquid on particle i that is mobile to flow into the bridge [-]

μ_l .....Dynamic viscosity of liquid [$kg \cdot m^{-1} \cdot s^{-1}$]

μ_g .....Dynamic viscosity of ambient gas [$kg \cdot m^{-1} \cdot s^{-1}$]

ρ_l .....Density of the liquid [$kg \cdot m^{-3}$]

ρ_g .....Density of the ambient gas [$kg \cdot m^{-3}$]

ρ_p .....Density of the particles [$kg \cdot m^{-3}$]

σ .....Surface tension [$kg \cdot s^{-2}$]

Superscripts

+ .....Dimensionless quantity

i .....Particle index

norm .....Normal direction

tang .....Tangential direction

t .....Terminal

w .....Water

gly ..... Glycerine

p ..... Particle

ref ..... Reference quantity

4.9 References

[1] G. Toschkoff, J.G. Khinast, Mathematical modeling of the coating process., Int. J. Pharm. 457 (2013) 407–22. doi:10.1016/j.ijpharm.2013.08.022.

[2] P. Darabi, K. Pougatch, M. Salcudean, D. Grecov, A novel coalescence model for binary collision of identical wet particles, Chem. Eng. Sci. 64 (2009) 1868–1876.

[3] M. Scheel, R. Seemann, M. Brinkmann, M. Di Michiel, A. Sheppard, B. Breidenbach, et al., Morphological clues to wet granular pile stability., Nat. Mater. 7 (2008) 189–193. doi:10.1038/nmat2117.

[4] F.M. Orr, L.E. Scriven, A.P. Rivas, Pendular rings between solids: meniscus properties and capillary force, J. Fluid Mech. 67 (1975) 723. doi:10.1017/S0022112075000572.

[5] P. Darabi, T. Li, K. Pougatch, M. Salcudean, D. Grecov, Modeling the evolution and rupture of stretching pendular liquid bridges, Chem. Eng. Sci. 65 (2010) 4472–4483. doi:10.1016/j.ces.2010.04.003.

[6] S. Dodds, M. Carvalho, S. Kumar, Stretching liquid bridges with moving contact lines: The role of inertia, Phys. Fluids. 23 (2011). doi:10.1063/1.3623427.

[7] S. Dodds, M.S. Carvalho, S. Kumar, The dynamics of three-dimensional liquid bridges with pinned and moving contact lines, J. Fluid Mech. 707 (2012) 521–540. doi:10.1017/jfm.2012.296.

[8] X. Pepin, D. Rossetti, S. Iveson, S. Simons, Modeling the Evolution and Rupture of Pendular Liquid Bridges in the Presence of Large Wetting Hysteresis., J. Colloid Interface Sci. 232 (2000) 289–297.

doi:10.1006/jcis.2000.7182.

[9] D. Rossetti, S.J.R. Simons, A microscale investigation of liquid bridges in the spherical agglomeration process, Powder Technol. 130 (2003) 49–55. doi:10.1016/S0032-5910(02)00225-5.

[10] S. Herminghaus, Dynamics of wet granular matter, Adv. Phys. 54 (2005) 221–261. doi:10.1080/00018730500167855.

[11] W.B. Haines, Studies in the physical properties of soils: II. A note on the cohesion developed by capillary forces in an ideal soil1, J. Agric. Sci. 15 (1925). doi:http://dx.doi.org/10.1017/S0021859600082460.

[12] Fisher. R. A, On the capillary forces in an ideal soil: correction of formulae given by WB haines, J. Agric. Sci. 16 (1926) 492–505. doi:http://dx.doi.org/10.1017/S0021859600007838.

[13] V.P. Mehrotra, K.V.S. Sastry, Pendular Bond Strength Between Unequal-Sized Spherical Particles, Powder Technol. 25 (1980) 203–214.

[14] O. Pitois, P. Moucheront, X. Chateau, Liquid Bridge between Two Moving Spheres: An Experimental Study of Viscosity Effects., J. Colloid Interface Sci. 231 (2000) 26–31. doi:10.1006/jcis.2000.7096.

[15] L.J. McLaughlin, M.J. Rhodes, Prediction of fluidized bed behaviour in the presence of liquid bridges, Powder Technol. 114 (2001) 213–223. doi:10.1016/S0032-5910(00)00325-9.

[16] Z. Grof, C.J. Lawrence, F. Stepánek, The strength of liquid bridges in random granular materials., J. Colloid Interface Sci. 319 (2008) 182–92. doi:10.1016/j.jcis.2007.11.055.

[17] Y.I. Rabinovich, M.S. Esayanur, B.M. Moudgil, Capillary forces between two spheres with a fixed volume liquid bridge: Theory and experiment, Langmuir. 21 (2005) 10992–10997. doi:10.1021/la0517639.

[18] Z. Wei, Y.-P. Zhao, Growth of liquid bridge in AFM, J. Phys. D. Appl. Phys. 40 (2007) 4368–4375. doi:10.1088/0022-3727/40/14/036.

[19] Y. Muguruma, T. Tanaka, Y. Tsuji, Numerical simulation of particulate flow with liquid bridge between particles (simulation of centrifugal tumbling granulator), Powder Technol. 109 (2000) 49–57. doi:10.1016/S0032-5910(99)00226-0.

[20] D. Shi, W.L. Vargas, J.J. McCarthy, Heat transfer in rotary kilns with interstitial gases, Chem. Eng. Sci. 63 (2008) 4506–4516. doi:10.1016/j.ces.2008.06.006.

[21] F.R.. De Bisschop, W.J.. Rigole, A physical model for liquid capillary bridges between adsorptive solid spheres: The nodoid of plateau, J. Colloid Interface Sci. 88 (1982) 117–128. doi:10.1016/0021-9797(82)90161-8.

[22] Y. Chen, Y. Zhao, H. Gao, J. Zheng, Liquid bridge force between two unequal-sized spheres or a sphere and a plane, Particuology. 9 (2011) 374–380. doi:10.1016/j.partic.2010.11.006.

[23] R.H. Davis, D. a. Rager, B.T. Good, Elastohydrodynamic rebound of spheres from coated surfaces, J. Fluid Mech. 468 (2002) 107–119. doi:10.1017/S0022112002001489.

[24] C.M. Donahue, C.M. Hrenya, R.H. Davis, Stokes's cradle: Newton's cradle with liquid coating, Phys. Rev. Lett. 105 (2010) 34501. doi:10.1103/PhysRevLett.105.034501.

[25] X. Li, M.L. Hunt, T. Colonius, A contact model for normal immersed collisions between a particle and a wall, J. Fluid Mech. 691 (2012) 123–145. doi:10.1017/jfm.2011.461.

[26] P. Gondret, M. Lance, L. Petit, Bouncing motion of spherical particles in fluids, Phys. Fluids. 14 (2002) 643–652. doi:10.1063/1.1427920.

[27] F. Gollwitzer, I. Rehberg, C. a. Kruelle, K. Huang, Coefficient of restitution for wet particles, Phys. Rev. E - Stat. Nonlinear, Soft Matter Phys. 86 (2012) 1–10. doi:10.1103/PhysRevE.86.011303.

[28] V.S. Sutkar, N.G. Deen, T.P. Johan, J.A.M. Kuipers, V. Salikov, B. Crüger,

et al., A Novel Approach to Determine Wet Restitution Coefficients Through a Unified Correlation and Energy Analysis, AIChE J. 61 (2015) 769–779. doi:10.1002/aic.

[29] A.A. Kantak, M.C. Hrenya, H.R. Davis, Initial rates of aggregation for dilute, granular flows of wet particles, Phys. Fluids. 21 (2009) 23301. doi:10.1063/1.3070830.

[30] F. Yang, Interaction Law for a Collision Between Two Solid Particles in a Viscous Liquid, (Ph. D.) Thesis Calif. Inst. Technol. (2006). doi:etd-05262006-120244.

[31] F. Štěpánek, M.A. Ansari, Computer simulation of granule microstructure formation, in: Chem. Eng. Sci., 2005: pp. 4019–4029. doi:10.1016/j.ces.2005.02.030.

[32] G. Lian, C. Thornton, M.J. Adams, A Theoretical Study of the Liquid Bridge Forces between Two Rigid Spherical Bodies, J. Colloid Interface Sci. 161 (1993) 138–147. doi:http://dx.doi.org/10.1006/jcis.1993.1452.

[33] M.A. Erle, D.C. Dyson, N.R. Morrow, Liquid bridges between cylinders, in a torus, and between spheres, AIChE J. 17 (1971) 115–121. doi:10.1002/aic.690170125.

[34] T. Mikami, H. Kamiya, M. Horio, Numerical simulation of cohesive powder behavior in a fluidized bed, Chem. Eng. Sci. 53 (1998) 1927–1940. doi:10.1016/S0009-2509(97)00325-4.

[35] C.D. Willett, M.J. Adams, S.A. Johnson, J.P.K. Seville, Capillary bridges between two spherical bodies, Langmuir. 16 (2000) 9396–9405. doi:10.1021/la000657y.

[36] O. Harireche, A. Faramarzi, A.M. Alani, A toroidal approximation of capillary forces in polydisperse granular assemblies, Granul. Matter. 15 (2013) 573–581. doi:10.1007/s10035-013-0425-9.

[37] S.J.R. Simons, J.P.K. Seville, M.J. Adams, An analysis of the rupture energy

of pendular liquid bridges, Chem. Eng. Sci. 49 (1994) 2331–2339. doi:10.1016/0009-2509(94)E0050-Z.

[38] P.R. Mazzone D. N., Tardos G. I, The Behavior of Liquid Bridge Between Two Relatively Moving Particles, Powder Technol. 51 (1987) 71–83.

[39] J. Eggers, T.F. Dupont, Drop formation in a one-dimensional approximation of the Navier-Stokes equation, J. Fluid Mech. 262 (1994) 205–221. doi:10.1017/S0022112094000480.

[40] D.T. Papageorgiou, On the breakup of viscous liquid threads, Phys. Fluids. 7 (1995) 1529. doi:10.1063/1.868540.

[41] X. Zhang, R.S. Padgett, O.A. Basaran, Nonlinear deformation and breakup of stretching liquid bridges, J. Fluid Mech. 329 (1996) 207. doi:10.1017/S0022112096008907.

[42] E.J. Vega, J.M. Montanero, M. a. Herrada, C. Ferrera, Dynamics of an axisymmetric liquid bridge close to the minimum-volume stability limit, Phys. Rev. E. 90 (2014) 13015. doi:10.1103/PhysRevE.90.013015.

[43] M. Wu, J. Khinast, S. Radl, Direct Simulation of Film Flow on Spheres to Investigate Liquid Bridge, in: 2014 AICHE Annu. Meet. Novemb. 16, Atlanta, Vereinigte Staaten (USA), 2014.

[44] L.A. Easo, R. Kumar, R. Ren, R. Carl, Numerical Study of the Formation of a Liquid Bridge Between Two Spheres with Uniform Film Thickness, in: 2014 AIChE Annu. Meet. Novemb. 18, Atlanta, 2014.

[45] S. Radl, J.G. Khinast, S. Sundaresan, On the Filling Rate of a Liquid Bridge Between Wet Particles, in: 2013 AIChE Annu. Meet. Novemb. 03-08, San Francisco, Vereinigte Staaten (USA), 2013.

[46] D. Shi, J.J. McCarthy, Numerical simulation of liquid transfer between particles, Powder Technol. 184 (2008) 64–75. doi:10.1016/j.powtec.2007.08.011.

[47] B. Mohan, C. Kloss, J. Khinast, S. Radl, Regimes of liquid transport

through sheared beds of inertial smooth particles, Powder Technol. 264 (2014) 377–395. doi:10.1016/j.powtec.2014.05.045.

[48] S.S. Deshpande, L. Anumolu, M.F. Trujillo, Evaluating the performance of the two-phase flow solver interFoam, Comput. Sci. Discov. 5 (2012) 14016. doi:10.1088/1749-4699/5/1/014016.

[49] a. Eddi, K.G. Winkels, J.H. Snoeijer, Short time dynamics of viscous drop spreading, Phys. Fluids. 25 (2013) 13102. doi:10.1063/1.4788693.

[50] S. Radl, S. Sundaresan, A drag model for filtered Euler-Lagrange simulations of clustered gas-particle suspensions, Chem. Eng. Sci. 117 (2014) 416–425. doi:10.1016/j.ces.2014.07.011.

[51] C. Kloss, C. Goniva, S. Amberger, S. Pirker, LIGGGHTS Open Source DEM: Models, Features, Parallelism and Quality Assurance, in: 8th Int. Conf. CFD Oil Gas, Metall. Process Ind., 2011. http://www.sintef.no/projectweb/cfdconf/.

"The whole secret of a successful life is to find out what is one's destiny to do, and then do it."

(Henry Ford, 1863-1947)

5

Liquid Transport Rates during Binary Collision of Unequally-sized Particles*

In this chapter, we study the liquid transport between particles of different sizes, as well as build a dynamic liquid bridge model to predict liquid transport between these two particles. Specifically, the drainage process of liquid adhering to two unequally-sized, non-porous wet particles is simulated using Direct Numerical Simulations (DNS). Same as in our previous work (Wu et al., AIChE Journal, 2016, 62:1877-1897), we first provide an analytical solution of a proposed dynamic liquid bridge model. We find that such an analytical solution also describes liquid transport during collisions of unequally-sized particles very well. Finally, we show that our proposed model structure is sufficient to collapse all our direct numerical simulation data. Our model is hence able to predict liquid transport rates in size-polydisperse systems for a wide range of parameters.

I. * This chapter is based on: M. Wu, J.G. Khinast, S. Radl. Liquid Transport Rates during Binary Collisions of Unequally-sized Particles. Powder Technology 309 (2017), 95 – 109.

5.1 Introduction

Granular particle beds are usually composed of particles with different properties (i.e., shape, size, density, etc. [1]). It is well known that particle-size polydispersity and shape significantly influence the transport of mass and liquid in a fluidized bed [1,2] and spouted beds system [3]. Therefore, a better understanding of these systems (i.e., that involving particles of different sizes) helps to improve the control of many engineering applications, including fluidization, mixing, agglomeration, or coating. In addition, bi-and polydisperse fluidized bed systems often show a greater mixing performance [4–7]. Furthermore, other researches showed that wide particle size distributions result in smoother fluidization of dry systems [8–11]. Naturally, the question arises how polydispersity affects wet fluidized beds, i.e., three-phase systems in which a thin liquid layer (or droplets) is present on the particles' surface. In these systems two additional complications arise: (i) the prediction of the amount of liquid in each liquid bridge, and (ii) the magnitude of cohesive forces due to these bridges.

The rate of liquid bridge formation (i.e., the amount of liquid in the bridge as a function of time) plays an important role with respect to the bridge's rupture energy. Donahue et al. [12] revealed that controlling the liquid bridge volume connecting two target particles is the key in obtaining the wet-collision results of their experiment. Thus, the amount of liquid present in the bridge is decisive whether particles separate or agglomerate [13]. In summary, it is important to quantify these interactions to predict the overall flow behaviour and the size of agglomerates in a fluidized bed. Although liquid transport processes between particles are always encountered in nature and in industrial applications [14–17], it is still difficult to quantify the associated transport rates of liquid. This is because the liquid transport between particles and the rate of exchange of liquid onto the particle surfaces is rather complex.

Next, we briefly review the latest development of liquid bridge formation in mono- and polydisperse particle beds. This is to motivate our present study that

attempts to close the gap in understanding related to the rate of liquid bridge formation in systems involving unequally-sized particles.

Many researchers have studied the liquid-bridge and capillary-forces effects for monodisperse particle systems. For example, Hotta et al. [18], introduced a gorge method to calculate the capillary forces between particles by estimating the capillary force at the neck of the liquid bridge. Xu, et al. [19] employed a CFD-DEM approach to simulate a wet spouted bed of particles by using a static capillary force model. Mikami et al. [20] developed a bridge force model between particles as a function of the dimensionless liquid bridge volume and separation distance based on numerical simulation of the Young-Laplace equation (YLE). Due to the complexity of using the YLE to describe the geometry of liquid surfaces, researchers introduced a toroidal approximation. This approximation treats the interface between liquid and air as a circular arc [21–24]. Another question is associated with the maximum separation distance for a stable liquid bridge. Therefore, Lian et al. [22] introduced a simple cube root relation between this rupture distance and the liquid bridge between equally-sized particles for small contact angles. However, all of this previous work assumes that the volume of liquid in the bridge is known – the effect of the initial liquid distribution (e.g., the liquid film present on the particles' surface) on the bridge volume is not modelled. Furthermore, all simple approximation methods assumed the meniscus of the bridge profile to be circular, and the liquid flow into the bridge was not predicted. Although some of these models assumed a zero contact angle when extracting the liquid bridge shape [25,26], the limitation of all these models is that the approximations are no longer correct for the liquid bride formation close to saturation. In these systems the liquid content is so high that the curvature of the gas-liquid interface and the Laplace pressure approaches zero [27]. In order to get the exact profile of the liquid bridge in these situations, one has to use numerical simulations to solve the YLE, or numerically solve the Navier-Stokes equations for a gas-fluid multiphase system. The latter approach also allows extracting the dynamic evolution of the gas-liquid interphase position, which

provides data for building a dynamic bridge model. Only recently, our group [28] has employed such a simulation method based on the volume of fluid (VOF) approach to simulate liquid bridge formation. It allows a reconstruction of the interface deformation as a function of time, and ultimately to build a dynamic liquid bridge model. Such a model then provides a detailed and more rigorous understanding of how to predict liquid bridge forces in wet particulate systems.

So far, little attention has been devoted to wet polydisperse particle beds, especially with respect to the flow rate of liquid present on the particles' surface into the bridge. Orr et al. [29], were one of the first that studied liquid bridges with great rigor, and who derived a simple expression for the bridge shape and force (i.e., the adhesion force in contact with the sphere and the flat wall). Later, Willett et al. [24], provided a numerical solution for liquid bridge forces between spheres of equal and unequal radii, but still assuming the liquid bridge volume being known. In addition, Soulié et al. [30] proposed a similar capillary model for wet polydisperse granular materials based on the interparticle distance and the liquid bridge volume between two particles of different sizes. A similar approach has been used later by Richefeu et al. [31]. Moreover, Sprakel et al. [27], provided a theoretical thermodynamic analysis of the capillary bridges between a sphere and a plate, as well as between spheres with equal or unequal particle size. This work considered both extremes, i.e., when the capillary bridge reaches the limit of saturation, and when the capillary bridge becomes very small. However, their work still considered a static situation, and the transient formation of the bridge was not considered. Recently, Chen et al. [32] presented a mechanical model for liquid bridges and the associated forces for two unequally-sized spherical particles, or a sphere and a flat plate. This study neglected gravitational effects, used the simple toroidal approximation to estimate the liquid bridge shape, and did not predict the dynamic filling of the bridge. The obvious drawbacks of all these approaches is that the liquid transport between particles and the flow of liquid into the liquid bridge has been neglected during the phase when particles approach each other.

To get an impression of different methods that have been employed for liquid bridge modelling, we next briefly summarize the methods that were used for studying liquid bridges. Essentially, there are two approaches: the first method is using simple approximation (i.e., toroidal approximation) based on the simplification of geometry [33–35]; the second approach solves the Young-Laplace equation (YLE) numerically [24], or analytically by solving a simplified YLE [22]. Only very recently, researchers started the simulation of liquid transport between two particles using a full solution of the Navier-Stokes equation [28,36,37]. Only the latter method provides a detailed description of the dynamic formation of the liquid bridge as shown in our previous work that used Direct Numerical Simulation (DNS) [28]. In this paper, we are going to extend our previous model to be valid as well for polydisperse particle systems.

5.1.1 Goals and Structure

In the current contribution we study the liquid bridge and liquid transport between two wet unequally-sized particles, i.e., we focus on particle-size effects on liquid bridge formation. We use a VoF-based Direct Numerical Simulation (DNS) approach to simulate both the motion of the liquid and the surrounding gas. We extend the method used in Wu et al. [28], to be available for bi-and polydisperse particle system. Our final goal is building a dynamic model to predict the liquid bridge volume during the filling process between these two unequally-sized particles. Thus, we fit our DNS data to a postulated liquid bridge filling model.

5.2 Methodology

5.2.1 Setup and Initial Conditions

Two smooth particles of unequal sizes are fixed in space, i.e., their relative particle velocity is assumed to be zero. We define particle 1 to have a smaller radius than that of particle 2, and we fix the radius of particle 2 while varying the radius of particle 1 in what follows. We consider particles fully wetted, i.e., the two particles are initially fully covered by uniformly thick films. As shown in Figure 5.1, O_1 and

O_2 are the two particle centres, R_1 and R_2 are the particles' radii, and h_1 and h_2 are the initial film thicknesses for particle 1 and particle 2, respectively. In the present work we consider systems in which h_1 and h_2, i.e., the dimensional film thicknesses, are equal for both particles. S is defined as the half separation distance between two particle surfaces. Moreover, we consider an axisymmetric liquid bridge, such that that we can perform corresponding two-dimensional simulations with adequate numerical resolution in a feasible time.

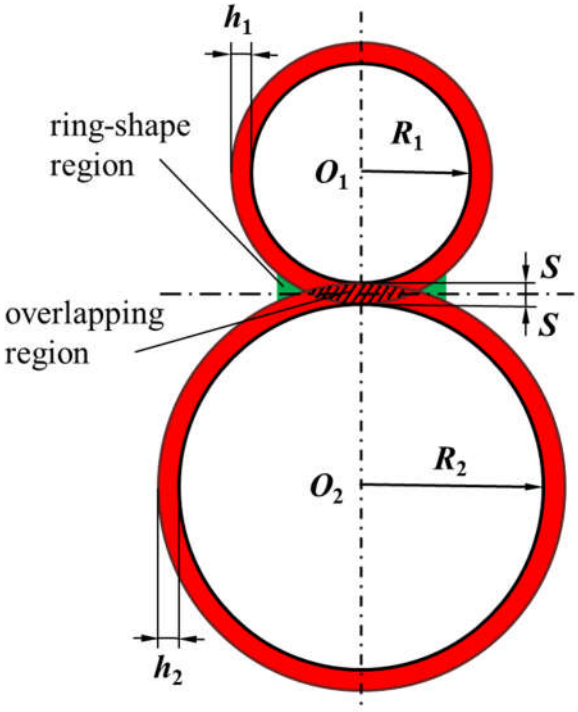

Figure 5.1: Particle configuration, and illustration of the calculation of the initial bridge shape.

In addition, and as shown in Figure 5.1, the initial shape of the liquid bridge region (i.e., the green-shaded ring) has been set according to the initial film height, the separation distance and the particle radii. This is done considering the following line of thoughts: as we assume particles to be static, we cannot predict the deformation of liquid films on the particle surfaces before the films overlap. Therefore, we assume that liquid in the overlapping region (i.e., the black-shaded region in Figure 5.1) of the liquid films is instantaneously displaced. This liquid flows into a ring-shaped region (i.e., the green-shaded ring in Figure 5.1). Thus, we consider an initial bridge that has a cylindrical shape, and which dimensions

are calculated purely based on geometric arguments. The calculation of this "geometrical bridge volume" for unequally-size particle is detailed below in section "Geometrical Bridge Volume".

Also, in our simulations there is no gravity, and no other forces act on the system. Consequently, there is only one physical reason why liquid residing in the films on the particle surfaces flows into the liquid bridge: the pressure in the film (adhering to the particle surface, and far away from the bridge) can be estimated as $p_{s,1} \approx 2\sigma/R_1$ for particle one, and similarly for particle 2. The pressure in the liquid bridge region, however, can be approximated as $p_{V_b} \approx -\sigma/R_{curve}$. Here R_{curve} is the radius of curvature of the liquid bridge surface. Thus, the relative pressure in the liquid bridge region is always negative or zero, while that in the film is always positive. Hence, a pressure difference between the particle surface and the liquid bridge region exists, driving the liquid into the bridge. This liquid flow will not stop until the pressure difference reaches zero, or the liquid film on the particle surface ruptures.

In order to render the system dimensionless, we choose the following key dimensional reference quantities:

$$\begin{aligned} R_{eff} &= 2R_1R_2/(R_1+R_2); \quad t_{ref} = R_{eff}\mu_l/\sigma \\ U_{ref} &= \sigma/\mu_l; \qquad P_{ref} = \sigma/R_{eff}; \end{aligned} \tag{5.1}$$

Where R_{eff} is the effective particle radius, t_{ref} is a relevant reference time scale chosen to be the ratio of the effective particle radius and the capillary speed, U_{ref} is the velocity scale (i.e., the capillary speed), and P_{ref} is the pressure scale chosen (i.,e., a typical capillary pressure given by surface tension over the effective particle radius).

The key dimensionless parameters are then:

$$
\begin{aligned}
&h_1^+ = h_1/R_2;\ h_2^+ = h_2/R_2;\ h_0 = (h_1+h_2)/2;\ h_0^+ = h_0/R_2;\ S^+ = S/R_2, R_r = R_1/R_2 \\
&t^+ = t/t_{ref};\ L_{p1}^+ = L_{p1}/R_{eff}^3;\ L_{p2}^+ = L_{p2}/R_{eff}^3;\ L_{p,0}^+ = \left(L_{p1}^+ + L_{p2}^+\right)/2;\ V_b^+ = V_b/R_{eff}^3 \\
&\rho_{ratio} = \rho_l/\rho_g;\ \mu_{ratio} = \mu_l/\mu_g;\ Re = \sigma R_{eff}\rho_l/\mu_l^2;\ Oh = \mu_l/\sqrt{\rho_l \sigma R_{eff}} = 1/\sqrt{Re}
\end{aligned}
\qquad (5.2)
$$

Where, h_1^+, h_2^+ are dimensionless initial film heights for particle 1 and particle 2 respectively, and h_0^+ is the average film height, which quantifies the amount of liquid in the particle system. S^+ is the dimensionless separation distance, and R_r is the ratio of the small and large particle diameter; t^+ is the dimensionless time, L_{p1}^+, L_{p2}^+ and V_b^+ are the amount of liquid on the particles' surfaces and the bridge volume normalized with the reference volume (i.e., the effective particle radius cubed); ρ_{ratio} and μ_{ratio} are density and viscosity ratio between liquid and ambient gas, respectively. The Reynolds number *Re* is defined based on the capillary speed, fluid viscosity and the effective particle radius. *Oh* is an Ohnesorge number which is simply the inverse of the square root of the Reynolds number.

5.2.2 Simulation Approach and Liquid Bridge Volume Calculation Strategy

The simulations were performed using a Volume of Fluid (VoF) approach, specifically the implementation "*interFoam*" [38] in the open-source software package OpenFOAM®. The two-fluid flow is modelled with the Navier-Stokes equation

$$
\frac{\partial(\rho \boldsymbol{U})}{\partial t} + \nabla \cdot (\rho \boldsymbol{U}\boldsymbol{U}) = -\nabla p + \mu\left[\nabla \boldsymbol{U} + (\nabla \boldsymbol{U})^T\right] + \boldsymbol{F}_b \qquad (5.3)
$$

$$
\nabla \cdot \boldsymbol{U} = 0 \qquad (5.4)
$$

where $\boldsymbol{U}$ is the local velocity shared by the two fluids, ρ is the local density, p is the local pressure, and $\boldsymbol{F}_b$ are body forces, which include only surface tension effects at the interface in the present work. We stress that effects due to gravity have been neglected in our simulation, simply because viscous and capillary effects are dominant in situations involving relevant particle systems where particles have a diameter smaller than the capillary length.

We consider two immiscible fluids, i.e. gas and liquid, density and viscosity are constant in each phase, but can be discontinuous at the interface. We use a phase volume fraction indicator α in the transport equation of velocity field to represent the interface phase:

$$\frac{\partial \alpha}{\partial t} + \nabla \cdot (\boldsymbol{U}\alpha) = 0 \qquad (5.5)$$

The phase function α can proceed within the range $0 < \alpha < 1$, with alpha being zero (or unity) in regions occupied by the gas (or the liquid), respectively. The local average density and viscosity are computed from the volume fraction as:

$$\rho = \rho_l \alpha + \rho_g (1-\alpha) \qquad (5.6)$$

$$\mu = \mu_l \alpha + \mu_g (1-\alpha) \qquad (5.7)$$

Where ρ_l (or μ_l) and ρ_g (or μ_g) are the density (or the dynamic viscosity) of the liquid and gas, respectively.

We assumed that two particles with different sizes are completely wet, i.e., there is no three-phase contact line initially. Our preliminary results shown in Figure 5.5 suggest that the liquid transport process can be divided into three stages: a fast filling stage (i.e., $t^+ < 1$) in which the typical shape of the bridge is established; a viscous filling stage (i.e., $1 < t^+ < 154$) and a post rupture stage (i.e., $154 < t^+$). This is in line with our previous work on mono-disperse systems [28], in which we also observed film rupture on the particle with the thinner film. Note, we currently use the "*interfoam*" solver only for the first two stages: after the film gets ruptured, a three-phase dynamic contact line appears (see Figure 5.5, panel for $t^+ = 154.7$), and our solver will deliver inaccurate (but still physical) predictions of the liquid bridge shape post rupture [28]. To circumvent this problem, we did not consider data collected after film rupture events in our analysis. Again, this is in line with our previous work [28]. All relevant simulation parameters and numerical schemes are listed in Table 5.1.

Parameter	Value	Comment
Δt^+	$5 \cdot 10^{-3}$	Dimensionless time step
Δh	0.05 - 0.33	Dimensionless mesh resolution
Time derivative scheme	backward	Second order, implicit
Laplacian scheme	Gauss linear corrected	Unbounded, second order, conservative
Convection scheme (for U)	Gauss linear	Unbounded, second order
Convection scheme (for α)	Gauss vanLeer	van Leer limiter

Table 5.1: Simulation parameters and numerical schemes used in the VoF simulations.

The liquid-gas interphase can be easily determined from the DNS data by analysing the distribution of the phase fraction. Consequently, the interface position can be determined at $\alpha = 0.5$. Hence, we have taken a simple, yet effective sampling method to detect the gas-liquid of the film and the bridge formed between the particles.

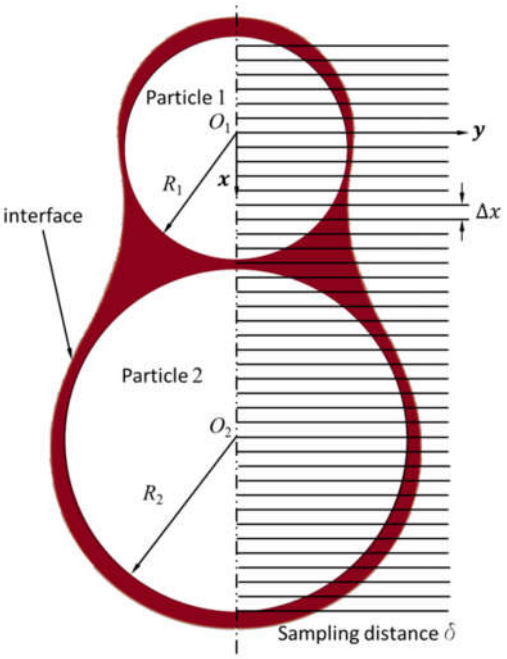

Figure 5.2: Sketch of the sampling approach used to detected neck positions on the large and small particle.

As can be seen in Figure 5.5 (zoomed region for $t^+ = 1.33$ indicating the liquid velocity), liquid from the small particle surface is transferred faster into the bridge than from the bigger one. Thus, the liquid film on the upper (smaller) sphere is no longer spherical-shell shaped, but quickly deforms into a complex shape. Therefore, and in order to get accurate data, we will not just sample along the distance between O_1 and O_2 as shown in Figure 5.2 as we did in previous work [28]. Instead, we use a sampling procedure which takes place from the top pole of particle 1 to the bottom of particle 2 with an interval of Δx and a large enough maximum sample distance δ (see Figure 5.2). By doing so, we obtain a list of data for the phase value along each sampling line, and subsequently the interface position. We then need to define which portion of the fluid in the system is considered to be in the liquid bridge. This is done by using the same approach as used in our previous work [28], and which considers the following line of thoughts: in case one would analyze the thickness profile on each particle, one can observe a certain angular position where the film is thinnest. We have used this local minimum to mark the extent of the liquid bridge. Specifically, we denote these positions of the minima as the "neck" positions, which separate the bridge from the film adhering to the particle surface. Clearly, in case the film ruptures, this will happen at these neck positions. After the interface positions and neck position have been determined, we can calculate the liquid bridge volume by using a direct integration method (DIM) presented in our previous work [28].

5.2.3 Proposed Model for Liquid Bridge Filling

The DNS of liquid flow on unequally-size particles during their collision indicates that the mechanism of liquid bridge formation consists of the following steps: first the liquid-covered particles approach each other. Then, the films coalesce, a liquid bridge is formed between the particles, and finally liquid drains into the bridge. Ultimately, film rupture may occur, which is not considered here in greater detail. Thus, similar to our previous work [28] it is reasonable to differentiate between two stages of the filling process of liquid bridge: (I) a

capillary-force driven initial stage (fast filling), and (II) a viscous filling stage (slow filling). We define stage I to end after a (viscous) reference time scale of t_{ref}, i.e., a dimensionless time of $t^+=1$, was reached. This reference time in Equation 5.1 is different from that in the monodisperse system by definition, as the effective particle radius affects the reference time scale.

As shown next, we employ two different sub-models to predict the liquid bridge volume in each of these two stages. By employing an overall mass balance it is then straightforward to predict the liquid residing on the contacting particles. Specifically, for the initial stage, we aim to correlate the bridge volume at $t^+=1$ with the most important process parameters. Therefore, we choose the key geometrical parameters, which are (i) the average initial film height h_0, (ii) the half separation distance S and (iii) the particle seize ratio R_r.

Our model to predict the time evolution of liquid bridge volume in stage II ($t^+ > 1$) is the same as reported in our previous work [28], extended to account for unequally-sized particles. Specifically, we use a phenomenological closure for the flow rate between the film and the bridge compartment. We assume the flow rate to be proportional to the difference of the mobile fraction of the liquid on the particle, and half of the bridge volume. Moreover, we define a mobility parameter $\phi_{m,i}$ to predict the mobile fraction of liquid presented on particle surface. This parameter is the ratio of the liquid mobile to flow on the particle i's surface, divided by the total liquid content on particle i. In Chapter 5.4 we show that the mobility parameter is a function of the initial film height and the particle separation, as well as the particle size. For what follows we accept $\phi_{m,i}$ as a time-independent parameter that is fixed during the filling process. Next, we introduce a dimensionless filling-rate parameter a_i (which one can assume to be specific for each particle i), as well as a reference time scale t_{ref}. We then postulate a simple differential equations for predicting the liquid content $L^+_{p,i}$ on each particle i which reads:

$$\frac{dL_{p1}^{+}}{dt^{+}} = \frac{-a_i}{t_{ref}}\left(L_{p1}^{+}\phi_{m1} - \frac{V_b^{+}}{2}\right)$$
$$\frac{dL_{p2}^{+}}{dt^{+}} = \frac{-a_i}{t_{ref}}\left(L_{p2}^{+}\phi_{m2} - \frac{V_b^{+}}{2}\right) \quad (5.8)$$

$$\frac{dV_b^{+}}{dt^{+}} = -\left(\frac{dL_{p1}^{+}}{dt^{+}} + \frac{dL_{p2}^{+}}{dt^{+}}\right) \quad (5.9)$$

Appropriate initial conditions, as well as the assumption that a_i is a constant for a pair of particles sharing the same bridge, lead to the analytical solution documented in appendix A of our previous work [28].

5.3 Geometrical Bridge Volume

The goal of this paper is to study liquid bridge formation between two unequally-sized particles, and hence it is useful to define a reference bridge volume based on some geometrical arguments. Therefore, we choose the precise geometrical bridge volume (this corresponds to "model II" in our previous work [28]) as the reference bridge volume. This volume is used to normalize the early stage model for the liquid bridge volume (see our "Results" section). This geometrical bridge volume is calculated by assuming the liquid in the overlap region (see black-shade region in Figure 5.1) to be displaced when particles approach each other. Liquid in the overlap region is assumed to flow into a ring-shaped area (see Figure 5.1; more details on the calculation are available in our previous work [28], and are not repeated here for brevity). This evaluation of bridge volume requires an iterative procedure, which makes it more expensive and less attractive for larger-scale DEM-based simulations. However, the bridge volume defined in such a way is more accurate, as it is closer to our results of the DNS as we will demonstrate in or "Results" section below.

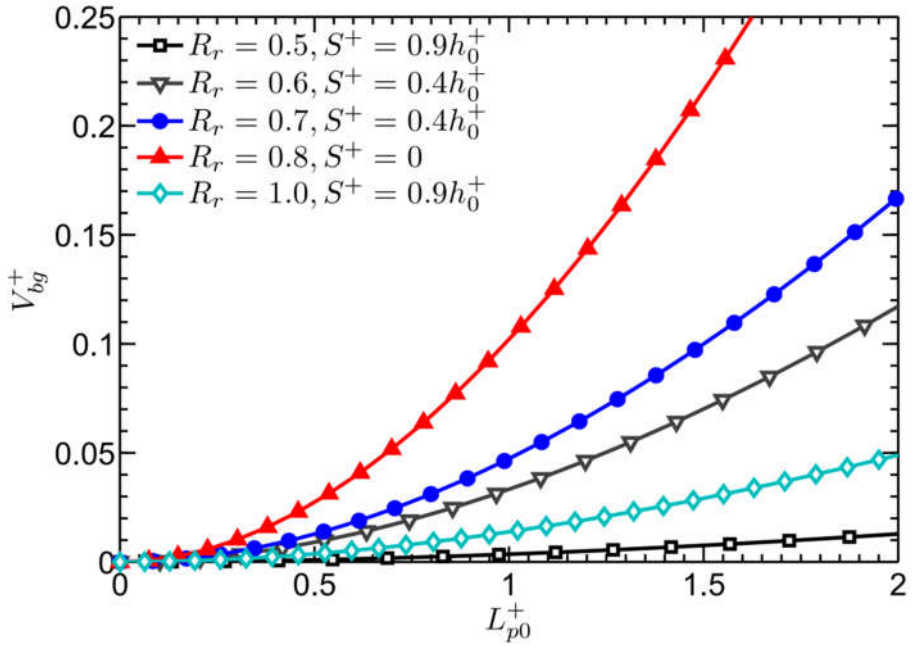

Figure 5.3: Effects of the separation distance and particle size on the bridge volume as function of initial liquid content, L_{p0}^+ is the average initial liquid content on particles, V_{bg}^+ is the total geometrical bridge volume.

We next highlight some trends of the geometrical bridge volume of an unequal-size particle pair, and how this volume is affected by the particle size ratio, the separation distance, and the initial film height. The subsequent figures and text, $V_{b,g}$ is the type II geometrical bridge volume as introduced in previous work [28]. Figure 5.3 shows that the normalized particle size (i.e., R_r) and the separation distance have a significant effect on the bridge volume, as indicated by Figure 5.3 (black triangles and blue cycles). Also, the bridge volume increases monotonically, but non-linearly, with increasing (initial) liquid content for every choice of separation distance. Also, it can be observed that the bridge volume decreases with increasing separation distance, finally approaching zero for $S^+ = h_0^+$ as it should be. The physical interpretation of this fact is that for the situation in which the separation equals the initial film thickness, the overlapping region of a thin film between two particles vanishes. We also can see from the figure that particles with identical size and larger separation distance (i.e., R_r = 1, light-green diamonds) have smaller bridge volumes compared to smaller particles at zero separation (red triangles shown in Figure 5.3). Again, this highlights the strong

effect of the separation distance on the liquid bridge volume. Interestingly, at identical (dimensionless) separation, mono-disperse particles (i.e., $R_r = 1$, light-green diamonds) imply a larger dimensionless liquid bridge volume than particles of different size (i.e., $R_r = 0.5$, black squares).

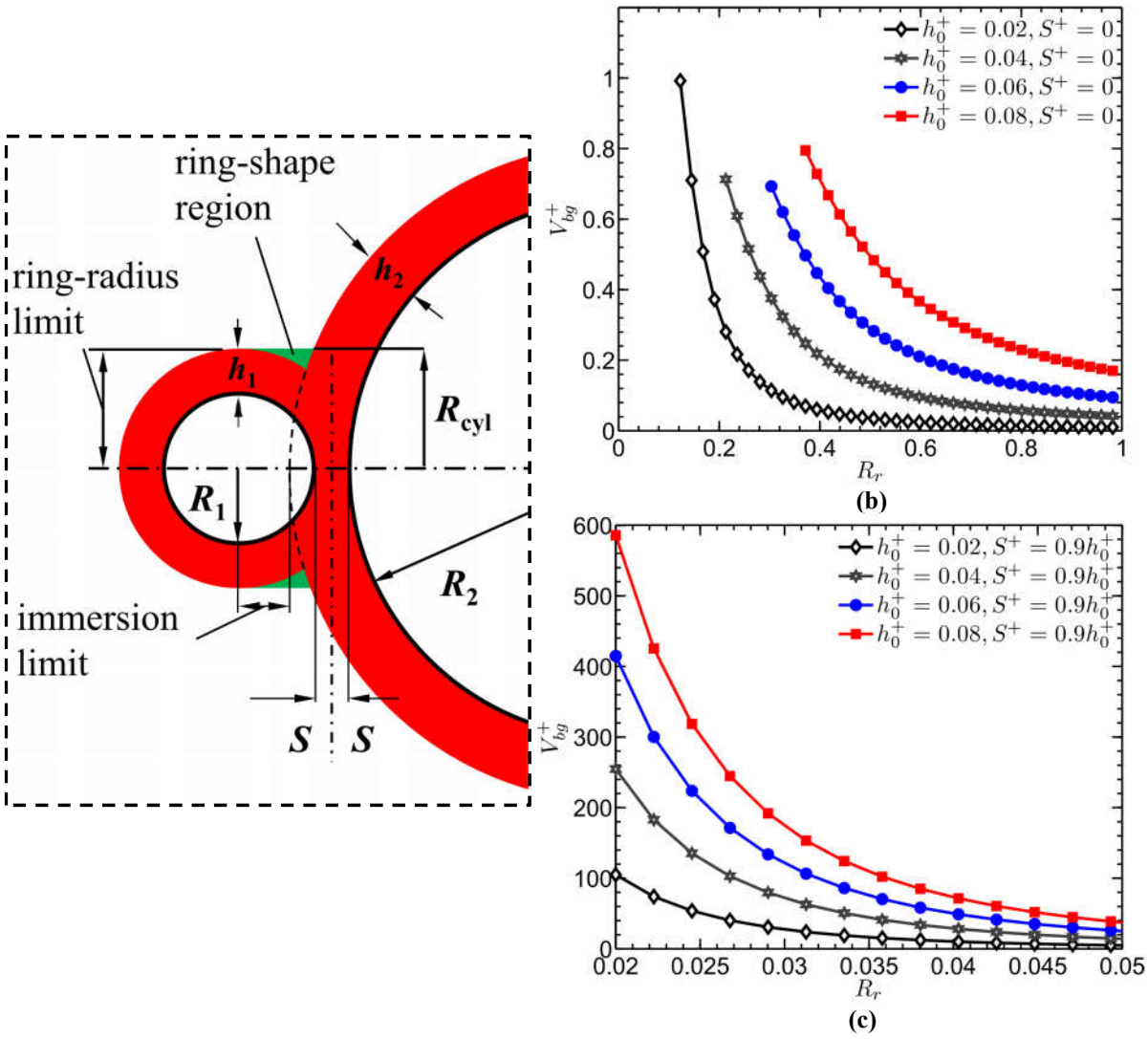

Figure 5.4: Geometrical bridge volume versus particle size ratio R_r. Panel (a) illustrates the limiting case when a small particle becomes immersed in the liquid layer of the larger particle. Panel (b): geometrical bridge volume versus particle size ratio R_r with different initial film heights and zero separations. Panel (c): geometrical bridge volume versus particle size ratio R_r with different initial film heights and larger separations. h_0 is the average initial film height, and we have chosen $h_0 = h_1 = h_2$.

Figure 5.4 (panel b and c) shows the general behavior of the dimensionless geometrical bridge volume as a function of the particle size ratio. Thus, the key

message of this figure is that the (normalized) bridge volume decreases when the particles become more identical in size, i.e., R_r approaches unity.

Another key observation is that for extremely small particle size ratios and thick films our definition of a geometrical bridge volume breaks down. Panel (a) illustrates these limiting conditions for the geometrical bridge calculation: the first obvious limit is that the radius of the smaller particle (i.e., particle 1) plus the distance between two particle surfaces must be larger than the initial film height of the larger particle (particle 2). Thus, we require $R_1 + 2S > h_2$, and hence we must ensure $R_r > h_2^+ - 2S^+$ in order to compute a meaningful geometrical bridge volume. Since the smaller particle would be completely immersed in the liquid layer of the larger particle otherwise, we call this limit the "immersion limit". The second limit is imposed by the radius R_{cyl} of the ring-shaped region of the liquid bridge (i.e., the region shaded in green in Figure 5.1). In case R_{cyl} is larger than $R_1 + h_1$, it is also not possible to define a geometrical bridge volume. This is simply because the assumption of ring-shaped (cylindrical) liquid bridge is no longer consistent with the geometrical arrangement of the particles and the films. Hence, we denote this critical situation as the "ring radius limit".

Panel (b) in Figure 5.4 shows the change of the bridge volume for particles ratios from 0.1 to 1 with different initial film heights and zero separation distance. For all these figures the limiting size ratio for the "immersion limit" discussed above has not been reached. Still, the normalized liquid bridge volume can reach values close to unity, and varies significantly with R_r. This indicates that the relative size ratio is a key influence parameter when estimating the liquid bridge volume.

In contrast, panel (c) shows the bridge volume for particle size ratios ranging from 0.02 to 0.05 with larger separations. In this case neither the "immersion limit", nor the "ring radius limit" has been reached. A large value of the dimensionless (geometrical) liquid bridge volume indicates that for these situations the collision approaches the limit of a collision in which both particles are fully immersed in a liquid. While it was impossible to simulate such extreme

diameter ratios as shown in Figure 5.4c in the present contribution, we speculate that the exact details of the bridge shape are irrelevant for these situations. This is simply because of the above mentioned argument connected to the large dimensionless bridge volume, which effectively has the physical meaning of a collision occurring fully immersed in the liquid phase.

5.4 Results

5.4.1 Early Stage Model

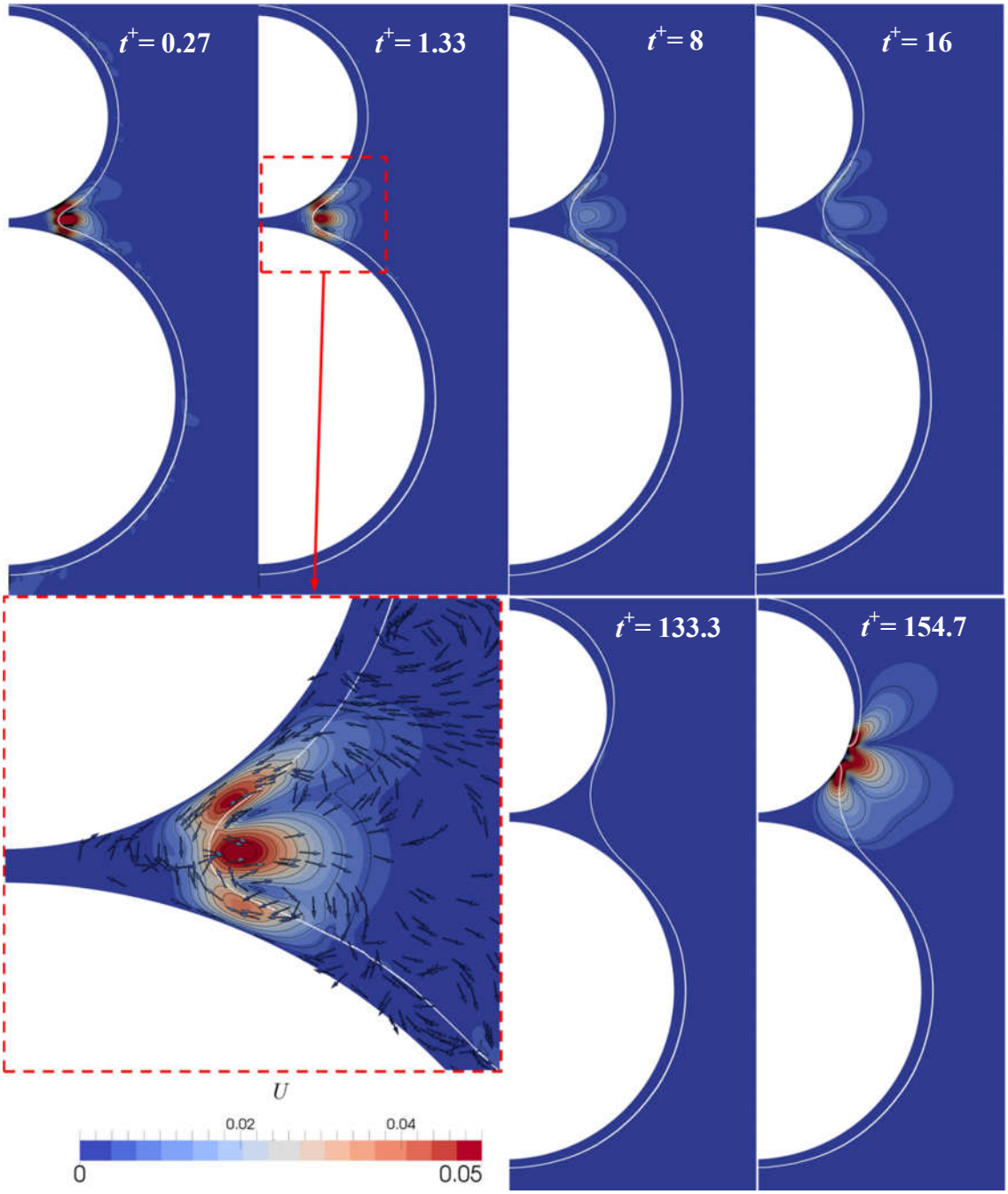

Figure 5.5: Typical velocity field for liquid transport from the particles' surface to the bridge region between two unequally-sized particles (R_1 = 0.6, R_2=1, S^+ = 0.027, $h_0 = h_1 = h_2$ = 0.06 R_2).

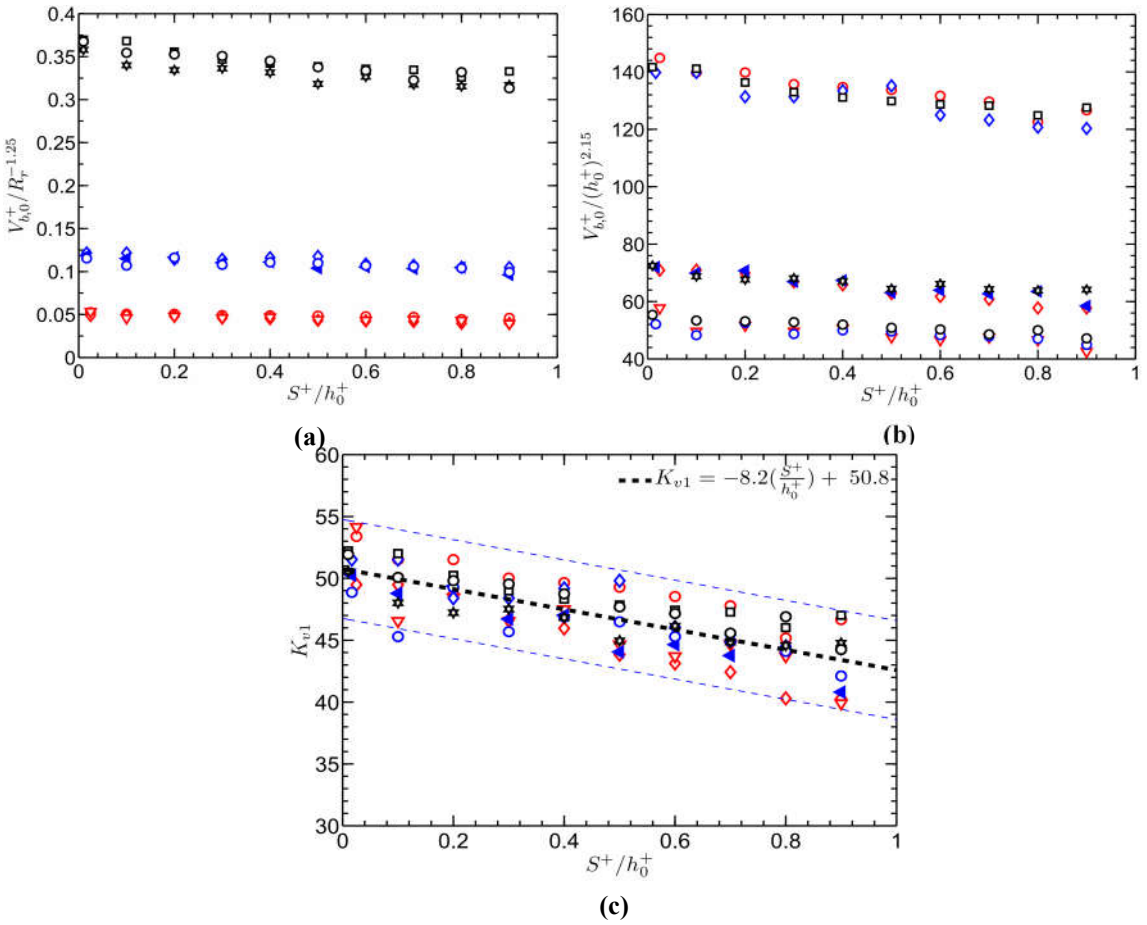

Figure 5.6: Initial bridge model (K_{v1}) coefficient based on different particle radius ratio (R_r) and initial film height (h_0) vs. normalized separation distance. Panel (a): initial bridge volume normalized with $R_r^{-1.25}$ for different initial film highs, red markers: initial film high h_0 = 0.04 R_2, blue markers: h_0 = 0.06 R_2, black markers: h_0 = 0.1 R_2. Panel (b): initial bridge volume normalized to $h_0^{2.15}$ for different particle-radius ratios, from top to bottom, R_r = 0.45, R_r = 0.75 and R_r = 0.95. Panel (c) initial bridge volume normalized with both $R_r^{-1.25}$ and $h_0^{2.15}$. The thin dashed lines indicate an error of +/- 8%. Red circles: R_r = 0.45 and h_0^+ = 0.04; Red diamonds: R_r = 0.75 and h_0^+ = 0.04; Red triangles: R_r = 0.95 and h_0^+=0.04. Blue diamonds: R_r = 0.45 and h_0^+ = 0.06; Blue left triangles: R_r = 0.75 and h_0^+ = 0.06; Blue circles: R_r = 0.95 and h_0^+ = 0.06. Black squares: R_r = 0.45 and h_0^+ = 0.1; Black hexagrams: R_r = 0.75 and h_0^+ = 0.1; Black circles: R_r = 0.95 and h_0^+ = 0.1.

As illustrated in Figure 5.5, the initial bridge forms very quickly and the inertia of the fluids (i.e., that of the liquid and the surrounding gas) plays an important role. Due the difficulty to model the inertial effects in our analytical model, we hence define a fixed initial bridge volume for "early times". Specifically, we choose one reference time at t^+=1 as the "early time". We then attempt to model the initial bridge volume by defining the variable K_{v1}, which is the value of the total simulated bridge volume at t^+=1, demarcated as ($V_{b,0}^+$), over the particle ratio R_r

to the power of some exponent m and the average initial film height h_0^+ to the power of some exponent n:

$$K_{v1} = \frac{V_{b,0}^+}{R_r^m \left(h_0^+\right)^n} \qquad (5.10)$$

This definition is based on the idea that the initial bridge volume is some function of the (initial) film height and the ratio of the particles' radii. Thus, there is no need to compute the geometrical bridge volume defined above. Instead, we hope that appropriate exponents in Eqn. 5.10 lead to a collapse of our data for $V_{b,0}^+$. Indeed, we can see from our data shown in Figure 5.6 that this ansatz reasonably collapses our DNS results with a linear model once we choose m and n correctly: firstly, by choosing m = -1.25 and normalizing the initial bridge only with the term originating from the particle size ratio R_r, we observe three groups of data based on the initial film height (see Figure 5.6, panel a); secondly, by choosing n = 2.15 and only normalization the bridge volume using the term origination from the initial film height h_0, we can see the collapsed DNS data forms three groups based on different values for R_r (see panel b in Figure 5.6); finally, by combining panel a and b, i.e., normalization with both terms in the denominator in Eqn. 5.10, we arrive at the final model illustrated in panel c. The error of this fitted model shown in equation 5.11 is around 8%, which is also illustrated in panel c of Figure 5.6.

$$K_{v1} = -8.2\frac{S^+}{h_0^+} + 50.8 \qquad (5.11)$$

From equations 5.10 and 5.11 we can now formulate the final expression for $V_{b,0}^+$:

$$V_{b,0}^+ = R_r^{-1.25}\left(h_0^+\right)^{2.15}\left(-8.2\frac{S^+}{h_0^+} + 50.8\right) \qquad (5.12)$$

This model is comparable to our model for the monodisperse particles system ([28]; for a monodisperse particle system the particle size ratio R_r is 1). Then, equation 5.12 can be simplified to

$$V_{b,0}^{+} = \left(h_0^{+}\right)^{2.15}\left(-8.2\frac{S^{+}}{h_0^{+}} + 50.8\right) \qquad (5.13)$$

We have confirmed that we obtain a comparable initial bridge model by comparing this new result to our previous results for monodisperse systems [28]. Thus, Eqn. 5.13 is simply a more rigorous form of our previous work only valid for $R_r = 1$.

In summary, our model for K_{v1} given by Eqn. 5.12 could already be used to compute $V_{b,0}^{+}$ for short collisions (or collisions involving very viscous liquids) between two unequally-sized wet particles. In these situations the amount of liquid draining into the bridge would be negligible compared to that formed simply due to the squeezing of the liquid by the approaching particles. Most important, the model presented in Eqn. 5.12 does not require an iterative numerical evaluation of the geometrical bridge volume, but simply the rather computationally efficient evaluation of two power law functions, as well as some additions and product evaluations.

Despite this, we next still aim on using the detailed geometrical bridge volume to normalize the simulated initial bridge volume. We do this since this model already accounts for the effect of the separation distance and film height on the bridge volume. Thus, we expect that normalization with the geometrical bridge volume yields an even simpler model for the bridge volume. By doing so, we define the variable K_{v2} as the ratio of the simulated initial bridge volume, the geometrical bridge volume, the particle ratio, and h_0^{+}:

$$K_{v2} = \frac{V_{b,0}^{+}}{V_{b,g}^{+} R_r^{m}\left(h_0^{+}\right)^{n}} \qquad (5.14)$$

Again, m and n are parameters that are used as exponents of the particle ratio and initial film heights, respectively, helping to collapse all data into a single curve. V_{bg} is the "type II" geometrical bridge volume introduced in our previous work [28]. The result of our analysis is displayed in Figure 5.7, indicating that we can fit the collapsed data to a parabolic function. This model is a bit different from the monodisperse system (the monodisperse system has been fitted as linear function): However, the exponent of the initial film heights has been chosen again as n = 0.2 (in line with our model for the monodisperse system reported in [28]), which collapses all initial film heights. By choosing m = 0.4 for the exponent of the particle size ratio, we suggest a parabolic relationship between the normalized liquid bridge volume and the separation distance:

$$K_{v2} = 1.4\left(\frac{S^+}{h_0^+}\right)^2 + 2.4 \qquad (5.15)$$

The error for this model is around 8%, which can also be seen from Figure 5.7. Hence, the expression for the initial bridge volume $V_{b,0}^+$ is:

$$V_{b,0}^+ / V_{b,g}^+ = R_r^{0.4}\left(h_0^+\right)^{0.2}\left(1.4\left(\frac{S^+}{h_0^+}\right)^2 + 2.4\right) \qquad (5.16)$$

We again can obtain the model for the monodisperse particle system in case we set R_r equal to 1, which yields

$$V_{b,0}^+ / V_{b,g}^+ = \left(h_0^+\right)^{0.2}\left(1.4\left(\frac{S^+}{h_0^+}\right)^2 + 2.4\right) \qquad (5.17)$$

Although the model here is a parabolic function which is different from our previous work on monodisperse particle systems [28], the exponent n for the initial film height still equals 0.2. This exponent is identical to the one we previously used for monodisperse particle systems.

In summary, the model for K_{v1} and K_{v2} presented above can be used to calculate the bridge volume at t^+=1. We next focus on the calibration of parameters in the

proposed viscous bridge-filling stage. This stage can be used to predict the time evolution of the liquid bridge at longer times, for which viscous effects play a significant role.

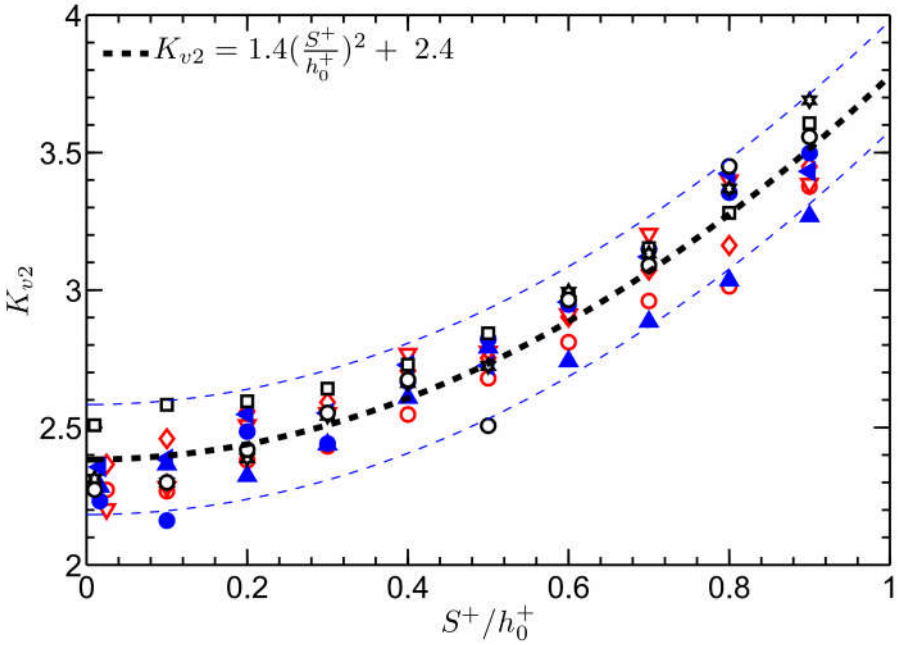

Figure 5.7: Initial bridge model (K_{v2}) coefficient based on different radius ratio (R_r) and initial film high (h_0) vs. normalized separation distance. The thin dashed lines indicate an error of +/- 8%. (Red circles: R_r = 0.45 and h_0^+ = 0.04; Red diamonds: R_r = 0.75 and h_0^+ = 0.04; Red triangles: R_r = 0.95 and h_0^+ =0.04. Blue up triangles: R_r = 0.45 and h_0^+ = 0.06; Blue left triangles: R_r = 0.75 and h_0^+ = 0.06; Blue circles: R_r = 0.95 and h_0^+ = 0.06. Black squares: R_r = 0.45 and h_0^+ = 0.1; Black hexagrams: R_r = 0.75 and h_0^+ = 0.1; Black circles: R_r = 0.95 and h_0^+ = 0.1)

5.4.2 Viscous Filling Model

We now consider the time evolution of the bridge volume and the liquid present on particles' surface, and how this is affected by different parameters (see Figure 5.8). Based on this data, we obtain the mobility parameters (defined in Section 2.3) by running the simulations to a dimensionless time of $t^+ = 100$. We have used a mesh size of $\Delta h = \Delta x / h_0 = 0.1$. We find that cases initialized with $h_0 = 0.04 \cdot R_2$ exhibit film rupture at dimensionless evolution times equal to approximately 100 with this mesh size. Film rupture still does not happen at this time for cases with larger initial film heights (i.e., $h_0 = 0.06 \cdot R_2$ and $h_0 = 0.1 \cdot R_2$), and even after $t^+ = 1000$ we do not observe film rupture for these cases. However, data between zero and $t^+ = 100$ already provides us with enough data to fit our dynamic model.

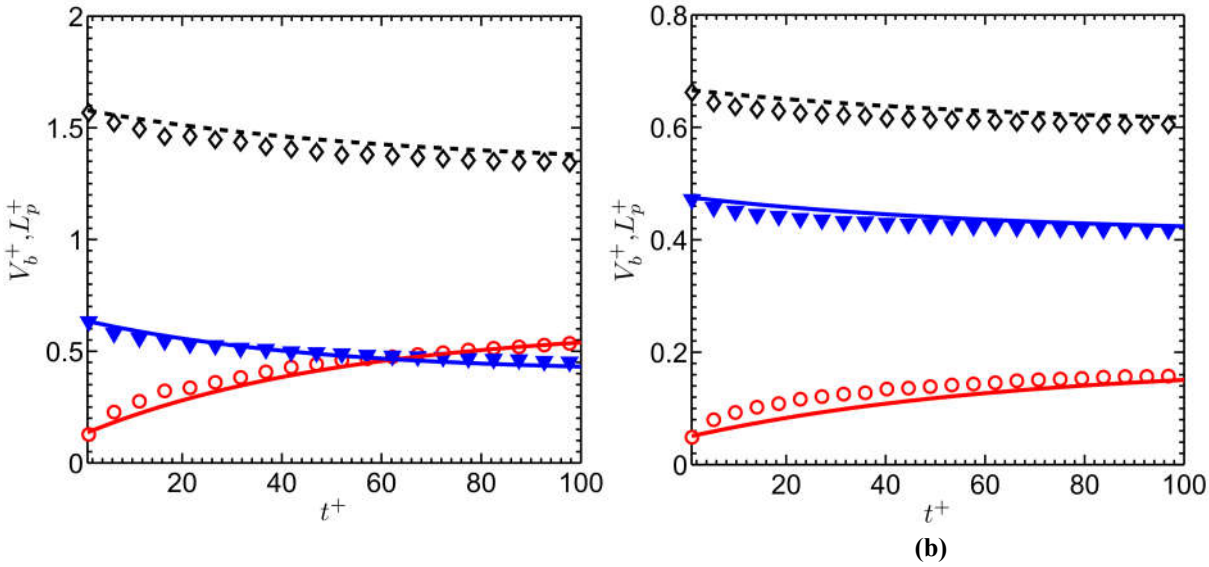

(b)

Figure 5.8: Fitted model (lines) vs. DNS data (symbols) over time; Red circles: liquid bridge volume (V_b^+); Blue triangles: liquid content on particle 1 (L_{p1}^+); Black diamonds: liquid content on particle 2 (L_{p2}^+); panel (a): R_r = 0.65, S^+ = 0.018, and h_0 = 0.06 R_2 ; panel (b): R_r = 0.85, S^+ = 0.012, and h_0 = 0.04 R_2

Specifically, we obtain the parameters $\phi_{m1} = 0.66$, $\phi_{m2} = 0.22$ for Figure 5.8a, and $\phi_{m1} = 0.2$, $\phi_{m2} = 0.14$ for Figure 5.8b. Thus, we find that the mobility parameter of particle 1 is larger than that of particle 2 (note, particle 1 has a smaller particle size than particle 2). Physically, this means that more liquid drains from the smaller particle, consistent with the simple arguments based on the higher capillary pressure on particle one discussed in Chapter 5.2.1. Furthermore, we find that the dimensionless filling rate coefficient a_i for long times (i.e., $t^+ = 100$) is approximately 0.01. This value fits all our data reasonably well for the chosen evolutional time of $t^+ = 100$. Hence, we accept a_i to be a universal constant from now on.

Figure 5.9 shows a test of our model for other combinations of particle size ratios, initial film heights and separation distances. These results reveal that our model is indeed able to describe the filling process well. Also, we can observe from Figure 5.9a that larger initial film heights always lead to a larger bridge volume. From Figure 5.9b we see that smaller particle size ratios always lead to larger dimensionless bridge volumes. This is due to the fact that the reference volume is

smaller (i.e., the effective particle diameter is smaller), and consistent with our simple model for the geometrical bridge volume presented in Chapter 5.3.

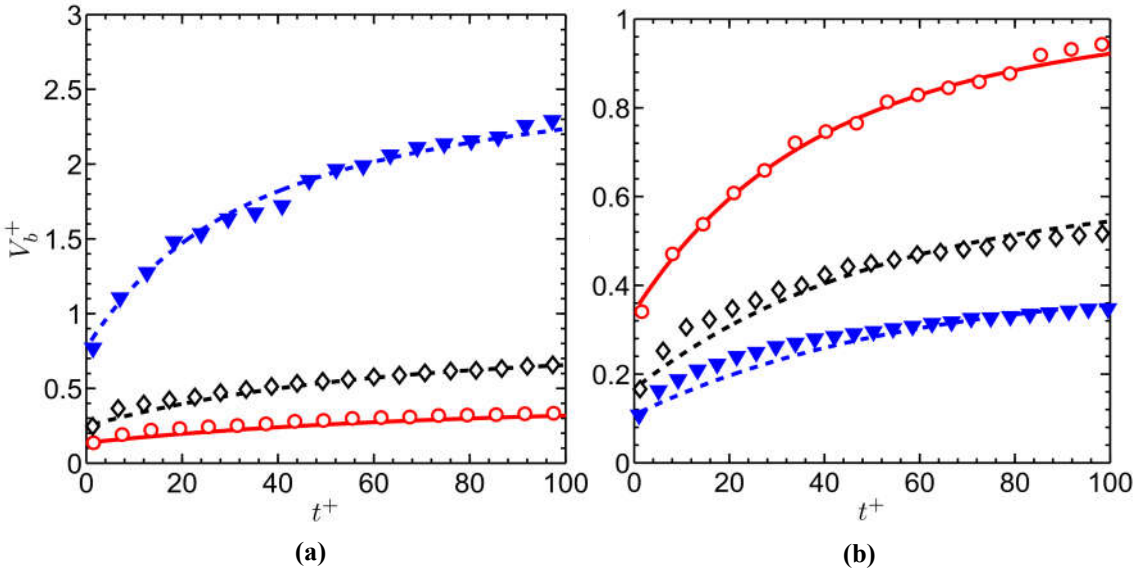

Figure 5.9: Liquid bridge volume over time: fitted model (lines) vs. DNS data (symbols). Panel (a): Red circles: $R_r = 0.5$, $S^+ = 0$, $h_0^+ = 0.04$; Black diamonds: $R_r = 0.6$, $S^+ = 0$, $h_0^+ = 0.06$; Blue triangles: $R_r = 0.55$, $S^+ = 0.005$, $h_0^+ = 0.1$. Panel (b): Red circles: $R_r = 0.45$, $S^+ = 0.018$, $h_0^+ = 0.06$; Black diamonds: $R_r = 0.7$, $S^+ = 0.018$, $h_0^+ = 0.06$; Blue triangles: $R_r = 0.95$, $S^+ = 0.018$, $h_0^+ = 0.06$

Additionally, we can see that the filling process levels off after about 100 dimensionless time units. This time unit is also suggested by the inverse of the constant a_i which has been fixed before. A time of 100 is long enough for most cases, as the filling process is almost completed and in most cases, thin films have already ruptured at this point in time. Therefore, using the current coefficient $a_i = 0.01$ seems more appropriate, compared to the value of 0.025 that we previously reported for the monodisperse cases [28]. One reason for this difference is that in the current contribution we have run the simulations for longer times. Also, it appears that the particle size ratio has a subtle effect on the liquid drainage rate: our model (with $a_i = 0.01$) tends to undepredict the DNS data for increasing R_r (see the data reported in panel b of Figure 5.9), and hence one might want to use the somewhat larger value for a_i for monodisperse systems as suggested in Wu et al. [28].

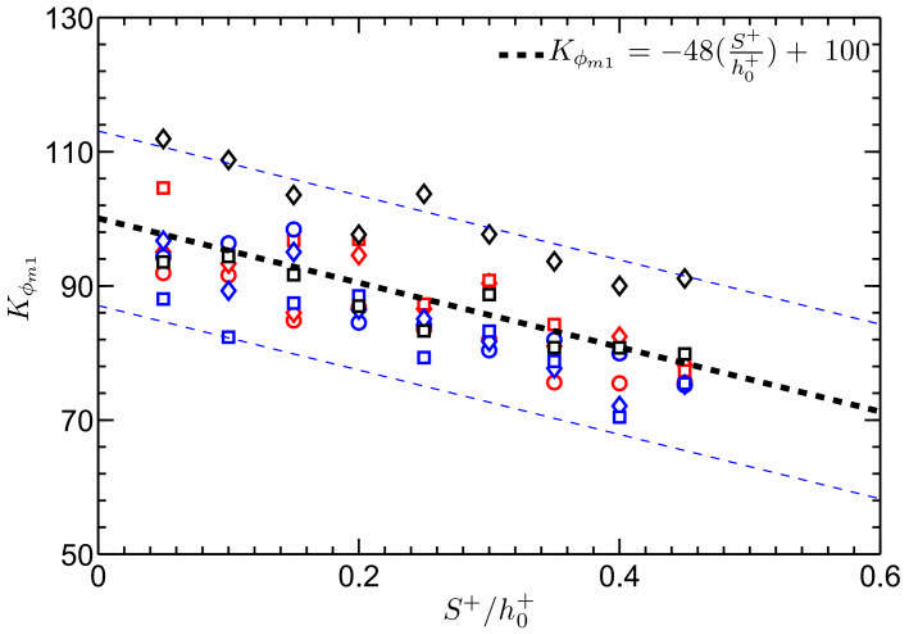

Figure 5.10: $K_{\phi m1}$ as function of separation *S* for different particle ratios. The thin dashed lines indicate an error of +/- 13%. (Red circles: R_r = 0.5 and h_0^+ = 0.04; Red diamonds: R_r = 0.7 and h_0^+ = 0.04; Red squares: R_r = 0.9 and h_0^+ =0.04. Blue circles: R_r = 0.5 and h_0^+ = 0.06; Blue diamonds: R_r = 0.7 and h_0^+ = 0.06; Blue squares: R_r = 0.9 and h_0^+ = 0.06. Black circles: R_r = 0.5 and h_0^+ = 0.1; Black diamonds: R_r = 0.7 and h_0^+ = 0.1; Black squares: R_r = 0.9 and h_0^+ = 0.1)

We now aim to demonstrating that our model is able to represent data for a variety of dimensionless initial film heights, particle size ratios and separation distances. Therefore, we have collected the mobility parameters by fitting the data from a large array of DNS. Also, we now make an attempt to model ϕ_{m1} and ϕ_{m2} separately. Equation 5.18 defines the variable $K_{\phi_{m1}}$ as the ratio of the mobility coefficient of particle 1 (i.e., ϕ_{m1}), the particle size ratio R_r, and the initial (average) film height h_0.

$$K_{\phi_{m1}} = \frac{\phi_{m1}}{R_r^m \left(h_0^+\right)^n} \qquad (5.18)$$

Here, m and n are some exponents of the particle size ratio and the average initial film height, which help to collapse the data into one curve. When picking m = -2 and n = 2, we obtain a model for $K_{\phi_{m1}}$ which is supported by our data shown in Figure 5.10, and which reads:

$$K_{\phi_{m1}} = 100\left(1 - 0.48\frac{S^+}{h_0^+}\right) \qquad (5.19)$$

The error for the model K_{ϕ_1} is about 13%, which can also be seen from Figure 5.10. In summary, and by combining equations 5.18 and 5.19, one can now calculate the mobility coefficient ϕ_{m1} from the particle size ratio R_r, the average film height h_0^+ and the separation distance S^+ as:

$$\phi_{m1} = 100\,R_r^{-2}\left(h_0^+\right)^2\left(1 - 0.48\frac{S^+}{h_0^+}\right) \qquad (5.20)$$

Specifically, in case the particle size ratio R_r equals unity (i.e., we consider a monodisperse particle system), we can simplify equation 5.20 as function of average initial film height and separation distance.

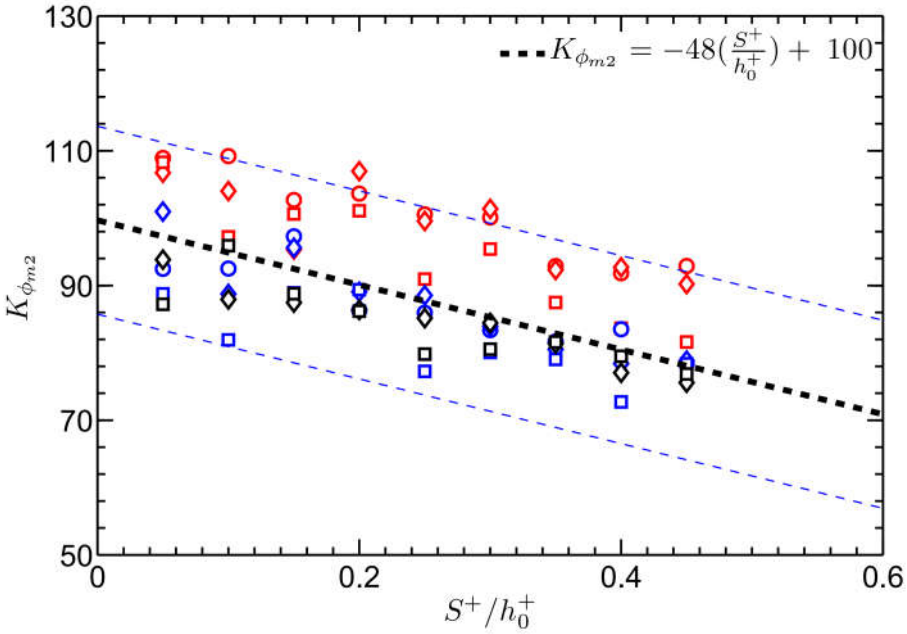

Figure 5.11: $K_{\phi_{m2}}$ as function of separation S for different particle ratios. The thin dashed lines indicate an error of +/- 13%. (Red circles: R_r = 0.5 and h_0^+ = 0.04; Red diamonds: R_r = 0.7 and h_0^+ = 0.04; Red squares: R_r = 0.9 and h_0^+=0.04. Blue circles: R_r = 0.5 and h_0^+ = 0.06; Blue diamonds: R_r = 0.7 and h_0^+ = 0.06; Blue squares: R_r = 0.9 and h_0^+ = 0.06. Black circles: R_r = 0.5 and h_0^+ = 0.1; Black diamonds: R_r = 0.7 and h_0^+ = 0.1; Black squares: R_r = 0.9 and h_0^+ = 0.1)

Similarly, we can define a variable $K_{\phi_{m2}}$ to collapse our data for the mobility coefficient of particle 2:

$$K_{\phi_{m2}} = \frac{\phi_{m2}}{R_r^m \left(h_0^+\right)^n} \qquad (5.21)$$

Here, m and n are again parameters that are used as exponents of the particle ratio and average initial film height to collapse all our data for the mobility coefficient into a single curve. In order to be consistent with the mobility coefficient computed for particle 1 in the limit $R_r = 1$, we must choose $n = 2$. Then, by choosing $m = 0.62$, we collapse all our data for K_{ϕ_2} as shown in Figure 5.11, and propose the following closure relationship for it:

$$K_{\phi_{m2}} = 100\left(1 - 0.48\frac{S^+}{h_0^+}\right) \qquad (5.22)$$

The error for the model K_{ϕ_2} is about 13%, which can also be seen from Figure 5.11. Again, we have ensured consistency for the limit $R_r = 1$ by using the same factors in Eqn. 5.19 and 5.22. In summary, we can calculate the mobility coefficient of particle 2 for a known particle size ratio R_r, an average film height h_0, and a certain separation distance via:

$$\phi_{m2} = 100\, R_r^{0.62} \left(h_0^+\right)^2 \left(1 - 0.48\frac{S^+}{h_0^+}\right) \qquad (5.23)$$

Again, for particle ratio $R_r = 1$, we can simplify the above model and arrive at a closure relationship that is consistent with that of a monodisperse particle system. This indicates that the mobility coefficient of both particles is only function of the average initial film height and the separation distance, same as in our previous work [28]. Note, that we have not added the difficulty to consider different film heights on the particles in the present work. However, such an extension is rather straight forward.

In summary, we presented a model for the liquid mobility that describes liquid transfer from the particle surfaces to the liquid bridge. The model describes all our results for various particle size ratios, average initial film heights and separation distances by appropriate scaling using some exponents to these

parameters. For specific cases, i.e., when R_r equals unity (i.e., a monodisperse system is considered), we find that the present model is slightly different from our previous model reported for monodisperse systems [28]. The reason for the differences is that we currently collect data for longer times (i.e., $t^+ = 100$), which we could not do in our previous study [28].

5.4.3 Film rupture and Driving Pressure

It is interesting to consider the pressure distribution in the film near the film rupturing event. From Figure 5.12 it can be seen that thin film always ruptures at the neck position with the current mesh ($\Delta h = 0.1$) for a sufficiently long times. Additionally, we can see in Figure 5.12 that thin films always rupture on the surface of the smaller particle (i.e., particle 1) for all cases. The reason is that the pressure difference between particle 1 and the bridge region is always larger than the one between particle 2 and the bridge region. Clearly, this is due the smaller radius of particle 1 that causes a higher curvature and pressure in the corresponding film: by using Young-Laplace equation, the pressure on particle 1 can be approximated as $P_1 = 2\sigma / R_1$, while $P_2 = 2\sigma / R_2$, and $R_2 > R_1$, resulting in $P_1 > P_2$. We can also confirm these findings in the pressure plots shown in Figure 5.12. Unfortunately, we could not precisely predict the processes after film rupture, since we did not employ a sound model for the contact line motion (i.e., we currently only consider a fixed contact angle). Although we speculate that these processes are still predicted qualitatively correct, this fact does not allow us to establish a model after the film rupturing event. Since our model currently is only based on data before the film ruptures, and data post film rupture is discarded, this appears to be unproblematic.

5.5 Discussion

In this study, we focus on liquid transport between two unequally-sized spherical particles based on key parameters (i.e., particle radius, initial film height and separation distance). We also provide a model for the prediction of dynamic

liquid-bridge formation between particles of different sizes, by assuming a quasi-static flow situation which is based on the assumption that particle relative motion does not affect the liquid bridge formation. As demonstrated in our previous work [28], one can perform a time scale analysis to obtain a quantitative understanding of situations in which such a quasi-static assumption is appropriate. In the following we consider a sedimenting bi-disperse particle population, and summarize the most important findings of such a time scale analysis.

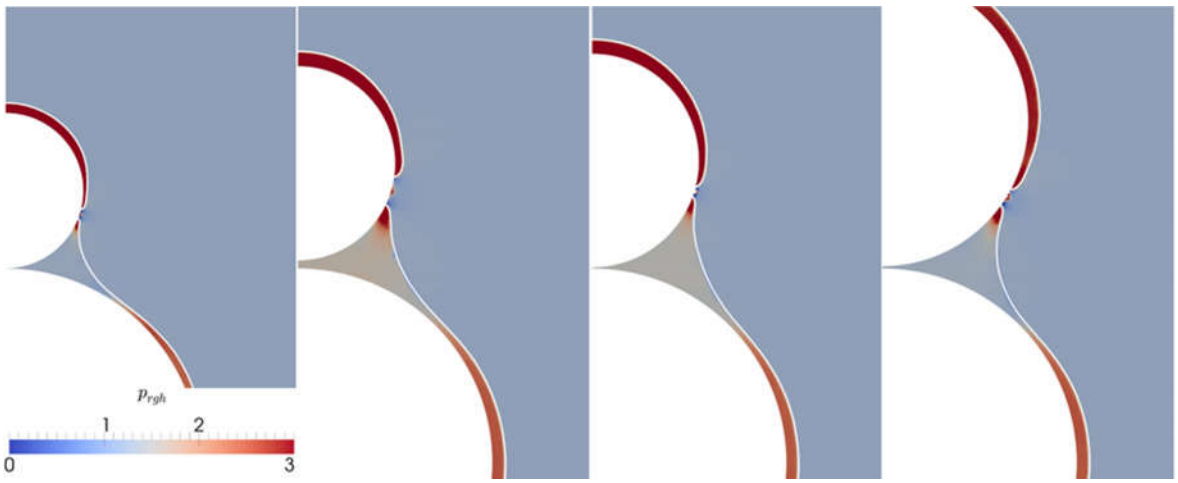

Figure 5.12: Pressure distribution of film rupture for different particle ratios, separation and film heights. Panel (a): $R_r = 0.4$, $S^+ = 0$, $h_0^+ = 0.04$; panel (b): $R_r = 0.5$, $S^+ = 0.021$, $h_0^+ = 0.06$; panel (c): $R_r = 0.55$, $S^+ = 0.003$, $h_0^+ = 0.06$; panel (d): $R_r = 0.75$, $S^+ = 0.006$, $h_0^+ = 0.06$.

Compared with the larger particle (i.e., particle 2), the smaller particle (i.e., particle 1) will accelerate more rapidly because of its lower particle volume. Thus, we use the effective scales associated with particle 1 to characterize the system. When considering the acceleration of particle 1 due to surface tension forces, it is obvious that the characteristic time scale (denoted as t_{acc}) for the particles to accelerate to a typical speed of liquid flow (i.e., $u_{ref} = \sigma / \mu_l$) must be larger than the time scale for liquid bridge formation to justify the quasi-static assumption for bridge filling. Also, the time for the particle to cross the film (denoted as t_{cross}) must be larger than the time scale for liquid bridge formation. t_{acc} can be calculated from a force balance on a particle by assuming that the liquid bridge only exhibits a cohesive force due to surface tension, and that the particle accelerates to u_{ref}.

The corresponding dimensionless acceleration time scale (with $t_{ref} = R_{eff}\mu_l/\sigma$ being the reference time scale) is $t_{acc}^{+} = R_1^2\rho_p\sigma/\left(R_{eff}\mu_l^2\right) = R_1\rho_p\sigma\left(R_r+1\right)/\left(2\mu_l^2\right)$, where $R_{eff} = 2R_1/\left(R_r+1\right)$ and $R_r = R_1/R_2$. The time for a particle to cross the film can be calculated from a typical particle-particle relative velocity u_{rel} and the film thickness, i.e., $t_{cross} = h_0/u_{rel}$. The corresponding dimensionless crossing time scale (with the Stokes setting velocity as relative velocity) is $t_{cross}^{+} = 9h_0\mu_g\sigma/\left[2R_1^2R_{eff}\mu_l\left(\rho_p-\rho_g\right)g\right] = 9h_0^{+}\mu_g\sigma\left(R_r+1\right)/\left[4R_1^2R_r\mu_l\left(\rho_p-\rho_g\right)g\right]$, where h_0^{+} is the average dimensionless film-thickness (with R_2 being the reference length), μ_g is the ambient gas viscosity, and ρ_p is the particle density.

Mixture	μ [Pa·s]	ρ [kg·m-3]	σ [N/m]
Water	$1 \cdot 10^{-3}$	1000	0.073
Glycerine/water-60/40%	0.0115	1153	0.0673
Glycerine/water-79/21%	0.05	1204	0.0647
Glycerine/water-90/10%	0.22	1238	0.0634
Pure glycerine	1.12	1262	0.0631

Table 5.2: Properties of different water-glycerine mixtures.

In summary, the assumption of no-moving particles in our simulations requires that both dimensionless time scales are much larger than unity. Following our previous work [28], and using typical properties of various water-glycerine mixtures summarized in Table 5.2 [39], we have summarized these key dimensionless parameters in Table 5.3. While situations with highly viscous fluids (i.e., pure glycerine) appear to conflict with our quasi-static assumption, Table 5.3 highlights that for most systems involving liquids with a water-like viscosity our quasi-static assumption is valid. This is in line with previous findings in mono-disperse systems [28].

Glycerine/water	R_1 [m]	R_r	$\rho_p[kg \cdot m^{-3}]$	h_0^+	t_{ref} [s]	t_{acc}^+	t_{cross}^+	Oh
water	5e-6	0.5	1000	0.01	9.15e-8	273	363	0.045
Glycerine/water-60/40%	5e-6	0.5	1000	0.01	1.14e-6	1.91	29.2	0.51
Glycerine/water-79/21%	5e-6	0.5	1000	0.01	5.15e-6	0.097	6.45	2.38
Glycerine/water-90/10%	5e-6	0.5	1000	0.01	2.31e-5	4.91e-3	1.44	9.62
Pure glycerine	5e-6	0.5	1000	0.01	1.18e-5	1.89e-4	0.28	48.6
Water	1e-5	0.7	2000	0.04	1.61e-7	1240	147	0.034
Glycerine/water-60/40%	1e-5	0.7	2000	0.04	2.01e-6	8.65	11.8	0.38
Glycerine/water-79/21%	1e-5	0.7	2000	0.04	9.09e-6	0.44	2.61	1.79
Glycerine/water-90/10%	1e-5	0.7	2000	0.04	4.08e-5	0.022	0.58	7.24
Pure glycerine	1e-5	0.7	2000	0.04	2.09e-4	8.55e-4	0.11	36.7
Water	1e-5	0.9	5000	0.1	1.44e-7	3450	128	0.036
Glycerine/water-60/40%	1e-5	0.9	5000	0.1	1.80e-6	24.2	10.3	0.4
Glycerine/water-79/21%	1e-5	0.9	5000	0.1	8.13e-6	1.23	2.27	1.75
Glycerine/water-90/10%	1e-5	0.9	5000	0.1	3.65e-5	0.062	0.51	7.65
Pure glycerine	1e-5	0.9	5000	0.1	1.87e-4	2.39e-3	0.1	38.7

Table 5.3: Summary of parameters relevant for liquid transfer in typical polydisperse particle beds

The typical relative velocity at impact plays an important role in our analysis of the time scale for film crossing. Similar to what we have done in our previous work [28], we now consider systems of different particle sizes. The bi-disperse suspension is allowed to freely sediment (under the action of gravity), and the speed and orientation of particle-particle collisions is recorded. The simulations were based on the approach used by Radl and Sundaresan [40] (a dimensionless grid resolution of $\Delta x / d_p = 3$ was used, where d_p is the diameter of the larger particles), with identical fluid, but different particle properties. The soft-particle

Euler-Lagrange model available in the code CFDEM® [41] has been used, and statistics were collected over a sufficiently long time, i.e., 40 times of the particle relaxation time ($t_{relax} = u_t / g$). A list of simulation parameters and conditions is provided in Table 5.4, and results are summarized in Figure 5.13. We find that the typical impact speed is in the order of 10% of the particles' terminal settling velocity, and that particle collisions are primarily oblique (i.e., the particles' relative speed in the tangential direction is greater than that in the normal direction). Again, this data supports our assumption of quasi-static bridge filling for a wide range of wet bi-and polydisperse particulate system with rather thick liquid films and a rather low liquid viscosity.

Parameter	Value
Domain size – x (m)	$53 \cdot d_p$
Domain size – y (m)	$53 \cdot d_p$
Domain size – z (m)	$213 \cdot d_p$
Boundary conditions	Fully periodic
Gravitational acceleration: g (m/s^2)	9.81
The larger particle diameter of the system: d_p (m)	$1.50 \cdot 10^{-4}$
Particle density: ρ_p (kg/m^3)	1,500
Gas density: ρ_g (kg/m^3)	1.3
Gas viscosity: μ_g (Pa·s)	$1.8 \cdot 10^{-5}$

Table 5.4: System parameters and boundary conditions used in the simulations of a freely sedimenting bi-disperse particle suspension.

One could argue that the relative speed of particles in a wet collision event is depending on the process. We have only considered a fluidized bed without cohesive particle-particle interactions in our present contribution. It is clear that the appropriateness of our model for a specific application (which might involve cohesive force, or much different collision dynamics) should be tested prior to its usage. We have decided to postpone such a study to future work, since a large

array of simulation would have to be performed for bi- and polydisperse suspensions in order to draw general conclusions.

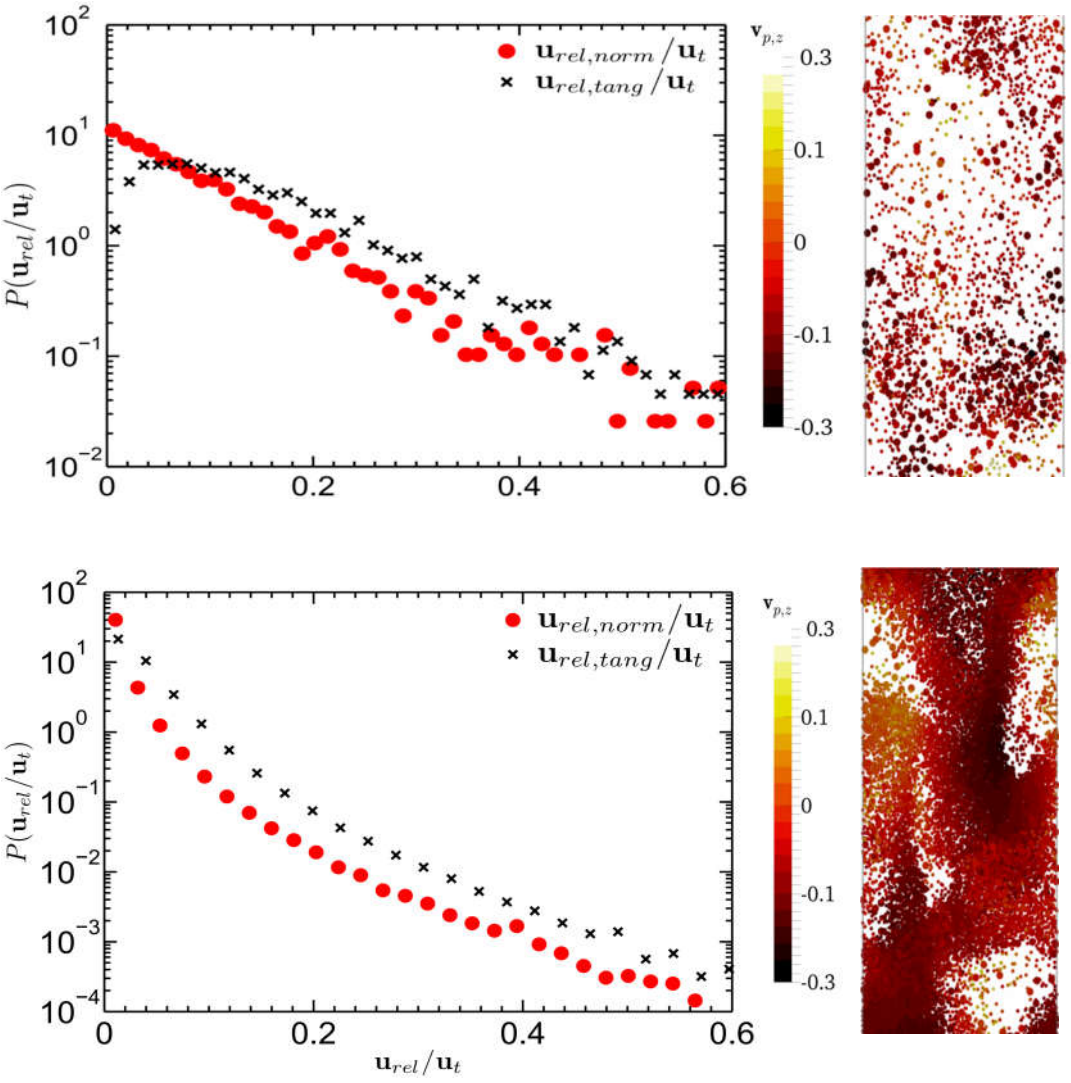

Figure 5.13: Distribution of polydisperse particle collision velocities in the normal and tangential direction, as well as illustration of the vertical velocity distribution (bottom panel: R_r = 0.5, ϕ_p = 0.3) and dense (top panel; R_r = 0.5, ϕ_p = 0.05) cloud of freely sedimenting particles (the inserts illustrate individual-particle velocities in the vertical direction).

5.6 Conclusions

A liquid transport model between wet particles of different size has been presented in this paper. This model is an extension of our previous work [28]. The model is based on DNS data which were obtained by extracting the interface position, defining the characteristic neck position, and integrating the interface

position to quantify the liquid bridge filling process. This model allows us to predict the dynamically evolving liquid bridge volume, and the liquid remaining on the particle surfaces in polydisperse particle systems. Our more precise prediction of the bridge volume is essential for improved predictions of the liquid bridge rupture energy: a comparison of these differences when using the liquid bridge volume model of Shi and McCarthy [42] and our newly developed model reveals large differences for the rupture energy (see Appendix D). Thus, we expect that our dynamic model for the liquid bridge volume is especially important for dilute systems where energy dissipation during collisions is of critical importance.

Our model differentiates between (i) a fast initial bridge formation stage where the dimensionless time is less than a reference time for capillary-driven viscous flow, and (ii) a subsequent slower viscous filling stage where viscous effects are dominant. The initial stage model is based on DNS data at a dimensionless time of $t^+ = 1$. Our initial stage model can be used as a first estimate for the liquid bridge volume in short particle collisions, and is an extension of the model prosed by Shi and McCarthy [42]. The postulated model for the viscous filling stage model is an extension of our previous work [28], however now is also fit for systems involving unequally-sized particles. Our present model relies on a universal parameter a_i (i.e., a characteristic dimensionless filling time), as well as dimensionless liquid mobility parameters ϕ_{m1} and ϕ_{m2} of the contacting particles. A model equation for these mobility parameters has been proposed. Specifically, we consider that the mobilities are functions of the particle size ratio, the film height and the separation distance. In summary, our model is valid for liquid bridge formation between two unequally-sized particles coated with thin continuous films (i.e., an initial relative film height of less than 10% of the particle radius).

Our previous study indicated that grid refinement plays an important role in the final stages of film flow where the film ruptures. In order to get a precise model for the filling process at long times, as well as to correctly predict film rupture, it is

essential to use a fine enough computational mesh in future simulations. This clearly limited the current study to axisymmetric configurations. Consequently, considering non-continuous films, e.g., discrete droplets present on the particles' surface, remains a task for future studies. However, we hope that our study is a significant step forward to better understand the equilibration of liquid residing on the surface of particles with that present in a liquid bridge.

5.7 Appendices

Appendix D – The Effect of the Liquid Bridge Volume Model on Capillary Forces

The liquid bridge volume is an input parameter in almost the totality of models for calculating the capillary and viscous force between two wet particles. Thus, different models for liquid bridge volume will lead to different characteristics of the resulting cohesive force. Therefore, in this appendix, we attempt to quantify this difference by using our newly developed model. Specifically, we compute and compare the capillary force by using three different liquid bridge models: (1) the constant bridge model of Shi and McCarthy [42]; (2) the early bridge volume model presented in this paper; (3) and the bridge volume from our dynamic filling model considering the limit of infinitely long times.

In order to make a comparison, we pick the parameters of the particle system as follows:

- Initial film heights of $h_0^+ = 0.01$ (i.e., a thin film), and $h_0^+ = 0.1$ (i.e., thick film) are considered
- Particle ratio of $R_r = 0.5$
- Surface tension equal to 0.07 $N \cdot m^{-1}$

The constant liquid bridge volume is provided by the model of Shi and McCarthy [42]

$$V_b = \frac{L_{p1}}{2}\left(1-\sqrt{1-\frac{R_2^2}{\left(R_1+R_2\right)^2}}\right)+\frac{L_{p2}}{2}\left(1-\sqrt{1-\frac{R_1^2}{\left(R_1+R_2\right)^2}}\right) \qquad (D.1)$$

Where L_{p1} and L_{p2} are the initial liquid contents on particle 1 and particle 2, respectively. The total liquid bridge is composed of liquid from both contacting particles.

The early stage of liquid bridge is modelled by equation 5.12. To make the comparison easier, we use a case of zero separation to compute the initial bridge volume. We then simply calculate the initial bridge to be:

$$V_{b,0}^{+} = 50.8 R_r^{-1.25} \left(h_0^{+}\right)^{2.15}. \qquad (D.2)$$

The maximum liquid bridge volume can be obtained by setting the filling time to $t^{+} = \infty$, consequently the expressions of liquid bridge model in the Appendix A of our previous work [28] can be rewritten as:

$$V_b^{+} = V_{b,0}^{+} - C_1 \frac{\frac{2r_1}{a_i} + 2\phi_{m1}}{r_1} - C_2 \frac{\frac{2r_2}{a_i} + 2\phi_{m1}}{r_2} \qquad (D.3)$$

$$r_1 = \frac{-a_i\left(\phi_{m1} + \phi_{m2} + 1 + \sqrt{\left(\phi_{m1} - \phi_{m2}\right)^2 + 1}\right)}{2} \qquad (D.4)$$

$$r_2 = \frac{-a_i\left(\phi_{m1} + \phi_{m2} + 1 - \sqrt{\left(\phi_{m1} - \phi_{m2}\right)^2 + 1}\right)}{2} \qquad (D.5)$$

$$\begin{aligned} C_1 = {} & \frac{-a_i^2\phi_{m2}L_{p2,0}^{+} - \left(2a_i r_2\phi_{m1} + 2a_i^2\phi_{m1}^2 + a^2\phi_{m1}\right)L_{p1,0}^{+}}{2\left(r_2 - r_1\right)} \\ & + \frac{\left(a_i^2\phi_{m1} + a_i^2 + a_i r_2\right)V_{b,0}^{+}}{2\left(r_2 - r_1\right)} \end{aligned} \qquad (D.6)$$

$$C_2 = \frac{a_i^2\phi_{m2}L_{p2,0}^{+} + \left(2a_i r_1\phi_{m1} + a_i^2\phi_{m1} + 2a_i^2\phi_{m1}^2\right)L_{p1,0}^{+} - \left(a_i r + a_i^2\phi_{m1} + a_i^2\right)V_{b,0}^{+}}{2\left(r_2 - r_1\right)} \qquad (D.7)$$

Where $V_{b,0}^{+}$ is the initial bridge volume, $L_{p1,0}^{+}$ and $L_{p2,0}^{+}$ is the initial liquid content on the particle surfaces, and ϕ_{m1} and ϕ_{m2} can be calculated by using equations 5.20 and 5.23.

We employ the force model provided by Mikami et at. [20] to calculate the capillary force due to liquid bridge.

$$
\begin{aligned}
F_{cap} &= \pi R_2 \sigma \left(e^{AS^+ + B} + C \right) \\
A &= -1.1 \left(V_b^+ \right)^{-0.53} \\
B &= \left(-0.34 \ln \left(V_b^+ \right) - 0.96 \right) \theta^2 - 0.019 \left(V_b^+ \right) + 0.48 \\
C &= 0.0042 \ln \left(V_b^+ \right) + 0.078
\end{aligned}
\qquad (D.8)
$$

Here S^+ is the surface to surface distance normalized by R_2 (R_2 is the size of the bigger particle, and θ is the contact angle which is assumed to be zero for our fully wet particle system). When a liquid bridge between particles reached a critical distance, the bridge ruptures and liquid is redistributed. This rupture distance is given by Lian et al. [22], and reads:

$$h_{rup} = \left(1 + 0.5\theta\right) \left(V_b^+ \right)^{1/3} \qquad (D.9)$$

The liquid bridge force is present as long as the bridge exists, and it vanishes when the liquid bridge ruptures at the critical rupture distance. The bridge forces are normalized by the capillary force scale $2\pi\sigma R_2$, and the rupture distance is scaled by R_2. The resulting capillary bridge force plots are shown in Figure D1.

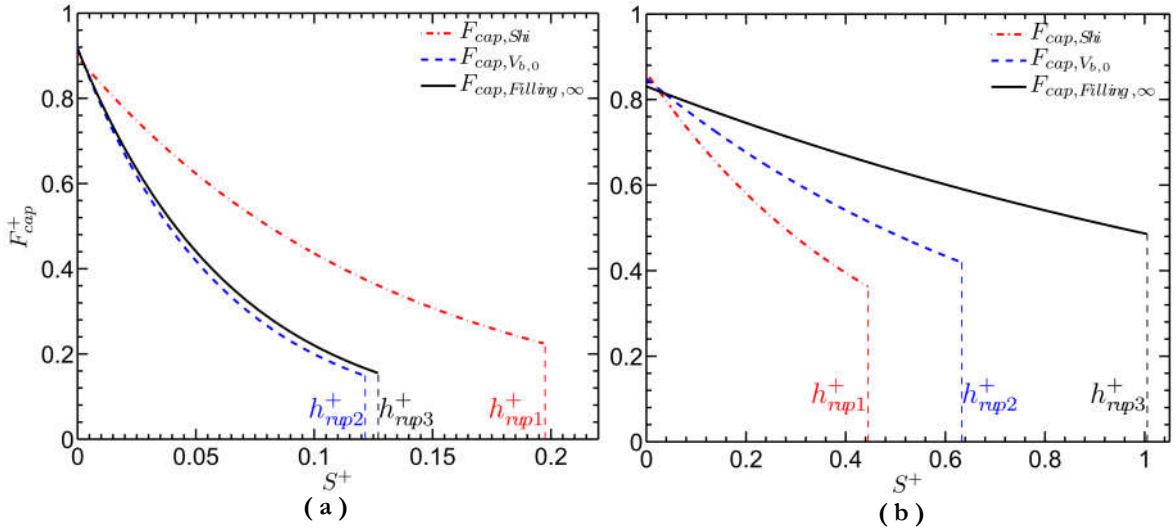

Figure D 1. The capillary bridge force versus the separation distance and critical rupture distance h_{rup}. h_{rup1} is the rupture distance based on the constant bridge model of Shi and McCarthy, h_{rup2} is the rupture distance based on our early stage bridge model, and h_{rup3} is the rupture distance based on the dynamic bridge model when the filing time t^+ is infinitely large . Panel (a) shows data with an initial film height of $h_0^+ = 0.01$; for panel (b) $h_0^+ = 0.1$

Figure D1 shows that the bridge forces are indeed affected by the liquid bridge volume model. Panel (a) indicates that there is not much difference between the bridge forces of our early stage bridge model and the dynamic filing model when particles are initialized with very small film heights. However, the model of Shi and McCarthy overpredicts the capillary bridge force when compared to our models. Panel (b) shows that the filling of the liquid bridge volume indeed affects the bridge force. The rupture distance in case the particles are initialized with a larger film height (i.e., $h_0^+ = 0.1$) differs for the different liquid bridge volume models: the dynamic bridge model predicts the biggest bridge force, as well as larger rupture distance.

5.8 Nomenclature

Latin Symbols

a_i ..... Dimensionless filling rate parameter [-]

d_p ..... Particle diameter of the larger particle [m]

g ..... Gravity [m/s^2]

h_0 ..... Average initial film height of the particle pair [m]

h_i ..... Initial film height of particle i [m]

$L_{p,0}$ ..... Reference volume of liquid on the particle [m^3]

$L_{p,i}$ ..... Volume of liquid present on the particle i [m^3]

m ..... Mass of the particle [kg]

$\mathbf{n}_{ij}$ ..... Unit normal vector [-]

Oh ..... Ohnesorge number [-]

p ..... Pressure [Pa]

p_{ref} ..... Reference pressure [Pa]

p_s ..... Pressure at the particle surfaces [Pa]

p_{V_b} ..... Pressure at the liquid bridge [Pa]

R_1 ..... Particle radius of the smaller particle (particle 1)[m]

R_2 ..... Particle radius of the larger particle (particle 2)[m]

R_{cyl} ..... Radius of the initial cylinder region [m]

R_{curve} ..... Radius of curvature of the liquid bridge surface [m]

Re ..... Reynolds number [-]

S ..... Half separation distance between particles [m]

t .....Time [s]

t_{acc} .....Acceleration time scale [s]

t_{cross} .....Film crossing time scale [s]

t_{relax} .....Particle relation time [s]

t_{ref} .....Reference time scale [s]

u_{ref} .....Reference fluid velocity [m·s]

u_{rel} .....Relative particle-particle velocity [m/s]

U .....Fluid velocity [m/s]

V_b .....Liquid bridge volume [m^3]

$V_{b,0}$ .....Initial bridge volume [m^3]

$V_{b,g}$ .....Geometrical bridge volume [m^3]

DIM.....Direct integration method

DNS.....Direct Numerical Simulation

DEM.....Discrete element method

YLE.....Young-Laplace equation

Greek Symbols

α .....Phase fraction indicator [-]

$\beta_{\mathrm{cyl,i}}$ .....Initial filling angle on particle i that cause by geometry bride [rad]

Δt .....Time step [s]

Δx .....Grid spacing [m]

Δh .....Dimensionless grid spacing by initial film height [-]

ϕ_p .....Particle volume fraction [-]

ϕ_{mi} ..... Fraction of liquid on particle i that is mobile to flow into the bridge [-]

μ_l ..... Dynamic viscosity of liquid [kg · m^{-1} · s^{-1}]

μ_g ..... Dynamic viscosity of ambient gas [kg · m^{-1} · s^{-1}]

ρ_l ..... Density of the liquid [kg · m^{-3}]

ρ_g ..... Density of the ambient gas [kg · m^{-3}]

ρ_p ..... Density of the particles [kg · m^{-3}]

σ ..... Surface tension [kg · s^{-2}]

Superscripts

+ ..... Dimensionless quantity

i ..... Particle index

norm ..... Normal direction

tang ..... Tangential direction

t ..... Terminal

w ..... Water

gly ..... Glycerine

p ..... Particle

ref ..... Reference quantity

5.9 References

[1] C.K. Gupta, D. Sathiyamoorthy, Fluid Bed Technology in Materials Processing, CRC Press, 1998.

[2] D. Kunii, O. Levenspiel, Fluidization Engineering, Butterworth-Heinemann, 1991.

[3] H. Xu, W. Zhong, A. Yu, Z. Yuan, Spouting Characteristics of Wet Particles in a Conical-Cylindrical Spouted Bed, Ind. Eng. Chem. Res. 54 (2015) 9894–9902. doi:10.1021/acs.iecr.5b02742.

[4] M.G. Rasul, V. Rudolph, M. Carsky, Segregation potential in binary gas fluidized beds, Powder Technol. 103 (1999) 175–181. doi:10.1016/S0032-5910(98)00230-7.

[5] M. Wormsbecker, A. Adams, T. Pugsley, C. Winters, Segregation by size difference in a conical fluidized bed of pharmaceutical granulate, Powder Technol. 153 (2005) 72–80. doi:10.1016/j.powtec.2005.02.006.

[6] R. Fan, R.O. Fox, Segregation in polydisperse fluidized beds: Validation of a multi-fluid model, Chem. Eng. Sci. 63 (2008) 272–285. doi:10.1016/j.ces.2007.09.038.

[7] S.Y. Wu, J. Baeyens, Segregation by size difference in gas fluidized beds, Powder Technol. 98 (1998) 139–150. doi:10.1016/S0032-5910(98)00026-6.

[8] G. Sun, J.R. Grace, The effect of particle size distribution on the performance of a catalytic fluidized bed reactor, Chem. Eng. Sci. 45 (1990) 2187–2194. doi:10.1016/0009-2509(90)80094-U.

[9] H. Hatzantonis, C. Kiparissides, The effect of the mean particle size on the dynamic behaviour of catalyzed olefin polymerization fluidized bed reactors, Comput. Chem. Eng. 22 (1998) S127–S134. doi:10.1016/S0098-1354(98)00046-5.

[10] V. Wilk, H. Hofbauer, Influence of fuel particle size on gasification in a dual

fluidized bed steam gasifier, Fuel Process. Technol. 115 (2013) 139–151. doi:10.1016/j.fuproc.2013.04.013.

[11] J. Werther, Scale-up modeling for fluidized bed reactors, Chem. Eng. Sci. 47 (1992) 2457–2462. doi:10.1016/0009-2509(92)87076-3.

[12] C.M. Donahue, C.M. Hrenya, R.H. Davis, Stokes's cradle: Newton's cradle with liquid coating, Phys. Rev. Lett. 105 (2010) 34501. doi:10.1103/PhysRevLett.105.034501.

[13] S. Herminghaus, Dynamics of wet granular matter, Adv. Phys. 54 (2005) 221–261. doi:10.1080/00018730500167855.

[14] C. Voivret, F. Radjaï, J.Y. Delenne, M.S. El Youssoufi, Multiscale force networks in highly polydisperse granular media, Phys. Rev. Lett. 102 (2009). doi:10.1103/PhysRevLett.102.178001.

[15] J.K. Mitchell, K. Soga, Soil Composition and Engineering Properties, in: Fundam. Soil Behav., 2005: pp. 83–108.

[16] F. Radjai, V. Richefeu, Bond anisotropy and cohesion of wet granular materials., Philos. Trans. A. Math. Phys. Eng. Sci. 367 (2009) 5123–5138. doi:10.1098/rsta.2009.0185.

[17] G. Toschkoff, J.G. Khinast, Mathematical modeling of the coating process., Int. J. Pharm. 457 (2013) 407–22. doi:10.1016/j.ijpharm.2013.08.022.

[18] K. Hotta, K. Iinoya, The capillary binding force of a liquid bridge, Powder Technol. 12 (1975) 195. doi:10.1016/0032-5910(75)80014-3.

[19] H. Xu, W. Zhong, Z. Yuan, A. Yu, CFD-DEM study on cohesive particles in a spouted bed, Powder Technol. (2016). doi:10.1016/j.powtec.2016.09.006.

[20] T. Mikami, H. Kamiya, M. Horio, Numerical simulation of cohesive powder behavior in a fluidized bed, Chem. Eng. Sci. 53 (1998) 1927–1940. doi:10.1016/S0009-2509(97)00325-4.

[21] P. Pierrat, H.S. Caram, Tensile strength of wet granular materials, Powder

Technol. 91 (1997) 83–93. doi:10.1016/S0032-5910(96)03179-8.

[22] G. Lian, C. Thornton, M.J. Adams, A Theoretical Study of the Liquid Bridge Forces between Two Rigid Spherical Bodies, J. Colloid Interface Sci. 161 (1993) 138–147. doi:http://dx.doi.org/10.1006/jcis.1993.1452.

[23] M. Urso, C. Lawrence, M. Adams, Pendular, Funicular, and Capillary Bridges: Results for Two Dimensions., J. Colloid Interface Sci. 220 (1999) 42–56. doi:10.1006/jcis.1999.6512.

[24] C.D. Willett, M.J. Adams, S.A. Johnson, J.P.K. Seville, Capillary bridges between two spherical bodies, Langmuir. 16 (2000) 9396–9405. doi:10.1021/la000657y.

[25] M.A. Erle, D.C. Dyson, N.R. Morrow, Liquid bridges between cylinders, in a torus, and between spheres, AIChE J. 17 (1971) 115–121. doi:10.1002/aic.690170125.

[26] Y.I. Rabinovich, M.S. Esayanur, B.M. Moudgil, Capillary forces between two spheres with a fixed volume liquid bridge: Theory and experiment, Langmuir. 21 (2005) 10992–10997. doi:10.1021/la0517639.

[27] J. Sprakel, N.A.M. Besseling, M.A. Cohen Stuart, F.A.M. Leermakers, Capillary adhesion in the limit of saturation: Thermodynamics, self-consistent field modeling and experiment, Langmuir. 24 (2008) 1308–1317. doi:10.1021/la702222f.

[28] M. Wu, S. Radl, J.G. Khinast, A model to predict liquid bridge formation between wet particles based on direct numerical simulations, AIChE J. 62 (2016) 1877–1897. doi:10.1002/aic.15184.

[29] F.M. Orr, L.E. Scriven, A.P. Rivas, Pendular rings between solids: meniscus properties and capillary force, J. Fluid Mech. 67 (1975) 723. doi:10.1017/S0022112075000572.

[30] F. Soulié, F. Cherblanc, M.S. El Youssoufi, C. Saix, Influence of liquid

bridges on the mechanical behaviour of polydisperse granular materials, Int. J. Numer. Anal. Methods Geomech. 30 (2006) 213–228. doi:10.1002/nag.476.

[31] V. Richefeu, M.S. El Youssoufi, R. Peyroux, F. Radjaï, A model of capillary cohesion for numerical simulations of 3D polydisperse granular media, Int. J. Numer. Anal. Methods Geomech. 32 (2008) 1365–1383. doi:10.1002/nag.674.

[32] Y. Chen, Y. Zhao, H. Gao, J. Zheng, Liquid bridge force between two unequal-sized spheres or a sphere and a plane, Particuology. 9 (2011) 374–380. doi:10.1016/j.partic.2010.11.006.

[33] O. Harireche, A. Faramarzi, A.M. Alani, A toroidal approximation of capillary forces in polydisperse granular assemblies, Granul. Matter. 15 (2013) 573–581. doi:10.1007/s10035-013-0425-9.

[34] V.P. Mehrotra, K.V.S. Sastry, Pendular Bond Strength Between Unequal-Sized Spherical Particles, Powder Technol. 25 (1980) 203–214.

[35] S.J.R. Simons, J.P.K. Seville, M.J. Adams, An analysis of the rupture energy of pendular liquid bridges, Chem. Eng. Sci. 49 (1994) 2331–2339. doi:10.1016/0009-2509(94)E0050-Z.

[36] L.A. Easo, R. Kumar, R. Ren, R. Carl, Numerical Study of the Formation of a Liquid Bridge Between Two Spheres with Uniform Film Thickness, in: 2014 AIChE Annu. Meet. Novemb. 18, Atlanta, 2014.

[37] Wu, M and Khinast, J G and S, Radl, Towards A Refined Model for Liquid Bridge Volume Between Wet Particles, in: 11th. World Congr. Comput. Mech. (WCCM XI), Barcelona, Spain, 2014.

[38] S.S. Deshpande, L. Anumolu, M.F. Trujillo, Evaluating the performance of the two-phase flow solver interFoam, Comput. Sci. Discov. 5 (2012) 14016. doi:10.1088/1749-4699/5/1/014016.

[39] a. Eddi, K.G. Winkels, J.H. Snoeijer, Short time dynamics of viscous drop spreading, Phys. Fluids. 25 (2013) 13102. doi:10.1063/1.4788693.

[40] S. Radl, S. Sundaresan, A drag model for filtered Euler-Lagrange simulations of clustered gas-particle suspensions, Chem. Eng. Sci. 117 (2014) 416–425. doi:10.1016/j.ces.2014.07.011.

[41] C. Kloss, C. Goniva, A. Hager, S. Amberger, S. Pirker, Models , algorithms and validation for opensource DEM and CFD-DEM, Prog. Comput. Fluid Dyn. 12 (2012) 140–152. doi:10.1504/PCFD.2012.047457.

[42] D. Shi, J.J. McCarthy, Numerical simulation of liquid transfer between particles, Powder Technol. 184 (2008) 64–75. doi:10.1016/j.powtec.2007.08.011.

"It does not matter how slowly you go, so long as you do not stop"

(Confucius, 551 BC - 479 BC)

6

The Effects of Liquid Bridge Model Details on the Dynamics of Wet Fluidized Beds [*]

We simulate wet fluidized beds of particles in small periodic domains using the CFD-DEM approach. A liquid bridge is formed upon particle-particle collisions, which then ruptures when the particle separation exceeds a critical distance. The simulations take into account both surface tension and viscous forces due to the liquid bridge. We perform a series of simulations based on different liquid bridge formation models: (i) the static bridge model of Shi and McCarthy [1], (ii) a simple static version of the mode of Wu et al. [2], as well as (iii) the full dynamic bridge model of Wu et al. [2]. We systematically compare the differences caused by different liquid bridge formation models, as well as their sensitivity to system parameters. Finally, we provide recommendations for which systems a dynamic liquid bridge model must be used, and for which application this appears to be less important.

I. [*] This chapter is based on: M. Wu, J.G. Khinast, S. Radl. The effects of Liquid Bridge Model on the Dynamics of Wet Fluidized beds. AIChE Journal 2017, revised manuscript in preparation.

6.1 Introduction

Wet fluidized beds of particles, and wet granular flow in general, are of great importance in wide range of industrial processes, e.g., in food industries, the energy sector and pharmaceutical industries [3]. Unfortunately, the flow of wet particles is difficult to predict, making it challenging to design or optimize these processes. For example, capillary and viscous forces acting between two particles are affected by a range of parameters (e.g., the liquid viscosity, or the particles' surface roughness), making it challenging to fully describe a wet fluidized bed particle system with a mathematical model. Most important, these cohesive forces not only affect particle flows[4], but also play an important role in the formation of agglomerates, hence they directly affect product properties [5]. Therefore, the proper control of these cohesive forces in particulate system is key to successfully perform many fluidized bed process such as coking, agglomeration, coating or wet powder handing[6–9]. Also, a sound understanding of the transport mechanisms in these wet gas-particle system will aid on improving design and scale-up of these systems. For example, often a certain fluidization velocity is adjusted to avoid segregation or agglomeration [8] necessitating a quantitative understanding of how much liquid content is acceptable for successful operation. It is exactly this question that motivates our present study.

Specifically, in what follows we focus on applications in the pharma and food sector, e.g., pharmaceutical fluidized bed dryers [8,10], wet spouted beds,[11] as well as fluid cokers [12] in which liquid injection plays a crucial role. For these systems a particle-based modeling must be adopted in case one aims on a fully predictive flow model. This is since continuum- or parcel-based models [13–18] lack an appropriate rheological model at present. We next briefly review recent progress in the field of particle-based modeling approaches to provide the necessary background.

6.1.1 Particle-based Models for Wet Fluidized Beds

Simulations of fluidized beds can be performed on multiple scales, allowing to gain insight on phenomena that are difficult to study via experiments[19]. Particle-based simulations can be performed on the most fundamental level by considering all flow details. Such particle-resolved Direct Numerical Simulations (PR-DNS) of flow in fixed fluidized beds allow a few hundred to approximately ten thousand particles to be simulated at extremely height computational cost.[20] This is already true for dry systems that do not contain a liquid film – in case the liquid film needs to be resolved, typically only small systems containing a few (i.e., between two and ten) particles are simulated. Thus, PR-DNS are beyond our current computational resources since we aim on a large array of system parameters that need to be varied, and systems that contain typically 10,000 or more wet particles. A review of the clustering granular and gas-solid flows has been presented in Fullmer and Hrenya et al.[21]

Fortunately, wet particle collisions and the associated liquid redistribution have recently been studied via both experiments [22,23] and simulations.[1,24] In case wet particles collide, liquid bridges form, which induce liquid bridge forces between particles. An extensive summary of liquid bridge effects on granular flows has been provided by Herminghaus [25]. Closures to predict forces due to pendular liquid bridges have been presented by a number of researchers [5,26,27]. However, all of them assumed a static bridge when calculating the bridge forces. One typical example is the model provided by Mikami et al.[5] who developed a liquid bridge cohesive force closure which is a function of the dimensionless liquid bridge volume and the separation distance based on a numerical simulation of the Laplace-Young equation. Furthermore, Shi and McCarthy[1] presented a liquid transfer model by assuming that the liquid bridge volume remains constant before bridge rupture. Also, these researchers tested their bridge model in a rotary drum spray-coating system. While the liquid bridge is composed of liquid from both contacting particles, the Shi and McCarthy[1] model does not consider the (i) nonlinearity inherent to a finite liquid film

thickness, as well as the (ii) dynamics of bridge filling. Most relevant to our present contribution is the work of Girardi et al.[28] who employed a CFD-DEM approach to study wet fluidized of particles in small periodic domains. While Girardi et al. considered cohesive forces between particles due to liquid bridges, they still used a static bridge model inspired by Shi and McCarthy[1] when calculating the bridge force. Similarly, the study of Askarishahi et al.[10] are lacked a detailed liquid bridge transfer and force model. Given the strong interest to perform such particle-based simulations of wet fluidized beds raises the central question of which model details will have the strongest impact on the predicted (i) fluidization speed, and (ii) agglomerate size for a given set of system parameters.

6.1.2 Goals and Structure

In this study, we simulate wet fluidized beds considering different liquid bridge models (i.e., the model of Shi and McCarthy[1], the dynamic model of Wu et al.[2] and a simplified version of the model of Wu et al.[2]). Specifically, we aim on answering the following questions

- for which systems the dynamic liquid bridge model of Wu et al.[2] is essential, i.e., for which situations the drainage rate of liquid into the bridge is relevant?
- Which model is the most suitable one in terms of picturing effects originating from changes in the liquid surface tension and viscosity?
- What are the most critical parameters for each model that need to be determined, e.g., during a calibration procedure?

Therefore, in Chapter 6.2 we describe the methodology used to simulate wet fluidized beds in our present study, including (i) an outline of the Navier-Stokes equations and the gas-particle coupling approach, (ii) relevant details of the liquid bridge filling models employed, as well as (iii) the capillary and viscous forces models used. In Chapter 6.3, we present a theoretical analysis of the motion associated with two-particle collisions, and detail on aspects related to the rupture

energy of a liquid bridge. Specifically, we employ three different bridge models, and compare differences – based on analytical results for particle motion – caused by different liquid bridge filling models. In Chapter 6.4 we present the main results, starting with the static bridge model and Bond number effects on the behaviour of the fluidized bed. We then compare results obtained between different bridges models and identify key parameters that affect our simulation results. Finally, we build a regime map that helps in deciding which bridge model appears most suitable for a given set of system parameters. We conclude with recommendations summarized in Chapter 6.5 that should guide the future application and extension of models for wet fluidized systems.

6.2 Methodology

6.2.1 Simulation Methodology

We perform the present simulations using an Euler-Lagrange approach for particles suspended in a gas in fully periodic domains. We represent particles as soft spheres, which contact interactions between spheres treated using a spring-dashpot model. While frictional effects are taken into account, rolling friction is not considered. The coupling of fluid and particle motion is performed using the closures implemented in CFDEM®.[29] The integrity of the used computer code is ensured by a number of verification and test cases (e.g., fluidization of a bed of particles, sedimentation of a single particle), which can be accessed online (www.github.com/CFDEMproject).

Particle translational and angular motion is found by solving the following equations:

$$m_i \frac{d\mathbf{v}_{p,\mathrm{i}}}{dt} = \sum_j \left(\mathbf{f}^n_{cont,ij} + \mathbf{f}^t_{cont,ij} + \mathbf{f}_{b,ij} \right) + \mathbf{f}_{g\to p,i} + m_i \mathbf{g} \qquad (6.1)$$

$$I_i \frac{d\boldsymbol{\omega}_i}{dt} = \mathbf{T}_i \qquad (6.2)$$

Continuum equations for fluid phase (gas)

$$\frac{\partial}{\partial t}\left(\rho_g\left(1-\phi_p\right)\right)+\nabla\cdot\left(\rho_g\mathbf{u}_g\left(1-\phi_p\right)\right)=0$$

momentum equations for fluid phase (gas)

$$\rho_g\left(1-\phi_p\right)\left(\frac{\partial\mathbf{u}_g}{\partial t}+\mathbf{u}_g\cdot\nabla\mathbf{u}_g\right)=-\nabla p_g+\nabla\cdot\boldsymbol{\tau}_g+\boldsymbol{\Phi}_d+\rho_g\left(1-\phi_p\right)\mathbf{g}$$

$\boldsymbol{\Phi}_d$ is the force exerted by the particles on the fluid per unit volume of the gas-particle mixture

$$\boldsymbol{\Phi}_d=-\frac{1}{V_j}\sum_i^{\text{cell}} w_{ij}\,\mathbf{f}_{g\to p,i}$$

$\mathbf{f}_{g\to p,i}$ is the total interaction force on particle i exerted by gas, w_{ij} is a weighting factor associated with the proximity of particle i and computational cell j, and V_j is the volume of a computational cell.

$$\mathbf{f}_{g\to p,i}=-V_{p,i}\nabla p_g+V_{p,i}\nabla\cdot\boldsymbol{\tau}_g+\mathbf{f}_{d,i}$$

$\mathbf{f}_{d,i}$ is the drag force which follows the model of Beetstra et al.[30]

$$\mathbf{f}_{d,i}=-V_{p,i}\beta_{p,i}\left(\mathbf{u}_g-\mathbf{v}_p\right)$$

$$\beta_{p,i}=\frac{18\mu_g}{d_p^2}\left(1-\phi_p\right)\left(g_1+g_2\right)$$

$$g_1=\frac{10\phi_p}{\left(1-\phi_p\right)^2}+\left(1-\phi_p\right)^2\left(1+1.5\sqrt{\phi_p}\right)$$

$$g_2=\frac{0.413Re_p}{24\left(1-\phi_p\right)^2}\left[\frac{\left(1-\phi_p\right)^{-1}+3\phi_p\left(1-\phi_p\right)+8.4Re_p^{-0.343}}{1+10^{3\phi_p}Re_p^{-(1+4\phi_p)/2}}\right]$$

$$Re_p=\frac{\left(1-\phi_p\right)\rho_g d_p\left|\mathbf{u}_g-\mathbf{v}_p\right|}{\mu_g}$$

Table 6.1: Governing equations for gas-solid flow

Where m_i is mass of particle i and $\mathbf{v}_{p,i}$ is the translational velocity of the particle, contact force exerted on particle i by particle j which includes a normal component ($\mathbf{f}^n_{cont,ij}$) and a tangential component ($\mathbf{f}^t_{cont,ij}$). Specifically, Particles are modeled as frictional and inelastic spheres, adopting a linear spring-dashpot model with frictional slider.[31] In addition, $\mathbf{f}_{b,ij}$ is the bridge force exerted on particle i by bridge j. Details of the liquid bridge force models will be introduced

in Section 6.2.4, $\mathbf{f}_{g\to p,i}$ is the interaction force on particle i caused by the fluidization of the particulate system with a gas. Relevant details are summarized in Table 6.1 below. I is the moment of inertia, $\boldsymbol{\omega}$ is the angular velocity of the particles and $\mathbf{T}_i$ is the total torque acting on particle i.

Spring-dashpot model and frictional slider model[31] have been used for particle-particle interaction.

$$\mathbf{f}^n_{cont,ij} = -k_n \delta^n_{ij} \mathbf{n}_{ij} - \gamma_{d,n} \mathbf{v}^n_{ij} \tag{6.3}$$

$$\mathbf{f}^t_{cont,ij} = \begin{cases} -k_t \delta^t_{ij} \mathbf{t}_{ij} - \gamma_{d,\mathrm{t}} \mathbf{v}^t_{ij} & \text{for } \left|\mathbf{f}^t_{cont,ij}\right| < \mu_{pp} \left|\mathbf{f}^n_{cont,ij}\right| \\ -\mu_{pp} \left|\mathbf{f}^n_{cont,ij}\right| \dfrac{\delta^t_{ij} \mathbf{t}_{ij}}{|\delta^t_{ij} \mathbf{t}_{ij}|} & \text{for } \left|\mathbf{f}^t_{cont,ij}\right| \geq \mu_{pp} \left|\mathbf{f}^n_{cont,ij}\right| \end{cases} \tag{6.4}$$

Where k_n is the normal spring constant $\gamma_{d,n}$ is the normal damping coefficient, δ_{ij} is the overlap between particles i and j, μ_{pp} is the friction coefficient. Parameters of the spring-dashpot model are given in Table 6.2.

The locally-average fluid velocity and pressure fields are governed by conservation of mass and momentum, which are outlined in Table 1. In this table, ρ_g is the density of the gas, ϕ_p is the fraction of cell volume, $\mathbf{u}_g$ is the gas velocity, p_g is the gas phase pressure, $\boldsymbol{\tau}_g$ is the gas phase deviatoric stress tensor, $V_{p,i}$ is particle volume and i is the particle index. $\boldsymbol{\Phi}_d$ is the total gas-particle interaction force per unit volume exerted on the particles. In our present study $\boldsymbol{\tau}_g$ is not taken into account for computing the total gas-particle force because it is not significant in gas-fluidized beds of particles. Thus, $\boldsymbol{\Phi}_d$ is composed of only a buoyancy force and the drag force, which play the most important role when computing $\mathbf{f}_{g\to p,i}$ in gas-particle flows. The drag model in this study has been presented by Beetstra et al.[30] Boundary conditions for the computational domain are fully periodic, which means that particles leaving through a boundary

are injected at the opposing side with identical translational and rotational speed. Detailed parameters of the simulations are given in Table 6.2.

Parameter	Value
Domain size – x: Δx (m)	0.008
Domain size – y: Δy (m)	0.032
Domain size – z: Δz (m)	0.008
Number of fluid grid – x: N_x	18
Number of fluid grid – y: N_y	72
Number of fluid grid – z: N_z	18
Gravitational acceleration: g (m/s^2)	9.81
Particle diameter: d_p (m)	1.45×10^{-4}
Particle density: ρ_p (kg/m^3)	1600
Normal spring constant: k_n (kg/s^2)	2.05
Normal spring damping: $g_{d,n}$ (kg/s)	3.43×10^{-6}
Friction coefficient: μ_{pp}	0.5
Restitution coefficient of the dry particles: e_{pp}	0.9
Gas density: ρ_g (kg/m^3)	2.28
Gas viscosity: μ_g (Pa s)	2.5×10^{-5}
Particle terminal setting velocity: v_t (m/s)	0.5
Froude number: $F_r=v_t^2/(d_p g)$	176
Reynolds number : $Re_p = \rho_g d_p v_t / \mu_g$	6.61
Particle time step: Δ_{tp} (s)	10^{-6}
Fluid time step: Δ_{tg} (s)	10^{-5}
Bond number: Bo	0.1 - 100
Bond and Capillary number product: $BoCa$	0.1 - 10000
Dimensionless initial film high of particle: h_0^+	0.0037, 0.0154, 0.036,0.1
Dimensionless particle surface asperities: h_ε^+	0.05

Table 6.2: typical dimensional simulation parameters

The above set of equations relies on the following key dimensionless parameters that govern the system.

- Particle Reynolds number $\mathrm{Re}_p = \rho_g d_p v_t / \mu_g$
- Particle volume fraction ϕ_p
- Froude number $Fr = v_t^2 / \left(d_p g \right)$
- Bond number: $Bo = \dfrac{6\gamma}{d_p^2 \rho_p g}$
- Capillary number: $Ca = \dfrac{\mu_l v_t}{\gamma}$
- Alternatively, a Capillary times Bond number that quantifies the importance of viscous forces over gravity and which is defined as

$$BoCa = \frac{6\mu_l v_t}{d_p{}^2 \rho_p g}$$

6.2.2 Liquid Bridge Filling Model

As mentioned earlier, we employ three different liquid bridge filling models. Specifically, we differentiate between three types of bridge models which are defined as follows:

- Model A: the static bridge model of Shi and McCarthy[1] which is simple and efficient, but known to incorrectly predict the film thickness effect on the bridge volume.[2]
- Model B: a static bridge model considering the expression for the initial bridge volume detailed in our previous work.[2] This model considers the initial film height and separation distance to predict the bridge volume, and is still simple and efficient.
- Model C: the dynamic filling model detailed in our previous work[2], where the transient liquid transport from the particle surface into the bridge is accounted for.

i) Model A

Model A is provided by Shi and McCarthy[1] which reads as follows:

$$V_b = \frac{L_{p,i}}{2}\left(1-\sqrt{1-\frac{R_j^2}{\left(R_i+R_j\right)^2}}\right)+\frac{L_{p,j}}{2}\left(1-\sqrt{1-\frac{R_i^2}{\left(R_i+R_j\right)^2}}\right) \quad (6.5)$$

Where $L_{p,i}$ and $L_{p,j}$ are the initial liquid contents (i.e., that when the particles' surfaces touch) on particle *i* and particle *j*, respectively. Thus, the total liquid bridge volume is composed of liquid from both contacting particles. Once we know the liquid content on the particle surface, we can calculate the liquid bridge volume based on equation 6.6. The liquid content $L_{p,i}$ on particle surface is related to the dimensionless film height as follows:

$$L_{p,i} = \frac{4}{3}\pi R^3\left(\left(1+h_0^+\right)^3-1\right) \quad (6.6)$$

Here R is the particle radius, and $h_0{}^+$is the dimensionless initial film height. Therefore, once knowing the liquid content on the particle surface, both the liquid content on the particle surface and the liquid bridge volume that forms upon a collision between particles is defined. Furthermore, the dimensionless initial film height as a function of the dimensionless liquid content on a particle is:

$$h_0^+ = \left(\frac{3L_{p,i}^+}{4\pi}+1\right)^{1/3}-1 \quad (6.7)$$

This result will be consequently used for the following liquid bridge calculation to ensure a fair comparison between the three different liquid bridge models, as well as to calculate the liquid loading level of a particle system as done by Girardi et al.[28] Note, in this previous work the liquid loading level was defined as the ratio between the liquid bridge volume and particle volume, which is given as:

$$\Lambda = \frac{V_b}{V_p} \quad (6.8)$$

However, in our present work we define the liquid loading level by using a more meaningful metric, which uses half the bride volume over particle volume:

$$\lambda = \frac{V_b}{2V_p} \qquad (6.9)$$

Therefore, combining equations 6.7-6.9, one can easily calculate the liquid loading λ and the corresponding dimensionless film height h_0^+ according to the model of Shi and McCarthy. We know that the initial film height h_0^+ is the key parameter to identify the liquid loading level in our previous work.[2] Therefore, these definitions will help us in our discussion below to quantify the liquid amount and make a fair comparison of simulations results for different filling models.

ii) Model B

Model B is defined as the "early stage" liquid bridge model given in our previous work.[2] Specifically, the liquid bridge volume is calculated based on the initial film height and the separation distance between the particle surfaces.

$$\frac{V_{b,0}^+}{\left(h_0^+\right)^{1.5}} = \left(-8\left(\frac{S^+}{h_0^+}\right)+10.5\right) \qquad (6.10)$$

Here $V_{b,0}^+$ is the dimensionless bridge volume at $t^+=1$, h_0^+ is the dimensionless average initial film height, and S^+ is the half separation distance between particle surfaces. However, as we found that the separation effect does not strongly affect liquid bridge filling during a particle collision, we neglect separation effects for the time being. Thus, we simply use the expression $V_{b,0}^+ = 10.5\left(h_0^+\right)^{1.5}$ to compute the bridge volume.

iii) Model C

Liquid transfer from particle surfaces to the liquid bridge region follows the liquid bridge model proposed in our previous work [2], as well as the ideas that defined "model C1" in Mohan et al.[32] In this dynamic liquid bridge model, the amount of liquid that flows into the liquid bridge region is tracked over time by solving

$$\begin{aligned}\frac{dL_{p,i}^{+}}{dt^{+}} &= -a_i\left(L_{p,i}^{+}\phi_{m,i} - \frac{V_b^{+}}{2}\right)\\ \frac{dL_{p,j}^{+}}{dt^{+}} &= -a_i\left(L_{p,j}^{+}\phi_{m,j} - \frac{V_b^{+}}{2}\right)\\ \frac{dV_b^{+}}{dt^{+}} &= -\left(\frac{dL_{p,i}^{+}}{dt^{+}} + \frac{dL_{p,j}^{+}}{dt^{+}}\right)\end{aligned} \tag{6.11}$$

Here $L_{p,i}^{+}$, $L_{p,i}^{+}$ are the liquid contents on particle i and j, a_i is the filling rate coefficient, ϕ_m are the mobility coefficients of the liquid on the particle (i.e., the relative amount of liquid that is able to flow into the liquid bridge region). All these parameters are made dimensionless using the following relations:

$$t_{ref} = \frac{d_p \mu_l}{2\gamma};\quad t^{+} = \frac{t}{t_{ref}};\quad L_{p,i}^{+} = \frac{L_{p,i}}{R^3};\quad L_{p,j}^{+} = \frac{L_{p,j}}{R^3} \tag{6.12}$$

Verification of the implementation of the used model C (i.e., a comparison between numerical simulation and an analytical solution), as well as a validation based on data from Direct Numerical Simulations is documented in Appendix A.

6.2.3 Bridge Rupturing Model

When the liquid bridge between two particles stretches beyond a critical distance, the bridge ruptures and the liquid in the bridge is redistributed (in our case equally to the two involved particles). This rupture distance is given by Lian et al.[33] which reads:

$$h_{rup} = \left(1 + 0.5\theta\right)V_b^{1/3} \tag{6.13}$$

h_{rup} is the critical rupture distance, θ is the contact angle. In our present contribution we assume a fully wetted case, i.e., θ is zero. The bridge force is present as long as the bridge exists, and it disappears when the bridge ruptures at the above defined critical distance.

In the next section we introduce the bridge force models which have been employed in our simulations.

6.2.4 Bridge Force Models

i) Capillary Force Model

Cohesive forces due to liquid bridge are incorporated by considering both capillary and viscous contributions. We use the force model provided by Mikami et al.[5] to calculate the capillary force caused by liquid bridge.

$$\begin{aligned} F_{cap} &= \pi R\gamma\left(e^{AD^{+}+B}+C\right) \\ A &= -1.1\left(V_b^{+}\right)^{-0.53} \\ B &= \left(-0.34\ln\left(V_b^{+}\right)-0.96\right)\theta^2-0.019\left(V_b^{+}\right)+0.48 \\ C &= 0.0042\ln\left(V_b^{+}\right)+0.078 \end{aligned} \tag{6.14}$$

Where D^{+} is the surface to surface distance between particles, R is reference particle radius, γ is surface tension. In case our used soft particles contact or overlap, we consider these situations as if the separation D^{+} is zero. In such a way, only coefficient B and C act in the above equation for contacting or overlapping particles. Examples of this situation can be seen in Figure 6.3 (contact distance between particles is zero).

ii) Viscous Force Model

We follow the model provided by Pitois et at.[27] to calculate viscous force between particles. This models accounts for the liquid bridge volume and reads

$$F_{\text{vis}} \approx -\frac{3}{2}\pi\mu_l R^2\frac{1}{D^{+}}\mathbf{v}^n X_v^2 \tag{6.15}$$

Where R is reference particle radius, D^{+} is the surface distance between two particles, and $\mathbf{v}^n$ is particle approaching velocity in normal direction. The correction coefficient X_v for the force model is given by

$$X_v = 1-\frac{1}{\sqrt{1+\dfrac{2V_b^{+}}{\pi R\left(D^{+}\right)^2}}} \tag{6.16}$$

The above force diverges for zero separation, and hence must consider a minimal particle distance. Therefore, we us a relative roughness, which is defined as the particle roughness divided by the particle diameter, that is set to $h_\varepsilon^+ = 0.05$. Thus, the particle surface roughness is $h_\varepsilon = 7.25 \cdot 10^{-6}$ m for all particles.

6.3 Theoretical Analysis

The liquid bridge volume is an input parameter in almost the totality of models for calculating the capillary and viscous force between two wet particles. Thus, it can be expected that different models for liquid bridge volume will lead to different characteristics of the resulting cohesive force. Therefore, in this section, we attempt to quantify this difference by using model A, model B, model C in a simple binary collision.

In order to make a comparison, we pick the parameters of the particle system as listed in Table 2. To make the comparison easier, we use a case of zero separation to compute the initial bridge volume, which can be simply calculated via $V_{b,0}^+ = 10.5\left(h_0^+\right)^{1.5}$. The maximum liquid bridge volume (for model C) can be obtained by setting the filling time to $t^+ = \infty$, consequently the expressions of liquid bridge model provided in Appendix A of Wu et al.[2] can be simplified to:

$$V_b^+ = V_{b,0}^+ - 2\left(C_1 \frac{r_1 + \phi_{m1} a_i}{a_i r_1} + C_2 \frac{r_2 + \phi_{m1} a_i}{a_i r_2} \right) \tag{6.17}$$

$$\begin{aligned} C_1 &= \frac{-a_i^2 \phi_{m2} L_{p2,0}^+ - \left(2 a_i r_2 \phi_{m1} + 2 a_i^2 \phi_{m1}^2 + a^2 \phi_{m1}\right) L_{p1,0}^+ + \left(a_i^2 \phi_{m1} + a_i^2 + a_i r_2\right) V_{b,0}^+}{2\left(r_2 - r_1\right)} \\ C_2 &= \frac{a_i^2 \phi_{m2} L_{p2,0}^+ + \left(2 a_i r_1 \phi_{m1} + a_i^2 \phi_{m1} + 2 a_i^2 \phi_{m1}^2\right) L_{p1,0}^+ - \left(a_i r + a_i^2 \phi_{m1} + a_i^2\right) V_{b,0}^+}{2\left(r_2 - r_1\right)} \end{aligned} \tag{6.18}$$

$$r_{1,2} = \frac{-a_i \left(\phi_{m1} + \phi_{m2} + 1 \pm \sqrt{\left(\phi_{m1} - \phi_{m2}\right)^2 + 1} \right)}{2} \tag{6.19}$$

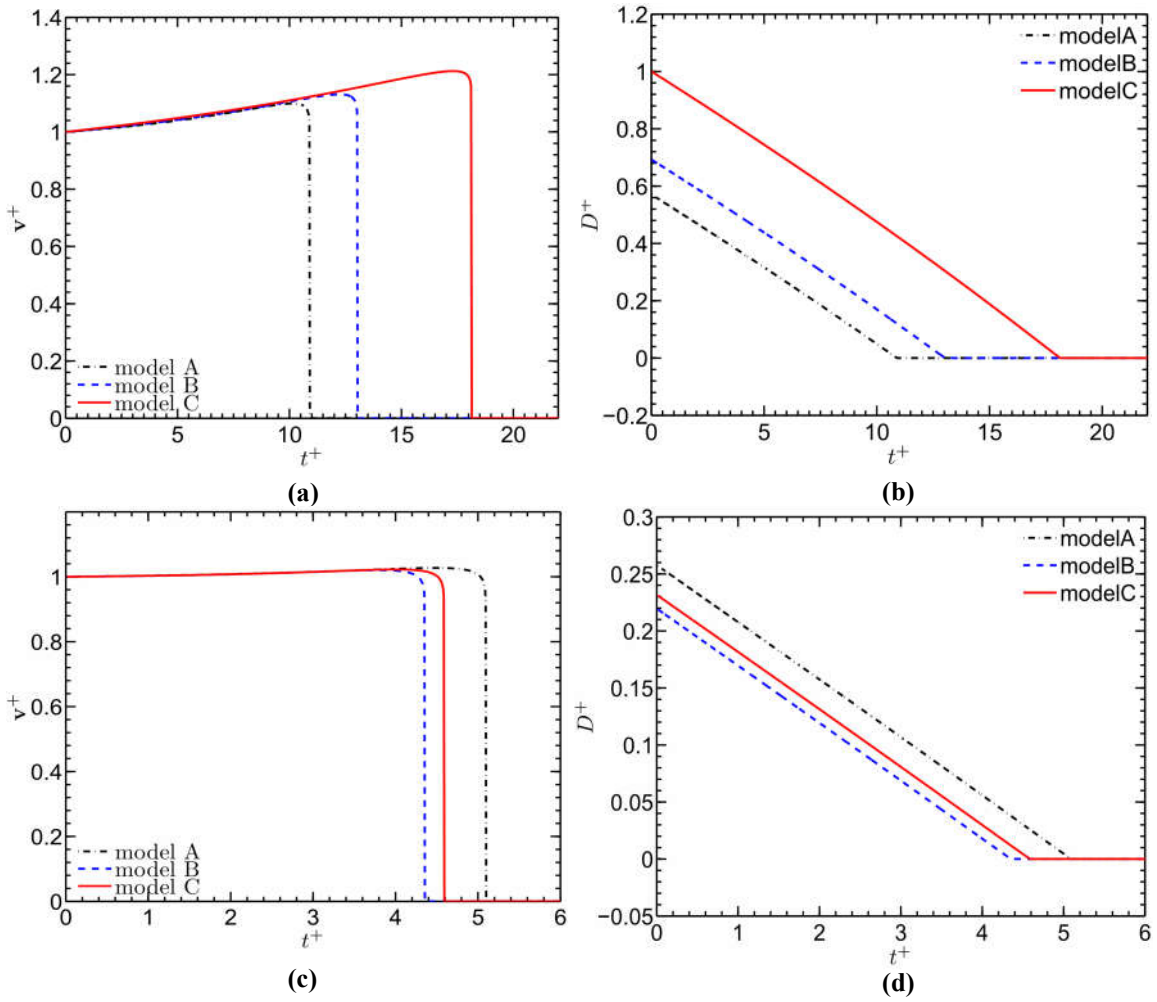

Figure 6.1: Temporal evolution of the relative particle-particle velocity (panels a and c) and distance (panels b and d) predicted by three different bridge models. The top panels were obtained by using $h_0{}^+ = 0.1$, $Bo = 200$, $BoCa = 90$, and the bottom panels by using $h_0{}^+ = 0.01$, $Bo = 200$, $BoCa = 90$; Particles were initialized with the particle terminal setting velocity at the rupture distance of the bridge.

The liquid bridge force is present as long as the bridge exists, and it vanishes when the liquid bridge ruptures at the critical rupture distance. The bridge forces (detailed in Section 6.2.4) are normalized by the capillary force scale $2\pi\gamma R$, and the rupture distance is scaled with the particle radius R.

Next, we analyze the motion of two approaching wet particles that are affected by capillary and viscous forces. For such a situation we have:

$$\vec{F}_{vis} + \vec{F}_{cap} = m\frac{d^2D}{dt^2} \qquad (6.20)$$

Where $\vec{F}_{vis}$ is the viscous force, $\vec{F}_{cap}$ is the capillary force, and m is the mass of one particle. For small particles (i.e., in case the particle size is smaller than the capillary length), the gravitational forces can be neglected, and only capillary and viscous forces affect particle motion. Substituting the capillary and viscous equations in Eqn. 6.21, and using appropriate initial conditions (i.e., the rupture distance h_{rup} and Stokes settling velocity u_t), we arrive at the following differential equation:

$$\begin{cases} \pi R\gamma\left(e^{A\left(\frac{D}{R}\right)+B}+C\right)-\frac{3}{2}\pi\mu_l R^2 X_v^2 = m\frac{d^2D}{dt^2} \\ D(0)=h_{rup}; \quad D'(0)=u_t \end{cases} \tag{6.21}$$

Where A, B and C are given by Eq. 6.13, X_v is presented by Eqn.6.16, and the particle terminal setting velocity is used as the initial velocity.

By integrating equation 6.21 together with liquid bridge models, we arrive at the theoretical analysis results of the interaction velocity and separation distance between two wet particles. Figure 6.1 shows the approaching velocities and separation distances between two wet particles and quantifies the effects due to three different bridge filling models, as well as the effect of the liquid loading level. The top panels (a) and (b) are obtained by using an initial film height of $h_0^+ = 0.1$, while the bottom panels by using an initial film height of $h_0^+ = 0.01$. Both cases consider Bo = 200, Ca = 0.45 and $BoCa$ = 90. As seen in Figure 6.1, the left column, velocities for all cases start from the initial Stokes setting velocity to a maximum velocity (around 1.2 time larger than that of terminal velocity for the thick film case, while for thin film this speed is nearly the same as u_t) before the two particles contact. Correspondingly, the distance between the particle surfaces (panels b and d) decreases from the rupture distance to zero separation at the contact position. In addition, we can observe from Figure 6.1 that there is not much difference between our early stage model (model B) and the dynamic filling model (model C) when particles are initialized with a very small film height. However, the model of Shi and McCarthy (model A) predicts larger particle

relative velocities and separation distance. In contrast, in panel (a) and (b), model C indeed affects particle motion due to the bridge forces: since in this case the particles are initialized with larger film heights, the non-linear relationship between film height and liquid bridge volume leads to strongly different results. Specifically, model C predicts the biggest velocity (panel a) and separation (panel b) for the case of comparably thick films.

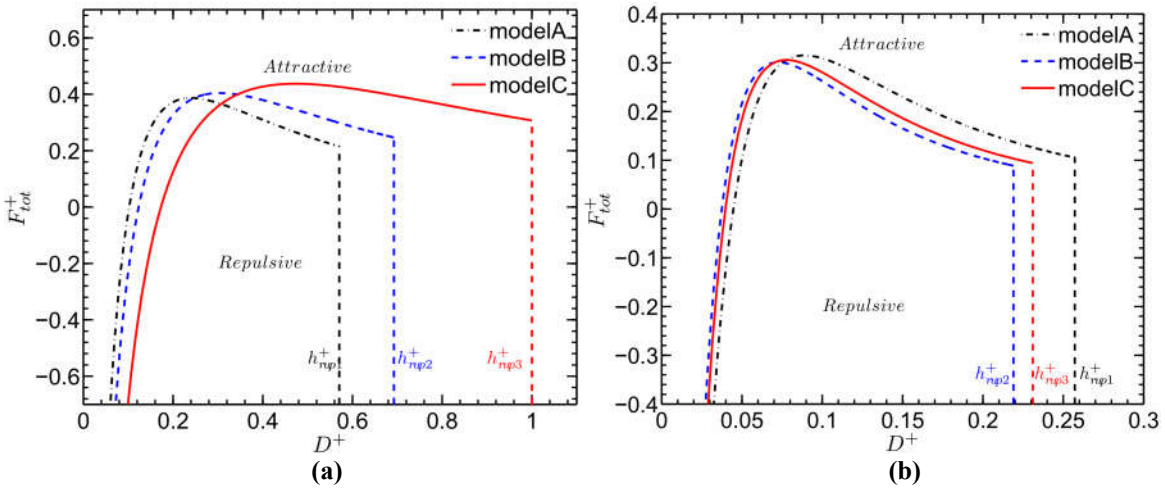

Figure 6.2: Dynamic forces exerted by a liquid bridge predicted by three different liquid bridge models (vertical lines the rupture distance). Panel (a): $h_0{}^+ = 0.1$, $Bo = 200$, $Ca = 0.45$, $BoCa = 90$; Panel (b): $h_0{}^+ = 0.01$, $Bo = 200$, $Ca = 0.45$, $BoCa = 90$.

Figure 6.2 shows the dynamic bridge forces (viscous force and capillary force) and rupture distances exerted by liquid bridge model A, B and C initialized with a thick film (panel (a)) and thin film (panel (b)). We can observe from Figure 6.2 that bridge forces are always composed of repulsive force and attractive force. In case the particle distance is small, the repulsive force is dominant, while for larger distance, the attractive force is dominant. Bridge forces only act on the particles when a liquid bridge is present between the particles. However, these bridge forces vanish as soon as the bridge between particles ruptures (see the vertical dashed line in Figure 6.2). That is why we can see for both panel (a) and (b) in Figure 6.2 that bridge forces of three bridge models predict strongly different rupture energies for the case of thick films. This is because of the difference of the rupture distance of three models due to different liquid contents present in the bridge region. In addition, the difference between panel (a) and panel (b) is the

initial liquid film height, which strongly affects the rupture distance, as well as the total force values to a lesser extent. Generally, the larger initial film height is initialized, the bigger the rupture distance and the larger bridge forces that act on the particles. Again, we can see that there is not much different between three models when particles are initialized with very small film height, and model A leads to the largest predicted bridge force. However, there is much difference between these three models when particles are initialized with a thick film: model C predicts the strongest force behaviour and largest rupture distance, and model A predicts substantially lower force and rupture distance values.

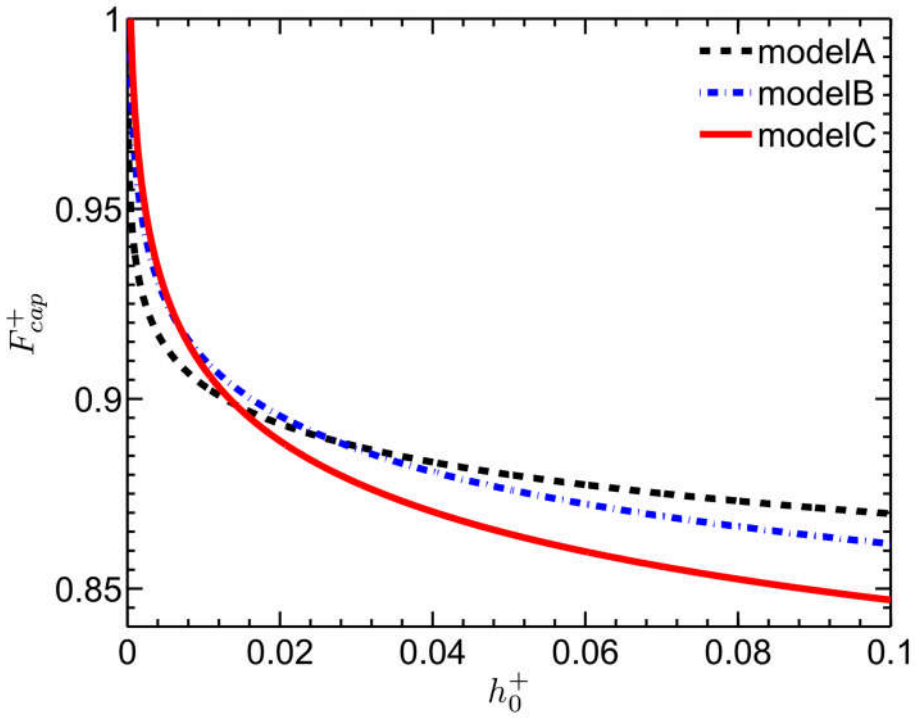

Figure 6.3: Capillary forces at contact based on the three bridge models and when using Mikami et al.'s capillary force model[5] **for different initial film heights, *Bo* = 200, *BoCa* = 90**

Figure 6.3 shows the capillary forces for threes bridge models when particles are contacting or overlapping (note that our spring-dashpot model allows small particle-particle overlaps to compute the contact force in the normal direction). It indicates that model C is affected most by the initial liquid film height over the full range of h_0^+ studied. However, the static bridge (model A) are more sensitive to initial liquid contents in the range of very thin films (i.e., for approximately $h_0^+ <$ 0.01). In summary Figure 6.3 shows that the capillary force is essentially

independent of the bridge models when particles contact or overlap. The capillary force is only to some degree dependent on the liquid initial film height h_0^+, and varies by maximum 15% for $0 < h_0^+ < 0.10$.

Figure 6.4 illustrates the work done by the bridge force until bridge rupture as a function of the initial liquid film height as predicted by the three bridge models. The work done compose of capillary and viscous work due to the bridge force. The total work is calculated by spatial integration of the bridge force over the full rupture distance, which has been presented in Pitois et al [34]

$$W_{cap} = \int_0^{h_{rup}} F_{cap} dD = 2\pi \cos\theta \left[(1+0.5\theta)(1-A)V_b^+ + \sqrt{\frac{2V_b}{\pi}} \right] \tag{6.22}$$

$$W_{vis} = \int_{h_\varepsilon}^{h_{rup}} F_{vis} dD = 1.5\pi Ca \left[\ln\left(\frac{A\sqrt{\pi}}{(1+A)^2} \right) - f(h_\varepsilon) \right] \tag{6.23}$$

$$f(h_\varepsilon) = \ln(h_\varepsilon) - 2\ln\left[h_\varepsilon + \sqrt{h_\varepsilon^2 + \frac{2V_b}{\pi}} \right] + 0.5\ln\left(\pi h_\varepsilon^2 + 2V_b\right) \tag{6.24}$$

$$W_{tot} = W_{cap} + W_{vis} \tag{6.25}$$

Where A is given by $A = \left(1 + 2(1+\theta/2)^2 \left(V_b\right)^{1/3} / \pi\right)^{0.5}$, the value of particle surface asperity h_ε is given in Table 6.2. The velocity profile used for computing the viscous force is chosen as the particle terminal setting velocity. As seen from Figure 6.4, the energy required for getting bridge rupture increases when increasing the initial film height of the particle system for all bridge models. However, the rupture energy for model C rises remarkably with increasing initial film height compared to the other two bridge models. Moreover, we can see from Figure 6.4 that there exists an initial film height (around $h_0^+ = 0.025$) after which a clear disparity of the rupture work predicted by the three bridge models can be observed. Thus, this initial film height demarcates a transition between situations in which there is not much difference between the three models, and for which a clear disparity of rupture energy exists. The physical origin of this observation is

that model B and C show a non-linear dependency of the bridge volume on the initial film height. In addition, model C considers the amount of liquid that is able to drain from the particle surface into the bridge, again causing an almost three-fold increase of the bridge's rupture energy for the thickest films.

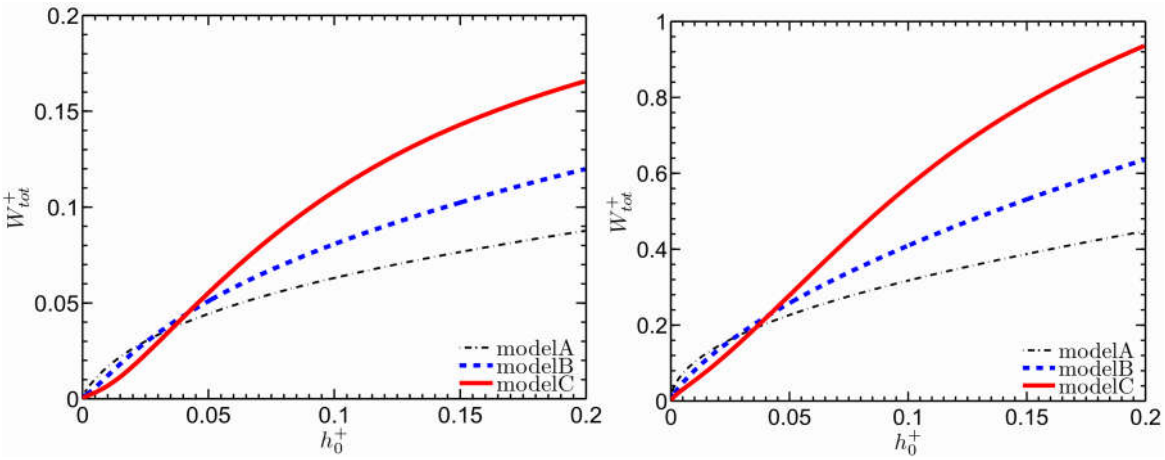

(a) *Bo* = 20, *BoCa* = 10 **(b) *Bo* = 200, *BoCa* = 10**

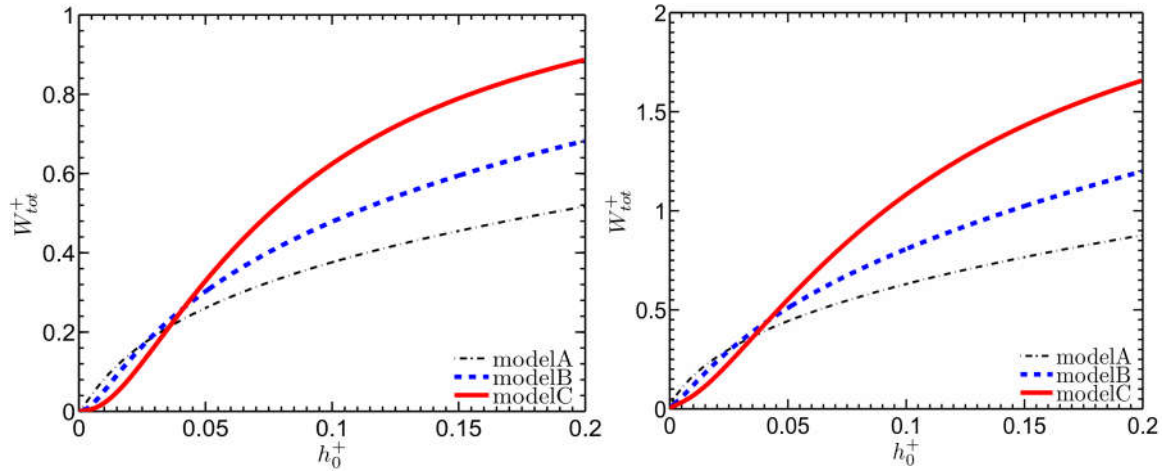

(c) *Bo* = 20, *BoCa* = 100 **(d) *Bo* = 200, *BoCa* = 100**

Figure 6.4: Dimensionless total work due to bridge forces predicted by three different bridge models versus the dimensionless initial film height. The work is normalized by with the particle's kinetic energy assuming it is moving with particle terminal setting velocity.

We also can see from Figure 6.4 shows the Bond number effect on the rupture energy exerted by bridge forces of three different bridge models. Four different *Bo* and *BoCa* numbers have been considered when preparing Figure 6.4. From left to tight in Figure 6.4, we fix *BoCa* number but increase *Bo* number from 20 to 200, and we found that the Bond number (i.e., a dimensionless surface tension force) critically affects the rupture energy as expected from the capillary force.

Specifically, more energy is required to cause bridge rupture when increasing the Bond number (surface tension) for all three bridge models. This is certainly physical and reasonable because surface tension definitely influences cohesive force between particles. Also, if we see the columns of the Figure 6.4, we found that increasing of the modified capillary number (*BoCa*) can also increase the rupture energy. This indicates that particle coated with liquid of higher viscosity requires more energy to get rupture when particles collide with one another.

However, we can identify two more important facts: (i) model C requires substantially more work for thick films while the opposite is true thin film. Thus, model A predicts somewhat larger rupture energies for thin films and much lower energy for thick films, and that there exists a critical film height for the transition from thin to thick films close to $h_0^+ = 0.025$. (ii) Rupture energy increases non-linearly with the Bond number in case we fix the value of *BoCa*, i.e., the relative importance of viscous and gravity forces. This is due to the fact that larger *Bo* values also increase viscous dissipation due to the overall higher particle relative speed during the approach phase.

6.4 Results and Discussion

6.4.1 Influence of Bond and Capillary number

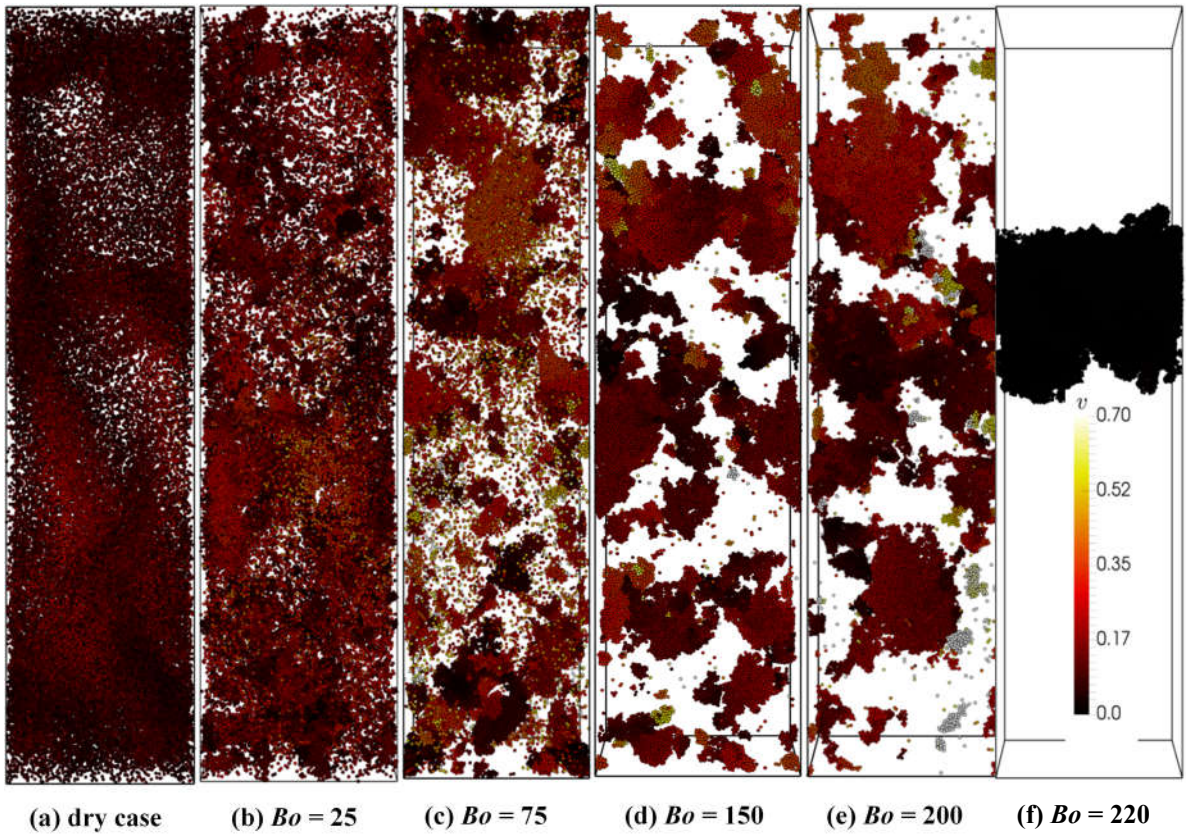

Figure 6.5: Snapshots of cluster morphology for various Bond numbers (particles are colored according their speed; the domain-average particle volume fraction is 0.05, the initial film height is $h_0^+ = 0.0154$, Ca = 0, corresponding to a liquid loading coefficient of $\Lambda = 0.003$).

We first consider the static bridge model (model A) to get an impression of how the Bound number effects the state of fluidization, and to compare our current simulation to the results of Girardi et al. [28]. Thirdly, we aim on studying the effect of the capillary number on predictions made on the basis of the bridge filling model A. Figure 6.5 shows some snapshots for a dry system and some wet systems covering a range of Bond numbers. The inhomogeneity inferred by a visual observation of clusters can also be observed in dry system (panel (**a**) in Figure 6.5). However, this clustering phenomenon in a dry system is typically ascribed to the instability of the homogeneously fluidized state caused by (i) inelastic collisions and (ii) the drastic change of the drag coefficient with the

particle concentration.[35] However, in the wet system, aggregation caused by the cohesive forces due to liquid bridges (see panels (b-f) in Figure 6.5) results in a very different pattern compared to that observed in the dry system. One can clearly see from Figure 6.5 that particles of the system become more cohesive when increasing the Bond number, and the agglomeration tendency of particles in the system becomes larger and larger. This type of fluidization of particle in turn requires larger slip velocity. However, a sufficiently large value of the Bond number (i.e., beyond $Bo = 200$) will cause the simulation domain generating only one agglomerate spanning in the domain (see panel (f)). When this phenomenon takes place, the fluidity of the fluidized beds will be blocked in our numerical setup, and no meaningful statistics physical properties can be obtained in the domain. As has been already argued in Girardi et al. [28], the domain size clearly affects this generation of a single agglomerate. Unfortunately, we must use a finite domain size for keeping the computational time needed to solve the governing equations in a feasible range. Consequently, all our studies bellow will not consider unphysical states as shown in panel (f) of Figure 6.5.

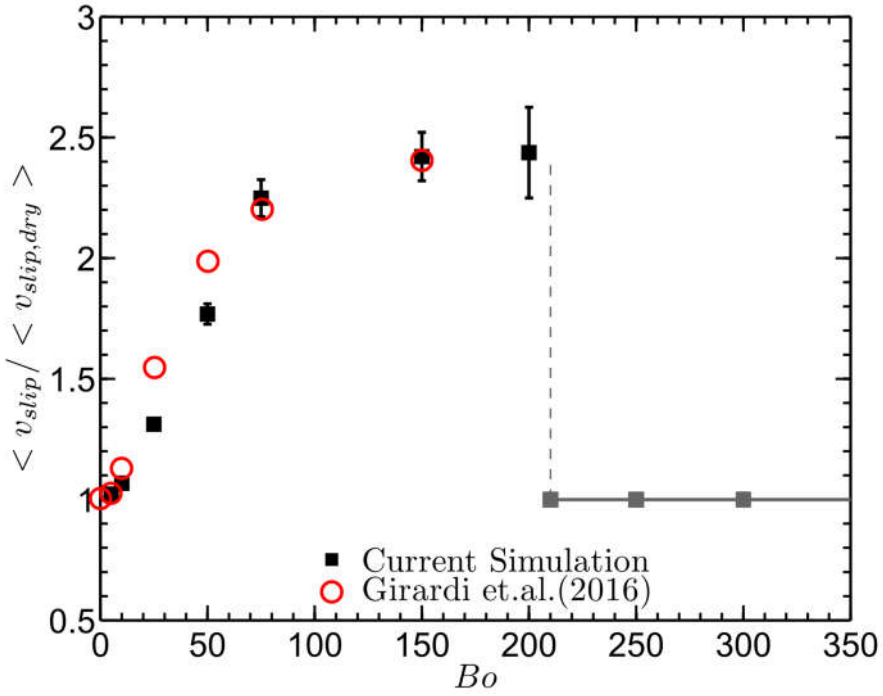

Figure 6.6: Domain average slip velocity at various *Bo* numbers for an initial film height of $h_0^+ = 0.0154$, corresponding to a liquid loading coefficient of $\Lambda = 0.003$ and using model A ($Ca = 0$).

We present in Figure 6.6 the domain average slip velocities extracted from data documenting statistical steady states in our CFD-DEM simulations. These simulations were performed considering a fixed liquid loading level of $\Lambda = 0.003$ and various *Bo* number. We also compare our current simulation results with the corresponding values obtained by Giradi et al.[28] (note they used a simple static liquid bridge filling model similar to our model A). One can see that liquid bridges make the system of particles more cohesive, in line with observations in recent publications.[9,28,36] The current simulation results show a well agreement with the results provided by Giradi et at.[28] However, the results of Giradi et at.[28] indicated a smaller Bond number (i.e., approximately *Bo* = 150) which results in a situation like that shown in Figure 6.5(f) compared our present simulations (i.e., *Bo* = 220). Based on our current simulations and observations, at *Bo* = 200, our system can still be fluidized and particle clusters in the domain can be observed (see panel (**e**) in Figure 6.5). This fluidization behavior will stop after the Bond number becomes larger than approximately 220 (see the gray points in Figure 6.6). We can also see from Figure 6.6 that the inhomogeneity of particle clusters in the domain increases, causing an increase of $<v_{slip}>$. One should notice that the pressure drop across the simulation domain maintained fixed throughout the simulation, and was chosen such that the total momentum of the system remained zero. Agglomerates of particles could be viewed as effectively larger "super particles". Therefore, the effective gas-particle drag coefficient decreases when agglomeration occurs, which consequently necessitates a greater slip velocity to achieve the same pressure drop.

Figure 6.7 shows the Bond number effect, and also illustrates the effect of viscous forces quantified by *BoCa* values of a: *BoCa* = 0.1, b: *BoCa* = 1.0, and c: *BoCa* = 10. These results are obtained by using model A and an initial film height of $h_0^+ =$ 0.0154. Figure 6.7 further illustrates that a greater slip velocity is required when increasing the Bond number of the fluidized system, also indicating that bed fluidity decreases with increasing *BoCa*. However, a greater increase of the slip velocity is observed with increasing *Bo* than with increasing *BoCa* value. We

speculate that the physical reason why *BoCa* has a smaller effect is that viscous forces appear only in case of significant particle relative speeds. The latter appears to be not the case in the comparably wet, dense agglomerates predicted by our simulations that form, deform and breakup relatively slowly. In summary, the decrease of bed fluidity due to increasing liquid bridge forces can be ascribed to particles agglomeration due to liquid bridge formation. These bridges make it more difficult for particles to move past each other and mix freely. This trend has also been observed in a previous experimental study.[37]

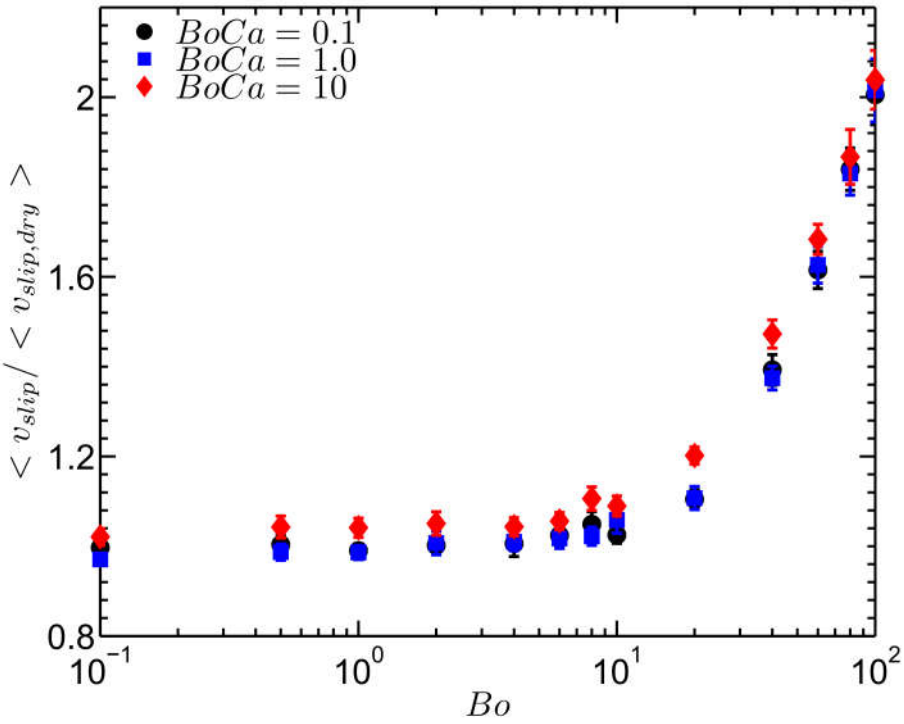

Figure 6.7: Domain average slip velocity versus Bond number for varying values of *BoCa*. Initial film height $h_0^+ = 0.0154$, liquid loading coefficient $\lambda = 0.0015$.

6.4.2 Comparison of Static Bridge Models

Model A (dark squares) and model B (blue circles) have been compared in Figure 6.8 when predicting the domain-average slip velocity $<v_{slip}>$ for various scenarios characterized by the *Bo* and *BoCa* numbers. The results are obtained by considering an initial film height of $h_0^+ = 0.0037$. As seen in Figure 6.8, model A requires greater slip velocity than model B which predicts a lower bed fluidity for thin films (i.e. $h_0^+ = 0.0037$). As been theoretically studied in paragraph 6.3,

model A predicts larger liquid bridge rupture energies due to larger bridge volume prediction for thin films. In addition, we can also identify more significant differences between panel (a) and panel (b): as seen from Figure 6.8 increasing both the *Bo* and *BoCa* number will result in the increase of slip velocity, but the effects from increasing the *Bo* number is stronger than that of an increase of the *BoCa* number. The prominent increase of the slip velocity $<v_{slip}>$ with *Bo* number starts at $Bo \sim O(10)$ when $BoCa \leq 1$ (panel (a) and panel (c)). This finding reveals that this *Bo* value is of great importance to characterize wet fluidization.

6.4.3 Comparison of Static and Dynamic Bridge Models

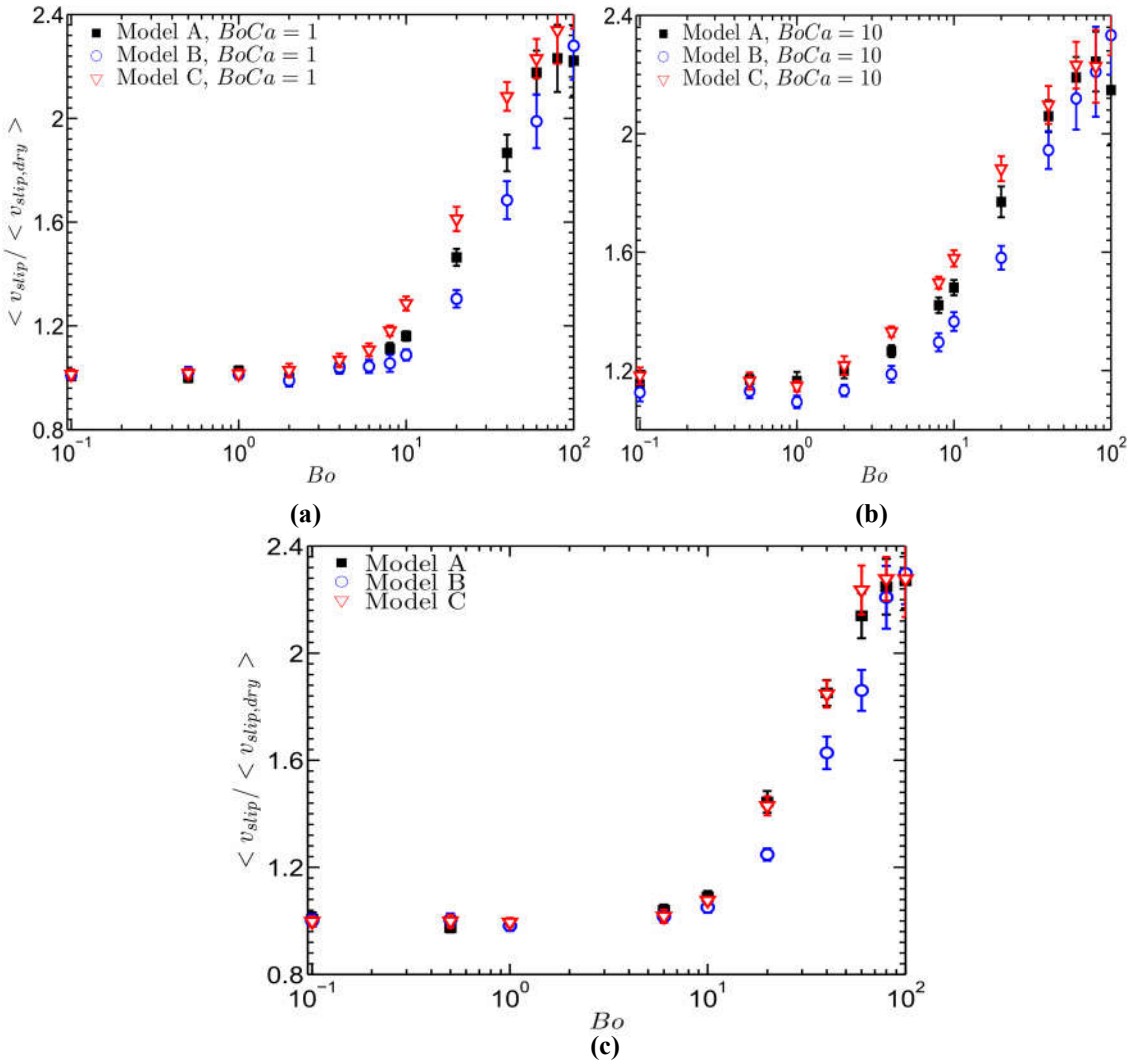

Figure 6.8: Domain average slip velocity for static bridge models A, B and C, compared with Bond number. Panel (a): $BoCa = 1$; Panel (b): $BoCa = 10$; Panel (c): $Ca = 0$. The initial film height is $h_0^+ = 0.0037$.

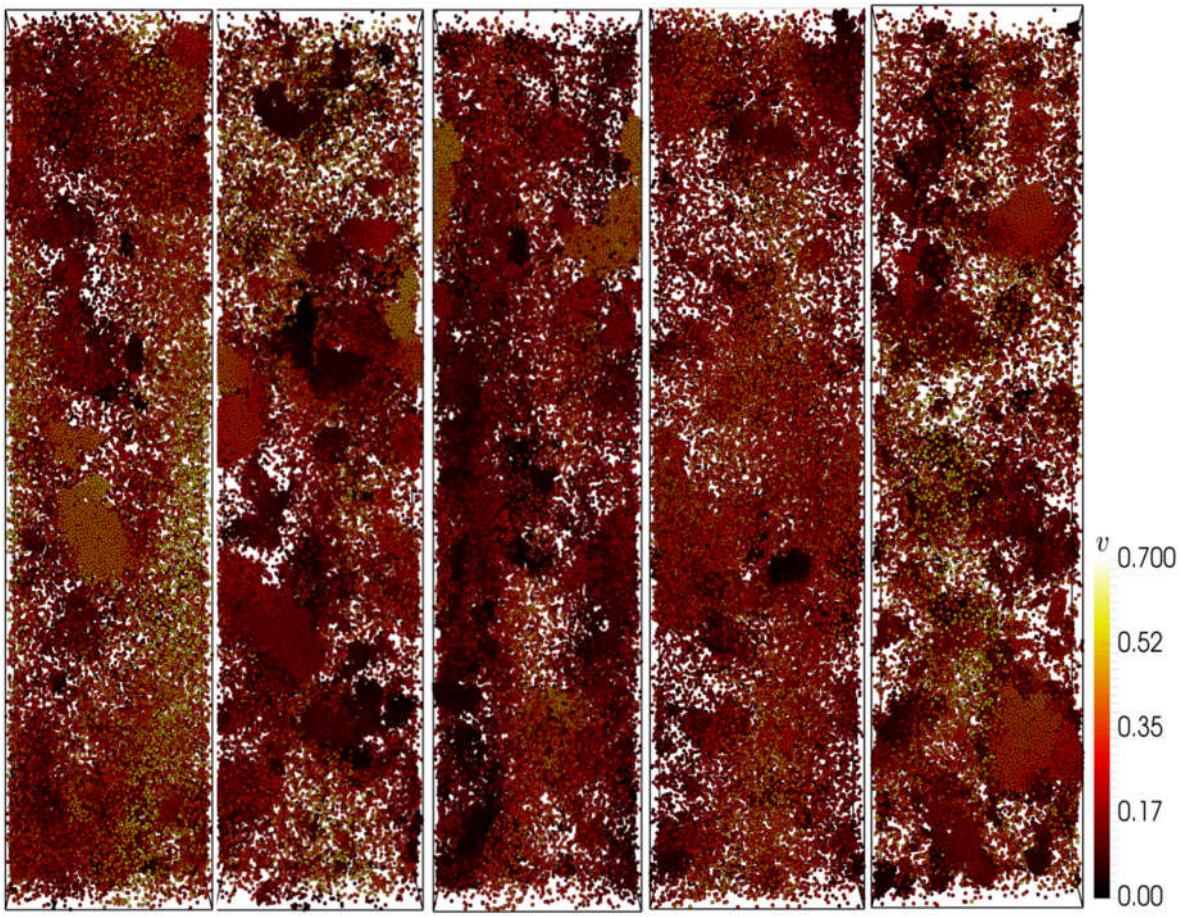

Figure 6.9: Snapshots of system morphology for three bridge models and various *BoCa* numbers at *Bo* = 20, initial film height h_0^+=0.0037.

All data in Figure 6.8 compares the difference among model A, model B and modelC when predicting the domain average slip velocity with varying *Bo* number and three *BoCa* numbers (panel (a): *BoCa* = 1, panel (b): *BoCa* = 10, panel (c): as well as no viscous effects, i.e., *BoCa* = 0). The results of Figure 6.9 are obtained considering an initial film height of h_0^+= 0.0037. As seen from Figure 6.9, all three models show a similar fluidization behavior. Again, *Bo* ~ *O* (1) demarcates the transitional point for the marked increase of the slip velocity with increasing *Bo* number. In addition, we found that model C always requires a greater slip velocity to balance the pressure drop which is used to determine the minimum fluidization velocity. Also, we find that model C is most sensitive to variations of the *BoCa* number. We can see that model C and model A present

more or less the same fluidization velocity when compared to model B if viscous effects are not present (see panel (c)). However, if we increase the *BoCa* number to a value of 0.1, we find that a disparity of the predicted slip velocity between model A and C appears, i.e., model C requires a greater slip velocity to balance the weight of the particles due to the formation of larger aggregates. Furthermore, model C predicts always larger cohesive forces than model B (as indicated by higher slip velocities, i.e., larger agglomerates) because model C always present more liquid bridge volume compared to model B.

Figure 6.9 show snapshots of system's particle velocity distribution for various Bond number and *BoCa* numbers. Snapshots are obtained based on an initial film height h_0^+=0.0037 and $BoCa = 20$. Figure 6.9 illustrates that the fluidization behaviors of the particle system is more or less the same for three bridge models using the same simulation parameters. Model A and model C show slightly larger inhomogeneities compared to that predicted by model B in case viscous forces are considered. However, the disparity between the bridge models after turning off viscous effects (i.e., setting $BoCa = 0$, see panel (a), panel (d)) is less pronounced. In summary, one can observe in these snapshots that viscosity helps accelerating agglomeration of particles. This trend has also been observed in experimental studies[37] before.

Figure 6.10 illustrates the average number of bridges per particle for the three bridge models with varying Bo number and using two different *BoCa* numbers (panel (a): $BoCa = 1$, panel (b): $BoCa = 10$). The results are based on an initial film height $h_0^+ = 0.0037$. As seen from Figure 6.10**,** the number of liquid bridges increases with increasing *Bo* number. This is easy to understand physically because the increasing level of cohesion in the fluidized bed will result in more particles heterogeneities, i.e., larger agglomerates. If we compare panel (a) and panel (b), we found that case setups characterized by larger *BoCa* values have a larger number of contacts between particles. This indicates that the increase of *BoCa* number also enhances the extent of particle agglomeration as expected.

Moreover, when we compare the number of contacts between the three bridge models, we find that simulations with model C always predicts a greater amount of particle contacts, especially if the *Bo* number is larger than 10. This finding agrees with the previous one in Figure 6.8 that (i) the *Bo* number is a key parameter to characterize wet fluidized bed, and that (ii) depending on the *Bo* and *BoCa* number the choice of an advanced liquid bridge filling model is justified.

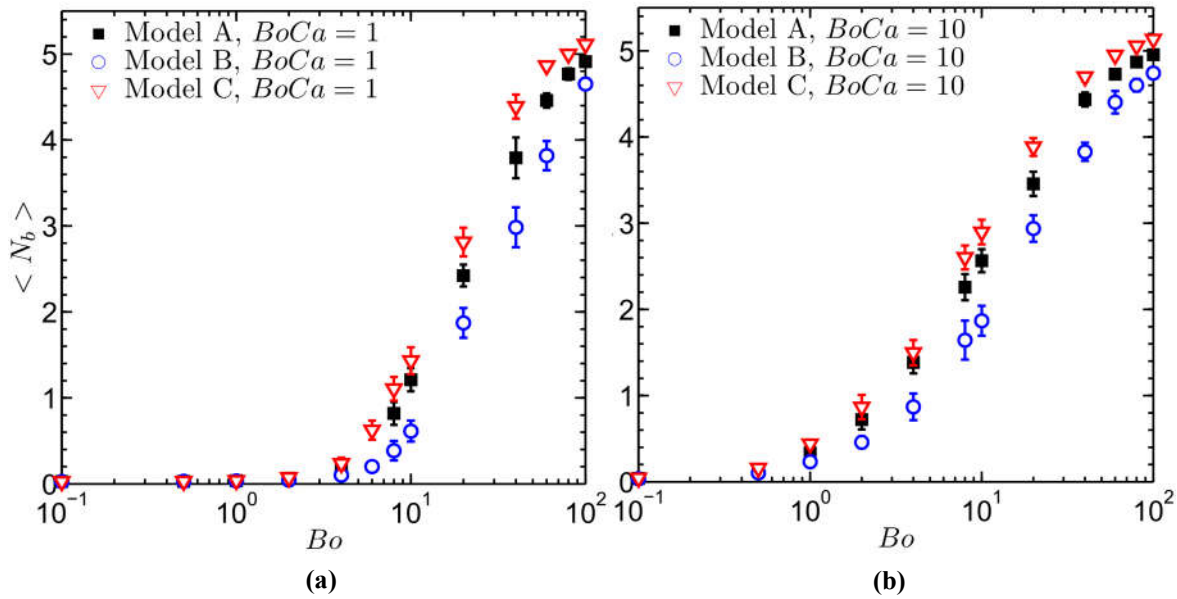

Figure 6.10: Average number of bridges per particle for three different bridge models versus the Bond number, initial fil height h_0^+=0.0037

Figure 6.11 illustrates the average number of bridges of each particle in the computational domain predicted by each of the three bridge filling models. The results are obtained based on $Bo = 20$, $BoCa = 1$, an initial film height of $h_0^+ = 0.0037$ and particle volume fraction of $\phi_p = 0.05$. Despite the fact that we consider only a single snapshot, we can infer from Figure 6.11 that the inhomogeneity of particle clusters predicted by model C (panel (c)) is tentatively larger compared to that predicted by the other two models. This highlights that the number of contacts per particle of model C is also larger. Moreover, as seen in the enlarged domain of panel (c), we observe that the number of contacts in agglomerated

regions (indicated by bright colors) is higher than in disperse regions (dark color), indicating that wet fluidized agglomerates are indeed densely packed.

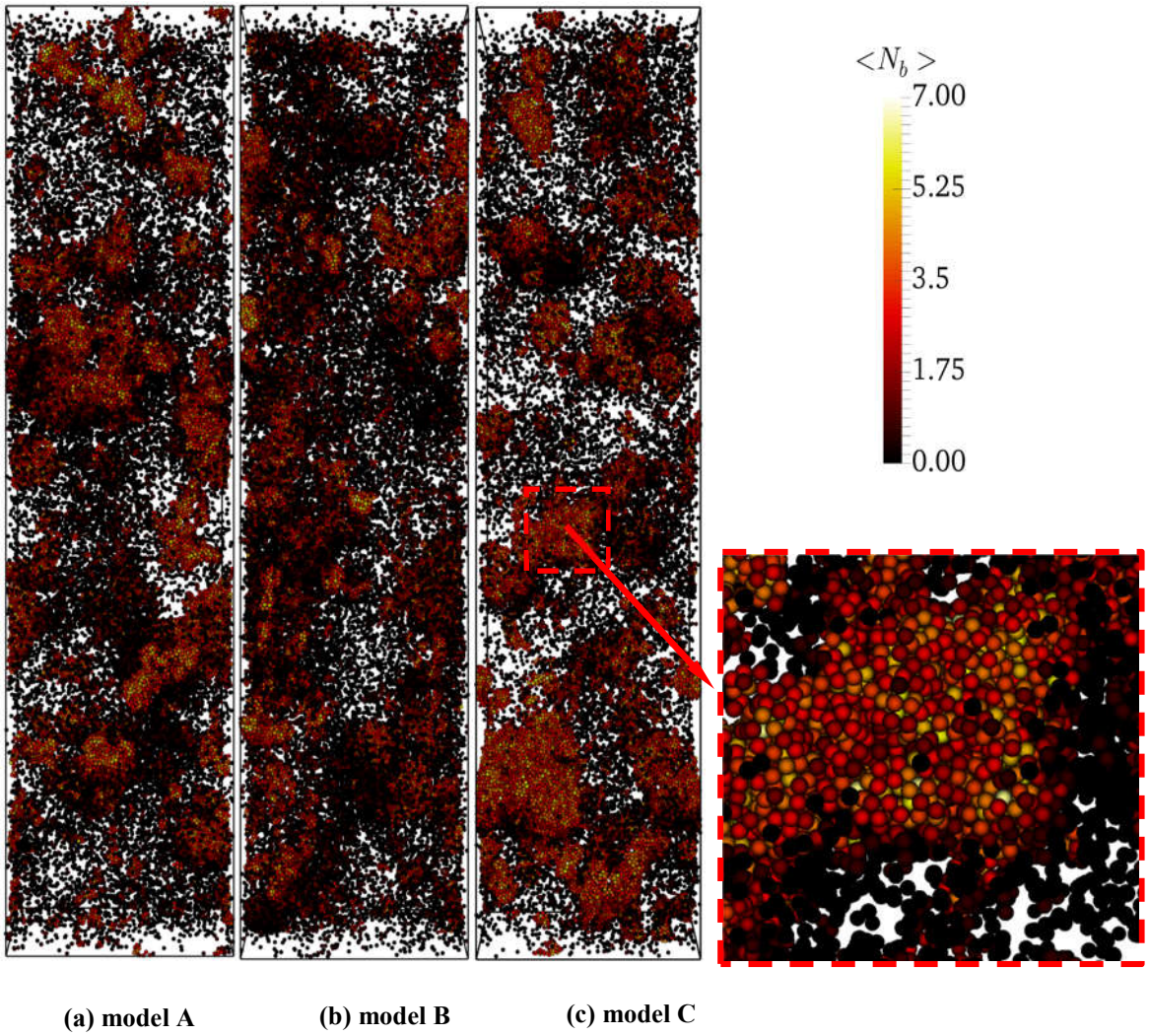

(a) model A **(b) model B** **(c) model C**

Figure 6.11: Snapshots average number of bridges for each particle for the three bridge models (*Bo* = 20, *BoCa* = 1 and ϕ_p = 0.05, h_0^+ = 0.0037).

6.4.4 Effect of the Global Liquid Content

Figure 6.12 shows the initial film height effect on the slip velocity for various *Bo* numbers at *BoCa* = 1 and for all three different bridge models. As seen from Figure 6.12, the initial film height indeed affects the fluidization behavior as predicted by all three bridge models. Clearly, cases initialized with more liquid generate larger agglomerates in the fluidized bed, necessitating a bigger slip velocity $<v_{slip}>$ to balance the weight of the particles in the simulation domain. In

addition, as observed from Figure 6.12, the obvious increase in slip velocity with increasing *Bo* number starts at $Bo \sim O(1)$. This indicates that the Bond number is of great importance in characterizing wet fluidized beds.

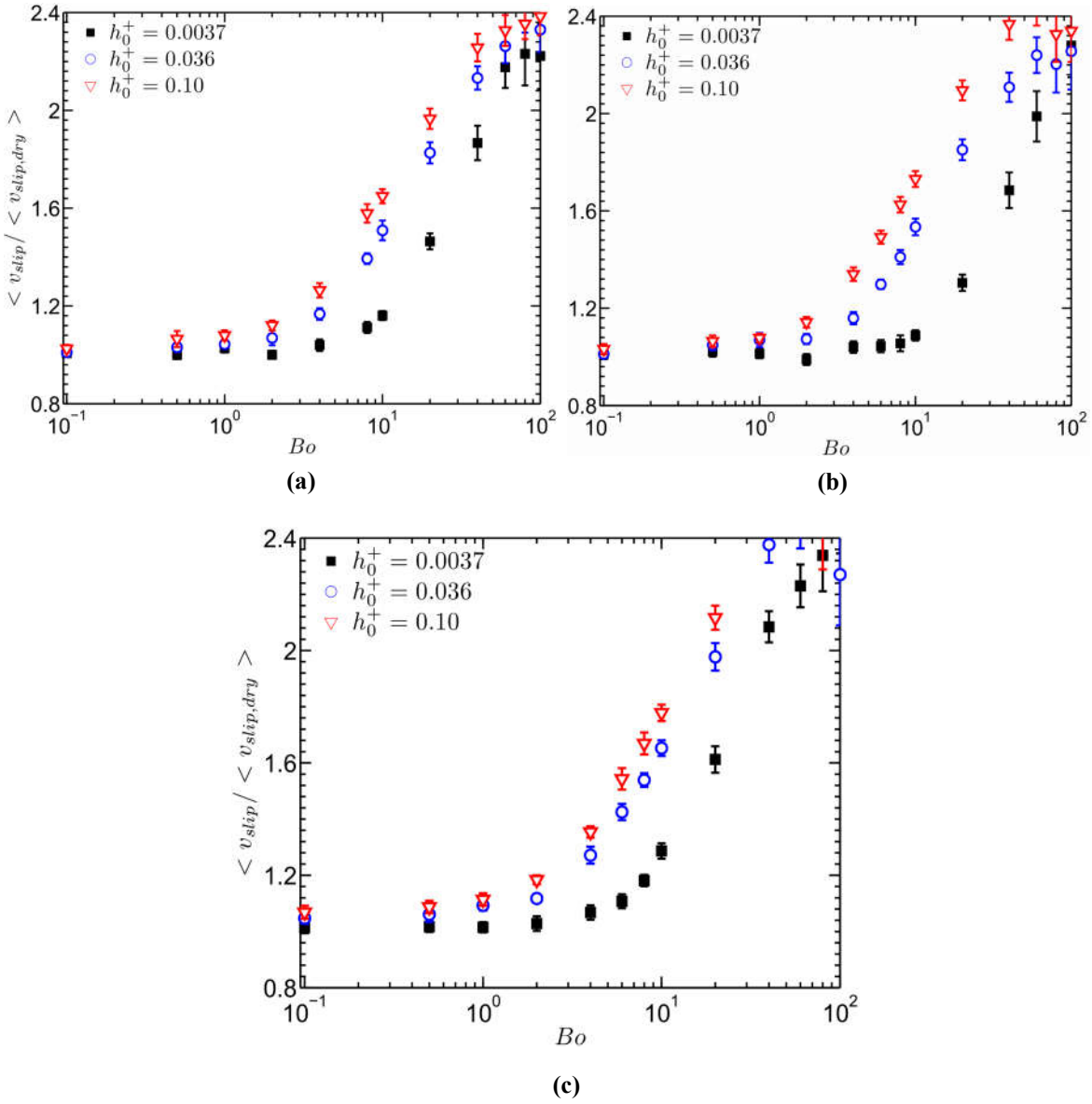

Figure 6.12: Effect of the initial film height h_0^+ on the domain-average slip velocity for various of Bond numbers *Bo*, and *BoCa* = 1. Panel (a): model A; Panel (b): model B; Panel (c): model C.

Furthermore, Figure 6.13 gives a comparison of how the three different bridge models effect the prediction of the slip velocity. While some quantitative differences can be identified, especially when comparing model B and model C, the predictions for all bridge models are similar, though. Most important, we find

that the liquid bridge loading level has a much stronger effect on the behavior of the fluidized beds compared to the effect due to the choice of the bridge model (compare Figure 6.12 and Figure 6.13).

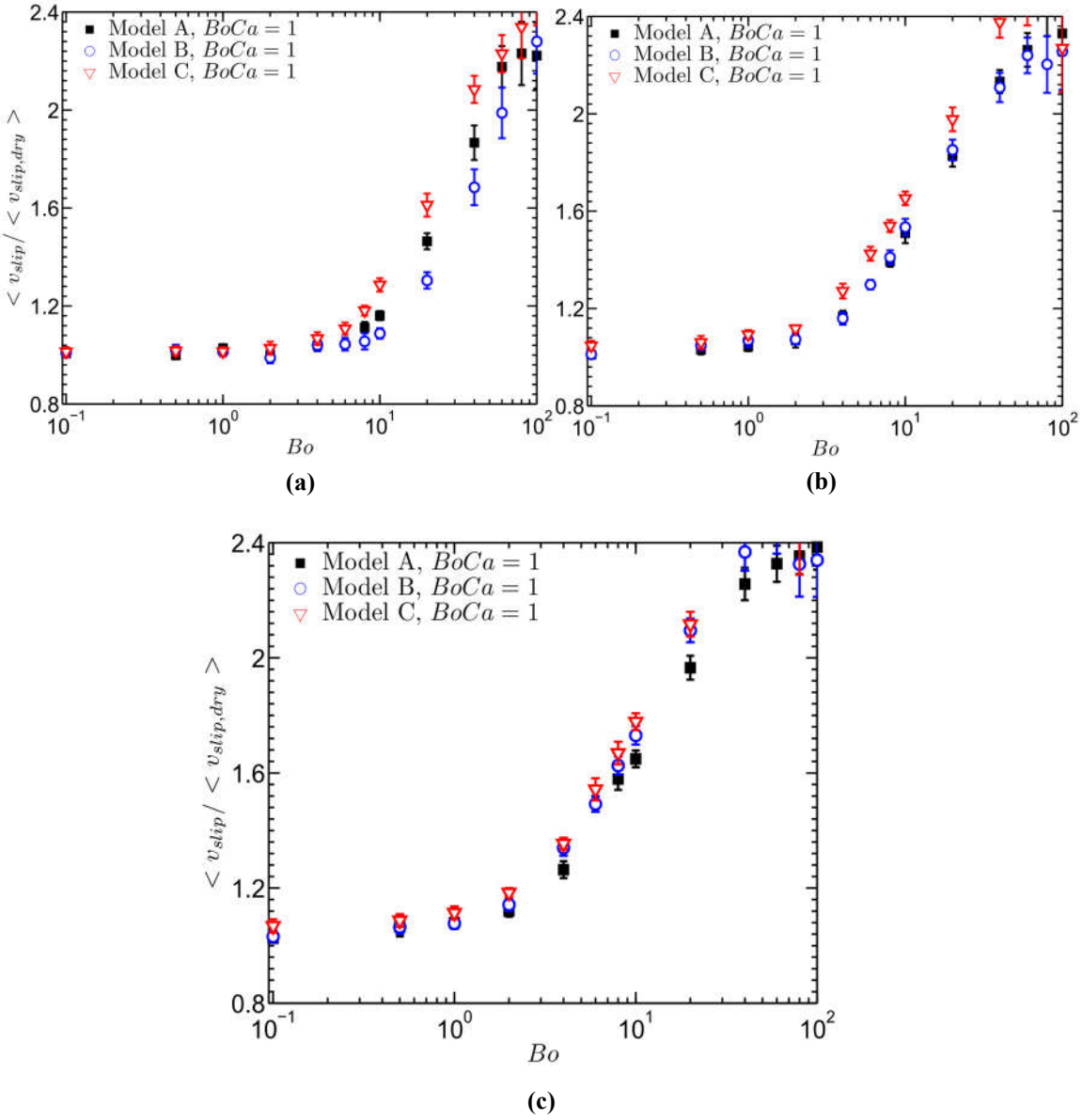

Figure 6.13: Comparison of the domain averaged slip velocity predicted by models A, B and C for various Bond numbers *Bo* and *BoCa* = 1 using different initial film heights: panel (a): h_0^+=0.0037; panel (b): h_0^+=0.036; panel (c): h_0^+=0.10.

6.4.5 Partitioning of Liquid between Surface and Bridge

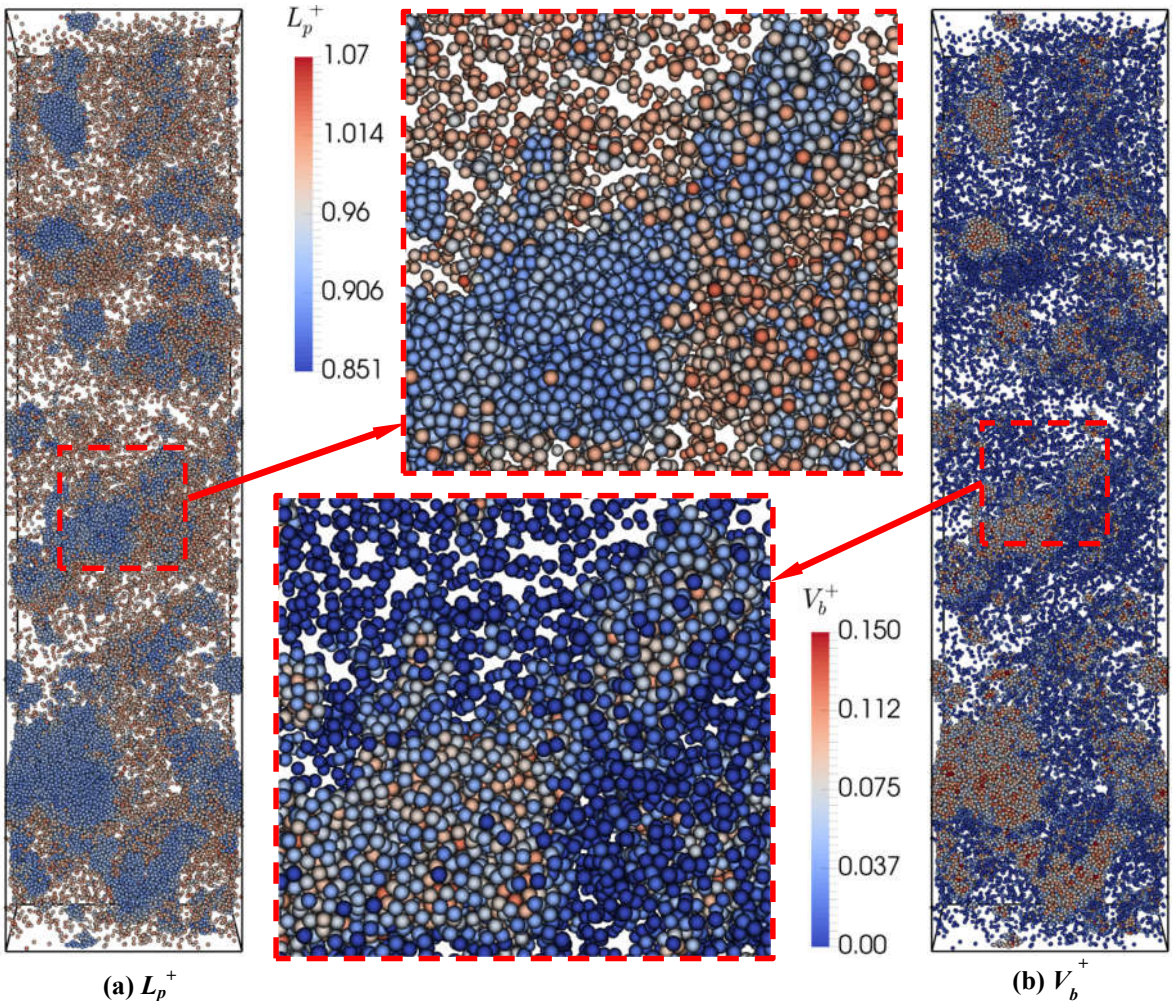

Figure 6.14: Snapshots illustrating the liquid distribution predicted by model C and Bo = 20, $BoCa$ = 1 and a film height h_0^+= 0.0037, panel (a): liquid amount present on the particle surface; panel (b): liquid in bridges between particles.

Figure 6.14 shows snapshots of the per-particle liquid content and amount present in liquid bridges (model C) for a system characterized by Bo = 20, $BoCa$ = 1 and initial film height h_0^+= 0.0037. Panel (a) shows the amount of liquid L_p^+ present on the particle surfaces in the simulation domain. As seen in the enlarge domain of panel (a), more liquid is present on the particle surfaces in comparably dilute regions, whereas less liquid is present on the particle surface in dense regions formed by agglomerates. Panel (b) shows the liquid bridge volume present between particles in the simulation domain. As seen in the enlarge domain of panel (b), the relative amount of liquid bridge volume present in the

agglomerates is higher than in comparably dilute regions. Figure 6.14 indicates that liquid is transferred from the particle surface to the bridge region when particles contact each other. As more particles are in contact, more liquid is transferred to the bridge regions and the larger the cohesive forces that prevent the agglomerate to break up. Interestingly, it appears that the total amount (i.e., the sum of liquid on the surface and in the bridge) is approximately constant throughout the computational domain. Since we have assumed that liquid was initially uniformly dispersed in the computational domain, this indicates that there is no strong tendency for a net transport of liquid towards agglomerates. In summary, we can support the hypothesis of a fixed total amount of liquid per particle in case liquid is initially well dispersed.

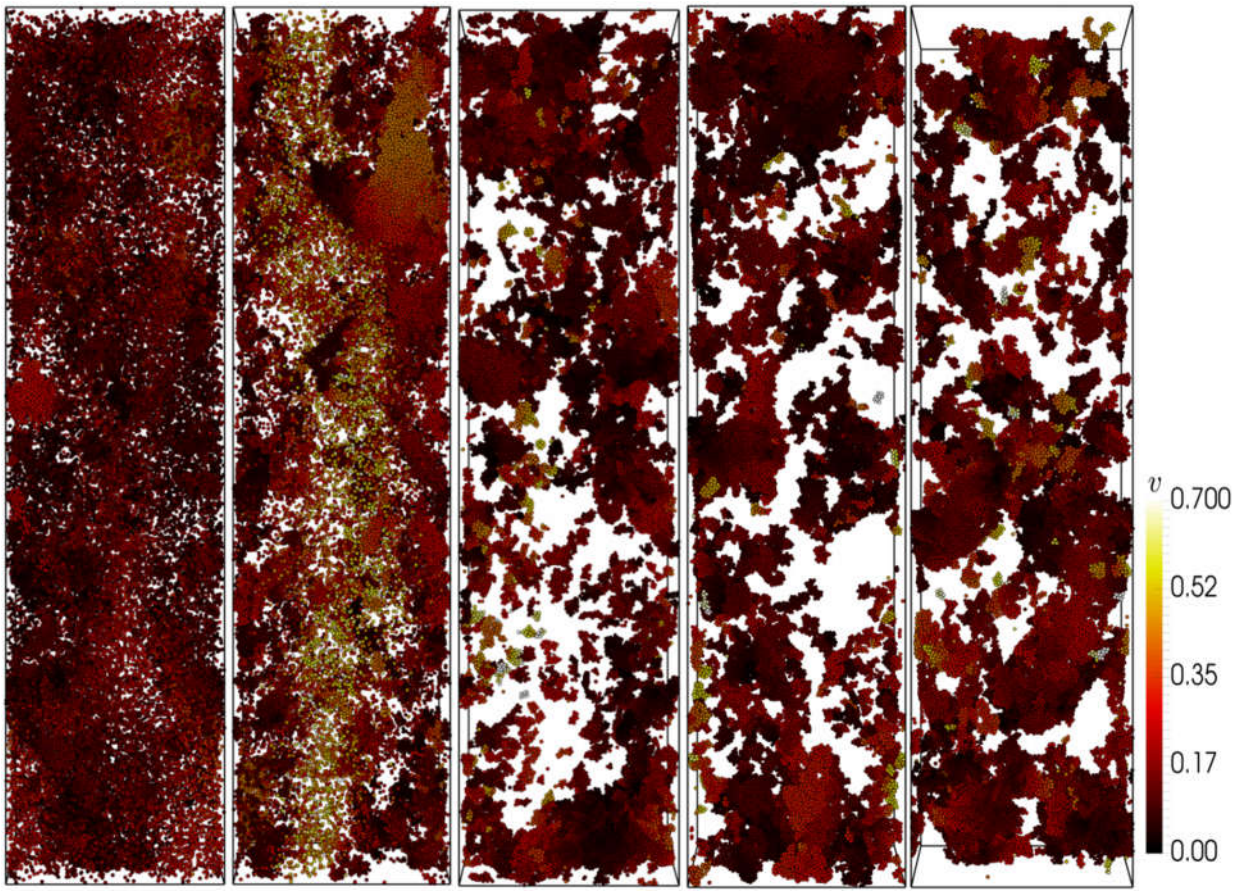

(a) *BoCa* = 0.25 **(b) *BoCa* =9** **(c) *BoCa* = 90** **(d) *BoCa* =360** **(e) *BoCa* = 1000**

Figure 6.15: Snapshots of system morphology for various *BoCa* numbers and a fixed Bond number of *Bo* = 10. The particle volume fraction in this domain is 0.05, and the initial film height is h_0^+ = 0.0037 (model C).

6.4.6 Influence of Viscosity

Figure 6.15 shows snapshots for wet systems for various *BoCa* numbers with a fixed Bond number of $Bo = 10$ and an initial film height of $h_0^+ = 0.0037$. Figure 6.15 correspond to model C, i.e., data for the slip velocity is represented by red triangles in Figure 6.16. Figure 6.15 and 6.16 illustrate that a comparably large change in the *BoCa* number is needed to result in a change of the inhomogeneous particle structures: panel (a) is obtained for conditions corresponding to very small *BoCa* values (i.e., the low *BoCa*-plateau shown in Figure 6.16); panel (b) represents typical conditions for the "lower rising region" shown in Figure 6.16, panel (c) illustrates a situation at the transition point at which model C gives different predictions than model B and C, and panels (d) and (e) represent conditions at very high *BoCa* numbers for which the slip velocity appears to level off again.

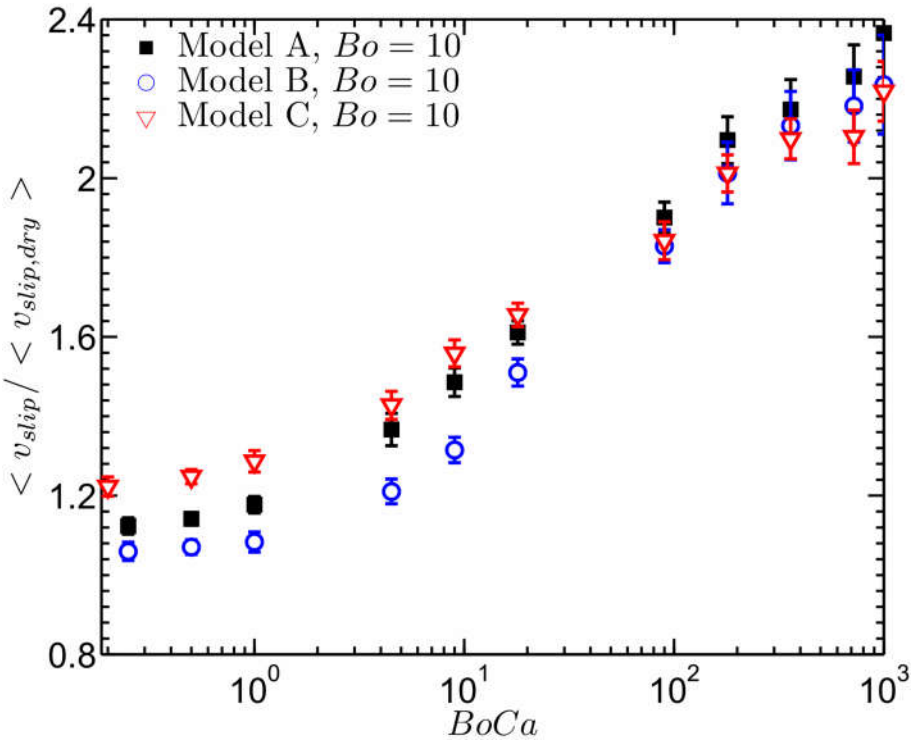

Figure 6.16: Comparison of domain-averaged slip velocity predicted by the three bridge models versus *BoCa* number and a fixed Bond number of *Bo=10*. The particle volume fraction in the domain is 0.05, and the initial film height is $h_0^+ = 0.0037$.

Figure 6.16 shows the results of slip velocity for various Bond numbers (but fixed *Bo* number), using the same conditions as used to prepare Figure 6.15. However, Figure 6.16 is also used to compared predictions made by thee three different bridge models. We can see from Figure 6.16 that the slip velocity $<v_{slip}>$ increases with increasing *BoCa* number, and that this increase in slip velocity is caused by an increasing amount of inhomogeneity in the particle distribution. Furthermore, we can observe from Figure 6.16 that model C predicts stronger agglomerate formation than other two models for $BoCa < 100$, while the opposite is true for larger *BoCa* values. This demonstrates that $BoCa = 100$ is of a certain importance when choosing a liquid bridge filling model for simulation wet fluidized beds: for systems with low to moderately high viscosities (characterized by *BoCa* between ca. 1 and 100) the liquid drainage rate appears to affect the partitioning between "surface liquid" and "bridge liquid". Clearly, for these systems the predictions of model C gradually approach that of model B, indicating that the liquid drainage rate affects the extent of agglomeration. If we further increase the *BoCa* number of the system, the effect of a finite drainage rate is reduced since the agglomerates span almost the totality of the computational domain. In summary, for systems characterized by $BoCa > 100$ it appears to be of lower importance to correctly predict the drainage rate (in systems in which liquid is initially well dispersed) since cohesive forces are dominating.

6.4.7 Regime Map for Effect of Model Details

As discussed in the previous section, both capillarity- and viscosity-based forces affect the particles' agglomerate behaviour, and in some regions of the parameter space the liquid bridge filling model is of importance. Therefore, when building a regime map that should help deciding which bridge model is appropriate, one must consider both the *Bo* and *BoCa* number. Also, the initial film height plays a certain role, however, we here avoid this complication since film heights are often anyhow not known accurately.

We have constructed the map shown in Figure 6.17 by considering that situations in which the prediction of model C differs more than 10% from that of the other models, model C is recommended due to its ability to model transient filling effects. Also, we consider regions characterized by very high *Bo* and *BoCa* as "false fluidization", since they result in the formation of a single, unphysically-large agglomerate in our simulation domain see (Figure 6.5, panel f). Finally, we have indicated a region denoted as "agglomerate retention region" in Figure 6.17, which is based on the findings of Boyce et al.[38–40] Specifically, in this region a dynamic bridge filling model (i.e., model C) is necessary to picture the spreading of liquid initially not homogeneously distribution in the particle bed.

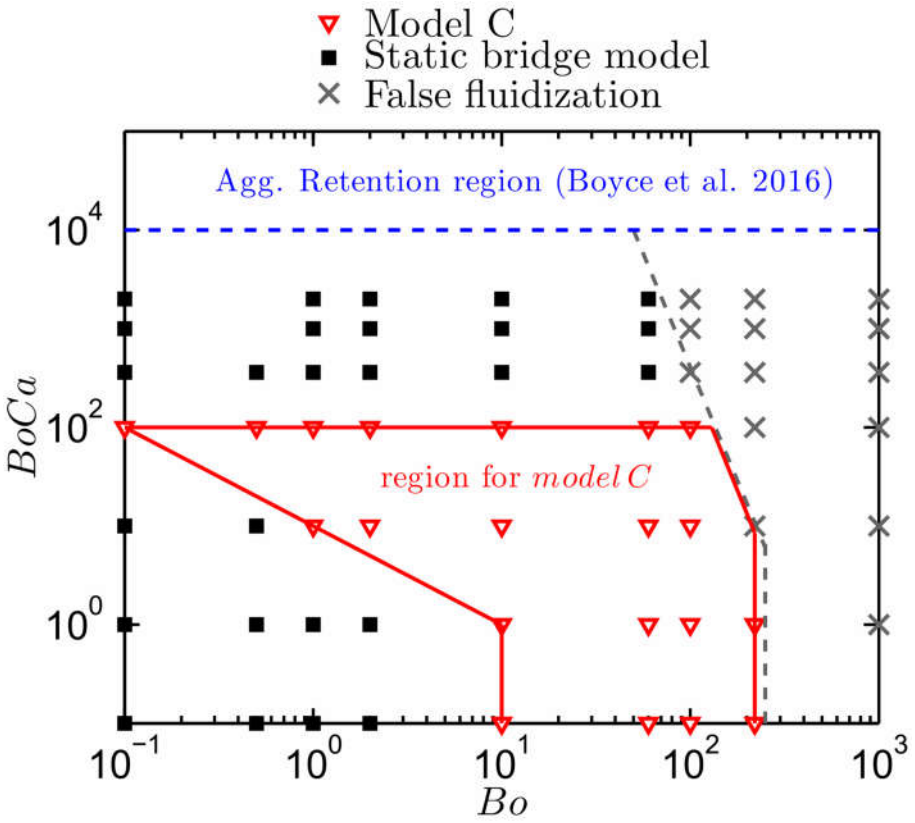

Figure 6.17: Regime map for wet fluidization indicating regions in which the use of model C critically affects the prediction of the sedimentation speed.

Figure 6.17 indicates that certain criteria are required to justify usage of a dynamic liquid bridge filling model. First, agglomeration must occur, i.e., the *Bo* number must be $O(1)$ or larger. Second, for intermediate values of *BoCa* agglomerate formation is not affected by the filling rate of the bridge, since the

liquid amount available at the instance when the collision occurs is sufficient to led the particles stick. Third, we find that there is no lower bound of the *BoCa* region, i.e., viscous effects are irrelevant when deciding whether model C should be used or not. Physically, this means that even in case of an infinite filling rate (i.e., zero viscosity) one must consider the amount of liquid that can be "harvested" from the surface of the particle surface.

6.5 Conclusions

We employ a CFD-DEM approach to study the fluidization behavior of wet particles in small periodic domain based on newly developed bridge filling models (model B and model C) and the well-known model of Shi and McCarthy[1] (model A). For the particle system considered, we find that the dynamic filling model (model C) has a small but significant effect on particle agglomeration, and consequently of the slip velocity, for some combinations of system parameters. It is now instructive to recall that the rupture energy of a liquid bridge strongly depends on the liquid bridge volume, but not the liquid bridge force at contact. Thus, we conclude that the behaviour of wet fluidized particle system is mainly governed by agglomerate deformation and not agglomerate formation: we speculate that the average sedimentation speed (and hence the average size) of agglomerates depends critically on how easy it is to rearrange the particles inside such an agglomerate. Indeed, an inspection of the transient behaviour of the particles in our simulations indicates that the initial formation of aggregates is very fast, i.e., in the order of a few reference time scales $t_{ref} = u_t / g$. Note, our simulations must be run typically in the order of 100 t_{ref}, i.e., much longer, to collect meaningful statistics. Hence, the formation of the aggregate certainly cannot be rate limiting, and using arguments simply based on the outcome of a single collision (i.e., a "wet" restitution coefficient) are less useful. In summary, the ability of agglomerates to break is controlled by the bridge forces at particles contact, explaining the often marginal effect of the liquid bridge filling model

We would like to view our results also in the light of the recent findings of Boyce et al.[38,39], who studied partially-wetted fluidized beds of particles over a range of Bond and capillary numbers (i.e., up to 100 and 1,000, respectively). This previous research also concluded that an "agglomerate breakup" regime exists, in line with our findings. The key difference between the work of Boyce et al.[39,40] is that they were able to also identify an "agglomerate retention region", which is absent in our simulations since we assume that liquid is homogeneously spread initially. Anyhow, it is clear that an initial non-uniform liquid distribution will support arguments for using model C, since the liquid spreading rate (which is strongly affected by the bridge filling rate) affects system behaviour in addition.

To sum up, the key findings of the present study can summarized as follows:

- liquid bridge forces lead to a clustering behavior that is qualitatively different from that of non-cohesive powders, and increases the gas speed that is required to support the weight of the particles. While this finding was previously put forward by Girardi et al., we established a quantitative understanding how the capillary number affects the required fluidization speed.
- The dimensionless film height appears to be the critical parameter that governs system behavior. It is therefore clear that future research should aim on refining the simple picture of a uniform film height on a single particle.
- Both the *Bo* and the *BoCa* number affect the bed's fluidization behavior. Increases of both the *Bo* number and the *BoCa* number increase the inhomogeneity of the wet fluidized system. Consequently, this requires higher gas-particle slip velocity to balance the weight of the agglomerates. However, the effects due to an increase of *BoCa* are of lower significance than that caused by an increase of the Bond number.
- There exists a maximum *Bo* number that allows one to fluidize the particles in a domain of limited spatial extent. Systems that are characterized by *Bo*

numbers exceeding this maximum value should be avoided, since the wet bed of particles cannot be fluidized.

- Liquid transfer rates from the particle surface to the bridge in the regime of relatively low to moderately high viscosity levels (i.e., $BoCa < 100$ and intermediate Bond numbers) become the rate limiting step, i.e., they affect agglomerate size and sedimentation speed. Thus, in this regime we recommend to choose a dynamic bridge model (model C) for simulation of wet fluidization.
- The dynamic filling model (model C) predicts a different fluidization behavior when the system is characterized by a small *BoCa* number. Therefore we suggest model C for this *BoCa* region ($BoCa < 100$). Static bridge models (i.e., model A and B) could be used in situations for which $BoCa > 100$ and the liquid is ensured to be uniformly distribution. For an initially non-uniform liquid distribution, however, model C is recommended even for large values of *BoCa*, since liquid spreading becomes rate limiting. Recalling that the capillary number can be interpreted as the ratio of bridge filling time and a characteristic time between collisions (Boyce et al.[39,40]), it appears that a simple criterion for judging the effect of liquid spreading is the capillary number.

Again, we would like to stress that a critical limitation of our current work was the assumption that liquid is uniformly distributed on the particle surface. Clearly, in case of high *Ca* numbers liquid spreading rates can be limited (to some extend) by bridge filling. In such a case, one would also clearly prefer a dynamic liquid bridge model to realistically picture the transport of liquid throughout the system. Finally, future work could probe the effect of particles stiffness, as well as work towards suitable experimental validation. Unfortunately, the latter is difficult due to difficulties to accurately measure the liquid distribution in moving granular materials.

6.6 Appendices

Appendix E: Verification and Validation of Model C to Analytical Solution and Direct Numerical Simulation (DNS) Data

The model for liquid transport between two particles (see equation 6.11) has been implemented in the LIGGGHTS® software. This model describes the finite rate of liquid transport from the particle surface to the bridge region. Specifically, it describes liquid bridge formation using a filling rate coefficient a_i and mobility coefficients ϕ_m.

An analytical solution of equation 6.11 has been presented in the Appendix A of our previous work (Wu et al.[2]) in case the initial conditions were known (i.e., initial liquid contents L_p^+, and initial bridge volume V_b^+):

$$V_b^+ = V_{b,0}^+ + C_1 \frac{\frac{2r_1}{a_i} + 2\phi_{m1}}{r_1}\left(e^{r_1 t^+} - 1\right) + C_2 \frac{\frac{2r_2}{a_i} + 2\phi_{m1}}{r_2}\left(e^{r_2 t^+} - 1\right) \qquad \text{(E.1)}$$

Where $V_{b,0}^+$ is the initial bridge volume, which is a function of the initial film height and the separation distance between two particles surfaces. The expressions for C_1, C_2, r_1 and r_2 can be found in the Appendix A of Wu et al[2].

The DNS of liquid bridge formation between two particles has been performed by using the Volume of Fluid (VoF) approach, specifically the solver “interFoam” in OpenFOAM® software. Moreover, the bridge volume has been captured by defining the two neck positions based on the position of the thinnest liquid film on particle surfaces. Consequently, the bridge volume can be calculated by a direct integration method (DIM). Details about DNS simulation and calculation of bridge formation has been introduced in Wu et al.[2]

In order to verify the implementation of the dynamic bridge model (model C) in LIGGGHTS®, we compared the results to (i) an analytical solution (see equation

E1), as well as to (ii) DNS data of the corresponding two particles system. Specifically, we used the following parameters for our verification study:

- initial film heights of $h_0^+ = 0.08$, and $h_0^+ = 0.065$
- the particles separation is $S^+ = 0$.

We can see from both Figure E1 and Figure E2 that the DEM simulation results show exactly the same behavior as the analytical solution. Although the DNS data does not perfectly agree with the proposed model, the DNS data predicts the trend of liquid transfer from particle surfaces to bridge region where liquid bridge forms between two particles reasonably well. Therefore, we conclude that our model has been implemented correctly, as well as that the liquid bridge formation process has been predicted correctly when compared to DNS data.

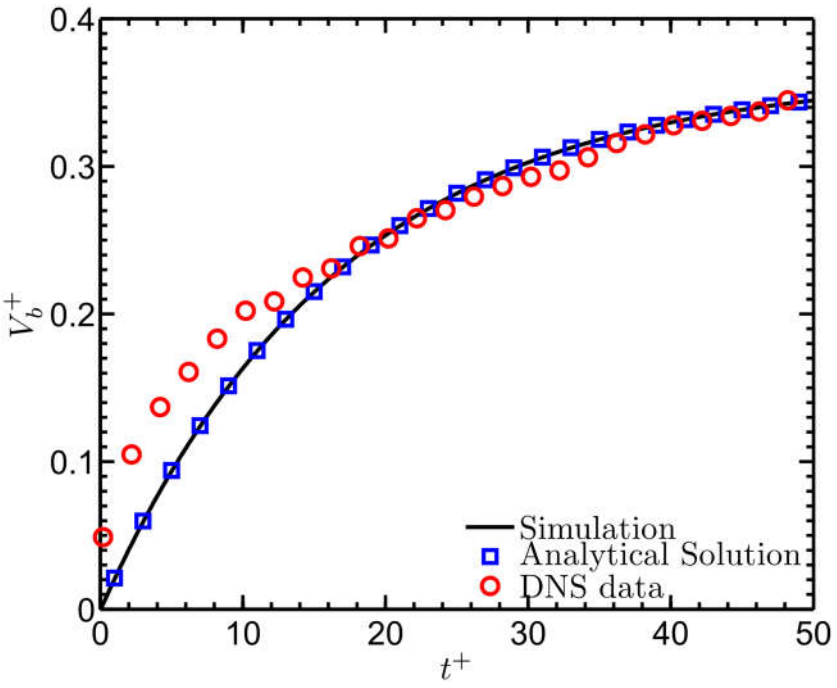

Figure E1: Liquid bridge volume over time for an initial film height of h_0^+=0.08 and a separation distance of S^+ =0: DEM simulated values (solid line) vs. analytical solution (blue squares) and DNS data (red circles)

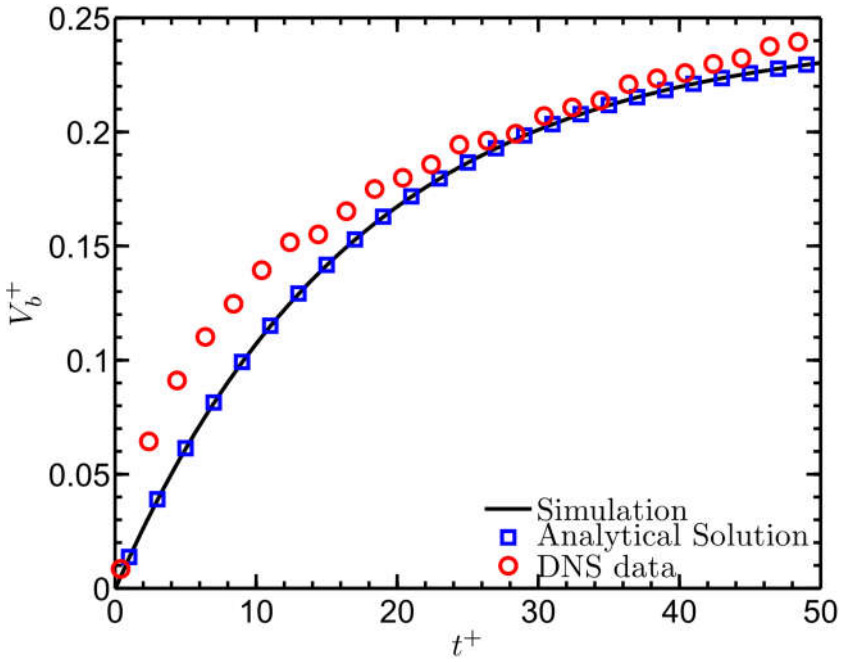

Figure E2: Liquid bridge volume over time for an initial film height of $h_0^+ = 0.065$ and a separation distance of $S^+ = 0$: DEM simulated values (solid line) vs. analytical solution (blue squares) and DNS data (red circles)

6.7 Nomenclature

Latin Symbols

a_i .....Dimensionless filling rate parameter [-]

Bo.....Bond number [-]

$BoCa$ .....Modified Capillary number [-]

Ca .....Capillary number [-]

d_p .....Particle diameter of the larger particle [m]

D.....Distance between particle surfaces [m]

DNS.....Direct Numerical Simulation

DEM.....Discrete element method

$\mathbf{f}_{g\rightarrow p,j}$ .....Interaction force on particle [kg· m· s^{-2}]

$\mathbf{f}_{d,i}$ .....Drag force [kg· m· s^{-2}]

Fr.....Froude number [-]

F_{cap} .....Capillary force [kg· m· s^{-2}]

F_{vis} .....Viscous force [kg· m· s^{-2}]

F_{tot} .....Total capillary and viscous forces [kg· m· s^{-2}]

g .....Gravity [m/s^2]

h_0 .....Average initial film height of the particle pair [m]

h_i .....Initial film height of particle i [m]

h_ε .....Particle surface roughness [m]

h_{rup} .....The rupture distance between two particlles [m]

I_i ..... Particle moment of inertia [kg · m^2]

k_n ..... Normal spring constant [kg/s^2]

k_t ..... Tangential spring constant [kg/s^2]

$L_{p,0}$ ..... Reference volume of liquid on the particle [m^3]

$L_{p,i}$ ..... Volume of liquid present on the particle i [m^3]

m_i ..... Mass of the particle i [kg]

$\mathbf{n}_{ij}$ ..... Unit normal vector [-]

N_b ..... Number of Liquid bridges [-]

N_p ..... Number of particles [-]

p_g ..... Gas phase pressure [Pa]

R ..... Particle radius [m]

Re_p ..... Particle Reynolds number [-]

S ..... Half separation distance between particles [m]

t ..... Time [s]

t_{ref} ..... Reference time scale [s]

$\mathbf{t}_{ij}$ ..... Unit tangential vector [-]

$\mathbf{T}_i$ ..... Torque on particle i [kg · m^2 · s^{-2}]

$\mathbf{u}_g$ ..... Ambient gas velocity [m · s^{-1}]

$< v_{slip} >$ ..... Domain-average slip velocity of wet fluidized beds [m · s^{-1}]

$< v_{slip,dry} >$ ..... Domain-average slip velocity of dry beds[m · s^{-1}]

V_b ..... Liquid bridge volume [m^3]

V_d .....Volume of the computational domain [m^3]

V_p .....Particle volume [m^3]

$V_{b,0}$ .....Initial bridge volume [m^3]

$V_{b,g}$ .....Geometrical bridge volume [m^3]

$\mathbf{v}_{p,i}$ .....Particle velocity [$m \cdot s^{-1}$]

$\mathbf{v}_{ij}^n$ .....Relative normal velocity of particle i and j [$m \cdot s^{-1}$]

$\mathbf{v}_{ij}^t$ .....Relative tangential velocity of particle i and j [$m \cdot s^{-1}$]

$\mathbf{v}_t$ .....Particle terminal setting velocity [$m \cdot s^{-1}$]

W_{cap} .....Rupture energy due to capillary force [$kg \cdot m^2 \cdot s^{-2}$]

W_{vis} .....Rupture energy due to viscous force [$kg \cdot m^2 \cdot s^{-2}$]

W_{tot} .....Total rupture energy [$kg \cdot m^2 \cdot s^{-2}$]

YLE .....Young-Laplace equation

Greek Symbols

$\beta_{p,i}$ .....Drag coefficient of particle i [$kg \cdot m^{-1}$]

δ_{ij}^n .....Overlap in normal direction between particle i and j [m]

δ_{ij}^t .....Overlap in tangential direction between particle i and j [m]

Δt .....Time step [s]

Δ_i .....Domain length in i direction [m]

Δ_{tp} .....Particle time step [s]

Δ_{tg} .....Fluid time step [s]

γ ..... Surface tension [N · s^{-1}]

$\gamma_{d,n}$ ..... Normal spring damping coefficient [kg · s^{-1}]

$\gamma_{d,t}$ ..... Tangential spring damping coefficient [kg · s^{-1}]

Λ ..... Dimensionless full bridge volume [-]

λ ..... Dimensionless half bridge volume [-]

μ_l ..... Dynamic viscosity of liquid [kg · m^{-1} · s^{-1}]

μ_g ..... Dynamic viscosity of ambient gas [kg · m^{-1} · s^{-1}]

μ_{pp} ..... Friction coefficient [-]

ω_i ..... Angular velocity of particle [s^{-1}]

ϕ_p ..... Particle volume fraction [-]

ϕ_{mi} ..... Fraction of liquid on particle i that is mobile to flow into the bridge [-]

$\mathbf{\Phi}_d$ ..... Force exerted by particles on fluid per unit volume [kg · m^{-2} · s^{-2}]

ρ_l ..... Density of the liquid [kg · m^{-3}]

ρ_g ..... Density of the ambient gas [kg · m^{-3}]

ρ_p ..... Density of the particles [kg · m^{-2}]

θ ..... Liquid-gas-particle contact angle [rad]

$\boldsymbol{\tau}_g$ ..... Gas phase stress tensor [kg · m^{-1}· s^{-2}]

Superscripts

+ ..... Dimensionless quantity

ref ..... Reference quantity

<> ..... Average quantity

i .....Particle index

$norm$ .....Normal direction

$tang$.....Tangential direction

t .....Terminal

p.....Particle

g.....Gas

6.8 References

[1] D. Shi, J.J. McCarthy, Numerical simulation of liquid transfer between particles, Powder Technol. 184 (2008) 64–75. doi:10.1016/j.powtec.2007.08.011.

[2] M. Wu, S. Radl, J.G. Khinast, A model to predict liquid bridge formation between wet particles based on direct numerical simulations, AIChE J. 62 (2016) 1877–1897. doi:10.1002/aic.15184.

[3] G. Toschkoff, J.G. Khinast, Mathematical modeling of the coating process, Int. J. Pharm. 457 (2013) 407–422. doi:10.1016/j.ijpharm.2013.08.022.

[4] R. Wilson, D. Dini, B. Wacherm, A Numerical Study Exploring the Effect of Particle Properties on the Fluidization of Adhesive Particles, AIChE J. 62 (2016) 1467–1477. doi:10.1002/aic.15162.

[5] T. Mikami, H. Kamiya, M. Horio, Numerical simulation of cohesive powder behavior in a fluidized bed, Chem. Eng. Sci. 53 (1998) 1927–1940. doi:10.1016/S0009-2509(97)00325-4.

[6] J.P.K. Seville, R. Clift, The effect of thin liquid layers on fluidisation characteristics, Powder Technol. 37 (1984) 117–129. doi:10.1016/0032-5910(84)80011-X.

[7] L.J. McLaughlin, M.J. Rhodes, Prediction of fluidized bed behaviour in the

presence of liquid bridges, Powder Technol. 114 (2001) 213–223. doi:10.1016/S0032-5910(00)00325-9.

[8] M. Wormsbecker, T. Pugsley, The influence of moisture on the fluidization behaviour of porous pharmaceutical granule, Chem. Eng. Sci. 63 (2008) 4063–4069. doi:10.1016/j.ces.2008.05.023.

[9] V.S. Sutkar, N.G. Deen, A. V. Patil, V. Salikov, S. Antonyuk, S. Heinrich, et al., CFD-DEM model for coupled heat and mass transfer in a spout fluidized bed with liquid injection, Chem. Eng. J. 288 (2016) 185–197. doi:10.1016/j.cej.2015.11.044.

[10] M. Askarishahi, M.-S. Salehi, S. Radl, Full-Physic s Simulations of Spray-Particle Interactionin a Bubbling Fluidized Bed, AIChE J. in press (2016). doi:http://dx.doi.org/10.1002/aic.15616.

[11] N. Epstein, J.R. Grace, Spouted and Spout-Fluid Beds- Fundamentals and Applications, Cambridge University Press, Cambridge, 2010. doi:http://dx.doi.org/10.1017/CBO9780511777936.

[12] P.K. House, M. Saberian, C.L. Briens, F. Berruti, E. Chan, Injection of a Liquid Spray into a Fluidized Bed: Particle-Liquid Mixing and Impact on Fluid Coker Yields, Ind. Eng. Chem. Res. 43 (2004) 5663–5669. doi:10.1021/ie034237q.

[13] K. Agrawal, P.N. Loezos, M. Syamlal, S. Sundaresan, The role of meso-scale structures in rapid gas–solid flows, J. Fluid Mech. 445 (2001) 151–185. doi:10.1017/S0022112001005663.

[14] S. Radl, C. Radeke, J.G. Khinast, S. Sundaresan, Parcel-Based Approach For The Simulation Of Gas-Particle Flows, 8th Interantional Conf. CFD Oil Gas, Metall. Process Ind. (2011) 1–10.

[15] Y. Igci, A.T. Andrews IV, S. Sundaresan, S. Pannala, T. O'Brien, Filtered two-fluid models for fluidized gas-particle suspensions, AIChE J. 54 (2008) 1431–1448. doi:10.1002/aic.11481.

[16] T.J. O'Brien, A multiphase turbulence theory for gas-solid flows: I. Continuity and momentum equations with Favre-averaging, Powder Technol. 265 (2014) 83–87. doi:10.1016/j.powtec.2014.01.030.

[17] S. Schneiderbauer, S. Pirker, Filtered and heterogeneity-based subgrid modifications for gas-solid drag and solid stresses in bubbling fluidized beds, AIChE J. 60 (2014) 839–854. doi:10.1002/aic.14321.

[18] J. Capecelatro, O. Desjardins, R.O. Fox, Numerical study of collisional particle dynamics in cluster-induced turbulence, J. Fluid Mech. 747 (2014) R2. doi:10.1017/jfm.2014.194.

[19] N.G. Deen, M. Van Sint Annaland, M.A. Van der Hoef, J.A.M. Kuipers, Review of discrete particle modeling of fluidized beds, Chem. Eng. Sci. 62 (2007) 16. doi:10.1016/j.ces.2006.08.014.

[20] S. Tenneti, S. Subramaniam, Particle-Resolved Direct Numerical Simulation for Gas-Solid Flow Model Development, Annu. Rev. Fluid Mech. 46 (2014) 199–230. doi:10.1146/annurev-fluid-010313-141344.

[21] W.D. Fullmer, C.M. Hrenya, The Clustering Instability in Rapid Granular and Gas-Solid Flows Granular medium: solid particles in the absence of an interstitial (carrier) phase or in the presence of a negligible gas phase, Annu. Rev. Fluid Mech. 49 (2017) 485–510. doi:10.1146/annurev-fluid-010816-060028.

[22] B. Crüger, V. Salikov, S. Heinrich, S. Antonyuk, V.S. Sutkar, N.G. Deen, et al., Coefficient of restitution for particles impacting on wet surfaces: An improved experimental approach, Particuology. 25 (2016) 1–9. doi:10.1016/j.partic.2015.04.002.

[23] C.M. Donahue, C.M. Hrenya, R.H. Davis, Stokes's cradle: Newton's cradle with liquid coating, Phys. Rev. Lett. 105 (2010) 34501. doi:10.1103/PhysRevLett.105.034501.

[24] P. Darabi, K. Pougatch, M. Salcudean, D. Grecov, A novel coalescence

model for binary collision of identical wet particles, Chem. Eng. Sci. 64 (2009) 1868–1876. doi:10.1016/j.ces.2009.01.017.

[25] S. Herminghaus, Dynamics of wet granular matter, Adv. Phys. 54 (2005) 221–261. doi:10.1080/00018730500167855.

[26] C.D. Willett, M.J. Adams, S.A. Johnson, J.P.K. Seville, Capillary bridges between two spherical bodies, Langmuir. 16 (2000) 9396–9405. doi:10.1021/la000657y.

[27] O. Pitois, P. Moucheront, X. Chateau, Liquid Bridge between Two Moving Spheres: An Experimental Study of Viscosity Effects., J. Colloid Interface Sci. 231 (2000) 26–31. doi:10.1006/jcis.2000.7096.

[28] M. Girardi, S. Radl, S. Sundaresan, Simulating wet gas-solid fluidized beds using coarse-grid CFD-DEM, Chem. Eng. Sci. 144 (2016) 224–238. doi:10.1016/j.ces.2016.01.017.

[29] C. Kloss, C. Goniva, A. Hager, S. Amberger, S. Pirker, Models , algorithms and validation for opensource DEM and CFD-DEM, Prog. Comput. Fluid Dyn. 12 (2012) 140–152. doi:10.1504/PCFD.2012.047457.

[30] R. Beetstra, M. a. van der Hoef, J. a. M. Kuipers, Drag force of intermediate Reynolds number flow past mono- and bidisperse arrays of spheres, AIChE J. 53 (2007) 489–501. doi:10.1002/aic.11065.

[31] P.A. Cundall, O.D.L. Strack, A discrete numerical model for granular assemblies, Géotechnique. 29 (1979) 47–65. doi:10.1680/geot.1979.29.1.47.

[32] B. Mohan, C. Kloss, J. Khinast, S. Radl, Regimes of liquid transport through sheared beds of inertial smooth particles, Powder Technol. 264 (2014) 377–395. doi:10.1016/j.powtec.2014.05.045.

[33] G. Lian, C. Thornton, M.J. Adams, A Theoretical Study of the Liquid Bridge Forces between Two Rigid Spherical Bodies, J. Colloid Interface Sci. 161 (1993) 138–147. doi:http://dx.doi.org/10.1006/jcis.1993.1452.

[34] O. Pitois, P. Moucheront, X. Chateau, Rupture energy of a pendular liquid

bridge, Eur. Phys. J. B. 23 (2001) 79–86. doi:10.1007/s100510170084.

[35] J. Li, J.A.M. Kuipers, On the origin of heterogeneous structure in dense gas-solid flows, Chem. Eng. Sci. 60 (2005) 1251–1265. doi:10.1016/j.ces.2004.09.083.

[36] H. Xu, W. Zhong, Z. Yuan, A. Yu, CFD-DEM study on cohesive particles in a spouted bed, Powder Technol. (2016). doi:10.1016/j.powtec.2016.09.006.

[37] G. Book, K. Albion, L. Briens, C. Briens, F. Berruti, On-line detection of bed fluidity in gas-solid fluidized beds with liquid injection by passive acoustic and vibrometric methods, Powder Technol. 205 (2011) 126–136. doi:10.1016/j.powtec.2010.09.002.

[38] C.M. Boyce, A. Ozel, J. Kolehmainen, CFD-DEM Simulation of Hydrodynamics in Wet Gas-Solid Fluidized Beds Wet Gas-Solid Fluidization, AIChE Annu. Meet. San Fr. Ver. Staaten. (2016).

[39] C.M. Boyce, A. Ozel, J. Kolehmainen, S. Sundaresan, C.A. McKnight, M. Wormsbecker, Growth and breakup of a wet agglomerate in a dry gas-solid fluidized bed, AIChE J. 63 (2017) 2520–2527. doi:10.1002/aic.15761.

[40] C.M. Boyce, A. Ozel, J. Kolehmainen, S. Sundaresan, Analysis of the effect of small amounts of liquid on gas-solid fluidization using CFD-DEM simulations, AIChE J. (2017). doi:10.1002/aic.15819.

"Live as if you were to die tomorrow. Learn as if you were to live forever."

(Mahatma Gandhi, 1869-1948)

7

The Virtual Sandbox *

A substantial part of current research is the virtualization of production processes, products, or phenomena in nature via computational models. For example, our research group aims on modeling production processes for drugs in order to achieve maximum product safety at minimum production costs. The results of our research are simulation programs, which are often accessible only by experts, and hence are difficult to communicate to a broader audience. Virtualization of processes and products is, however, of outstanding importance, and, for example, will be one of the cornerstones of the next industrial revolution. The overall goal of the Virtual Sand Box project is to increase the general public perception of research in the area of wet granular materials. This is realized by means of a physical sandbox, which is integrated with the particle simulation environment LIGGGHTS®. Specifically, the surface of the sand is recorded using a 3D Camera, and the geometry is then fed into LIGGGHTS®. Finally, a virtual model of the real-world sand surface can be reconstructed, and the benefits of such a virtual sand model can be explored by the user.

---

* This chapter is based on:

I. M. Wu, E. Reichel, J.G. Khinast, S. Radl. The Virtual Sandbox. Austria Particle Forum. 3 (2016).

II. Reichel, E., Redlinger-Pohn, J. D., Wu, M., Ecker, K., Wachtler, L., Bahar, B., Khinast, J., Eck, J. & Radl, S, The Virtual Sandbox: Forschendes Lernen am Beispiel der Partikelphysik,. 2016 In: Plus lucis.3/2016, p. 43-47.

7.1 Introduction

Wet granular materials, or cohesive powder (i.e., "sticky sand") – are essential for many products and processes, such as in the pharmaceutical and food industries, geophysics or mining technology. Cohesive effects in collections of particles are also essential in astrophysics: these effects contribute to the formation of planets [1,2], they are important to explain the cohesion of comets and asteroids [3]. The key to this understanding lies in the description of tiny liquid bridges [4–6] connecting particles. However, the particle and liquid bridge scale generally can be rather small, so that experimental techniques to look inside into these particle systems are often not available. Therefore, using computers to model and virtualize granular material is of great importance for a variety of engineering applications. That is the reason we use computer simulation and virtualization for this science communication project. A substantial part of this project is the virtualization of production processes, products, or phenomena in nature via computational models. For example, our research group aims on modeling production processes for drugs in order to achieve maximum product safety at minimum production costs. The results of our research are simulation programs, which are often accessible only by experts, and hence are difficult to communicate to a broader audience. Virtualization of processes and products is, however, of outstanding importance, and, for example, will be one of the cornerstones of the next industrial revolution.

7.1.1 Goals and Structure

The main goal of this work is to attract the curiosity of young people for scientific or technical issues, as well as to strengthen intuitive learning abilities of young people, and to let students understand why simulations are important in scientific research. In a more general context, this project will finally give the target groups (i.e., students from elementary school, secondary school and the general public) a more concrete understanding in the thematic areas of (i) physics and fluid mechanics, (ii) particle and process engineering, (iii) geology and hydrology, (iv)

software development and electronic data processing, (v) 3D surface measurement technologies, and (vi) new communication media.

Specifically, the project is aimed on people of three target groups: (1) publics in primary schools, (2) pupils in secondary schools, as well as (3) students and interested individuals. Target group (1) will be conducted with the following questions to deliver the message of the project: “What is the recipe for a sand castle?”, “Why do sand castles fall when the sun shines on them?” Target group (2) will be conducted to perform real-life, and virtual experiments to experience the advantages of computer simulations. We will help them answering to the questions, such as “Why do we need computer simulations?”, “How do computer simulations work?” Furthermore, a number of exercises are designed to answer the following questions: “What are significant properties of particles, and how to measures these properties?”, or “How dense can we pack particles, and why can we build castle on wet particles while not on dry particles?” The strategy to transport the content will be developed to conform with Austria’s national education strategy focusing on competence-based teaching. Finally, the usage of the virtual sandbox, and details regarding the underlying technology will be offered to target group (3) through a variety of events. For example, we plan to present the virtual sandbox during the “Long night of Research”, or TU Graz’ open house event. The primary goal is to make this target group aware of the cost and benefits of simulation tools, or why the development of simulation programs takes such a long time. In the end, we will make the broader audience to be aware of simulation-based technologies by showing them with a number of simulation cases from industrial projects.

7.2 Methodology

7.2.1 The Virtual Sandbox

The part is the heart of this project, and it consists of a portable version of the AR Sandbox by Oliver Kreylos [7]. And the installation and operation of AR Sandbox

has been performed several times before [7]. The installation requires a powerful simulation computer, a high performance graphics cards, a 3D camera, as well as the mechanical design of the sandbox. A sketch of the components of the sandbox has been given in Figure 7.1. The technology of an AR Sandbox is based on the projection of computer calculation data (e.g., the sand surface positions and flow of a liquid on the sand) into the real sandbox. In the framework of this project, the AR Sandbox will be enlarged to simulate particle motion, or the penetration of liquid into the pore structure of sand mixture (see sketch Figure 7.1).

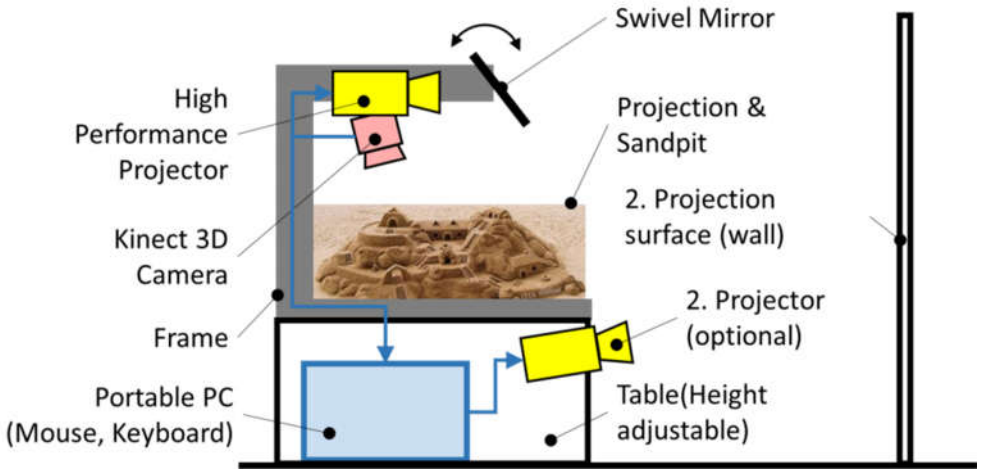

Figure 7.1: Sketch illustrating the concept of the virtual sandbox.

7.2.2 Surface Reconstruction and Simulations

A significant effort has been extended for the virtual sandbox software, to embed the particle simulation engine "LIGGGHTS ®"[8]. Specifically the surface of the sand which can be different shapes (i.e. the STL file of TU Graz Logo) has been reconstructed from the measured 3D data. This is realized by using existing software "Cloudcompare"[9], which contains a surface reconstruction algorithm[10]. Furthermore, "Cloudcompare" already enables grid in the appropriate format (i.e., STL, VTK) to export the geometry grid which can be directly used in the particle simulator (i.e., LIGGGHTS ®) (see sketch Figure 7.2).

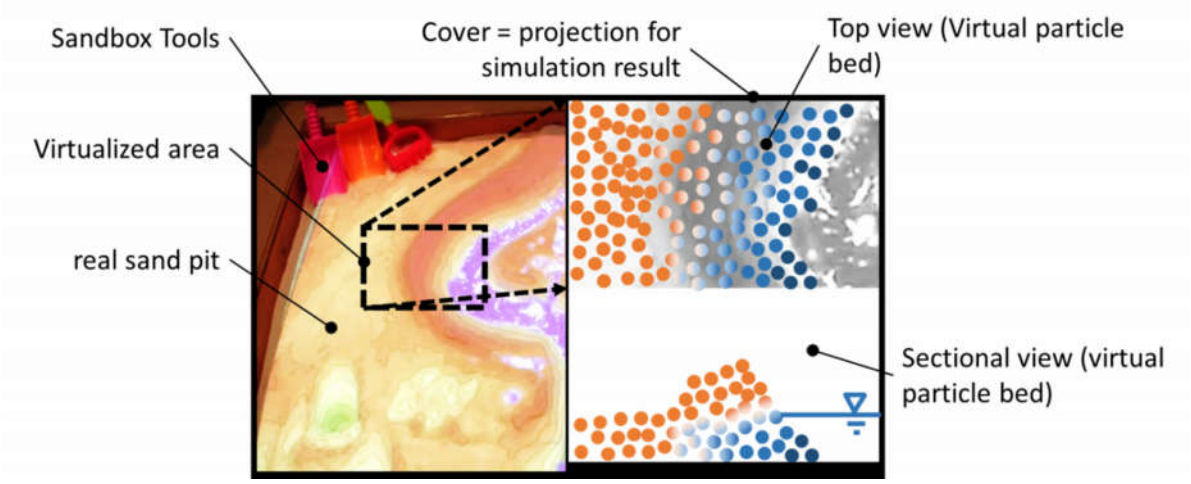

Figure 7.2: Planned virtual sandbox (point of view from the top, on the left half of the sandbox is to see the projection surface to the visualization of simulation results is shown on the right half of the already established version with extended reality).

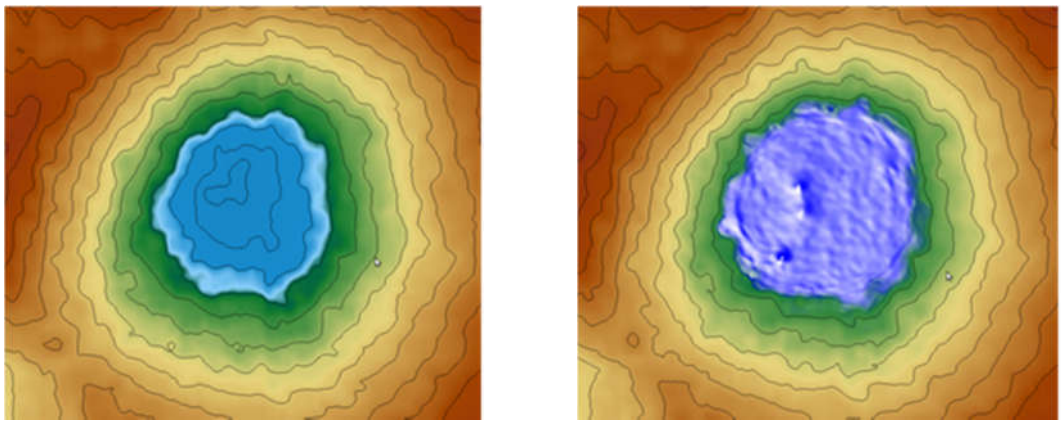

(a) (b)

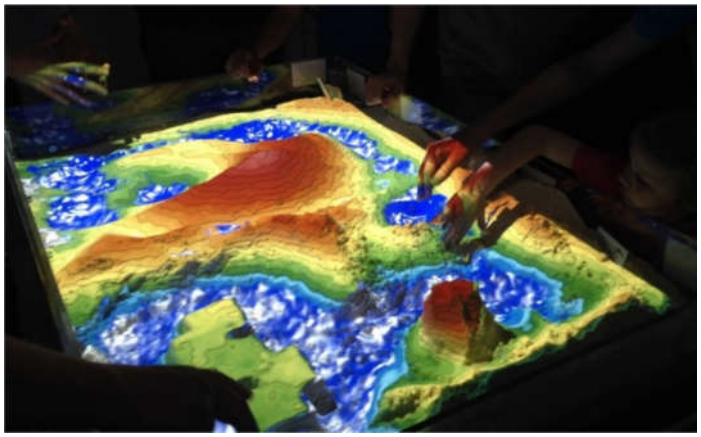

(c)

Figure 7.3: Sand surface based on different altitude without liquid (panel a), liquid injection in the region of lower altitude (panel b), the full virtual sandbox from the Langen Nacht der Forschung 2016 (panel c).

7.3 Results

The sandbox results are presented in two stages, in the first stage, we use the AR sandbox software to virtualize the sand surface based on different altitude of the surfaces, and inject liquid in the lower altitude region (i.e. a lake), that is what we call the virtual sandbox. The virtual liquid can also flow from high altitude region (i.e. mountain areas) to lower altitude region (i.e. lake regions) (see Figure 7.3).

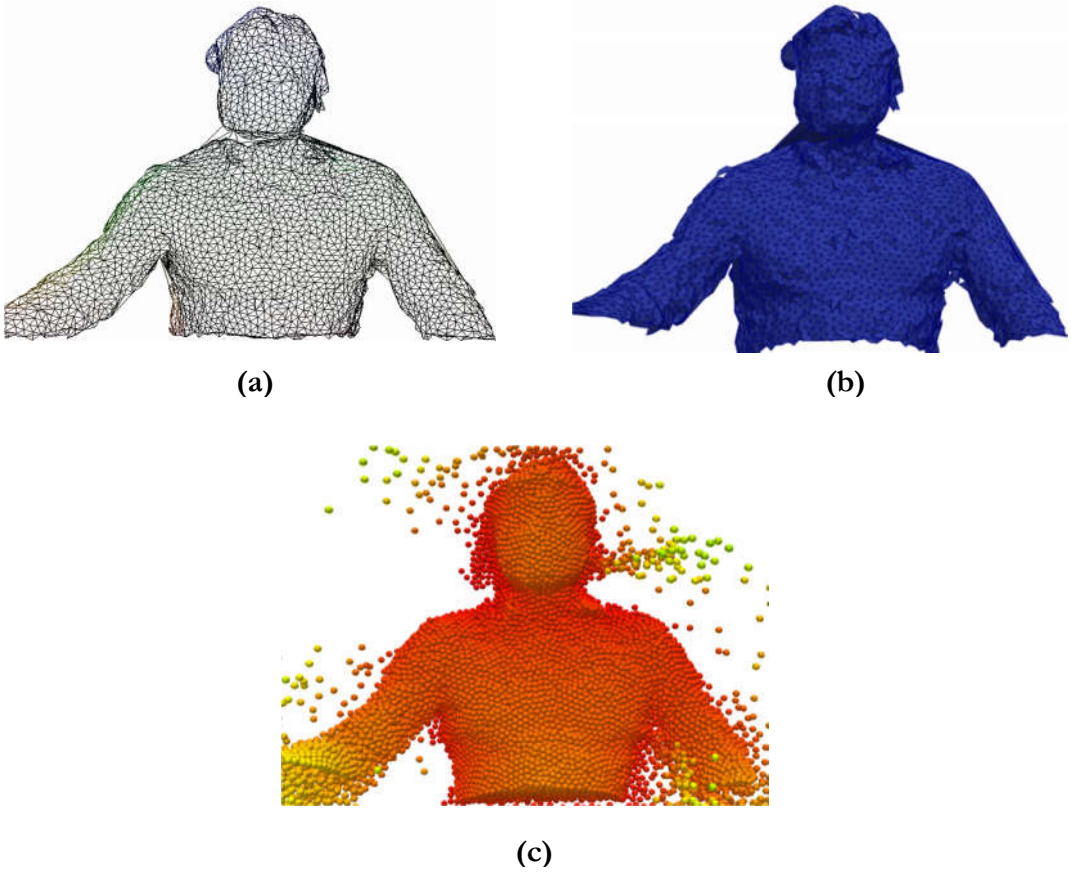

Figure 7.4: The procedure of conversion of figure a person by 3D camera to be fed into the particle simulator LIGGGHT® (a: 3D camera measure surface topology, b: generate triangle mesh, c: run simulation on the mesh).

The second stage, we use a Kinect sensor to capture the sand surface, and then convert this spatial information (i.e., data points on the sand surface) to STL-formatted files that can be read into LIGGGHTS®. We first test this procedure by using the 3D Kinect camera to measure the surface topology of a person (see Figure 7.4 panel a), then we generate the triangle mesh (see Figure 7.4 panel b),

finally we use the triangle mesh (STL file) in LIGGGHTS® to run simulation (i.e., filing particles into topology, see Figure 7.4 panel c). Another concrete example for testing the procedure is to record the surface of a TU Graz Logo by the 3D camera. The TU Graz Logo is constructed by wet sand in the real sandbox. Then, we convert the wall surface to a STL file, and load into LIGGGHTS® for simulation (an example is show in Figure 7.5).

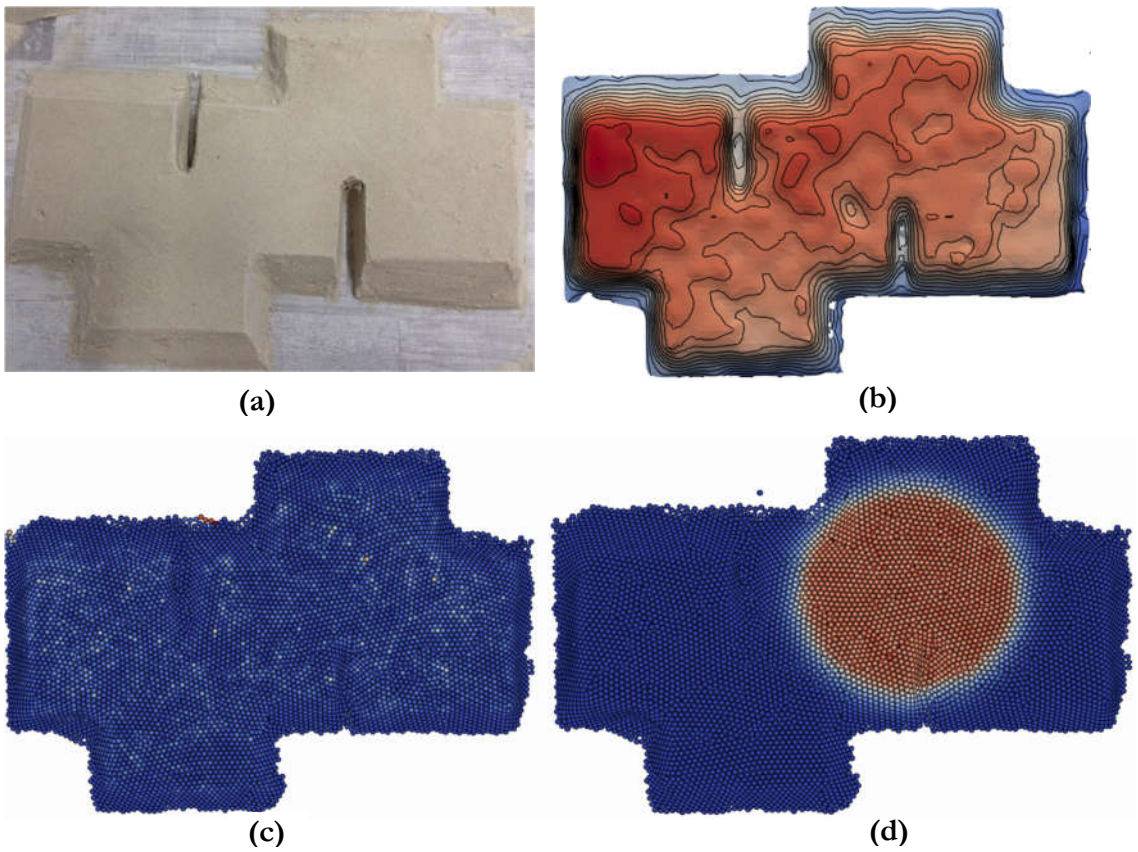

Figure 7.5: Conversion of the output of the Kinect camera to be fed into the particle simulator LIGGGHT® (i.e., a: camera output, c: conversion of the geometry to vtk and stl format, c: filling of the geometry with particles, d inject liquid on the particle bed to study liquid saturation).

As seen in Figure 7.5, panel (a) is camera output of a TUG logo surface composed of real wet sand, we then convert and reconstruct the geometry into a STL file (see panel (b)), this STL geometry can then be loaded in particle based software (LIGGGHTS®) for simulations. Panel (c) shows the filling of particles into the TUG logo STL geometry. Furthermore, we can do some experiment further, i.e.

liquid spreading on a static particle bed, as seen in panel (d), liquid saturate and spread on “TUG” logo particle beds.

7.4 Conclusions

The central product of the Virtual Sandbox project is, needless to say, a virtual sandbox: with a Kinect camera, a projector, a simulation computer and smart software available in the web, we can measure the 3D surface profile of the sand. With this information, one can compute height contours, or perform some simple simulations, e.g., the flow of water on the sand surface. All this can be projected back onto the sand surface, allowing users of the sandbox to interact with the calculations.

7.5 References

[1] F.G. Bridges, K.D. Supulver, D.N.C. Lin, R. Knight, M. Zafra, Energy Loss and Sticking Mechanisms in Particle Aggregation in Planetesimal Formation, Icarus. 123 (1996) 422–435. doi:10.1006/icar.1996.0168.

[2] J. Blum, G. Wurm, The Growth Mechanisms of Macroscopic Bodies in Protoplanetary Disks, Annu. Rev. Astron. Astrophys. 46 (2008) 21. doi:10.1146/annurev.astro.46.060407.145152.

[3] D.C. Richardson, P. Michel, K.J. Walsh, K.W. Flynn, Numerical simulations of asteroids modelled as gravitational aggregates with cohesion, Planet. Space Sci. 57 (2009) 183–192. doi:10.1016/j.pss.2008.04.015.

[4] S. Herminghaus, Dynamics of wet granular matter, Adv. Phys. 54 (2005) 221–261. doi:10.1080/00018730500167855.

[5] M. Scheel, R. Seemann, M. Brinkmann, M. Di Michiel, A. Sheppard, B. Breidenbach, et al., Morphological clues to wet granular pile stability., Nat. Mater. 7 (2008) 189–193. doi:10.1038/nmat2117.

[6] M. Wu, S. Radl, J.G. Khinast, A model to predict liquid bridge formation between wet particles based on direct numerical simulations, AIChE J. 62

(2016) 1877–1897. doi:10.1002/aic.15184.

[7] O. Kreylos, Augmented Reality Sandbox, (2015) http://idav.ucdavis.edu/~okreylos/ResDev/SARndbox.

[8] C. Kloss, C. Goniva, S. Amberger, S. Pirker, LIGGGHTS Open Source DEM: Models, Features, Parallelism and Quality Assurance, in: 8th Int. Conf. CFD Oil Gas, Metall. Process Ind., 2011. http://www.sintef.no/projectweb/cfdconf/.

[9] D. Girardeau-Montaut, CloudCompare, (2015). http://www.cloudcompare.org.

[10] M. Kazhdan, M. Bolitho, H. Hoppe, Poisson Surface Reconstruction, Proc. Symp. Geom. Process. (2006) 61–70. doi:10.1145/1364901.1364904.

"Don't cry because it's over, smile because it happened"

(Dr. Seuss, March 2, 1904 – September 24, 1991)

8

Conclusions and Outlook

8.1 Conclusions

A new model to predict dynamic liquid bridge formation between two wet particles has been presented in this thesis. This model is based on DNS data, which were obtained by extracting the interface position from VoF-based simulations of the bridge filling process. The liquid bridge volume was defined based on a characteristic neck position, and a direct integration method was employed to calculate the liquid bridge volume. This allowed us building a dynamic model for predicting the bridge volume, and the liquid remaining on the particle surfaces. Such a model might help to refine our picture of wet particle collisions that previously focused exclusively on predictions of the coefficient of restitution (Donahue et al.,[1], Sutkar et al.[2]). Our model differentiates between (i) a fast initial bridge formation stage where the dimensionless time is less than a reference time for capillary-driven viscous flow, and (ii) a subsequent slower viscous filling stage where viscous effects are dominant. The initial stage model is based on a geometrical reference volume, and has been calibrated with DNS data at a dimensionless time of $t^+ = 1$. Our initial stage model can be used as a first estimate for the liquid bridge volume in short particle collisions, and is an extension of the model prosed by Shi and McCarthy[3]. The postulated model for the viscous filling stage model relies on a universal parameter a_i (i.e., a characteristic dimensionless filling time), as well as dimensionless liquid mobility parameters ϕ_{m1} and ϕ_{m2} of the contacting particles. A model equation for these mobility parameters has been proposed. Specifically, we consider that the mobilities are functions of the film height and the separation distance. In summary, our model is valid for liquid bridge formation between two identical particles coated with thin continuous films (i.e., an initial relative film height of less than 10% of the particle radius). We observed that our results obtained from the DNS are independent of the Reynolds number, as well as the density ratio between the liquid coating the particles and the ambient gas. This suggests that

our model is applicable to a wide range of gas-particle systems involving wet particulate systems.

Liquid transport rate between two unequally-sized particles has been presented in Chapter 4. A liquid transport model to predict liquid bridge formation has been extended to bi-and polydisperse particle system. The model is based on DNS data which were obtained by extracting the interface position, defining the characteristic neck position, and integrating the interface position to quantify the liquid bridge filling process. This model allows us to predict the dynamically evolving liquid bridge volume, and the liquid remaining on the particle surfaces in polydisperse particle systems. Our more precise prediction of the bridge volume is essential for improved predictions of the liquid bridge rupture energy: a comparison of these differences when using the liquid bridge volume model of Shi and McCarthy [3] and our newly developed model reveals large differences for the rupture energy (see Appendix A in chapter 5). Thus, we expect that our dynamic model for the liquid bridge volume is especially important for dilute systems where energy dissipation during collisions is of critical importance. Our previous study indicated that grid refinement plays an important role in the final stages of film flow where the film ruptures. In order to get a precise model for the filling process at long times, as well as to correctly predict film rupture, it is essential to use a fine enough computational mesh in future simulations. This clearly limited the current study to axisymmetric configurations. Consequently, considering non-continuous films, e.g., discrete droplets present on the particles' surface, remains a task for future studies. However, we hope that our study is a significant step forward to better understand the equilibration of liquid residing on the surface of particles with that present in a liquid bridge.

In chapter 6, we employ a CFD-DEM approach to study the fluidization behavior of wet particles in small periodic domain based on newly developed bridge filling models (model B and model C) and the well-known model of Shi and McCarthy[3] (model A). For the particle system considered, we find that the

dynamic filling model (model C) has a small but significant effect on particle agglomeration, and consequently for the slip velocity, for some combinations of system parameters. It is instructive to recall that the rupture energy of a liquid bridge strongly depends on the liquid bridge volume, but not the liquid bridge force at contact. Thus, we conclude that the behaviour of wet fluidized particle system is mainly governed by agglomerate deformation and not agglomerate formation: we speculate that the average sedimentation speed (and hence the average size) of agglomerates depends critically on how easy it is to rearrange the particles inside such an agglomerate. Indeed, an inspection of the transient behaviour of the particles in our simulations indicates that the initial formation of aggregates is very fast, i.e., in the order of a few reference time scales $t_{ref} = u_t / g$. Note, our simulations must be run typically in the order of 100 t_{ref}, i.e., much longer, to collect meaningful statistics. Hence, the formation of the aggregate certainly cannot be rate limiting, and using arguments simply based on the outcome of a single collision (i.e., a "wet" restitution coefficient) are less useful. In summary, the ability of agglomerates to break is controlled by the bridge forces at particles contact, explaining the often marginal effect of the liquid bridge filling model. We would like to view our results also in the light of the recent findings of Boyce et al.[4,5], who studied partially-wetted fluidized beds of particles over a range of Bond and capillary numbers (i.e., up to 100 and 1,000, respectively). This previous research also concluded that an "agglomerate breakup" regime exists, in line with our findings. The key difference between the work of Boyce et al.[4,5] is that they were able to also identify an "agglomerate retention region", which is absent in our simulations since we assume that liquid is homogeneously spread initially. Anyhow, it is clear that an initial non-uniform liquid distribution will support arguments for using model C, since the liquid spreading rate (which is strongly affected by the bridge filling rate) affects system behaviour in addition.

8.2 Outlook

Our DNS simulation study indicates that grid refinement plays an important role in the final stages of film flow where the film ruptures. In order to get a precise model for the filling process at long times, as well as to correctly predict film rupture, it is essential to use a fine enough computational mesh in the simulations (i.e., the dimensionless grid resolution Δh should be 0.12 or smaller). This clearly limited the current study to axisymmetric configurations. Hence, our study is only a step forward to better understand the equilibration of liquid on particles and in liquid bridged in a particle bed. Still work needs to be done in the future, specifically, it would be interesting to: (1) experimentally support the observed film rupturing event for long times; (2) investigate the wetting of initially completely dry particle, and particles that have a complex morphology; (3) quantify the effect of particle relative motion on the liquid bridge formation process. Consequently, considering non-continuous films, e.g., discrete droplets present on the particles' surface, remains a task for future studies. However, we hope that our study is a significant step forward to better understand the equilibration of liquid residing on the surface of particles with that present in a liquid bridge.

Also, regarding the CFD-DEM studies that aim on the dynamics of wet fluidized beds, we would like to stress that a critical limitation of our current work was the assumption that liquid is uniformly distributed on the particle surface. Clearly, in case of high Ca numbers liquid spreading rates can be limited (to some extend) by bridge filling. In such a case, one would also clearly prefer a dynamic liquid bridge model to realistically picture the transport of liquid throughout the system. Finally, future work could probe the effect of particles stiffness, as well as work towards suitable experimental validation. Unfortunately, the latter is difficult due to difficulties to accurately measure the liquid distribution in moving granular materials.

The knowledge gained during this thesis could be useful to dynamically predict liquid transport from particle surfaces into bridge region based on DNS data. This model can then be implemented into DEM code to handle more particles (e.g., half millions of particles in a periodic domain). Future work could focus on experimentally studying the process of liquid bridge formation between two particles. This will require robust image acquisition and illumination hardware (i.e., a high speed camera and LED panels), as well as smart software to calculate and interpret the image data (e.g., the neck positions of film height during bridge formation process). Also, it would be interesting to measure the slip velocity of wet fluidized beds of particles as well as the liquid saturation of particles. Measuring the rate of liquid transport among particle clusters in process engineering is expected to be useful for, e.g., coating and dry in pharmaceutical engineering, where the homogeneity of the liquid film on a single particle or particle attrition is of interest.

8.3 References

[1] C.M. Donahue, C.M. Hrenya, R.H. Davis, Stokes's cradle: Newton's cradle with liquid coating, Phys. Rev. Lett. 105 (2010) 34501. doi:10.1103/PhysRevLett.105.034501.

[2] V.S. Sutkar, N.G. Deen, T.P. Johan, J.A.M. Kuipers, V. Salikov, B. Crüger, et al., A Novel Approach to Determine Wet Restitution Coefficients Through a Unified Correlation and Energy Analysis, AIChE J. 61 (2015) 769–779. doi:10.1002/aic.

[3] D. Shi, J.J. McCarthy, Numerical simulation of liquid transfer between particles, Powder Technol. 184 (2008) 64–75. doi:10.1016/j.powtec.2007.08.011.

[4] C.M. Boyce, A. Ozel, J. Kolehmainen, S. Sundaresan, C.A. McKnight, M. Wormsbecker, Growth and breakup of a wet agglomerate in a dry gas-solid fluidized bed, AIChE J. 63 (2017) 2520–2527. doi:10.1002/aic.15761.

[5] C.M. Boyce, A. Ozel, J. Kolehmainen, S. Sundaresan, Analysis of the effect of small amounts of liquid on gas-solid fluidization using CFD-DEM simulations, AIChE J. (2017). doi:10.1002/aic.15819.